Advances in Civil Engineering

Noise and Vibration Caused by Transportation Infrastructure Systems

Lead Guest Editor: Chao Zou
Guest Editors: Wei He, Quanmin Liu, and Ziyu Tao

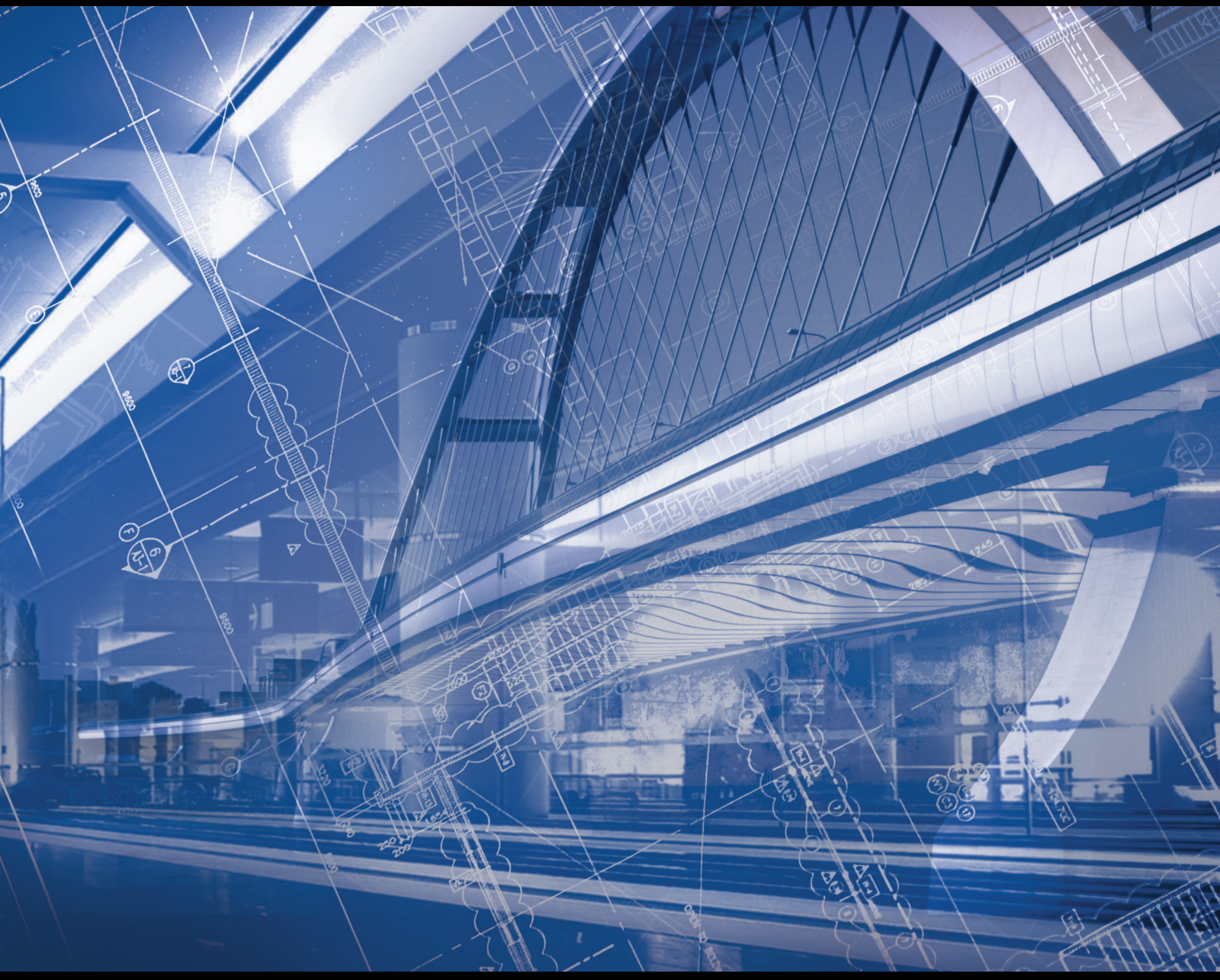

Noise and Vibration Caused by Transportation Infrastructure Systems

Advances in Civil Engineering

Noise and Vibration Caused by Transportation Infrastructure Systems

Lead Guest Editor: Chao Zou
Guest Editors: Wei He, Quanmin Liu, and Ziyu Tao

Contents

A Case Study on Annoyance Noise Caused by Metro Railway at a TOD Developed Depot
Qiang Liu, Zhongxu Kang, Hougui Zhang, Ruixiang Song, and Ge Li
Research Article (10 pages), Article ID 3173567, Volume 2022 (2022)

Clock Synchronization Algorithm for Structural Modal Measurement
Junliang Hu, Kai Li, Chaoxian Yan, Huawei Guo, Nannan Cui, Shiping Huang, and Xiaoyan Ding
Research Article (9 pages), Article ID 7864160, Volume 2022 (2022)

Hindawi
Advances in Civil Engineering
Volume 2023, Article ID 5213452, 14 pages
https://doi.org/10.1155/2023/5213452

Research Article

Seismic Reduction Performance of Wrap Rope Connection Devices for Continuous Girder Bridges

Yanfang Liu,[1,2] **Wenxue Zhang**,[1] **Xiuli Du**,[1] **and Weigang Bao**[2]

[1]*College of Architecture and Civil Engineering, Beijing University of Technology, Beijing 100124, China*
[2]*China Communications Construction Company Limited, Beijing 100088, China*

Correspondence should be addressed to Yanfang Liu; liuyanfang1@ccccltd.cn

Received 18 August 2022; Revised 19 September 2022; Accepted 24 November 2022; Published 7 March 2023

Academic Editor: Wei He

In this article, wrap rope connection device (WRCD), which considers the relative acceleration of piers and beam as a control variable, is proposed for improving the current situation of continuous girder bridges whose bearing force of a single pier is along the longitudinal direction and based on the synergy principle. The WRCD device, which meets the slow displacement requirements of temperature and vehicle load under normal operation, is implemented and used to improve the performance of the sliding bearing pier. During earthquakes, because of the amplification effect of the wrap rope, the instantaneous large stiffness state in the longitudinal force can be achieved. Based on the shaking table test of a typical continuous girder bridge for examining the performance of the WRCD during earthquakes, the dynamic characteristics, structural acceleration, displacement, and strain responses of the structure under different frequency spectra, and seismic input intensities are analyzed and the seismic reduction performance of the WRCD is demonstrated. This analysis demonstrated that, by activating WRCD, the ratio of the acceleration response of the fixed bearing pier to the sliding bearing pier increased from 10% to 57%; moreover, the force on each pier appeared more uniform. Furthermore, with an increase in the input intensity of the earthquake, the displacement of the primary beam and the seismic response of the fixed pier bottom considerably decreased and the synergy effect of each pier was more prominent. Under certain site conditions, the WRCD can effectively improve the synergy effect between the sliding bearing piers and fixed bearing pier; however, the improvement in the obtained result is directly associated with the seismic input characteristics. The design parameters of the WRCD should be determined as per different site conditions and the optimum application range of the WRCD.

1. Introduction

Continuous girder bridges are bridge structures commonly used in practical engineering. They account for >40% of the total length of bridges in China. Moreover, in recent years, the construction of continuous girder bridges has shown a gradually increasing trend in quantity and the span of such bridges has steadily increased. The number of spans between the expansion joints has increased from 3-4 to 10–12, and the length of expansion joints are large. With an increase in span and expansion joint length, the design status has not sufficiently changed for the single-fixed bearing to meet the displacement requirement caused by temperature and vehicle load along the longitudinal direction. During earthquakes, the longitudinal seismic load of the superstructure is almost completely held by the single-fixed bearing pier, and the seismic potential of the sliding bearing piers is not completely utilized with the same structural size [1]. Although the ductility of fixed bearing piers can improve the aseismic performance of structures by increasing the reinforcement ratio, this method requires to inevitably produce certain damage in the structure, which is challenging to repair. The most common method to improve the seismic performance of the continuous girder bridges is by installing multiple isolation devices. Researchers have performed substantial research on installing isolation bearings and viscous dampers for continuous beam bridges and obtained considerable research results [2–8]. Kelly and

Eidinger [9] and Kelly [10] proposed the system theory and design method of laminated rubber bearing and performed tensile test research on their approach. Tyler and Robinson [11], Hwang et al. [12], and Abe et al. [13] performed tests on lead-core rubber bearings and obtained the equivalent linear model and hysteretic energy dissipation performance of lead-core rubber bearings. Peng et al. [14] and Zhang et al. [15] examined the seismic behavior of hyperboloid spherical supports. Ou et al. [16], Yan et al. [17], and Shen et al. [18] developed new composite metal dampers and examined their performances. The abovementioned research results provide a foundation for the research and design of bridge damping and isolation. However, no matter what type of damping and isolation device is adopted, a large relative displacement should be employed to achieve the ideal damping effect.

However, irrespective of the dampers and energy dissipation devices used, the ideal energy dissipation performance can be achieved only under large relative displacement between the beam and piers, and the initial stiffness of the energy dissipation devices does not match that of the fixed bearing. Therefore, the aseismic performance of the sliding bearing piers is not completely utilized, and the condition for the single-fixed bearing pier loaded alone has not been fundamentally changed. In recent years, some researchers have conducted systemic research on lock-up devices. However, these devices do not effectively reduce the seismic response of low piers [19, 20]. Owing to the challenges in price and maintenance, they do not have several applications in practical engineering.

Based on the synergy principle on which the wrap rope connection device (WRCD) is proposed, the seismic reduction performance of the WRCD under strong earthquakes has been examined through the shaking table test of a typical continuous beam bridge. The WRCD, which considers the relative acceleration of piers and beams as a control variable, is proposed in this study to improve the current situation of continuous girder bridges whose bearing force of a single pier is along the longitudinal direction and is based on the synergy principle. The WRCD is implemented and used to improve the performance of the sliding bearing pier. The study of different frequency spectra and input intensities were analyzed to reveal the seismic reduction performance of the WRCD through the dynamic characteristics, structural acceleration, displacement, and strain responses of the structure. This result provided a reference for its application in similar bridge structures.

2. Design of WRCD

The WRCD structural diagram is shown in Figure 1. Under normal operation conditions, the WRCD can meet the requirements of slow displacement of the temperature and vehicle load. During earthquakes, the relative acceleration between piers and the beam is considered the controlling variable to activate the rotating inertial force of the mass block, which is attached to the rotating shaft. Greater friction is then generated, which is amplified by the loops of wrap rope through the friction shaft and causes large instantaneous stiffness in the sliding bearing piers and attains the "Lock-up" state. The seismic inertial force of the superstructure is shared between the sliding bearing piers and the fixed bearing pier. Thus, the seismic response of the fixed bearing pier and the longitudinal displacement of the beam ends are reduced. When the input energy of an earthquake is considerable, certain energy can be consumed by the frictional force of the wrap rope, and seismic reduction performance is achieved. The WRCD comprises a rotating shaft ①, additional mass block ②, device backing plate ③, support plate ④, leg ⑤, winding cable ⑥, friction shaft ⑦, and assembly bolt ⑧. The WRCD is proposed based on the principle that uses the friction between the rope and wooden pile to form a self-locking system. When there is a relative movement trend, it can produce considerable friction.

3. Design of Shake Table Tests

3.1. Material Selection. There are multiple materials suitable for developing shaking table test models. Owing to the influence of material selection on the test results, the examination of the mechanical properties and selection criteria of the materials that are selected in the tests is necessary. The materials used vary as per the purposes of the tests. For example, elastic materials, such as steels and plexiglass, are generally used to study the response rules of structures, and elastic-plastic materials, such as concretes, are typically used to examine the damage characteristics and failure modes of structures.

The purpose of the shaking table test is to study the seismic reduction performance of the WRCD during earthquakes and to analyze the dynamic characteristics, acceleration, displacement, and strain responses of the structure under different frequency spectra and input intensities of earthquake excitation. The main beam and piers are composed of the steel material Q345D.

3.2. Similarity Coefficients. Determining three independent similarity coefficients as the primary similarity ratio in the shaking table test model design is usually necessary, and the similarity ratio of other physical quantities can be deduced using the basic similarity ratio. In practice, owing to the limitations of laboratory conditions and model materials, all physical quantities cannot be guaranteed to satisfy the similarity ratio. Therefore, we can obtain certain deduced similarity coefficients, the basic similarity coefficients of the design model, and other similarity coefficients of different physical quantities.

The maximum weight of the shaking table is 20 t and the size is 3 m × 3 m. The similarity coefficient of the length of the model is 1/30, which is affected by the size and the maximum bearing capacity of the shaking table. The similarity coefficient of acceleration is set to one. As the main beam and piers of the original structure are concrete materials, the similarity coefficient of the elastic modulus is 6.338. The similarity coefficients of other physical quantities

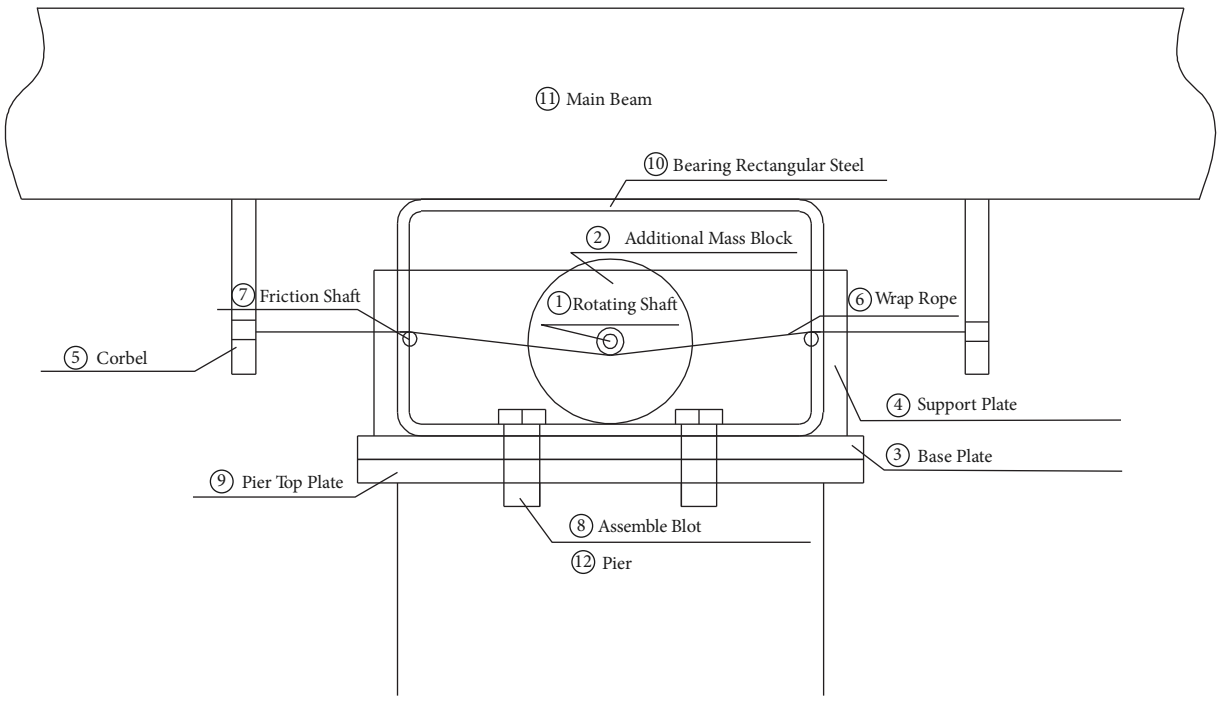

Figure 1: Wrap rope connection device structural diagram.

are derived using these three similarity coefficients. Table 1 lists the similarity ratio of each physical quantity.

3.3. Model Design. Based on the research of a typical continuous girder bridge with a span of $40.55 + 72 + 40.55$ m, a scale model was designed as per the aforementioned similarity ratio. For the shaking table test, the piers were considered as per the equal pier height. The height of the pier was designed as per the geometric similarity coefficients, and the section of the piers was designed as per the equivalent bending stiffness, which neglected the torsional stiffness and compressive stiffness; therefore, the rectangular pipe section was adopted for the simulation. The design parameters of the bridge piers are shown in Table 2. The main beam was modeled as a box section welded by channel steel 20B and steel plates.

3.4. Bearing Design. Four unequal edge angle steel were fixed with the ear plate at the bottom of the main beam and the bolt rod at the top of the piers to model the fixed support. The short leg of the unequal edge angle steel was fixed with the pier using M15 bolts, and the long leg was connected to the ear plate of the main beam using M12 bolts, as shown in Figure 2. The sliding bearing was designed using the integration of the support and WRCD. The base plate of the WRCD was fixed using a pre-embedded bolt rod at the top of the pier, and the sliding bearing was modeled as a polytetrafluoroethylene plate fixed between the $180 \times 100 \times 5\,\text{mm}^3$ rectangular steel plates arranged on the left and right sides of the base plate of the WRCD and the main beam, as shown in Figure 3.

Table 1: Similarity coefficients of every physical quantity (prototype/model).

Physical quantity	Similarity coefficient
Length (L)	1/30
Displacement (δ)	1/30
Elastic modulus (E)	6.338
Stress (σ)	6.338
Density (ρ)	190.154
Velocity (v)	0.183
Acceleration (a)	1
Time (t)	0.183
Frequency (f)	5.48
Stiffness (k)	0.211

3.5. Counterweight Design. Inertial force is the essential factor for the dynamic response of the structure [21–28] and inertial force, which has a causal relationship with the mass. Therefore, in the shaking table test, to accurately simulate the dynamic response characteristics of the model structure during earthquakes, the similarity in equivalent mass between the prototype structure and the model structure is an inevitable factor to be considered. As per the similarity criterion, the model material requires high density; however, the material itself cannot be realized. Therefore, manually adding mass is required for ensuring that the structure meets the quality similarity conditions.

This model uses a counterweight block to add mass. The mass of the counterweight block was divided into 5 and 10 kg, and the actual counterweights of the main beam and pier were 840 and 400 kg, respectively, as shown in Table 3.

Table 2: Comparison of replacement parameters of pier material.

	E (N/mm^2)	I_x (mm^4)	I_y (mm^4)	EI$_x$	EI$_y$
Prototype pier	3.250×10^4	2.310×10^{14}	9.760×10^{13}	—	—
Design	2.060×10^5	2.810×10^6	11.875×10^5	5.790×10^{11}	2.446×10^{11}
Actual	2.060×10^5	2.5520×10^6	8.477×10^5	5.260×10^{11}	1.746×10^{11}

Figure 2: Connection of fixed bearing pier.

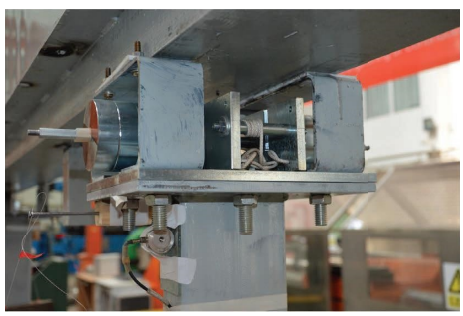

Figure 3: Connection of sliding bearing pier.

Table 3: Additional weight details.

Location	Prototype quality (t)	Model quality (kg)	Model deadweight (kg)	Calculate counterweight (kg)	Actual counterweight (kg)
Beam	5594.2	924.5	167.7	756.8	840
Pier	2116.69	349.8	16.2	333.6	400
Sum	7710.89	1274.3	183.9	1090.5	1240

3.6. Measuring Point Layout. The layout of measuring points primarily considers the dynamic characteristics, seismic response of the structure and stress, and deformation of key parts. A total of thirty-seven sensors were arranged in the entire bridge to test the dynamic characteristics and the seismic response of the structure. The layout of each sensor is shown in Figure 4. Among them were four pull-wire displacement sensors for measuring the absolute displacement of the main beam and pier top. There were five accelerometers to measure the acceleration at the beam end, pier top, and tabletop. There were four strain flowers (three channels for each strain flower), and 16 strain gauges were symmetrically arranged at the pier bottom to measure the strain.

4. Results and Discussion

Four ground motion records, namely, 1976 Qian An (EW), 1940 EL Centro (NS), 1952 Taft, and 1976 Tian Jin (NS), were selected as the seismic loading for different frequency spectra. The test ground vibration input is directly selected to represent the typical measured seismic records of different site types for shaking table tests. The selected measured seismic recording waves are the Qian'an wave with a duration of 21.93 s and the peak of 97.36 gals for the Class I sites; the El-Centro wave with a holding time of 53.73 s and a height of 341.7 gals for Class II sites; Taft wave with a holding time of 54.38 s and a peak of 175.83 gals for Class III sites; and Tianjin wave with a holding time of 19.19 s and

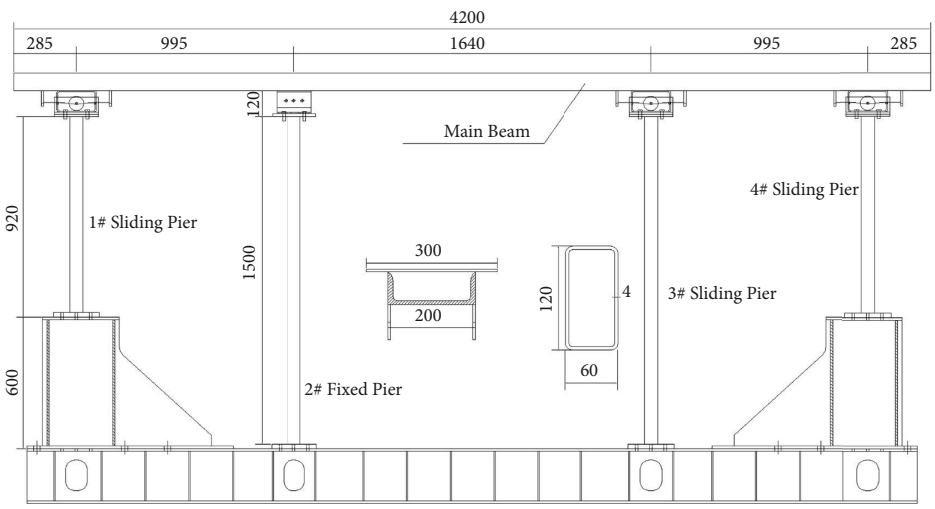

Figure 4: Layout of measuring points.

a height of 145.8 gals for Class IV sites. The Seismo Signal program is used to modify selected time histories such that the peak acceleration and period are compatible with the similarity coefficients. Figure 5 shows the time history used in the test for selected ground motion, and Figure 6 shows the response spectra for a selected ground motion for a 5% damping level.

4.1. Acceleration Responses. Figures 7–10 show the variation trend of the peak acceleration of each pier with different seismic input intensities under the action of EL Centro. For the sliding bearing piers, the maximum acceleration response value of the piers with WRCD decreases more than that without WRCD. For the fixed bearing pier, the maximum acceleration response value with WRCD increases compared to that without WRCD. The results demonstrated that when the WRCD is activated, the sliding bearing piers share the longitudinal seismic force of the superstructure, which is originally subjected to the fixed bearing piers.

Figure 11 shows the columnar comparison of the maximum acceleration response value of each pier with and without WRCD for a seismic peak acceleration of EL Centro wave of 0.4 g. The figure shows that after the WRCD was activated, the longitudinal overall stiffness of the structure increased, and the maximum acceleration response value of each sliding bearing piers decreased by 25%. The maximum acceleration response value of the fixed bearing pier increased by ~4.6 times.

The response of each pier tends to be uniform. The maximum acceleration response value of a fixed bearing pier without WRCD was ~10% of the maximum response value of the sliding bearing pier. After the WRCD was activated, the maximum acceleration response value of the fixed bearing pier was ~57% of the maximum response value of the pier with the sliding bearing pier.

4.2. Dynamic Characteristics. The test model is divided into two types: with and without WRCD. The basic period of the model structure can be obtained using the transfer function. Before each working condition, the structure is swept by white noise to measure the natural vibration rate of the model to determine whether the dynamic characteristics of the structure have changed. Table 4 shows the variation trend of dynamic characteristics of the two models under different working conditions. For the steel structure, the natural frequency of the structure slightly changes, indicating that the structure is still in the elastic stage with and without WRCD. Compared with the test model without WRCD, the natural frequency of the structure is reduced after using WRCD because there are five counterweights on both sides of the device. Owing to the increase in mass, the natural frequency of the model with WRCD is smaller than that without WRCD. The natural frequency with WRCD increases after a peak acceleration of 0.4 g, which demonstrates that with the change in ground motion input intensity, the dynamic characteristics of the bridge structure with WRCD changes, the function of the device considerably improves, and the overall performance of continuous girder bridges can be improved.

4.3. Displacement Responses. Figures 12–15 show the variation trend of the maximum displacement at the sliding bearing piers and the girder with the different seismic input intensities under the action of EL Centro. For the sliding bearing piers, the maximum displacement response value of each pier with WRCD generally increased compared to that without the WRCD. The displacement of the 1# sliding bearing pier increased by 33% on average, the 3# sliding bearing pier increased by 87% on average, and the 4# sliding bearing pier increased by 61% on average. The maximum displacement response value of WRCD was lower than that without the device for the 2# fixed bearing pier, with an average decrease of 31%.

For each sliding bearing pier without the device, the changing range of the maximum displacement response value of piers with the seismic input intensity was relatively less. When the peak acceleration was 0.1~0.4 g, the difference

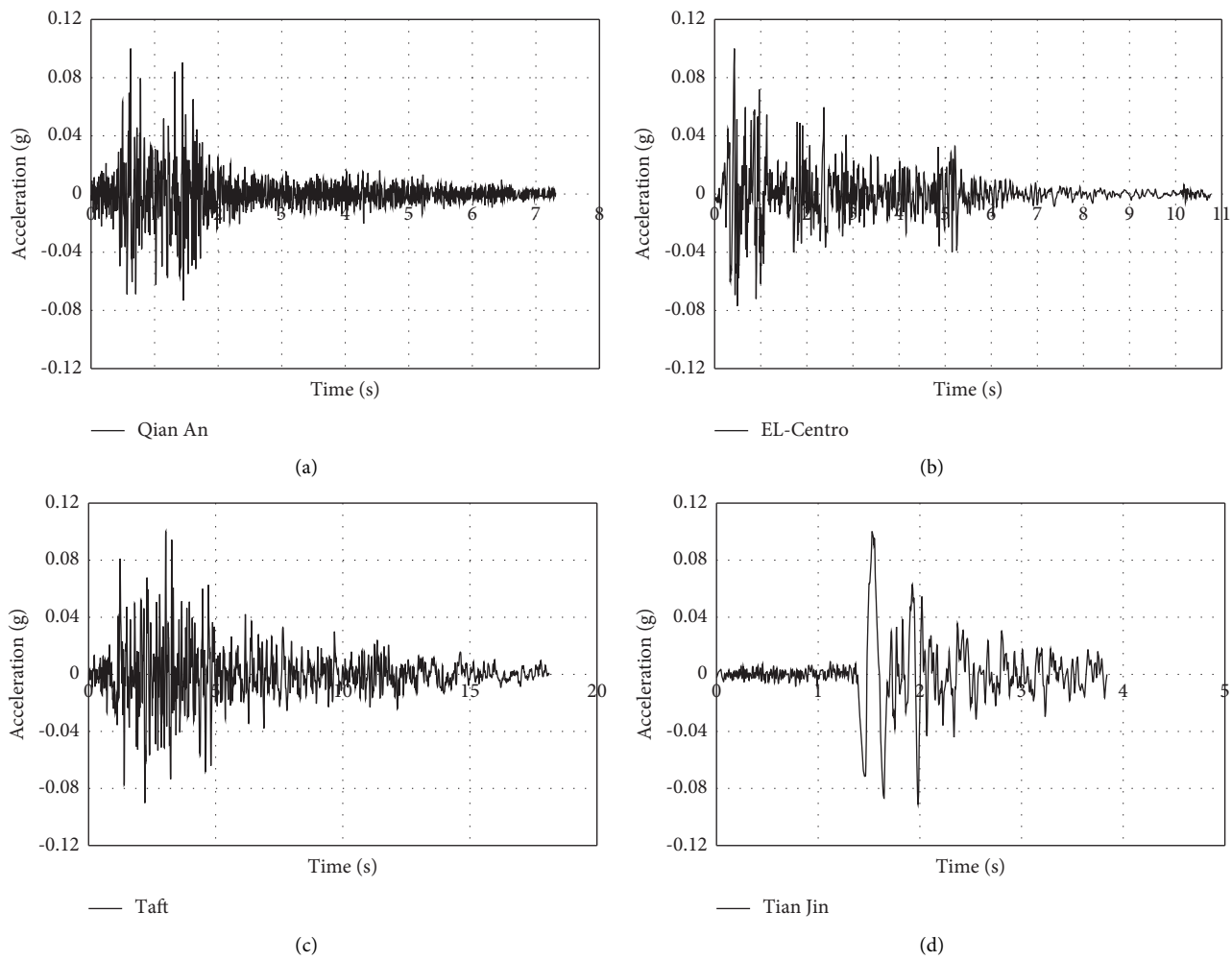

Figure 5: Time history curve of different ground motions: (a) Qian An, (b) EL-Centro, (c) Taft, and (d) Tian Jin.

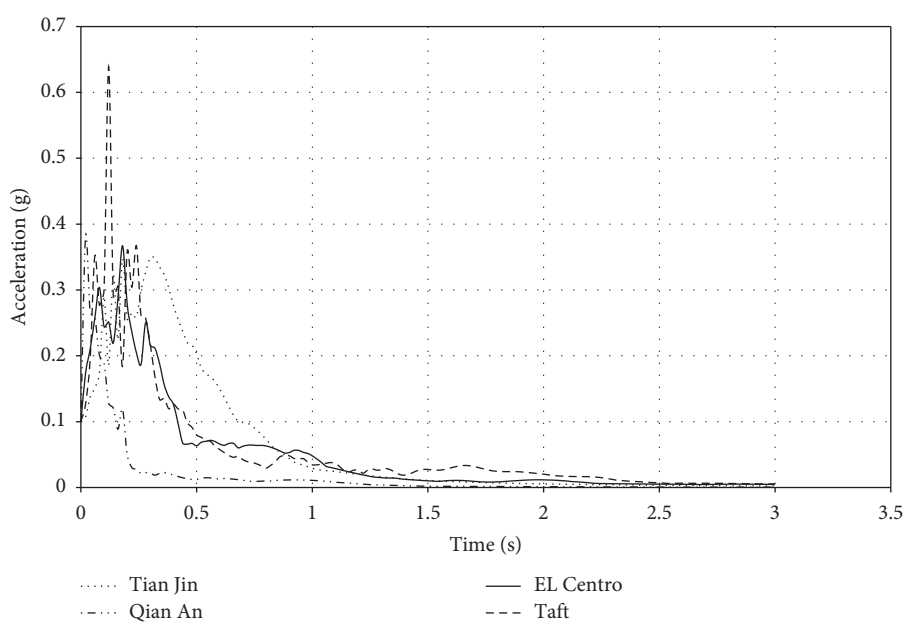

Figure 6: Response spectra of acceleration.

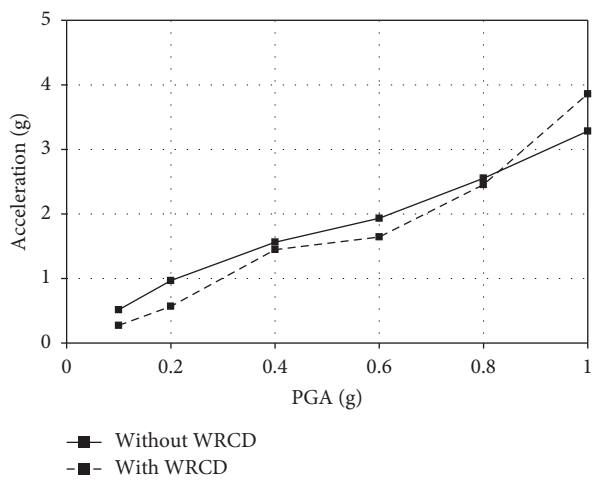

Figure 7: Maximum acceleration of 1# sliding pier top.

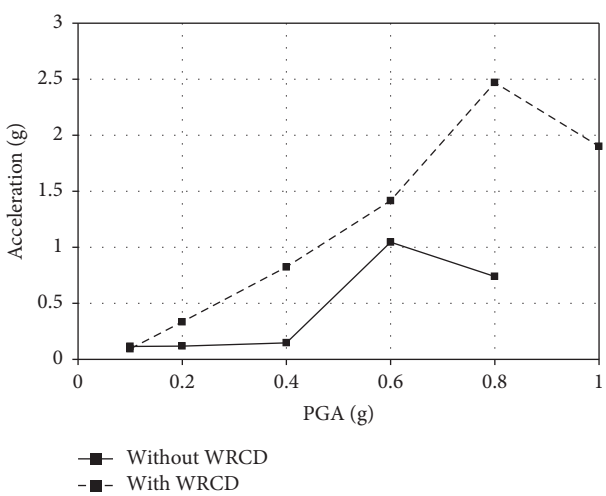

Figure 8: Maximum acceleration of 2# fixed pier top.

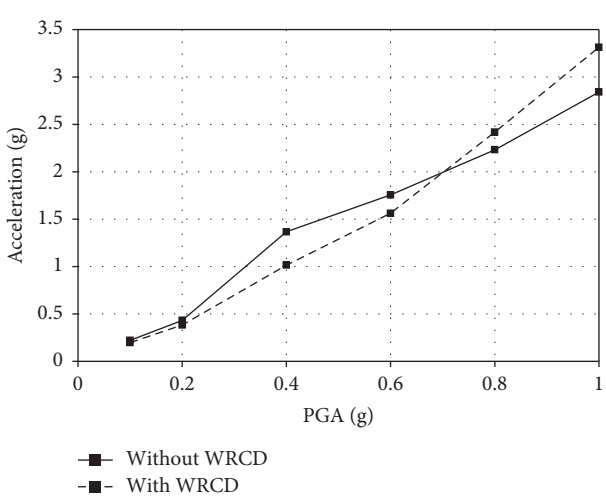

Figure 9: Maximum acceleration of 3# sliding pier top.

between the maximum displacement response values of the two models was small. The maximum displacement response value of piers with WRCD rapidly increased with the change

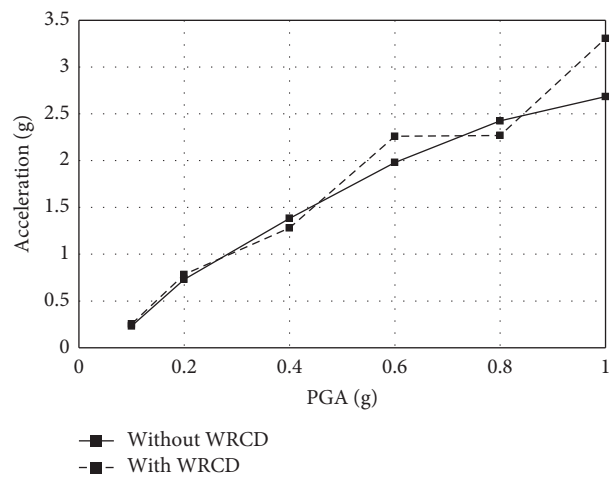

Figure 10: Maximum acceleration of 4# sliding pier top.

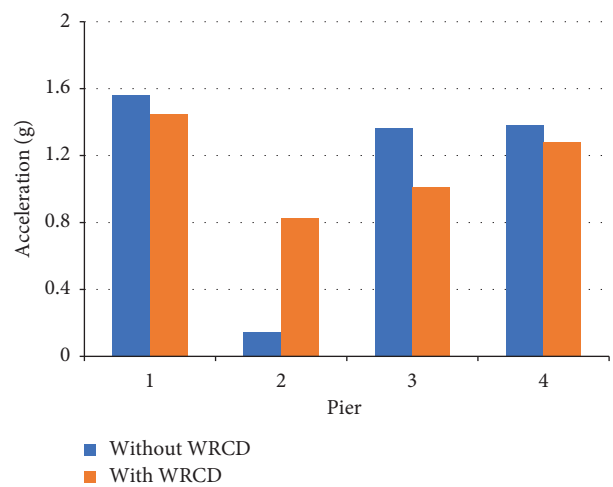

Figure 11: Maximum acceleration of pier top under El Centro input.

Table 4: Natural frequency of the two-test model.

Working condition	Without WRCD (Hz)	With WRCD (Hz)
Before loading	3.654	3.197
0.1 g	3.652	3.194
0.2 g	3.657	3.205
0.4 g	3.652	3.194
0.6 g	3.651	3.248
0.8 g	3.649	3.250
1.0 g	3.655	3.250

in seismic input intensity when the peak acceleration was between 0.6 and 1.0 g, for the setup without the device. The maximum difference in displacement between the two models was large. This demonstrates that when the WRCD is activated, the sliding bearing piers participate in the longitudinal force of the structure and share part of the inertial force of the main beam. With increasing seismic input intensity, the performance of WRCD is more prominent and the overall performance of the continuous girder bridge can be improved.

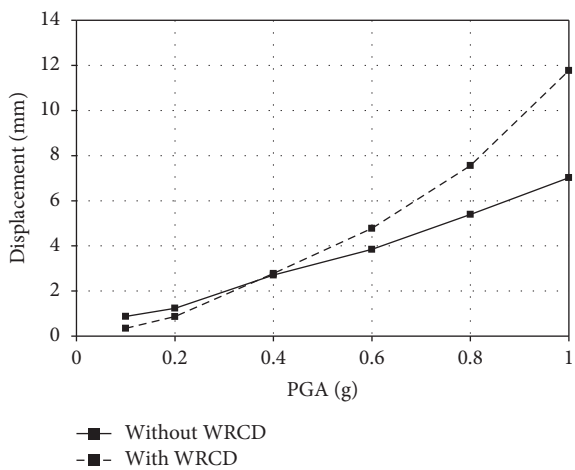

Figure 12: The maximum displacement of 1# sliding pier top.

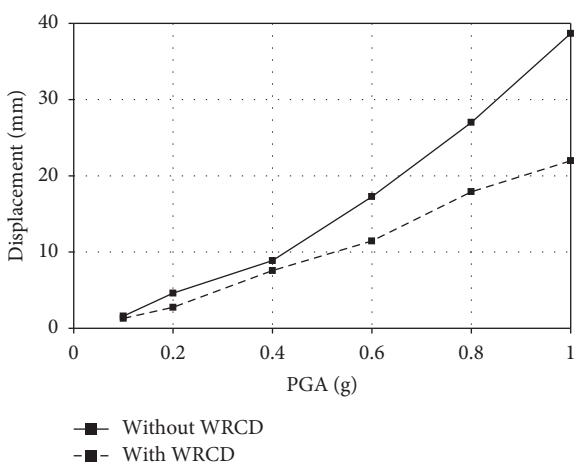

Figure 13: The maximum displacement of 2# fixed pier top.

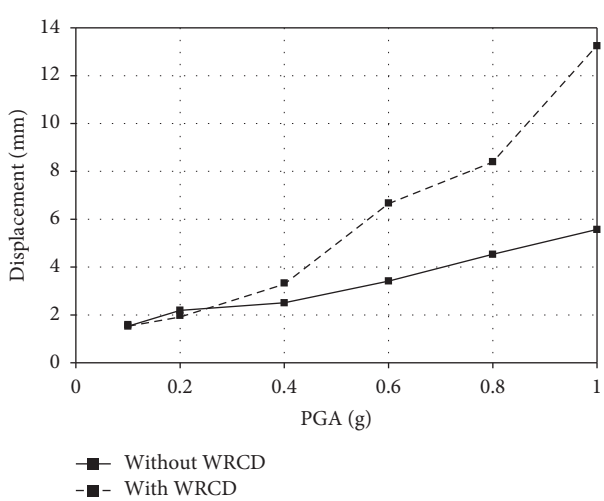

Figure 14: The maximum displacement of 3# sliding pier top.

4.4. Strain Responses. Figures 16–19 show the variation trend of the maximum strain response at the bottom of each pier with different seismic input intensities under the action

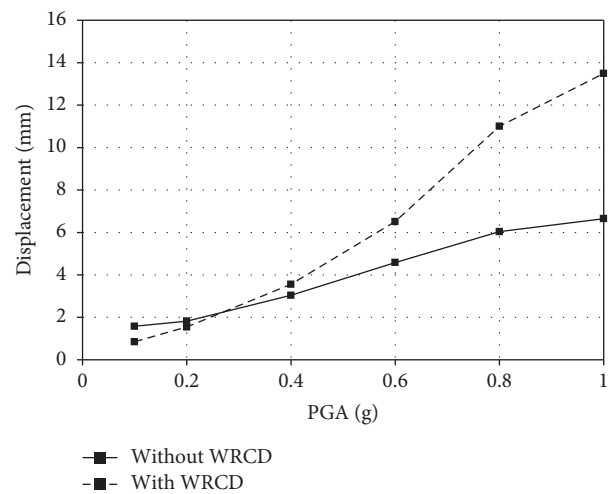

Figure 15: The maximum displacement of 4# sliding pier top.

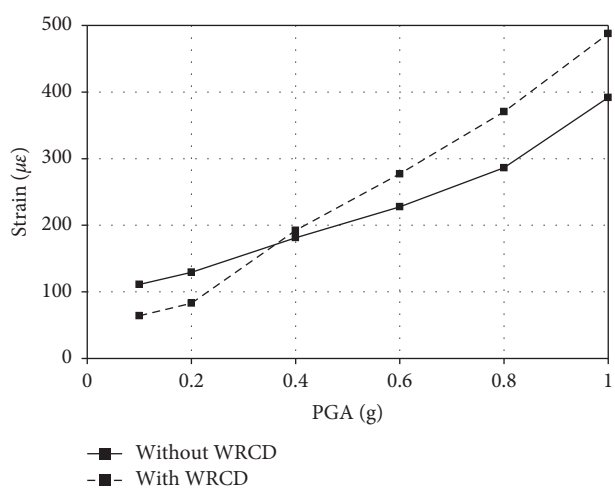

Figure 16: Maximum strain response at 1# sliding pier bottom.

of EL Centro. For sliding bearing piers, when the peak acceleration was 0.1–0.4 g, the maximum strain response value with WRCD was slightly lower than that without WRCD and the average reduction range was 30%. When the peak acceleration was 0.4 g, the two were close and the variation range was 7%. When the peak acceleration was 0.6–1.0 g, the maximum strain response value of the pier bottom of each pier with WRCD greatly increased than that without WRCD, and the average increase range was 50%. For the maximum strain response value of 2# fixed bearing pier bottom, the value with WRCD was lower than that without WRCD and the maximum decrease was 36% when the peak acceleration was 1.0 g.

From the variation trend of the curve, the maximum strain response at the bottom of each pier linearly changed with the seismic input intensity. For the sliding bearing piers without WRCD, the variation trend of the maximum strain response at the pier bottom with the seismic input strength was relatively low, whereas, with WRCD, the variation trend of the maximum strain response at the pier bottom with the seismic input strength was relatively steep. This indicated

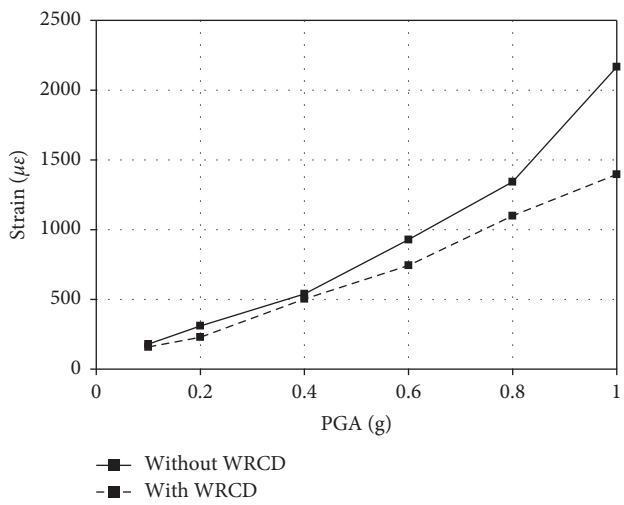

Figure 17: Maximum strain response at 2# fixed pier bottom.

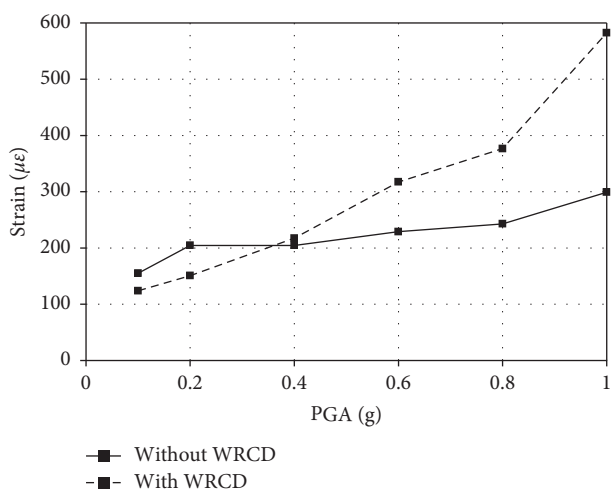

Figure 18: Maximum strain response at 3# sliding bearing pier bottom.

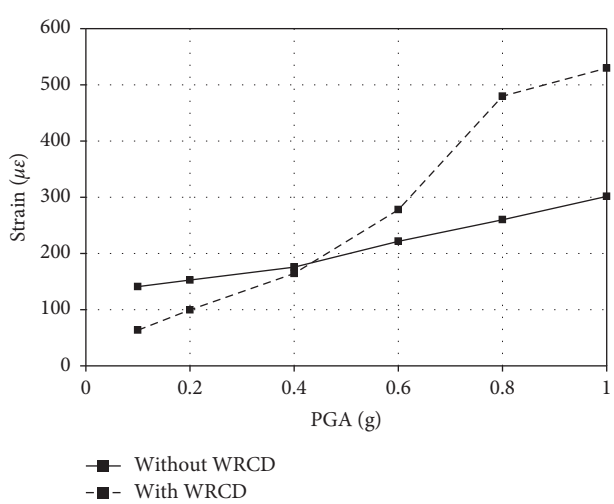

Figure 19: Maximum strain response at 4# sliding pier bottom.

that when the WRCD is activated, the sliding bearing piers contribute to the longitudinal force of the structure and share part of the inertial force of the main beam. Furthermore, with an increase in seismic input intensity, the seismic response of the fixed-bearing pier was reduced further, and the synergistic force effect of each pier was more prominent.

4.5. Responses for Different Frequency Spectra. Table 5 presents the peak acceleration response values of the sliding bearing pier with and without WRCD with different ground motion characteristics under four typical site conditions when the peak acceleration is 0.4 g. Owing to the Tian Jin ground motion of the Class IV site, the data collected without the WRCD test are wrong; hence, the value is not listed in the table. For the Qian An ground motion of Class I site, EL Centro ground motion of the Class II site, and Taft ground motion of the Class III site, the maximum acceleration response value of sliding bearing piers with WRCD with the same parameters was reduced and the reduction range was close. The maximum acceleration response value of the fixed bearing pier increased and the increased range was different. Under the seismic input of EL Centro in the Class II site and Taft in the Class III site, the increased amplitude was 4.6 and 7.8 times, respectively. However, under the Qian An ground motion of the Class I site, the increased amplitude was only 17.5%. The WRCD can effectively improve the cooperative force state between sliding bearing piers and fixed bearing pier of continuous girder bridges; however, the improvement result is directly associated with the ground motion characteristics.

Table 6 shows the comparison values of displacement responses of the pier top and main beam when the peak acceleration is 0.4 g under typical four site conditions with different ground motion characteristics. Under the seismic input of EL Centro in the Class II site, Taft in the Class III site, and Tian Jin in the Class IV site, the maximum displacement response value of sliding bearing piers increased with WRCD for the same setting parameters. Under the seismic input of EL Centro in the Class II site and Taft in the Class III site, the maximum increase in the amplitude of displacement response of sliding bearing piers was ~30%. Under the seismic input of Tian Jin in the Class IV site, the displacement of sliding bearing piers significantly increased (up to approximately two times). For the looser site, the displacement amplification effect of WRCD for sliding bearing piers was more prominent. For the displacement of the main beam, the variation rule was similar to the displacement of the sliding bearing piers. Compared to without WRCD, the maximum displacement response value of the main beam decreased and the decrease was more substantial under the seismic input of EL Centro in the Class II site and Taft in the Class III site and slightly reduced under the seismic input of Tian Jin in Class IV site.

Under the seismic input of Qian An ground motion in the Class I site, the performance of WRCD was not as considerable as that in other sites. However, the variation

Table 5: Maximum acceleration for different frequency spectra (g).

Peak acceleration (g)	Location	Qian An (I)			EL Centro (II)			Taft (III)			Tian Jin (IV)		
		Without WRCD 1	With WRCD 2	Relative error (2 − 1)/1	Without WRCD 1	With WRCD 2	Relative error (2 − 1)/1	Without WRCD 1	With WRCD 2	Relative error (2 − 1)/1	Without WRCD 1	With WRCD 2	Relative error (2 − 1)/1
0.4	P1	0.917	0.954	4.0%	1.563	1.447	−7.4%	1.669	1.674	0.3%	—	2.249	—
	P2	0.109	0.128	17.5%	0.147	0.824	459.2%	0.121	1.063	776.3%	—	1.876	—
	P3	1.304	1.043	−20.0%	1.366	1.014	−25.8%	1.915	1.891	−1.2%	—	2.664	—
	P4	0.82	0.761	−7.1%	1.384	1.281	−7.4%	1.778	1.547	−13.0%	—	2.208	—

Table 6: Maximum displacement for different frequency spectra (mm).

Peak acceleration (g)	Location	Qian An (I)			EL Centro (II)			Taft (III)			Tian Jin (IV)		
		Without WRCD 1	With WRCD 2	Relative error (2 − 1)/1	Without WRCD 1	With WRCD 2	Relative error (2 − 1)/1	Without WRCD 1	With WRCD 2	Relative error (2 − 1)/1	Without WRCD 1	With WRCD 2	Relative error (2 − 1)/1
0.4	P1	0.117	0.078	−33.4%	2.707	2.777	2.6%	2.653	3.355	26.4%	2.845	8.662	204.5%
	P2	0.161	0.349	117.4%	8.876	7.570	−14.7%	10.951	8.621	−21.3%	23.205	23.153	−0.2%
	P3	0.110	0.422	283.9%	2.505	3.333	33.1%	2.802	3.638	29.8%	3.652	10.057	175.4%
	P4	0.569	0.451	−20.8%	3.038	3.557	17.1%	4.319	4.255	−1.5%	3.686	10.796	192.9%

Table 7: Maximum strain response for different frequency spectra ($\mu\varepsilon$).

Peak acceleration (g)	Location	Qian An (I)			EL Centro (II)			Taft (III)			Tian Jin (IV)		
		Without WRCD 1	With WRCD 2	Relative error (2 − 1)/1	Without WRCD 1	With WRCD 2	Relative error (2 − 1)/1	Without WRCD 1	With WRCD 2	Relative error (2 − 1)/1	Without WRCD 1	With WRCD 2	Relative error (2 − 1)/1
0.4	P1	64.09	59.21	−7.6%	181.28	192.27	6.1%	187.99	221.56	17.9%	211.80	482.19	127.7%
	P2	100.71	109.86	9.1%	538.96	502.95	−6.7%	650.05	580.46	−10.7%	1466.72	1416.06	−3.5%
	P3	96.44	97.66	1.3%	204.47	217.29	6.3%	229.50	247.20	7.7%	274.06	543.23	98.2%
	P4	95.83	62.87	−34.4%	175.79	164.19	−6.6%	185.55	198.98	7.2%	247.20	493.79	99.8%

rule was slightly different. Under some site conditions, the WRCD can effectively improve the cooperative force state between sliding bearing piers and fixed bearing piers; however, the improvement result was directly associated with the ground motion characteristics.

Table 7 shows the comparison of maximum strain response at the bottom of each pier with different ground motion characteristics under four typical site conditions when the peak acceleration is 0.4 g. Similar to the displacement response, for the seismic input of EL Centro in the Class II site, Taft in the Class III site, and Tian Jin in the Class IV site, the maximum strain response value of sliding bearing piers, with WRCD with the same setting parameters, increased. Under the seismic input of EL Centro in the Class II site and Taft in the Class III site, the maximum increased amplitude of strain response of sliding bearing piers was 20%. Under the seismic input of Tian Jin in the Class IV site, the strain response of sliding bearing piers significantly increased, up to 1.2 times. The maximum strain response at the pier bottom of the fixed bearing pier decreased, and the maximum reduction in the three types of sites was 10%.

This result demonstrates that, under some site conditions, same as the displacement response, the WRCD can effectively improve the synergistic effect between the sliding bearing piers and the fixed bearing pier; however, the improvement result is directly associated with the seismic input characteristics.

5. Conclusions

This article proposed the WRCD based on the basic principle of cooperative force and considered the relative acceleration of piers and beams as the control variable. The shaking table test of a typical continuous girder bridge was conducted to examine the seismic reduction performance of the WRCD for the continuous girder bridges. Based on the tests, the results demonstrated the following observations:

(1) When the peak acceleration was 0.4 g, the natural frequency with WRCD increased, which shows that with the change in ground motion input intensity, the WRCD is activated such that the dynamic characteristics of the bridge structure changes, and the overall performance of continuous girder bridge can be improved.

(2) After the WRCD was activated, the maximum acceleration response value of each sliding bearing pier decreased by 25%, and the maximum acceleration response value of the fixed bearing pier increased by ~4.6 times, which is from 10% to 57% of the maximum response value of the pier with the sliding bearing pier.

(3) When the peak acceleration was between 0.1 and 0.4 g, the difference between the maximum displacement response values of the two models was small. When the peak acceleration was 0.6~1.0 g, compared to without WRCD, the maximum displacement response value of piers with WRCD rapidly increased with the change in seismic input intensity and the maximum displacement difference between the two models was large. When the WRCD was activated, the sliding bearing piers participated in the longitudinal force of the structure and share part of the inertial force of the main beam. With the increase in seismic input intensity, the performance of WRCD was more considerable and the overall performance of the continuous girder bridge can be improved.

(4) From the variation trend of the curve, the maximum strain response at the bottom of each pier changed linearly with the seismic input intensity. For the sliding bearing piers without the device, the variation trend was relatively gentle, and when the WRCD was activated, it was relatively steep. With increasing seismic input intensity, the seismic response of the fixed bearing was is further reduced, and the synergistic force effect of each pier was more considerable.

(5) This article compared the acceleration, displacement, and strain responses of the structure with different ground motion characteristics under four typical site conditions when the peak acceleration was 0.4 g. Under some site conditions, WRCD can effectively improve the cooperative force state between sliding bearing piers and fixed bearing piers; however, the improvement result was directly associated with the ground motion characteristics. It is necessary to determine the design parameters of the WRCD according to the different site conditions, and the optimum application range of the WRCD has been determined.

Data Availability

The data used to support the findings of this study are included within the article.

Conflicts of Interest

The authors declare that they have no conflicts of interest.

Acknowledgments

The authors would like to thank the workers, foremen, and safety coordinators of the main contractors for their participation. This work was supported by the National Natural Science Foundation of China (grant no. 51778022).

References

[1] C. F. Wang, X. C. Chen, and X. S. Xia, "Parameters analysis of the vibration distributing effect of longitudinal displacement limited continuous beam bridges," *Earthquake Engineering and Engineering Vibration*, vol. 32, no. 5, pp. 119–126, 2012.

[2] N. P. Kataria and R. S. Jangid, "Seismic protection of the horizontally curved bridge with semi-active variable stiffness damper and isolation system," *Advances in Structural Engineering*, vol. 19, no. 7, pp. 1103–1117, 2016.

[3] L. Y. Lu and C. C. Hsu, "Experimental study of variable-frequency rocking bearings for near-fault seismic isolation," *Engineering Structures*, vol. 46, pp. 116–129, 2013.

[4] A. Kashiwazaki, M. Tanaka, N. Tokuda, and T. Enomoto, "The earthquake and microtremor isolation floor system utilizing air springs and laminated rubber bearings," *TRANSACTIONS OF THE JAPAN SOCIETY OF MECHANICAL ENGINEERS Series C*, vol. 55, no. 512, pp. 847–852, 1989.

[5] L. P. Ren, S. H. He, H. Y. Yuan, and Z Zhu, "Seismic fragility analysis of bridge system based on fuzzy failure criteria," *Advances in Civil Engineering*, vol. 2019, Article ID 3592972, 13 pages, 2019.

[6] H. X. Jia, J. Q. Lin, and J. L. Liu, "Bridge seismic damage assessment model applying artificial neural networks and the random forest algorithm," *Advances in Civil Engineering*, vol. 2020, Article ID 6548682, 13 pages, 2020.

[7] F. W. Wu, J. F. Luo, W. Zheng et al., "Performance-based seismic fragility and residual seismic resistance study of a long-span suspension bridge," *Advances in Civil Engineering*, vol. 2020, Article ID 8822955, 16 pages, 2020.

[8] L. Tang, Z. H. Cheng, X. Z. Ling, S. Cong, and J. Nan, "Preparation and performance of graphene oxide/self-healing microcapsule composite mortar," *Smart Materials and Structures*, vol. 31, no. 2, Article ID 025022, 2022.

[9] J. M. Kelly and J. M. Eidinger, *Experimental Results of an Earthquake Isolation System Using Natural Rubber Bearings*, Reports No. UCBIEERC78l03, California, CA, USA, 1978.

[10] J. M. Kelly, "Tension buckling in multilayer elastomeric bearings," *Journal of Engineering Mechanics*, vol. 129, no. 12, pp. 1363–1368, 2003.

[11] R. G. Tyler and W. H. Robinson, "High-strain tests on lead-rubber bearings for earthquake loadings," *Bulletin of the New Zealand Society for Earthquake Engineering*, vol. 17, no. 2, pp. 90–105, 1984.

[12] J. S. Hwang, J. M. Chiou, L. H. Sheng, and J. H Gates, "A refined model for base-isolated bridges with Bi-linear hysteretic bearings," *Earthquake Spectra*, vol. 12, no. 2, pp. 245–273, 1996.

[13] M. Abe, J. Yoshida, and Y. Fujino, "Multiaxial behaviors of laminated rubber bearings and their modeling. I: experimental study," *Journal of Structural Engineering*, vol. 130, no. 8, pp. 1119–1132, 2004.

[14] T. B. Peng, J. Z. Li, and L. C Fan, "Analysis of vertical displacement of double spherical aseismic bearing," *J. Tung-chi Univ., Nat. Sci*, vol. 35, no. 9, pp. 1181–1185, 2007.

[15] Y. L. Zhang, Y. J. Zhang, and C. F. Wang, "Effect of vertical ground motion on seismic response of an isolated bridge with FPS," *J. Lanzhou Jiaotong Univ*, vol. 31, no. 1, pp. 18–22, 2012.

[16] J. P. Ou and B. Wu, "Experimental comparison on the properties of friction and mild steel yielding energy dissipations and their effects on reducing vibration of structure under earthquakes," *Earthquake. Eng. Eng. Dyn*, vol. 3, pp. 73–87, 1995.

[17] W. M. Yan, Y. Li, and Y. J. Chen, "The implication of a new type of metal alloy brace on seismic control of viaduts," *Journal of Beijing University of Technology*, vol. 38, no. 8, pp. 1167–1173, 2012.

[18] X. Shen, X. B. Ni, and A. J. Ye, "A new type of metallic damper for birdges aseismic performance in transverse direction," *Journal of Vibration and Shock*, vol. 33, no. 21, pp. 96–101, 2014.

[19] Z. H. Cheng and Y. S. Deng, "Bearing characteristics of moso bamboo micropile-composite soil nailing system in soft soil areas," *Advances in Materials Science and Engineering*, vol. 2020, Article ID 3204285, 17 pages, 2020.

[20] Y. S. Deng, Z. H Cheng, M. Z. Cai, Y Sun, and C Peng, "An experimental study on the ecological support model of dentate row piles," *Advances in Materials Science and Engineering*, vol. 2020, Article ID 6428032, 12 pages, 2020.

[21] X. S. Liu, W. Guo, J. Z. Li, and H Zhang, "Seismic study of skew bridge supported on laminated-rubber bearings," *Advances in Civil Engineering*, vol. 2020, Article ID 8899693, 17 pages, 2020.

[22] Y. T. Pang, "Seismic fragility assessment of an isolated multipylon cable-stayed bridge using shaking table tests," *Advances in Civil Engineering*, vol. 2017, Article ID 9514086, 12 pages, 2017.

[23] H. X. Gao, Y. Song, W. T. Yuan, H Lu, and S Cao, "Seismic design method of self-centring-segment bridge piers with tensile-type viscoelastic dampers," *Advances in Civil Engineering*, vol. 2021, Article ID 6688006, 12 pages, 2021.

[24] C. Zou, J. A. Moore, M. Sanayei, Z. Tao, and Y. Wang, "Impedance model of train-induced vibration transmission across a transfer structure into an over track building in a metro depot," *Journal of Structural Engineering*, vol. 148, no. 11, Article ID 04022187, 2022.

[25] H. Jin, Q. Tian, and Z Li, "Crack development of rebar rust in rubberized concrete using mesoscale model," *Construction and Building Materials*, vol. 321, Article ID 126409, 2022.

[26] L. H. Xu and M. Ma, "Dynamic response of the multilayered half-space medium due to the spatially periodic harmonic moving load," *Soil Dynamics and Earthquake Engineering*, vol. 157, Article ID 107246, 2022.

[27] Y. Pang, K. Wei, H. He, and W. Wang, "Assessment of lifetime seismic resilience of a long-spancable-stayed bridge exposed to structural corrosion," *Soil Dynamics and Earthquake Engineering*, vol. 157, Article ID 107275, 2022.

[28] Y. Pang and X. Wang, "Cloud-IDA-MSA conversion of fragility curves for efficient and high-fidelity resilience assessment," *Journal of Structural Engineering*, vol. 147, no. 5, Article ID 4021049, 2021.

Hindawi
Advances in Civil Engineering
Volume 2023, Article ID 9451361, 13 pages
https://doi.org/10.1155/2023/9451361

Research Article

Influence of Segmented Linings on the Micro-Pressure Wave of Tunnels

Tao Li,[1] **Mingyu Shao**,[1] **Weibin Ma**,[2] **Yanbin Liang**,[1] **and Yufei Fang**[2]

[1]*School of Transportation and Vehicle Engineering, Shandong University of Technology, Zibo 25000, China*
[2]*State Key Laboratory for Track Technology of High-speed Railway, Beijing 100081, China*

Correspondence should be addressed to Mingyu Shao; shaomingyu@sdut.edu.cn

Received 25 August 2022; Accepted 5 October 2022; Published 17 February 2023

Academic Editor: Chao Zou

When the tunnel has damages such as deformation and cracking, the lining structure should be set to reinforce the tunnel. In this study, a three-dimensional numerical method is performed to study the aerodynamic effects caused by the train passing through a tunnel with segmented linings at 350 km/h. The influence of the numbers, thickness, location, and types of the segmented lining structure on MPW is analyzed. The results show that the segmented linings located at the middle of the tunnel have a better mitigation effect on MPW than that of the normal linings, which increases with the segment number and the thickness of the linings. When the damage occurs near the entrance of the tunnel, a segmented lining structure with a constricted section slightly away from the tunnel entrance can be used to reduce its adverse effect on MPW.

1. Introduction

The impact of aerodynamic effects caused by high-speed trains entering tunnels increases with the speed-up of trains. Compression waves produced generated when the high-speed train enters a tunnel propagate along the tunnel near to the sonic speed and create a pulse wave at tunnel exits, usually called micro-pressure wave (MPW) [1]. The MPW causes problems such as noise pollution and even a sonic boom, which can lead to structural damage to the buildings surrounding the tunnel exit and negatively affect residents' normal lives [2–4]. Wide research has shown that assessing MPW and structural vibrations are associated with safety and discomfort caused in trains [5, 6]. Zou et al. developed an efficient computational model that can accurately predict over-track vibration levels for buildings supported on a transfer structure [7].

The train speed and blockage ratio are significant factors that affect the amplitude of MPW [8–13]. When the tunnel is under the influence of geology and construction, there are tunnel damages such as structural deformation and cracking [14]. Tunnel damage threatens traffic safety in tunnels and shortens the tunnels' maintenance cycle and service life. Adding linings technology is a popular way to prevent the occurrence or further expansion of cracks. However, adding linings inside the tunnel changes the clearance area and cross-sectional distribution of the tunnel, which affects the aerodynamic characteristics of the tunnel. The lining is to pour a certain thickness of reinforced concrete in the tunnel to prevent the tunnel from further cracking, damage, and deformation. Jin et al. studied the feature morphology of rubberized concrete by corrosion and expansion of reinforcement in rubberized concrete and the relationship between the deformation of staggered assembled shield tunnel and the disengaging of invert filling [15, 16].

Previously many researches were concentrated on the responses of the tunnel hood to MPW of the tunnel. Tunnel hood is an auxiliary structure specifically designed to reduce the impact of tunnel aerodynamics. Xiang et al. compared different tunnel entrance hoods and optimized hood designs to mitigate the pressure gradient [17]. Murray's theoretical research on the tunnel entrance hoods show that the installation of the tunnel hoods will increase the rise time of the initial compression wave, thereby decreasing the

pressure gradient [18]. Studies nowadays have contributed extensively to designing optimized tunnel hoods to reduce the amplitude of MPW at the tunnel exit [19–23]. Although related studies have been performed on the influences of tunnel hoods, limited investigations have been conducted on the effects of MPW behaviors of the linings. Based on the real vehicle experiments, dynamic model experiments, and numerical simulations method to analyze the aerodynamic effects of the train passing the tunnel with linings, Liu et al. pointed out that the influence of MPW is the most unfavorable when the linings are added at the tunnel entrance and the pressure amplitude increases with the thickness of the linings [24, 25]. Combined with the test results of the real vehicle, Gao found MPW and the comfort of the tunnel when the train passed through the lined tunnel and proposed that the impact section of the linings should not exceed 95% [26]. Shi et al. investigated the influence of linings length, thickness, and position on the pressure gradient at the tunnel exit through 3D numerical simulation and found that the impact of linings thickness was more significant than that of length [27]. Wang et al. analyzed the transient pressure characteristics of trains passing through tunnels with noncircular linings based on dynamic model experiments. The results show that reasonable distribution of circular linings can reduce the pressure amplitude of initial compression waves [28].

The above research has shown that adding a lining structure at the tunnel's entrance will adversely affect MPW, but the damage may occur anywhere in the tunnel. Therefore, the behaviors of the aerodynamic effect of the segmented lining structure are assessed in this study. In Section 2, the governing equations and mesh motion equations of the train moving in the tunnel are presented. In Section 3, the numerical calculation model of the train tunnel was established and validated with the dynamic model experiments. In Section 4, the influence of the linings' position, thickness, number of segments, and types on MPW characteristics of the tunnel exit was discussed. The results can provide a fundamental comprehension and reference to the design of the lining structure.

2. Numerical Calculation Method

2.1. Governing Equation. The flow field, produced by trains traveling through the tunnel, is 3D, viscous compressible, and turbulent [9, 29–31], which must follow the laws of continuity equations, momentum equations, and energy equations [32]. They can be written as

$$\frac{\partial p}{\partial t}+\frac{\partial}{\partial x_i}(\rho u_i)=0$$

$$\frac{\partial}{\partial t}(\rho u_i)+\frac{\partial}{\partial x_j}(\rho u_i u_j)=-\frac{\partial p}{\partial x_i}+\rho g\delta_{i2}+\frac{\partial}{\partial x_j}\left[\mu\left(\frac{\partial u_i}{\partial x_j}+\frac{\partial u_j}{\partial x_i}-\frac{2}{3}\delta_{ij}\frac{\partial u_i}{\partial x_i}\right)\right]+\frac{\partial}{\partial x_j}\left(-\rho\overline{u_i u_j}\right) \tag{1}$$

$$\frac{\partial}{\partial t}(\rho E)+\frac{\partial}{\partial x_i}\left[u_i(\rho E+p)\right]=\frac{\partial}{\partial x_j}\left(K\frac{\partial T}{\partial x_j}+u_i\tau_{ij}\right),$$

where ρ is the density of the air; u_i and u_j are the velocity components in the three directions of the flow field; x_i and x_j are the three components of the coordinate; p denotes the pressure; τ_{ij} is the shear stress in the flow field; K is the thermal conductivity coefficient; T is the temperature of the flow field; and μ is their dynamic viscosity of the air.

The term $-\rho\overline{u_i u_j}$ is the time-averaged Reynolds stresses which represent the turbulent momentum fluxes. Based on the Boussinesq hypothesis, the closed equations under the Boussinesq hypothesis:

$$-\rho\overline{u_i' u_j'}=\mu_t\left(\frac{\partial u_i}{\partial x_j}+\frac{\partial u_j}{\partial x_j}\right)-\frac{2}{3}\left(\rho\kappa+\mu_t\frac{\partial u_\kappa}{\partial x_\kappa}\right)\delta_{ij}, \tag{2}$$

where μ_t is the turbulent viscosity and κ is the turbulent kinetic energy.

The dynamic mesh method is usually accustomed to simulate the time-varying flow on domain boundaries due to train motion in tunnels. The motion can be a prescribed motion or an unprescribed motion which is determined based on the solution at the current time.

Generally, the integral form of the conservation equation for a general scalar, ϕ, on an arbitrary control volume, V, whose boundaries are moving, can be written as [31, 33]

$$\frac{d}{dt}\int_V \rho\phi\, dV+\int_{\partial V}\rho\phi\left(\vec{u}-\vec{u}_g\right)d\vec{A}=\int_{\partial V}\Gamma\nabla\phi\, d\vec{A}+\int_V S_\phi dV. \tag{3}$$

For solving (3), the differential term is discretized as follows:

$$\frac{d}{dt}\int_V \rho\phi\, dV = \frac{(\rho\phi V)^{n+1} - (\rho\phi V)^n}{\Delta t}, \tag{4}$$

where n and $n+1$ represent the value at the present and next time step. The $(n+1)th$ time step control volume, V^{n+1}, is computed from

$$V^{n+1} = V^n + \left(\sum_f^{nf} \frac{\delta V_j}{\Delta t}\right)\Delta t. \tag{5}$$

These equations can then be solved using dynamic meshing methods and updated with new volumes at each time step.

2.2. Computational Model. In this study, the CR400AF vehicle depicted in Figure 1(a) is selected to research the aerodynamic impact of the tunnels with segmented linings. Since the initial compression wave and MPW are mainly associated with the shape of the train nose, four-car marshaling carriages are modeled to improve computational efficiency. The shape of the train is simplified according to the recommendations of the CEN European Standard [34], as the accessory components of the high-speed train (such as pantograph, bogie, doors, and windows) have negligible influence on MPW. According to Chinese high-speed railway tunnel design standards, a double-track tunnel with a cross-sectional area of 100 m^2 is adopted for a high-speed train with a design speed of 350 km/h, and the centre-to-centre distance of the two tracks is 5 m. The cross section size of the tunnel is shown in Figure 1(b), and the length of the tunnel is 1000 m. Different numbers of segmented linings with various thicknesses are set within a certain length of 100 m at different locations of the tunnel to investigate the influences of the segmented linings on MPW, as shown in Figure 1(c).

2.3. Computational Domain and Boundary Conditions. The computational domain of the aerodynamic impacts generated by the trains traveling from the tunnel with segmented linings is composed of the atmosphere outside the tunnel portal and the atmosphere inside the tunnel, shown in Figure 2. Considering the acceleration process of the train and the full development of the wake [35], the length of the flow field outside the tunnel is taken as 500 m on both sides of the tunnel.

The train motion in the tunnel is simulated by the sliding mesh model and mesh dynamic layering method, so the entire computational domain is divided into four domains [30, 36]: a motion domain (region-2), two deformation domains (region-1 and region-3), and a fixed domain (region-4). As the train moves at speed as the surrounding motion domain, the lengths of deformation domains are changed to keep the entire computational domain unchanged during computation. *Interface* boundary conditions are used between the motion domain, the deformation domain, and the fixed domain to realize data exchange. The boundaries of the flow field outside the tunnel portal are defined as *pressure inlet* and *pressure outlet*, respectively. *No-slip wall* is defined as the train surface, ground, and tunnel wall. All walls are defined as *Adiabatic wall* with an initial temperature of 300 K.

2.4. Grid Generation Scheme. A hybrid grid scheme is adopted to divide the entire computational domain into blocks accounting for computational accuracy and speed [37]. The unstructured grid is used in the motion domain surrounding the train as the complicated shape of the train, and the geometrically complex parts of the train surface are locally refined. The deformation domains before and after the motion domain can be divided into high-quality structured grids, and the adjacent regions are connected by setting common nodes on the interface with the motion domain. The structured grid is also used in the fixed domain, and the regions near the segmented linings are refined to capture the influence of the local flow field on the MPW.

In order to evaluate the mesh density on the numerical results, four different grid numbers were taken into consideration, which are 3.98×10^6, 5.19×10^6, 6.60×10^6, and 8.12×10^6, respectively. The details of grids and the amplitude values of MPW calculated by 4 different numbers of grids are shown in Table 1. The results show that the amplitude values of MPW are very little when the number of the grids exceeds 5.19×10^6, which means that the computational accuracy and efficiency can be met when the mentioned mesh is used. In such cases, the grid of the train head and segmented linings are shown in Figure 3.

2.5. Measuring Points. The evaluation standard of MPW at the tunnel exit of a high-speed railway is that the amplitude values of MPW at 20 m and 50 m away from the tunnel exit are less than 50 Pa and 20 Pa, respectively [22].

Studies show that the magnitude of MPW emitting from the tunnel exit is almost proportional to pressure gradients of the wavefront of the initial compression wave reaching the tunnel exit and inversely proportional to the distance to the tunnel exit plane [38], which can be expressed as follows:

$$P_{MPW}(r,t) = \frac{2S}{\Omega cr}\left(\frac{\partial p}{\partial t}\right), \tag{6}$$

where S is the cross-sectional area of the tunnel exit, Ω denotes the solid angle around the tunnel exit portal, c is the speed of sound, r is the distance from the measuring point to the tunnel entrance, and $(\partial p/\partial t)$ demotes the pressure gradient at the tunnel exit.

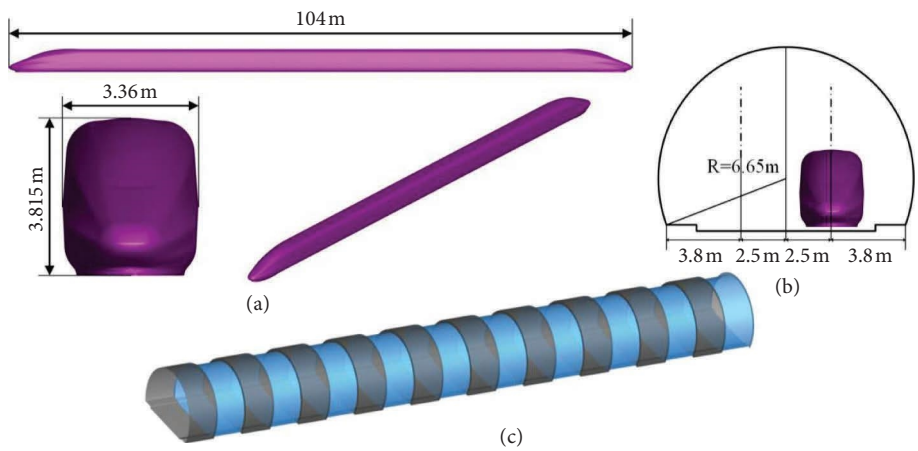

Figure 1: Schematic diagram of models. (a) Different views of CR400AF. (b) Tunnel section. (c) Linings.

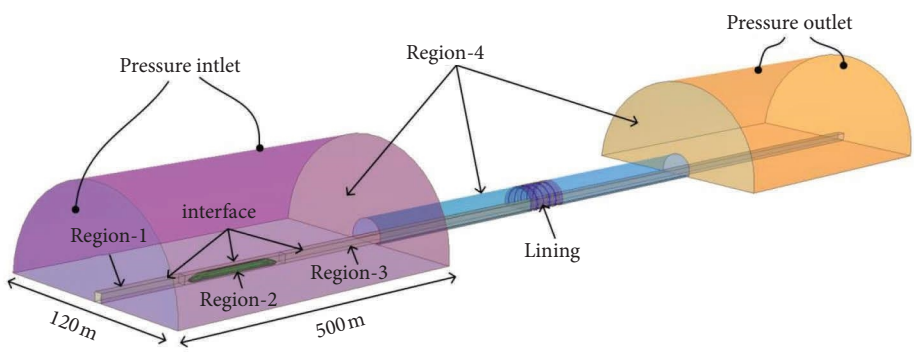

Figure 2: Computational domain and boundary conditions.

Table 1: Grid quantity and micropressure wave.

Grid quantity	3.98×10^6	5.19×10^6	6.60×10^6	8.12×10^6
MPW	72.0	68.4	68.1	67.5

Both the pressure gradient near the tunnel exits and MPW outside the tunnel are monitored simultaneously in the calculation. Two groups of monitoring points 1.2 m above the ground are arranged symmetrically on both sides of the tunnel centreline, as shown in Figure 4. The monitoring point located at 50 m inside the tunnel is marked as $T1$ and $T2$, and $M1$,2 and $M3$,4 denote the monitoring points located at 20 m and 50 m outside the tunnel, respectively.

3. Numerical Method Validation

To verify the accuracy of the presented method in the simulation, the numerical results are compared with that of the moving model test conducted by Central South University [39]. The model ratio in the test is 1 : 20, and the original lengths of the train and the double tracks tunnel are 51.7 m and 1000 m, respectively. A ring tunnel portal with a slope value of 1 : 1.25 is set at tunnel entrance. Both the transient pressure at 65.5 m from the entrance in the tunnel and MPW at 20 m from the exit outside the tunnel are measured in the test when the train passes the tunnel at 350 km/h. The numerical simulation is performed in the same condition as the moving model test.

ANSYS Fluent is used to explain the governing equation of flow motion. The ideal gas model is adopted in the calculation, and the *RNG k-ε* turbulence model is used due to the high turbidity. The coupling velocity and pressure are dealt with the *SIMPLE* algorithm, the gradient term is discretized by the *Green-Gaussian Cell-Based* method. The pressure term is discretized using the standard format, the other spatial terms are discretized by the second-order upwind format and the second-order implicit format is used in the time discretization.

The initial compression wave and MPW acquired by the numerical simulation and moving model tests are shown in Figure 5. It can be seen that the results calculated by the numerical method agree well with those of the moving model test. The amplitude values of MPW and the pressure gradient of the initial compression wave are also listed in Table 2. Because the numerical calculation model has assumptions and errors in the calculation process, the results of the numerical method are not exactly the same as those of the moving model test. The differences between the results from the numerical method and that of the moving model test are 2.86% and 2.60%, respectively. The results show that the numerical methods adopted can meet the requirements of calculation accuracy and efficiency. Thus, the mentioned

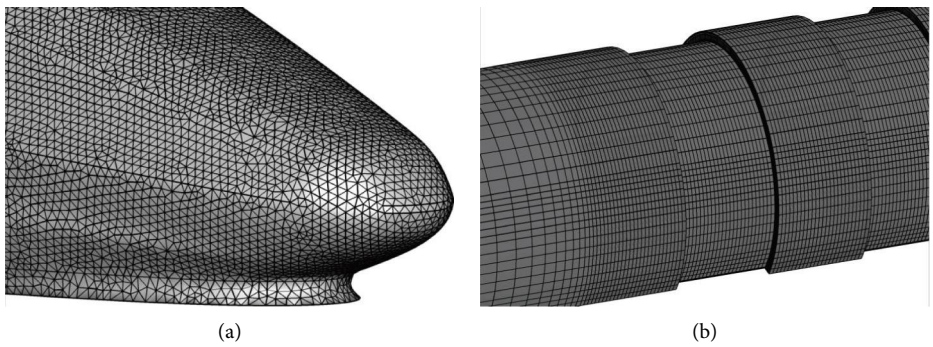

Figure 3: Model mesh. (a) Mesh of the train head. (b) Mesh of the lining.

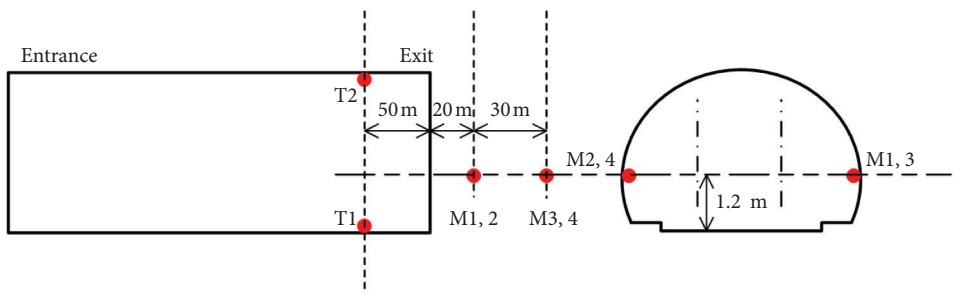

Figure 4: Layout monitoring points.

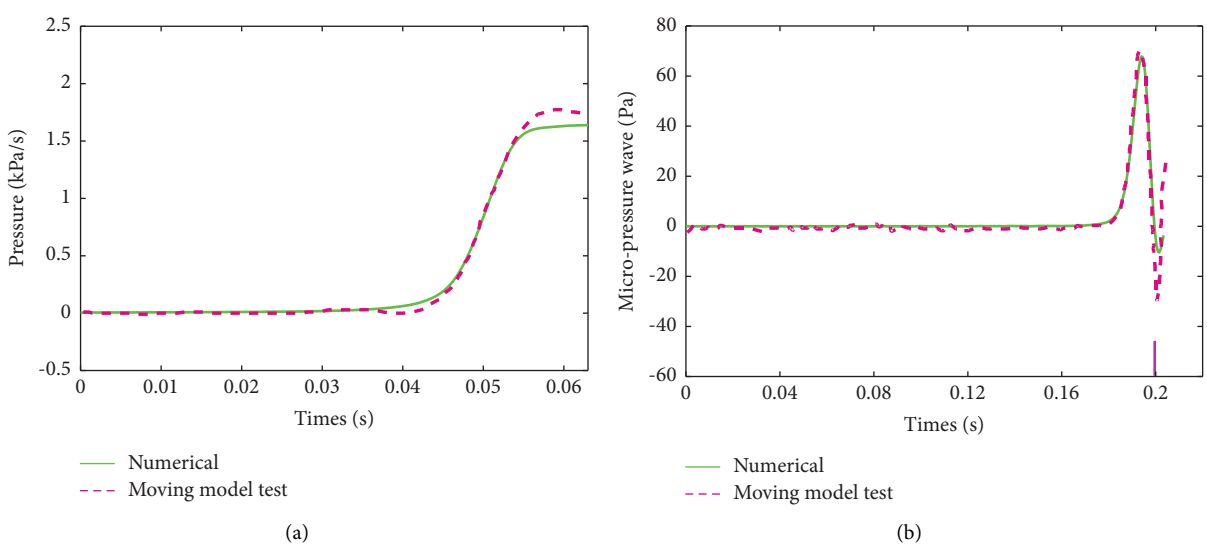

Figure 5: Comparisons of pressure curves obtained by numerical simulation and the experimental test. (a) Initial compression waves. (b) Micropressure waves.

Table 2: The maximum pressure gradient and the micropressure wave.

	Tests	Numerical	Diff./Ref. (%)
$(\partial P/\partial t)_{max}$ (kPa/s)	9.482	9.729	2.60
MPW (Pa)	70	68	2.86

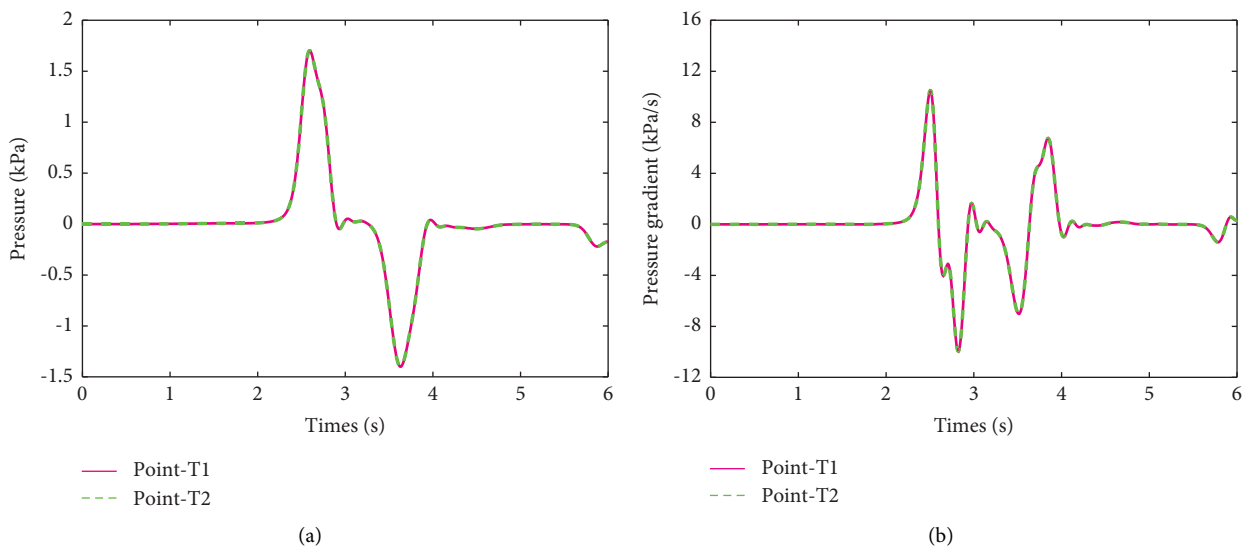

Figure 6: Comparison of initial compression waves in the same plane. (a) Pressure. (b) Pressure gradient.

method in this paper can be used to study the characteristics of MPW caused by the train passing through the tunnel.

4. Results and Discussion

4.1. Propagation Characteristics of Initial Compression Wave. The aerodynamics caused by the train traveling through the tunnel without linings at 350 km/h is simulated by the mentioned method. The comparison of the pressure and pressure gradient of two symmetrical measuring points in the same plane of the tunnel is shown in Figure 6.

It can be found that the results at $T1$ are basically the same as that at $T2$, which indicates that the initial compression wave presents a one-dimensional plane wave characteristic propagating in the tunnel [40]. Due to the relationship with the pressure gradient of the initial compression wave at the tunnel exit, the MPW outside the tunnel exit is also symmetrical, as shown in Figure 7. So, the results at the monitoring points on only one side ($T1$, $M1$, and $M3$) are considered in the subsequent discussion.

4.2. Influence of Linings Position and Quantity. The compress wave and MPW characteristics caused by a train passing through tunnels with normal linings and various numbers of segmented linings at different positions with a speed of 350 km/h are studied by numerical simulation.

For the normal linings located at the tunnel entrance, middle, and exit, the maximum values of pressure gradient at $T1$ and MPW at $M1$ and $M3$ are shown in Table 3. It can be found that both the pressure gradient and MPW increase compared to that without linings, which has an adverse effect on the aerodynamics of the tunnel. When the linings are located at tunnel middle and exit, the pressure gradient and MPW decrease compared to that without linings and a favorable effect is induced. The results also show that the mitigation effect on MPW is better when the linings are located near the tunnel exit.

The MPW at $M1$ and $M3$ when the trains travel through the tunnel with different numbers of segmented linings at different positions are shown in Figures 8 and 9, respectively.

It can be seen that the influence of the lining's position on MPW is basically the same for both normal linings and the different number of segmented linings. That is, the linings close to the tunnel middle and exit have a favorable effect on the mitigation of MPW, while an adverse effect will be induced when the linings locate near the entrance of the tunnel.

The amplitude values of MPW at 20 m and 50 m away from the tunnel exit are listed in Tables 4 and 5, respectively. It can be found that when the linings are located at the tunnel entrance and middle, the MPW generated by the tunnel with segmented linings decrease compared to that with normal linings. For the segmented linings locate at the middle and exit of the tunnel, the mitigation effects on the micropressure wave increase with the segment numbers due to the increscent dissipation effect caused by the linings. The amplitude values of MPW at $M1$ and $M3$ are 82.172 Pa and 35.096 Pa when a 30-segment lining is set at the tunnel exit, which is 4.789% and 5.277% lower than that of the tunnel without linings.

However, when the segmented linings are located at the tunnel entrance, the amplitude value of MPW increases gradually with the number of segments. The reason is that the shrinking section of the lining gets closer to the tunnel entrance as the increase of the segmented number and the compression effect of the air is dominant compared to the dissipation effect, which has an adverse impact on MPW. Therefore, the adverse effect of the linings located at the tunnel entrance can be reduced by a small number of segments. When a 10-segment lining is set at the entrance of the tunnel, the amplitude values of MPW at $M1$ and $M3$ are 91.225 Pa and 39.181 Pa, which are 5.701% and 5.749% higher than that of the tunnel without linings but decrease by 6.884% and 6.699% compared to that of the tunnel with normal linings.

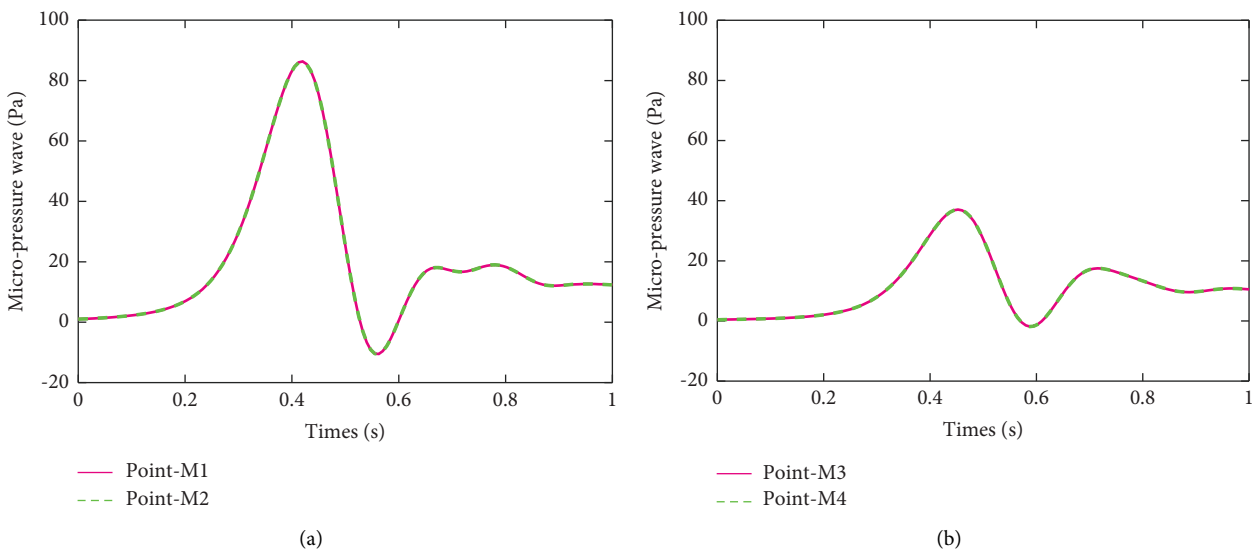

Figure 7: Comparison of micropressure wave in the same plane. (a) 20 m outside the tunnel exit. (b) 50 m outside the tunnel exit.

Table 3: The maximum pressure gradient and micro-pressure wave.

The position of the linings	Without linings	Entrance of the tunnel	Middle of the tunnel	Exit of the tunnel
$(\partial P/\partial t)_{max}$ at $T1$ (kPa/s)	10.49	12.06	10.43	11.20
MPW at $M1$ (Pa)	86.31	97.97	85.89	85.26
MPW at $M3$ (Pa)	37.05	42.00	36.92	35.05

4.3. Influence of Linings Thickness. The influence of the thickness of the linings on MPW is also studied. The aerodynamics caused by a train passing through the tunnel with normal and 10-segment linings of various thicknesses located at the middle of the tunnel is simulated by numerical methods.

The variations of MPW at 20 m and 50 m away from the tunnel exit are shown in Figures 10 and 11, respectively. The results show that MPW decrease slightly with the increment of linings thickness in a certain range for both normal linings and segmented linings due to the increscent dissipation effect.

The amplitude values of MPW at $M1$ and $M3$ are also given in Tables 6 and 7. It can be found that the amplitude values of MPW at two monitoring points drop by 0.629% and 0.707% when the thickness of the segmented linings changes from 0.4 m to 0.6 m.

Thus, the thickness of the lining structure can be designed according to the requirements of structural strength in engineering practice and a thick lining can be used as the cost allows to alleviate the MPW problem outside the tunnel exit.

4.4. Influence of Linings Type. The previous studies show that an effect is induced by the segmented linings located at the tunnel entrance and exit. The aerodynamics of the segmented linings with different types located at the tunnel middle and exit are simulated to study the influences of the linings type on MPW.

As shown in Figure 12, Type 1 denotes the segmented linings start with a constant section compared to the tunnel, while Type 2 denotes the segmented linings start with a constricted section, and 10 segments are set for both types with a thickness of 0.5 m.

When a train travels through the tunnels with different types of segmented linings, the MPW at 20 m and 50 m away from the tunnel portal are given in Figures 13 and 14, respectively.

It has shown quite a difference between the two types of segmented linings located at the entrance of the tunnel. For the segmented linings that start with a constant section (Type 1), the rising of the initial compression wave is divided into two stages, resulting in decreases in pressure gradient and MPW. While the segmented linings start with a constricted section (Type 2), the compression effect is enhanced due to the reduction of the clearance area of the tunnel entrance, which has an adverse on the micropressure wave. The amplitude values of MPW at the $M1$ and $M3$ are 95.787 Pa and 41.06 Pa, respectively, which are 4.999% and 4.796% higher than that with Type 1.

However, the results show little difference between the two types of segmented linings located at the exit of the tunnel. For the segmented linings end with constricted section (Type 1), the mitigation effect is better due to a smaller clearance area at the tunnel exit, as shown in equation (6). The amplitude values of MPW at the $M1$ and $M3$ are 83.204 Pa and 35.569 Pa, which are 0.375% and 0.829% smaller than that with Type 2.

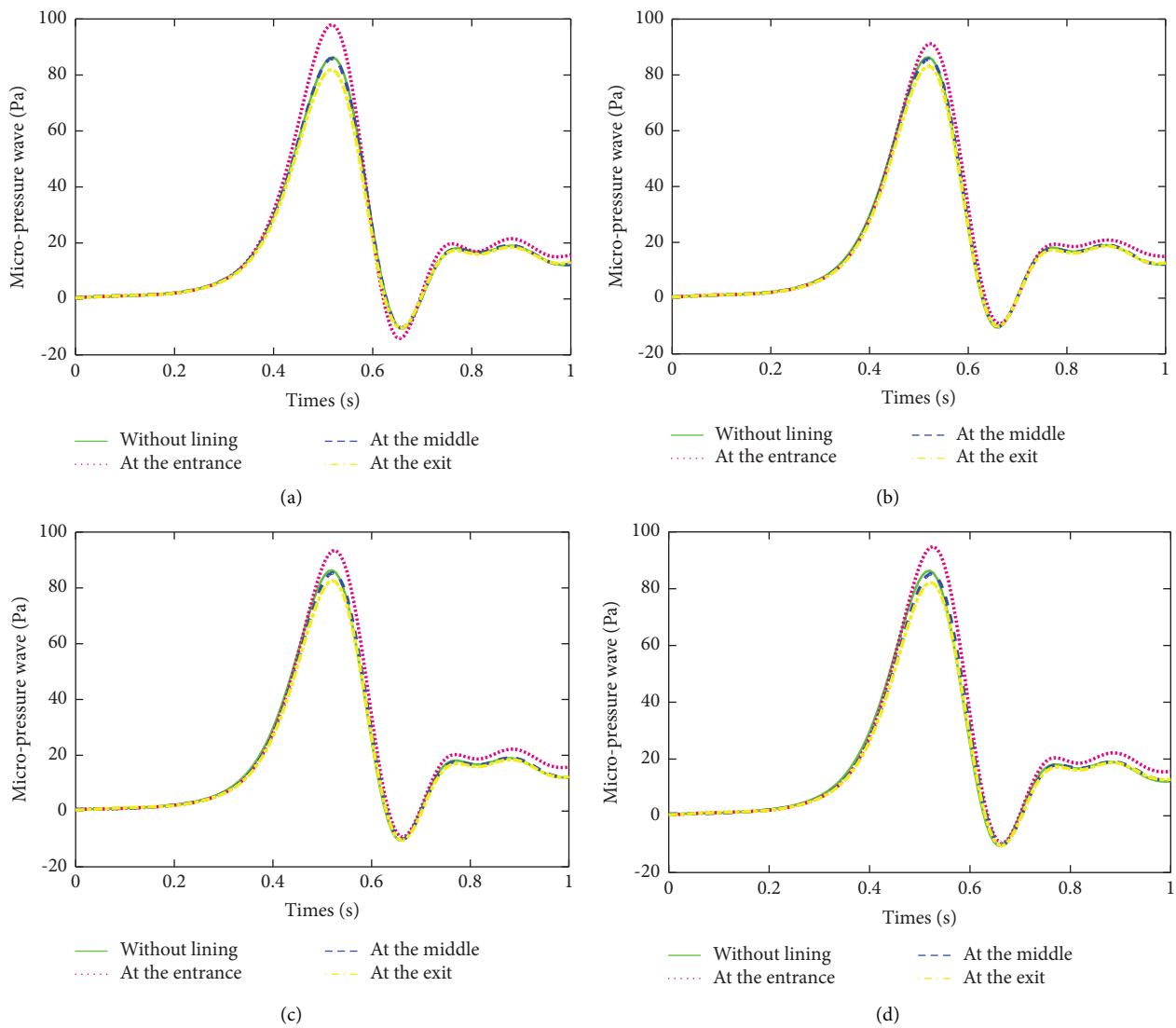

Figure 8: Comparison of the micro-pressure wave at $M1$. (a) Normal linings. (b) 10-segment linings. (c) 20-segment linings. (d) 30-segment linings.

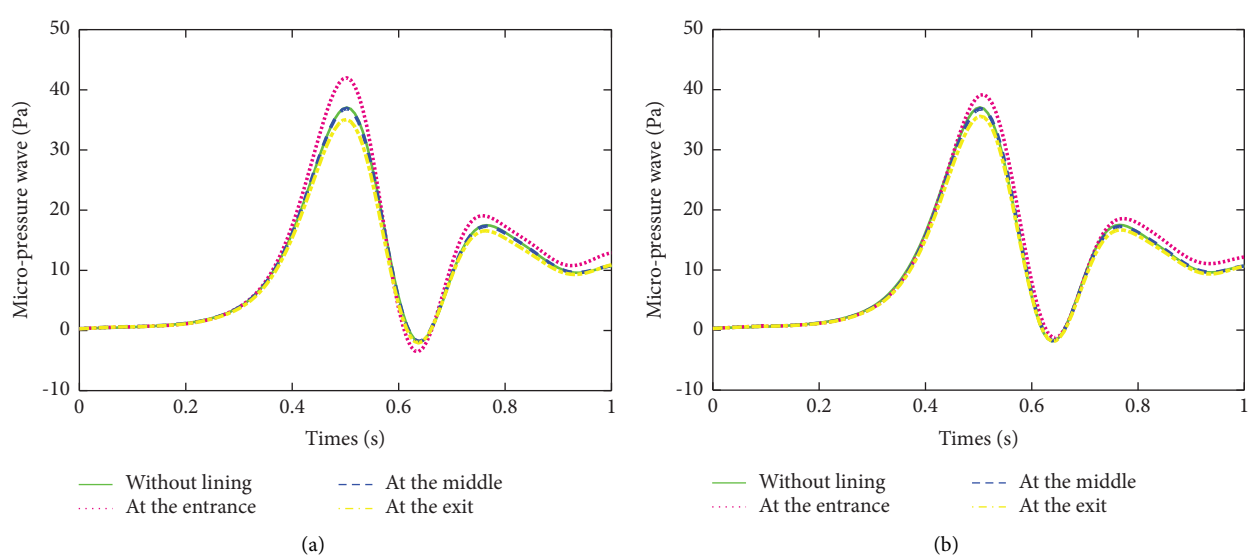

Figure 9: Continued.

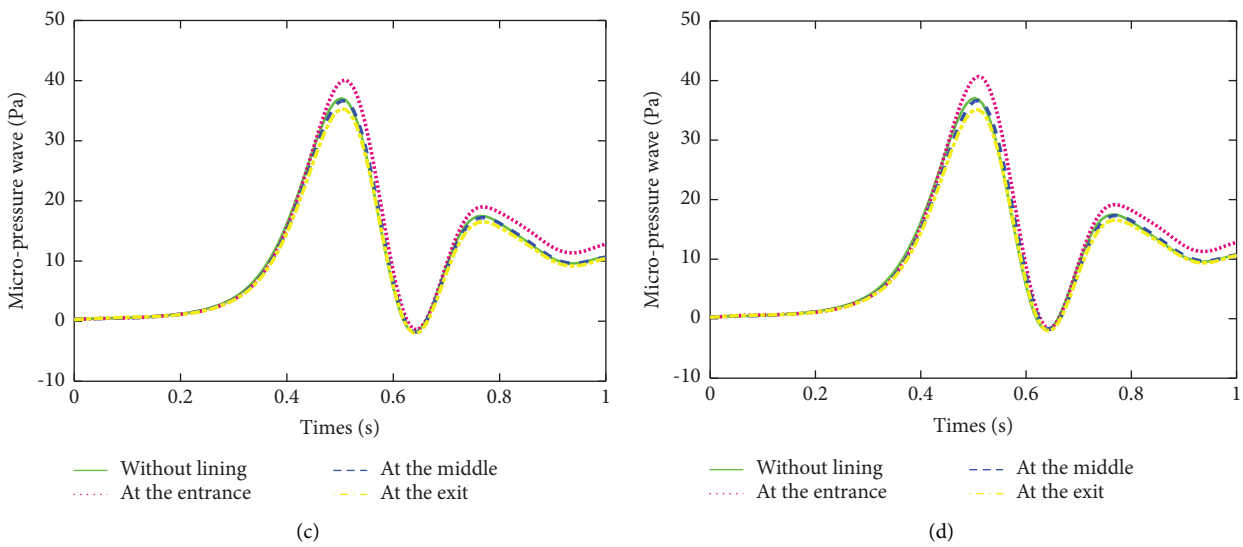

Figure 9: Comparison of the micropressure wave at $M3$. (a) Normal linings. (b) 10-segment linings. (c) 20-segment linings. (d) 30-segment linings.

Table 4: The amplitude values of the micro-pressure wave at $M1$.

The position of the linings	Without linings	Normal linings	Segmented linings		
			10-segment	20-segment	30-segment
Entrance of the tunnel		97.969	91.225	93.417	94.880
In the middle	86.305	85.888	85.769	85.440	85.258
In the exit		81.853	83.204	82.559	82.172

Table 5: The amplitude values of the micro-pressure wave at $M3$.

The position of the linings	Without linings	Normal linings	Segmented linings		
			10-segment	20-segment	30-segment
Entrance of the tunnel		41.994	39.181	40.105	40.701
In the middle	37.051	36.918	36.835	36.655	36.645
In the exit		35.053	35.569	35.286	35.096

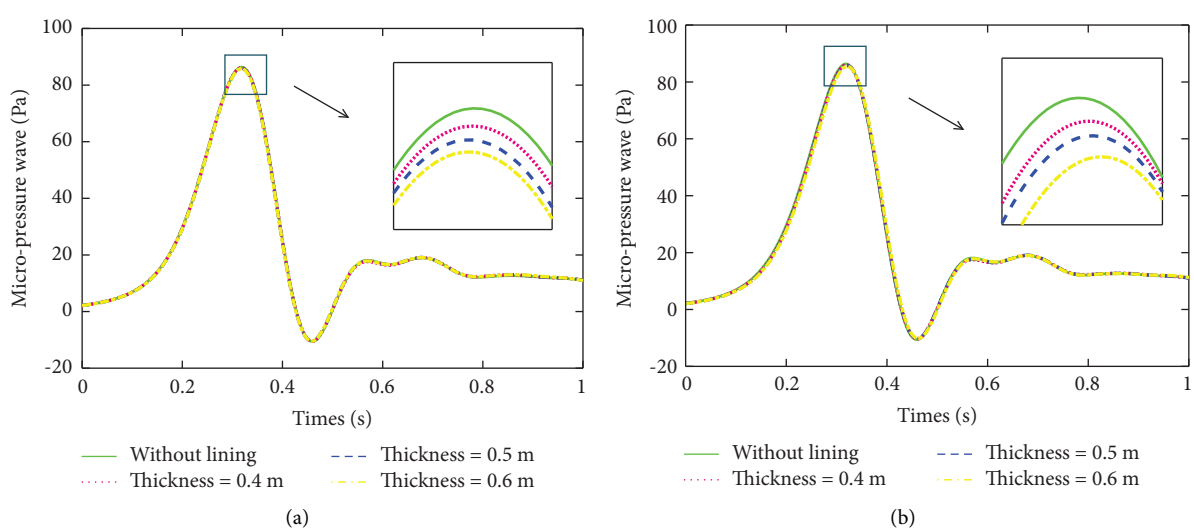

Figure 10: Comparison of the micropressure wave at $M1$. (a) Normal linings. (b) 10-segment linings.

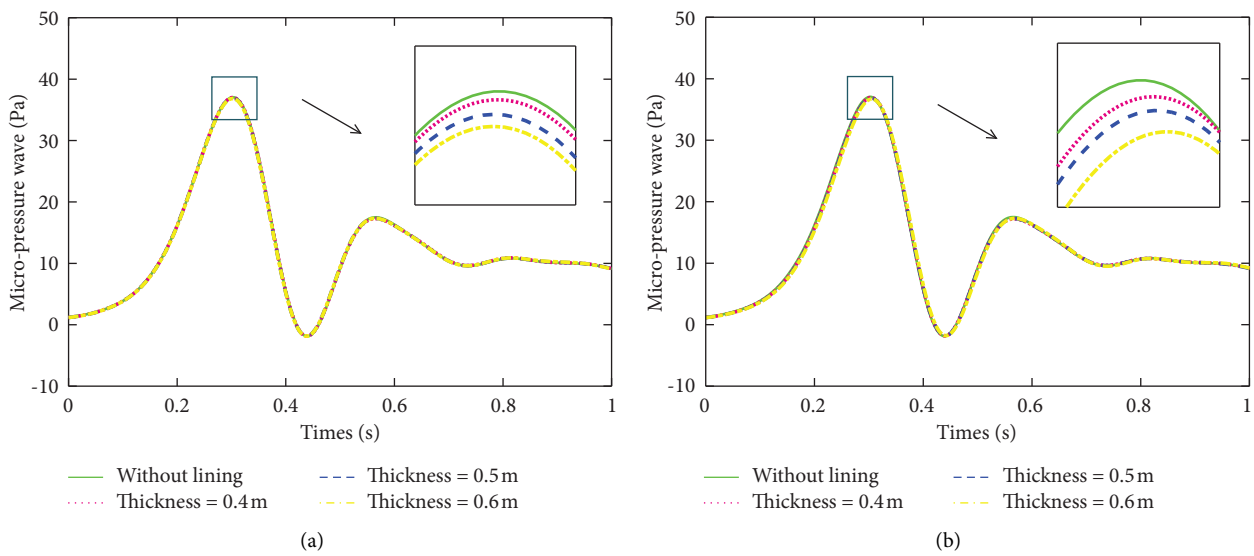

Figure 11: Comparison of the micropressure wave at $M3$. (a) Normal linings. (b) 10-segment linings.

Table 6: Comparison of amplitude values of the micropressure wave at $M1$.

MPW (Pa)	The thickness of linings (m)			
	0 m	0.4 m	0.5 m	0.6 m
Normal linings	86.305	86.076	85.888	85.741
Segmented linings		85.985	85.769	85.444

Table 7: Comparison of amplitude values of the micropressure wave at $M3$.

MPW (Pa)	The thickness of linings (m)			
	0 m	0.4 m	0.5 m	0.6 m
Normal linings	37.051	37.003	36.918	36.850
Segmented linings		36.933	36.835	36.672

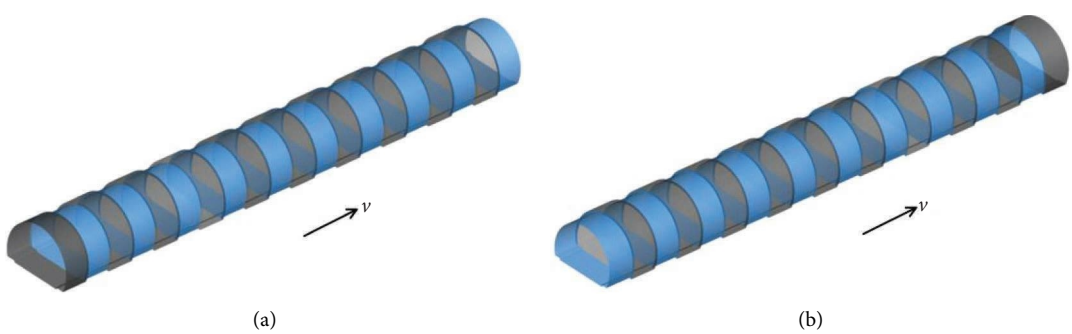

Figure 12: Different types of lining models. (a) Type 1. (b) Type 2.

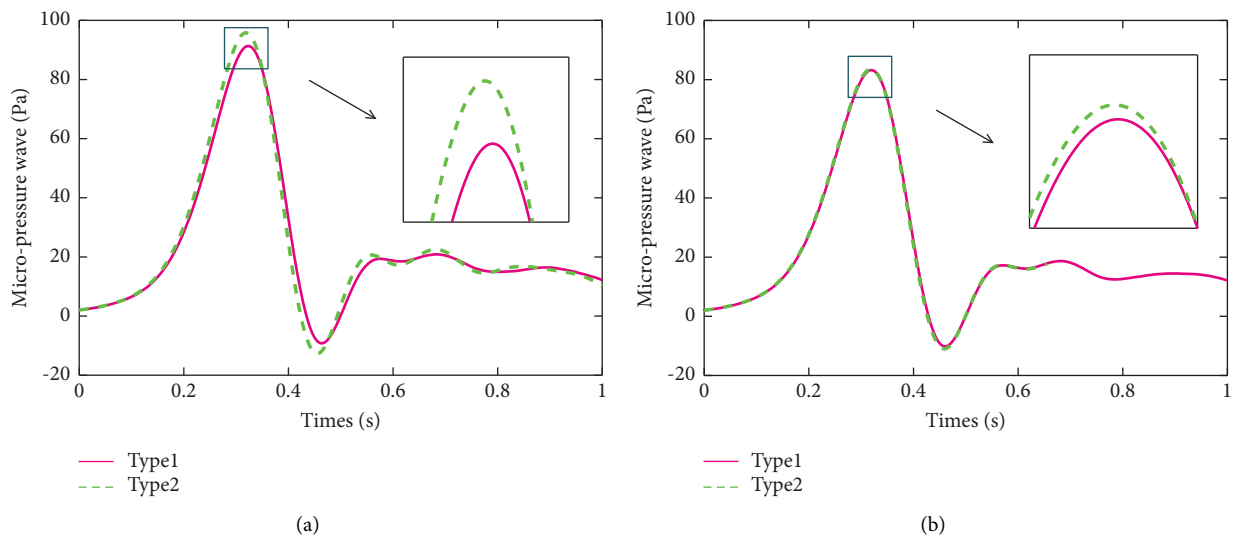

Figure 13: Comparison of the micropressure wave at $M1$. (a) Linings at the tunnel entrance. (b) Linings at the tunnel exit.

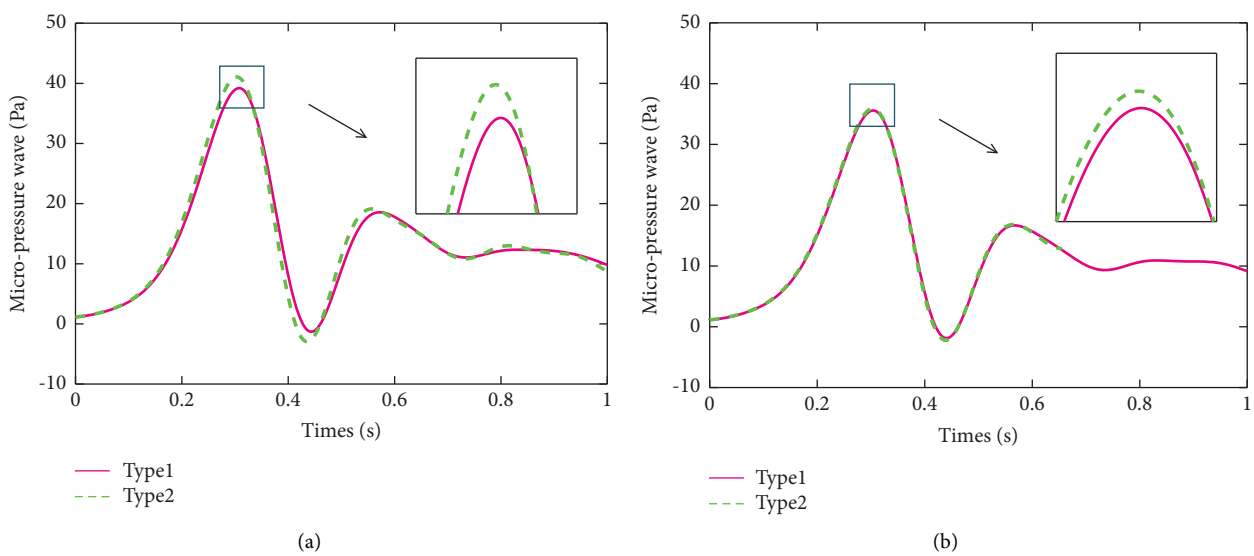

Figure 14: Comparison of the micropressure wave at $M3$. (a) Linings at the tunnel entrance. (b) Linings at the tunnel exit.

The results show that the type of segmented linings located at tunnel entrance has a greater impact on MPW. Therefore, a segmented lining structure can be used if damages occur close to the tunnel entrance, and the constricted section of the lining should be slightly away from the tunnel entrance.

5. Conclusions

In this paper, a 3D numerical method is used to research the aerodynamic impacts produced by trains traveling through a tunnel with linings at 350 km/h. The influence of the numbers, thickness, location, and types of the segmented lining structure on MPW are analyzed. The following can be concluded from the results:

(1) Both normal linings and segmented linings located at the entrance of the tunnel have an adverse effect on MPW, while a favorable effect is induced when the linings locate at the middle and exit of the tunnel and the mitigation effect is better for the linings at the tunnel exit.

(2) When the segmented linings are located at the tunnel entrance, the amplitude of MPW increases with the increase of the number of segments. When the segmented linings are located at the middle and exit of the tunnel, the amplitude of MPW decreases with the increase of the number of segments. In addition, when the linings are located in the tunnel middle, the segmented linings have a better mitigation effect on MPW than the normal linings, which increases with

the segment number of the linings. When a 30-segment lining structure with a thickness of 0.5 m is set near the exit of the tunnel, the amplitude values of MPW at 20 m and 50 m outside the tunnel decrease by 4.789% and 5.277%, respectively;

(3) The mitigation effects of both normal linings and segmented linings increase slightly with the thickness of the linings.

(4) When the damage occurs near the entrance of the tunnel, a segmented lining structure can be used to reduce its adverse effect on MPW and the constricted section of the lining structure should be slightly away from the tunnel entrance.

(5) The problem of tunnel damage can be repaired by adding segmented linings and reducing MPW. Other aerodynamic effects caused by train tunnel (such as train wind, transient pressure, passenger comfort, and so on) will be studied in future work.

Data Availability

All data generated or analyzed during this study are included in this article and are available upon request by contact with the corresponding author.

Conflicts of Interest

The author declares that there are no conflicts of interest.

Acknowledgments

This work was supported by the State Key Laboratory for Track Technology of High-Speed Railway (Grant no. 2021YJ056) and Natural Science Foundation of Shandong Province, China (Grant nos. ZR2020MA057 and ZR2021QE108), and Science and Technology R&D Program of China Railway (P2021G053).

References

[1] T. Miyachi, "Acoustic model of micro-pressure wave emission from a high-speed train tunnel," *Journal of Sound and Vibration*, vol. 391, pp. 127–152, 2017.

[2] D. Uystepruyst, M. William-Louis, and F. Monnoyer, "3D numerical design of tunnel hood," *Tunnelling and Underground Space Technology*, vol. 38, pp. 517–525, 2013.

[3] T. Aoki, K. Matsuo, and H. Hidaka, "Attenuation and distorsion of propagating compression waves in a high-speed railway model and in real tunnels," *Shock Waves in Condensed Matter and Heterogeneous Media*, vol. 1995, pp. 347–352, 1995.

[4] T. Fukuda, S. Ozawa, M. Iida, T. Takasaki, Y. Wakabayashi, and T. Miyachi, "Propagation of compression wave in a long tunnel with slab tracks," *Quarterly Report of RTRI*, vol. 46, no. 3, pp. 188–193, 2005.

[5] L. H. Xu and M. Ma, "Dynamic response of the multilayered half-space medium due to the spatially periodic harmonic moving load," *Soil Dynamics and Earthquake Engineering*, vol. 157, Article ID 107246, 2022.

[6] M. Ma, M. H. Li, X. Y. Qu, and H. G. Zhang, "Effect of passing metro trains on uncertainty of vibration source intensity: monitoring tests," *Measurement*, vol. 193, Article ID 110992, 2022.

[7] C. Zou, J. A. Moore, M. Sanayei, Z. Tao, and Y. Wang, "Impedance model of train-induced vibration transmission across a transfer structure into an overtrack building in a metro depot," *Journal of Structural Engineering*, vol. 148, no. 11, 2022.

[8] M. Bellenoue, B. Auvity, and T. Kageyama, "Blind hood effects on the compression wave generated by a train entering a tunnel," *Experimental Thermal and Fluid Science*, vol. 25, no. 6, pp. 397–407, 2001.

[9] W. Li, T. Liu, X. Huo, Z. Chen, Z. Guo, and L. Li, "Influence of the enlarged portal length on pressure waves in railway tunnels with cross-section expansion," *Journal of Wind Engineering and Industrial Aerodynamics*, vol. 190, pp. 10–22, 2019.

[10] R. Gawthorpe, "Pressure effects in railway tunnels," *Rail International*, vol. 31, pp. 10–17, 2000.

[11] D. Cross, B. Hughes, D. Ingham, and L. Ma, "A validated numerical investigation of the effects of high blockage ratio and train and tunnel length upon underground railway aerodynamics," *Journal of Wind Engineering and Industrial Aerodynamics*, vol. 146, pp. 195–206, 2015.

[12] J. M. Rivero, E. González-Martínez, and M. Rodríguez-Fernández, "A methodology for the prediction of the sonic boom in tunnels of high-speed trains," *Journal of Sound and Vibration*, vol. 446, pp. 37–56, 2019.

[13] M. Ito, "Improvement to the aerodynamic characteristics of Shinkansen rolling stock," *Proceedings of the Institution of Mechanical Engineers - Part F: Journal of Rail and Rapid Transit*, vol. 214, no. 3, pp. 135–143, 2000.

[14] T. Pei, L. Chen, X. Shi, and Y. Shi, "Study on treatment measures of cracks in lining of existing railway tunnel," *Railway Engineering*, vol. 2013, no. 04, pp. 76–79, 2013.

[15] H. Jin, Q. Tian, and Z. Li, "Crack development of rebar rust in rubberized concrete using mesoscale model," *Construction and Building Materials*, vol. 321, Article ID 126409, 2022.

[16] H. Jin, J. Su, and C. Zhao, "Relationship between invert-filling disengaging and deformation of shield tunnel using staggered assembled segment," *KSCE Journal of Civil Engineering*, vol. 26, no. 4, pp. 1966–1977, 2022.

[17] X. Xiang, L. Xue, and B. Wang, "Aerodynamic effects of inclined portals on the initial compression wave generated by a high-speed train entering a tunnel," *Journal of Fluids Engineering*, vol. 137, no. 12, Article ID 121104, 2015.

[18] P. Murray and M. Howe, "Influence of hood geometry on the compression wave generated by a high-speed train," *Journal of Sound and Vibration*, vol. 329, no. 14, pp. 2915–2927, 2010.

[19] T. h. Liu, H. q. Tian, and X. f. Liang, "Design and optimization of tunnel hoods," *Tunnelling and Underground Space Technology*, vol. 25, no. 3, pp. 212–219, 2010.

[20] X. Xiang, L. Xue, B. Wang, and W. Zou, "Mechanism and capability of ventilation openings for alleviating micro-pressure waves emitted from high-speed railway tunnels," *Building and Environment*, vol. 132, pp. 245–254, 2018.

[21] D. H. Kim, S. Y. Cheol, R. S. Iyer, and H. D. Kim, "A newly designed entrance hood to reduce the micro pressure wave emitted from the exit of high-speed railway tunnel," *Tunnelling and Underground Space Technology*, vol. 108, Article ID 103728, 2020.

[22] L. Zhang, M. z. Yang, X. f. Liang, and J. Zhang, "Oblique tunnel portal effects on train and tunnel aerodynamics based on moving model tests," *Journal of Wind Engineering and Industrial Aerodynamics*, vol. 167, pp. 128–139, 2017.

[23] M. S. Howe, M. Iida, T. Fukuda, and T. Maeda, "Theoretical and experimental investigation of the compression wave generated by a train entering a tunnel with a flared portal," *Journal of Fluid Mechanics*, vol. 425, Article ID S0022112000002093, 2000.

[24] F. Liu, W. Zhou, J. q. Niu, and J. Zhang, "Impact of increased linings on pressure transients induced by a train passing through a tunnel," *Sustainable Cities and Society*, vol. 45, pp. 314–323, 2019.

[25] F. Liu, S. Yao, J. Zhang, and Y. b. Zhang, "Effect of increased linings on micro-pressure waves in a high-speed railway tunnel," *Tunnelling and Underground Space Technology*, vol. 52, pp. 62–70, 2016.

[26] J. Gao, "Design analysis on reinforcement sleeves for high-speed railway tunnels based on aerodynamic effect," *Railway Quality Control*, vol. 44, no. 01, pp. 40–44, 2016.

[27] X. Shi, J. Wu, X. Leng, and D. Niu, "Influence of added lining on micro pressure wave of high speed railway tunnel portals," *Railway Engineering*, vol. 57, no. 10, pp. 53–55+59, 2017.

[28] T. Wang, X. Han, L. Zhang, B. Qian, Z. Sun, and H. Liu, "Effect of non-circular tunnel linings on pressure transients induced by high-speed train passes through a tunnel based on moving model test," *Journal of Wind Engineering and Industrial Aerodynamics*, vol. 214, Article ID 104649, 2021.

[29] Q. Fang, D. Zhang, Q. Li, and L. N. Y. Wong, "Effects of twin tunnels construction beneath existing shield-driven twin tunnels," *Tunnelling and Underground Space Technology*, vol. 45, pp. 128–137, 2015.

[30] W. Yang, E. Deng, M. Lei, P. Zhang, and R. Yin, "Flow structure and aerodynamic behavior evolution during train entering tunnel with entrance in crosswind," *Journal of Wind Engineering and Industrial Aerodynamics*, vol. 175, pp. 229–243, 2018.

[31] M. Rabani and A. K. Faghih, "Numerical analysis of airflow around a passenger train entering the tunnel," *Tunnelling and Underground Space Technology*, vol. 45, pp. 203–213, 2015.

[32] J. Du, Q. Fang, J. Wang, and G. Wang, "Influences of high-speed train speed on tunnel aerodynamic pressures," *Applied Sciences*, vol. 12, no. 1, p. 303, 2021.

[33] M. Shao, C. Ma, and S. Hu, "Effects of time-varying fluid on dynamical characteristics of cantilever beams: numerical simulations and experimental measurements," *Mathematical Problems in Engineering*, vol. 2020, Article ID 6679443, 18 pages, 2020.

[34] T. Wang, C. Hu, and Y. Gong, "Mitigation of micro-pressure wave at 400 km/h railway tunnel exit by oblique enlarged tunnel-hood," *Acta Aerodynamica Sinica*, vol. 39, no. 05, pp. 151–161, 2021.

[35] J. Niu, Y. Sui, Q. Yu, X. Cao, and Y. Yuan, "Numerical study on the impact of Mach number on the coupling effect of aerodynamic heating and aerodynamic pressure caused by a tube train," *Journal of Wind Engineering and Industrial Aerodynamics*, vol. 190, pp. 100–111, 2019.

[36] K. Liu, L. Jing, and M. Ren, "The characteristics of air wave induced by two high-speed trains passing by each other in a tunnel," *Advances in Mechanical Engineering*, vol. 10, no. 3, Article ID 168781401876697, 2018.

[37] L. Zhang, K. Thurow, N. Stoll, and H. Liu, "Influence of the geometry of equal-transect oblique tunnel portal on compression wave and micro-pressure wave generated by high-speed trains entering tunnels," *Journal of Wind Engineering and Industrial Aerodynamics*, vol. 178, pp. 1–17, 2018.

[38] A. Yamamoto, "Micro-pressure wave radiated from a tunnel exit," *Nihon Butsuri Gakkai Haru Bunkakai*, The Physical Society of Japan Spring Meeting), Japan, 1977.

[39] L. Zhang, H. Liu, N. Stoll, and K. Thurow, "Influence of tunnel aerodynamic effects by slope of equal-transect ring oblique tunnel portal," *Journal of Wind Engineering and Industrial Aerodynamics*, vol. 169, pp. 106–116, 2017.

[40] Y. Mei, R. Wang, and J. Xu, "Numerical simulation of initial compression wave induced by a high-speed train moving into a tunnel," *Chinese Journal of Computational Mechanics*, vol. 33, no. 1, pp. 95–101, 2016.

Hindawi
Advances in Civil Engineering
Volume 2022, Article ID 6759797, 15 pages
https://doi.org/10.1155/2022/6759797

Research Article

Discrete Element Simulation and Monitoring Analysis of Different Construction Methods of the Shallow Buried Bias Tunnel

Chenyu Ge,[1] Liping Su,[1] Lin Wang,[1] Shuo Xu,[2] and Pengqiang Yu[2]

[1]*Beijing Municipal Road and Bridge Co Ltd, Beijing 100045, China*
[2]*University of Science and Technology Beijing, Beijing 100083, China*

Correspondence should be addressed to Pengqiang Yu; yu_pengqiang@163.com

Received 30 August 2022; Accepted 30 September 2022; Published 13 October 2022

Academic Editor: Ziyu Tao

Affected by the bias stress, the mechanical properties of shallow buried bias tunnel construction are complex. The influence of different construction methods on the stability of the portal section of the shallow buried bias tunnel has received significant attention in past studies, but the microscopic mechanism of it has not been properly analyzed. In this study, the discrete element method is used to simulate the construction steps of the three-step method and the single side heading method with and without systematic bolt supports taking Qijiazhuang tunnel as the research object. The tunnel surrounding rock stress, vertical displacement, and surface deformation results under different working conditions are analyzed, and the mechanism of systematic bolt supports is analyzed from microscopic perspective. The results show that the single side heading method can gradually release the load and deformation and better play the supporting capacity of lining; the existence of systematic bolt improves the shear capacity of surrounding rock and enhances the arching effect, thus significantly reducing the vertical displacement of surrounding rock and surface deformation. Finally, compared with the field monitoring data, it is recommended to adopt the single side heading method with systematic bolt support for the construction of the portal section.

1. Introduction

With the rapid development of infrastructure construction in China, more and more highway and railway tunnel projects are being built. Due to the numerous mountains and complex geological conditions in China, a large number of tunnels inevitably pass through shallow buried, bias and weak surrounding rock areas [1–5]. The presence of shallow buried bias terrain will induce the bias stress. Meanwhile, the surrounding rock of cave entrance is often broken, affected by soft ground soil and seepage, and the topographic and geological conditions are complicated. Therefore, fully understanding the influence of different excavation methods and supporting schemes on the stability of surrounding rock of the shallow buried bias tunnel has an important reference for guaranteeing the stability of tunnel entrance and surface.

Model experiment and theoretical analysis are important methods to study geotechnical problems [6–10]. Lei et al. [4, 11, 12] studied the fracture mechanism of surrounding rock of the shallow buried bias tunnel under different bias angles by using model experiment and obtained the variation law of surrounding rock pressure of deep and shallow buried side with bias angle and compared with the calculation method in the standard. Teng et al. [13] derived the calculation formula of surrounding rock pressure of the shallow buried bias tunnel with small spacing considering the construction process and terrain slope by using theoretical analysis and the stress law of surrounding rock under different bias angles, and buried depths were analyzed and compared with the condition that ground surface was horizontal.

With the rapid development of computer and numerical simulation software, the numerical method has gradually become an effective method to analyze geotechnical engineering problems. Since the strong repeatability and the ability to simulate various working conditions, numerical simulation has been favored by many scholars [14–17]. Scholars at home and abroad used numerical methods to

simulate the excavation of the shallow bias tunnel and obtained the stress and deformation law of surrounding rock [1–3, 18]. Some scholars also considered the support and reinforcement conditions of real constructions in the numerical simulation, obtaining the stress and deformation law and evaluating the effect of field construction and reinforcement [5, 19–21]. Dong [19] analyzed the settlement deformation of the tunnel by numerical simulation and evaluated the effect of the existing supporting structure and the effect of the back pressure backfilling reinforcement measures. In addition to evaluating the effectiveness of existing supporting structures, numerical simulation can also be used to optimize construction methods for shallow bias tunnels [22–25]. Zhao et al. [22] simulated the portal section of the shallow buried bias tunnel by using ANSYS software and obtained the construction schemes that meet both the standards and the stability requirements. Numerical simulation can also be used to reveal the stress mechanism of the shallow buried bias tunnel. Yang et al. [26] studied the failure mechanism and treatment measures of the main support of the shallow buried bias tunnel.

The existing simulation is mostly based on the continuum mechanics method, and there are few studies on the mesoscopic mechanism of the stability of the shallow buried bias tunnel. The discrete element method (DEM) is an important method to study the mechanical behavior of discontinuous media from the perspective of mesoscopic force chain [27, 28]. As a typical discontinuous media, it is more appropriate to analyze the stability of surrounding rock of shallow buried bias tunnel excavation from microscopic perspective using the discrete element method (DEM) [29–37]. Therefore, the aim of this study is to use DEM to study the law of surrounding rock stress, displacement, and surface deformation under different support methods during the excavation of the shallow buried bias tunnel and analyze the microscopic mechanism of the shallow buried bias tunnel, taking Qijiazhuang tunnel as engineering background. The development law of cracks in the surrounding rock caused by tunnel excavation, the distribution characteristics of contact force, and the evolution law of pressure arch are analyzed from microscopic perspective. The optimal tunnel excavation method and support measures are obtained by comparing with the field monitoring data.

2. Project Overview

The Qijiazhuang tunnel is located in Qijiazhuang village, Mentougou district, Beijing. The starting and ending mileage of the left line is A1K70 + 075~A1K70 + 369.14, with the length of 294.14 m, whose maximum buried depth is 29 m. For right line, starting and ending mileage is AK70 + 076.286~AK70 + 375, with the length of 298.714 m, whose maximum buried depth is 41 m. The entrance and exit of the tunnel are located in the slope of the foothills. The tunnel portal, mileage A1K70 + 090~A1K70 + 195, is shallow buried and bias section, where the angle of surface slope is about 15~35°. The tunnel axis is basically orthogonal to the contour, and the bedrock is exposed above the entrance.

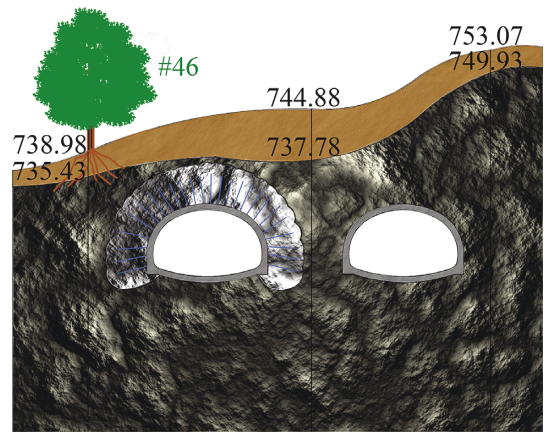

Figure 1: Schematic graph of section A1K70 + 115 of tunnel.

There are more than 60 cypress trees whose diameter is greater than 30 cm on the ground surface of the tunnel. The surface of slope is residual soils with the thickness of 0.5~2.0 m. Beneath the soil are strongly weathered andesites. The bias tunnel and distribution of rock and soil layers are shown in Figure 1, and the longitudinal section of tunnel is shown in Figure 2.

The surrounding rock is highly and moderately weathered, rock mass is broken, and joint fissure develops, and small range of water gushing in surrounding rock of tunnel entrance. According to criteria for surrounding rock mass classification in standard for engineering classification of rock mass (GB50218-2014) [38], the surrounding rock of the Qijiazhuang tunnel is defined as IV-V levels. Figure 3 shows the silts and residual soil on the surface of mountain slope.

Initial lining consists of section steel frame, system bolt and sprayed concrete, and mat reinforcement. Among them, the section steel frame adopts I22b steel with longitudinal spacing of 50 cm; the system bolt adopts φ25 bolt, whose length is 4 m, and hollow grouting is adopted. The longitudinal spacing of the bolt is 50 cm, and the circumferential spacing is 100 cm, using the plum-shaped arrangement; the sprayed concrete uses C25 concrete with the thickness of 28 cm.

3. Numerical Model

3.1. Working Conditions. According to different excavation methods (three-step method and single side heading method) and different support methods (with and without system bolt support), four work conditions are selected and are shown in Table 1.

3.2. Discrete Element Model Determination. The numerical model is established according to section A1K + 115 of tunnel, and the surrounding rock classification of the section is V level. The buried depth of left and right tunnel is 12 and 19 m, respectively. The width of excavated section of left and right tunnel is 44.71 m, and the height of the section is 11.861 m. Based on elastoplasticity theory, the size of the

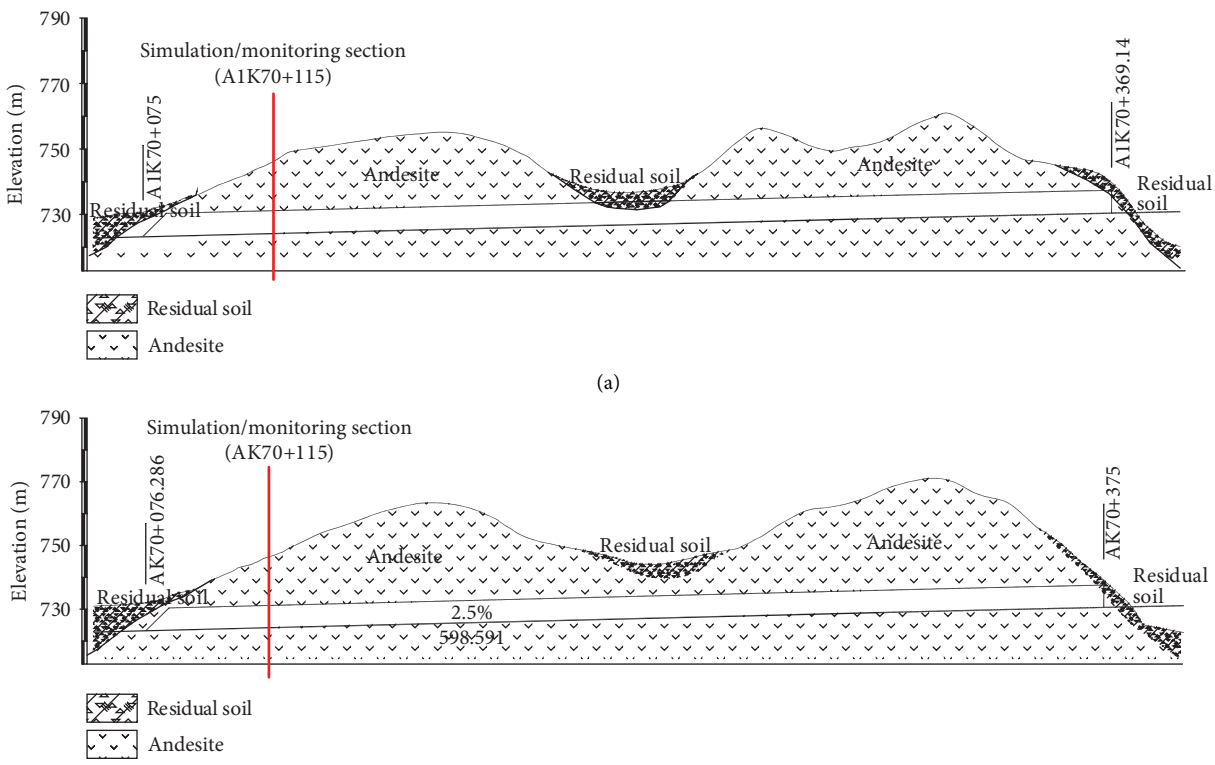

Figure 2: Longitudinal profile diagram of the Qijiazhuang tunnel: (a) longitudinal profile diagram of left line; (b) longitudinal profile diagram of right line.

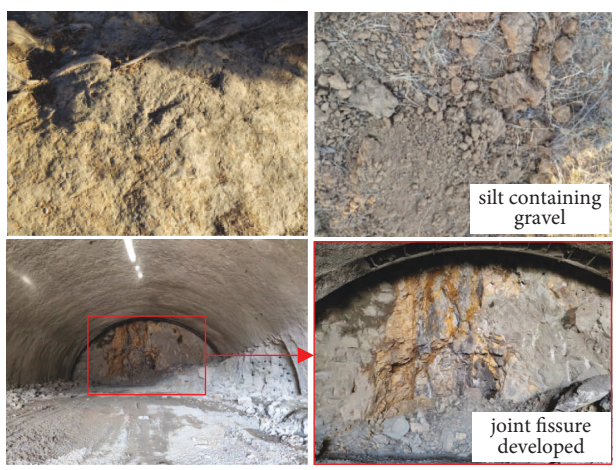

Figure 3: Geological features of surface residual soil and surrounding rock.

Table 1: Scheme of numerical simulation for different excavations and reinforcements.

Work condition	Excavation method	Support method
1	Three-step method	Initial support (without systematic bolt)
2	Three-step method	Initial support (with systematic bolt)
3	Single side heading method	Initial support (without systematic bolt)
4	Single side heading method	Initial support (with systematic bolt)

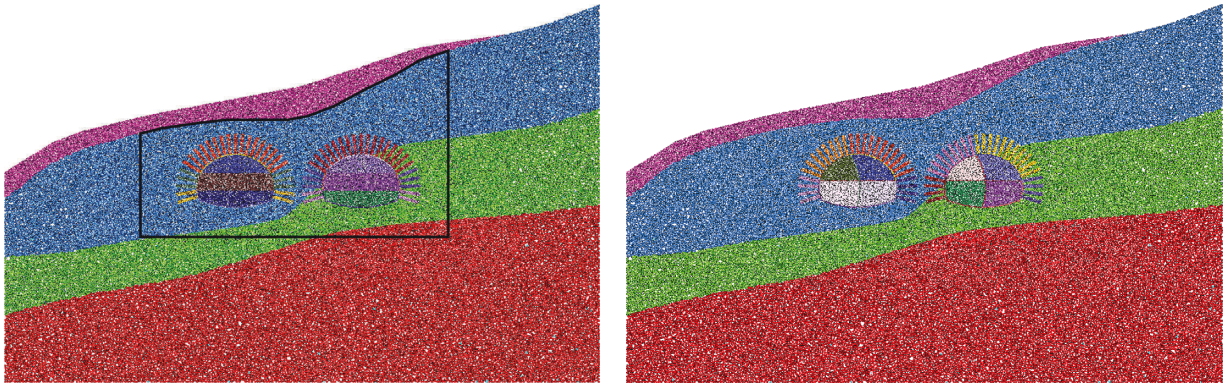

(a) (b)

Figure 4: Numerical model: (a) three-step method; (b) single side heading method.

model should be 3~5 times as long as the span of the tunnel to reduce the effect of boundary condition. As shown in Figure 4, the width and height of the model are 130 m and 82.67 m, respectively. The tunnel is located at the central axis of the model, the minimum point of the inverted arch is 38.168 m away from the bottom of the model, and the thickness of initial lining is 280 mm. Constraint of horizontal displacement is applied on the left and right boundaries of the model, and constraint of vertical displacement is applied on the bottom of the model, and the top of the model is freedom boundary condition. The system bolt and grout reinforcement range are equivalent to rectangle with 4.5 m length and 0.75 m width.

According to the "Particle-Size Refinement" method, the particles within the specified range are generated. The interparticle contact model adopts the linear parallel bond model, which is suitable for cemented materials such as rock. Besides, in order to improve the calculating efficiency, the radius of particles near the tunnel disperses from 0.035 to 0.255 m, which is shown in domain enclosed by black curve in Figure 4. While the radius of particles in other parts is between 0.255 and 0.367 m, the total amount of particles in the model is 162092. The initial stress of the model is obtained by applying the gravity field with 10.0 gravity acceleration. After equilibrium, the vertical stress at the bottom midpoint is 1.38 MPa, which is close to the stress of 1.264 MPa at the lower boundary obtained by the elastic theory. After excavation, parameters of initial lining are applied.

3.3. Model Parameters. Based on the tunnel design instructions, engineering investigation report, and engineering analogy, the macroscopic parameters of geomaterials could be determined. The macroscopic parameters of surrounding rock and strata are shown in Table 2.

According to the data provided by the engineering investigation report, the rock biaxial compression numerical test is adopted. By adjusting and optimizing the microscopic parameters continuously, the model parameters can be obtained by selecting the results of test which are close to the data of the report. The final micromechanical parameters of each stratum are shown in Table 3. The Mohr–Coulomb strength envelope of the moderately weathered rock is shown in Figure 5. Notably, the simulated cohesion and internal friction angle are in good agreement with the engineering investigation results.

The macroscopic parameters of the initial support are determined based on the equivalent calculation method. The parameters of section steel frame and steel mesh in the initial lining are converted to sprayed concrete, i.e., $E_c = E_0 + (A_s \cdot E_s)/A_c$, where E_0 and E_c are the elastic moduli of concrete before and after equivalent, respectively, E_s is the elastic modulus of steel, and A_c and A_s are the section areas of concrete and section steel frame, respectively. The systematic bolt is simulated by enhancing the value of parameters of rock mass.

4. Simulation Results and Discussion

4.1. Stress Results. Figure 6 shows the contact force distributions of the three-step method for each excavation stages (without systematic bolt support) and final stage, and Figure 7 shows the contact force distributions for the final excavation stage of the single side heading method. The horizontal, vertical, and shear stress of the position can be obtained by setting the measure circle. The stress within the circle is calculated by $\sigma_{ij} = 1/V \sum_c l_i f_j$, where l_i is the branch vector, defined as vector connecting center of particles, f_i is the contact force between particles, and V is the area of measure circle.

The black and red points in Figures 6(b) and 7 represent the positions of the first three highest horizontal and vertical stress, respectively.

4.1.1. Three-Step Method. As shown in Figure 6(a), with the depth enhancing, the contact force distribution of the initial state increases uniformly, and the stress of the deep buried side is greater than that of the shallow buried side [13]. The stress redistribution of surrounding rock is caused by excavation of each section. The decrease of contact force in

Table 2: Macromechanical parameters for numerical simulation.

Materials	Modulus of deformation E (GPa)	Poisson's ratio μ	Internal friction angle Φ (°)	Cohesion c (MPa)	Unit weight γ (kN/m^3)
Residual soil	21e-3	0.35	22	18e-3	18
Highly weathered rock	1.9	0.35	27	0.15	19.0
Moderately weathered rock	1.95	0.35	29	0.25	19.5
Slightly weathered rock	2.1	0.35	29	0.25	19.5
Initial lining	35	0.25	—	—	25
Bolt and grouting	11.0	0.25	30	1.35	20

Table 3: Micromechanical parameters for numerical simulation.

Materials	Density ρ (kg/m^3)	Coefficient of friction μ	Effective modulus E^* (Pa)	Normal-to-shear stiffness ratio K^*	Bond effective modulus $\overline{E}^*$ (Pa)	Bond normal-to-shear stiffness ratio $\overline{K}^*$	Tensile strength $\overline{\sigma}_c$ (Pa)	Cohesion $\overline{c}$ (Pa)	Friction angle $\overline{\varnothing}$ (°)
Residual soil	2000	0.4	50e-6	1	50e-6	1	80e-3	80e-3	32.5
Rock (highly weathered)	2300	0.6	1.0e-8	5.0	1.0e-9	5.0	9.0e-5	3.0e-5	32.50
Rock (moderately weathered)	2350	0.6	2.0e-8	5.0	2.0e-9	5.0	9.0e-5	3.0e-5	32.5
Rock (slightly weathered)	2400	0.6	2.0e-8	5.0	2.0e-9	5.0	9.0e-5	3.0e-5	35
Initial lining	2500	0.8	1.0e-8	5.0	20e-9	10	1.0e-25	1.0e-25	80
Bolt and grouting	2400	0.8	1.0e-8	5.0	6.0e-9	5.0	2.0e-6	8.0e-6	35

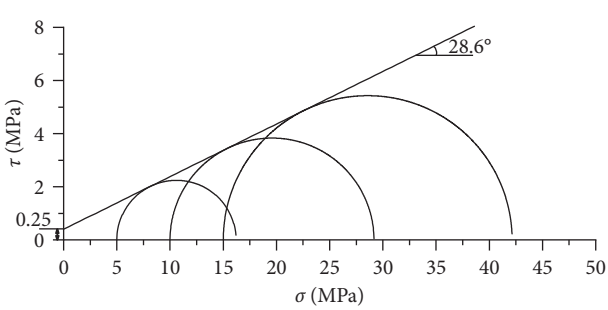

Figure 5: Strength envelope under biaxial compression (moderately weathered rock).

lower surrounding rocks is observed due to the release of pressure in excavation section. The rock above the tunnel spontaneously forms the arch structure. The stress in the range of bolt and grouting of work condition 2 are greater due to the adoption of bolt support, as shown in Figure 6(b).

According to the monitoring results of measure circles, the first three highest horizontal stress of work conditions 1 and 2 are 0.479, 0.421, 0.389 MPa and 0.535, 0.527, 0.476 MPa, respectively. Except the point of 0.476 MPa of work condition 2 is located in arch shoulder of right tunnel, other points are all located in arch footing. The first three highest vertical stress of work conditions 1 and 2 are 1.03, 0.984, 0.964 MPa and 1.06, 1.05, 1.01 MPa, respectively. Except these points of 0.984 and 1.06 MPa of work conditions 1 and 2 are located in mid-rock pillar, other points are all located in the lower part of surrounding rock of right tunnel. Obviously, work condition 2 shows the greater stress concentration.

The simulation results show that larger stress concentrations more likely occur at the arch footing, side wall, and mid-rock pillar in three-step method; the system bolt forms a strong bearing structure around the tunnel excavation section, transferring the load of upper rock and soil into depth part, resulting in the stress concentration at the arch footing, mid-rock pillar, and lining. In the actual construction, the support at these positions should be strengthened, and the right-side tunnel should be monitored to ensure the stability of surrounding rock.

4.1.2. Single Side Heading Method. As shown in Figure 7, similar with the result of the three-step method, the stress redistributions are caused by the excavation of each drift heading, and the decrease of contact force in lower surrounding rocks is found due to release of pressure of excavated sections. The rock above the tunnel spontaneously forms the arch structure, and the stress in the range of bolt and grouting of work condition 4 are higher. The stress of the deep buried side is greater than that of the shallow buried side due to the influence of terrain bias.

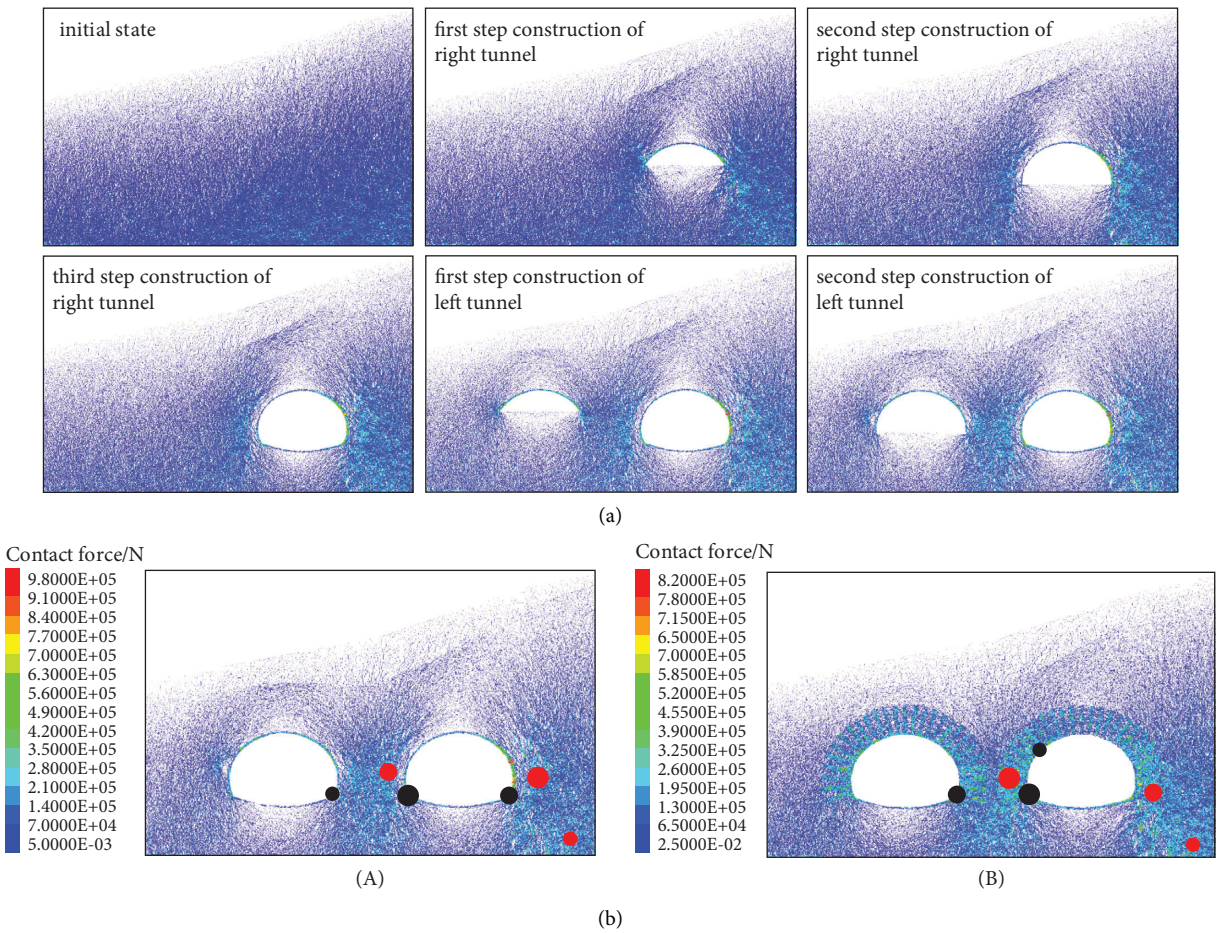

Figure 6: Distribution of contact forces of the three-step method: (a) distribution of contact forces for different excavation stages of the three-step method (without systematic bolt support); (b) distribution of contact forces for the final excavation stage of the three-step method: work condition 1 (A), work condition 2 (B).

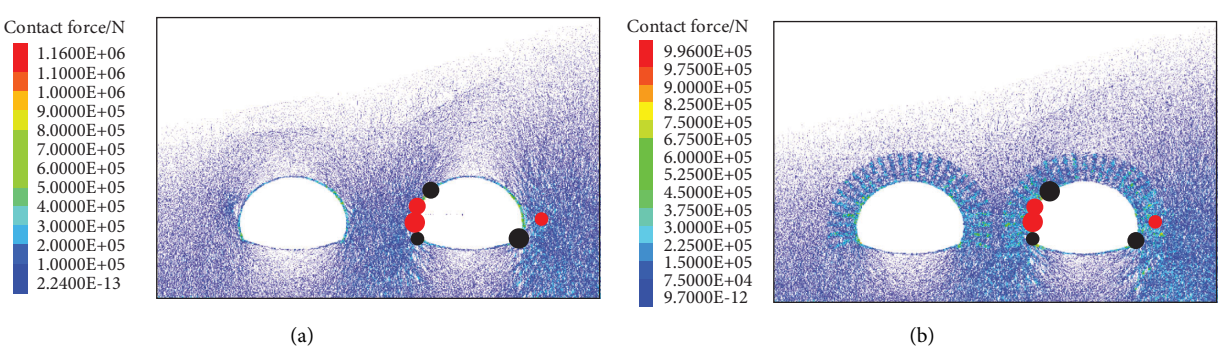

Figure 7: Distribution of contact forces for final excavation stage of the single side heading method: (a) work condition 3: the single side heading method without systematic bolt; (b) work condition 4: the single side heading method with systematic bolt.

According to the monitoring results of measure circles, the first three maximal horizontal stress of work conditions 3 and 4 are 0.52, 0.417, 0.41 MPa and 0.603, 0.565, 0.534 MPa, respectively. Except these points of 0.417 and 0.603 MPa located in arch shoulder of right tunnel, all other points located in the arch footing of right tunnel. The first three maximal vertical stress of work conditions 3 and 4 are 1.31, 1.15, 1.05 MPa and 1.19, 1.10, 1.02 MPa, respectively. Except these points of 1.05 and 1.02 MPa located in the right-side surrounding rock of right tunnel, all other points located in the left side wall of right tunnel. It is obvious that arch footing, arch shoulder, and side wall of right tunnel are the points of bearing greater stress, which is a disadvantage to the stability of the tunnel.

In the single side heading method, the positions of maximal stress are lining of right tunnel, which indicates that the single side heading method can give full play of bearing capacity of lining and alleviate surrounding rock stress concentration. Systematic bolt decreased the magnitude of vertical stress, but caused the increase of horizontal stress. Thus, the support at arch footing, arch shoulder, and side wall should be enhanced, and the monitoring frequency of mid-rock pillar should also be enhanced to guarantee stability of surrounding rock.

4.2. Displacement Results. Figure 8 shows the layout of surface and surrounding rock displacement measuring points. The displacement contours of different excavation stages of the three-step method and single side heading method without systematic bolt support are presented in Figures 9(a) and 10(a), respectively. Vertical displacement data measured by displacement measure circle are listed in Table 4.

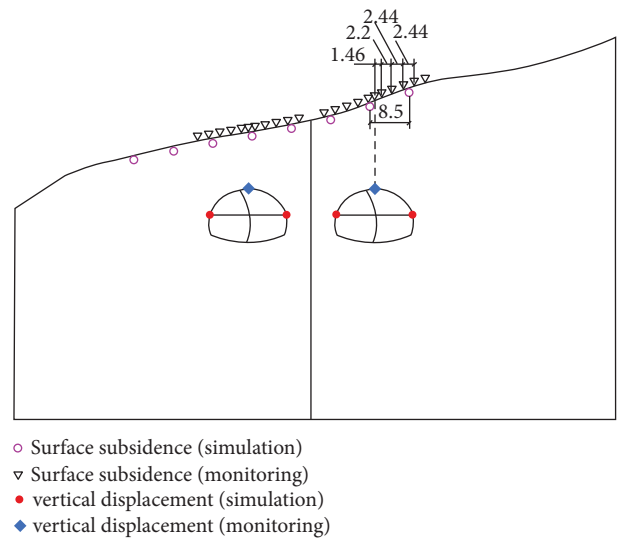

Figure 8: Layout of measuring points.

4.2.1. Three-Step Method. Figure 9 shows that the vertical displacement of surrounding rock gradually increased with the excavation of tunnel. The position of maximal vertical deformation is the vault of right tunnel, and large heave occurred in the bottom of left and right tunnel. Notably, the vertical displacement is unsymmetrical due to the influence of terrain bias.

For work condition 1, considering the shallow buried depth of left-upper part of right tunnel, the arching effect [39] is limited, which leads to the large vertical displacement of surrounding rock of left-upper part of right tunnel. After excavation of all sections, the vault subsidence of right and left tunnel is stabilized at 22.4 and 14.6 mm, respectively. The maximum vertical displacement occurs in the first step excavation stage of right tunnel, which is 14.5 mm, accounting for 64.7% of the total subsidence. Notably, the three-step method without applying systematic bolt has large vault subsidence, and large proportion of the vault subsidence was caused by the first step excavation.

Due to the use of bolt and grouting support, the bearing capacity of outer surrounding rock of tunnel section in work condition 2 is enhanced. Thus, the magnitude of vertical displacement is primarily depended on the surrounding rock stress, leading larger displacement in deep buried side. After the excavation of all sections, the vault subsidence of right and left tunnel is stabilized at 14.8 and 6.77 mm, respectively. Among them, the maximum subsidence occurred in the first step excavation stage of right tunnel, 11.6 mm, accounting for 78.4% of the total subsidence, followed by the second step excavation stage of right tunnel, 2.9 mm, accounting for 19.6% of the total subsidence. The magnitude of displacement of work condition 2 is less than that of work condition 1 due to the use of systematic bolt support.

4.2.2. Single Side Heading Method. Figure 10 shows that the vertical displacement of tunnel is concentrated at the vault, and vertical displacement of deep buried side is larger than that of shallow buried side due to the terrain bias.

Comparing the data in Figures 9 and 10 and Table 4, it can be found that the vault subsidence laws of the three-step method and the single side heading method are significantly different. Taking work conditions 1 and 3, for example, after excavation of left and right tunnels and removement of the temporary supports, the vault subsidence of right and left tunnel of work condition 3 is 14.4 and 10.9 mm, respectively. The maximum vertical displacement occurs in the rightt-up drift heading construction stage of right tunnel, which is 7.56 mm, accounting for 52.6% of the total subsidence. The vault subsidence and subsidence of arch waist generated by the three-step method is about 1.56 and 2.86 times as large as those of the single side heading method. It can be concluded that the single side heading method can gradually release the load and deformation, which is beneficial to make the support and control the magnitude of deformation.

It can also be noted that the ratio of vault subsidence of right-up drift heading excavation is maximum in all work conditions about the single side heading method. Therefore, the excavation of upper drift heading close to deep buried side is the key procedure that affects stability of the shallow buried bias tunnel, in constructions with the single side heading method. In this sense, for the real construction, the support should be applied in time and the monitoring frequency should be enhanced to prevent large deformation of surrounding rocks and ensure the safety of construction.

The results of vertical displacement in the vault of right tunnel, left arch waist of left tunnel, and arch waist of right tunnel are shown in Figure 11.

According to Table 4 and Figure 11, it can be concluded that the rule of displacement of different work conditions is basically consistent and the magnitude of displacement of the deep buried side is greater than that of the shallow buried side due to the terrain bias. There are sudden changes in the displacement curve of the left tunnel, which is caused by the excavation of the left tunnel, causing the disturbance of the

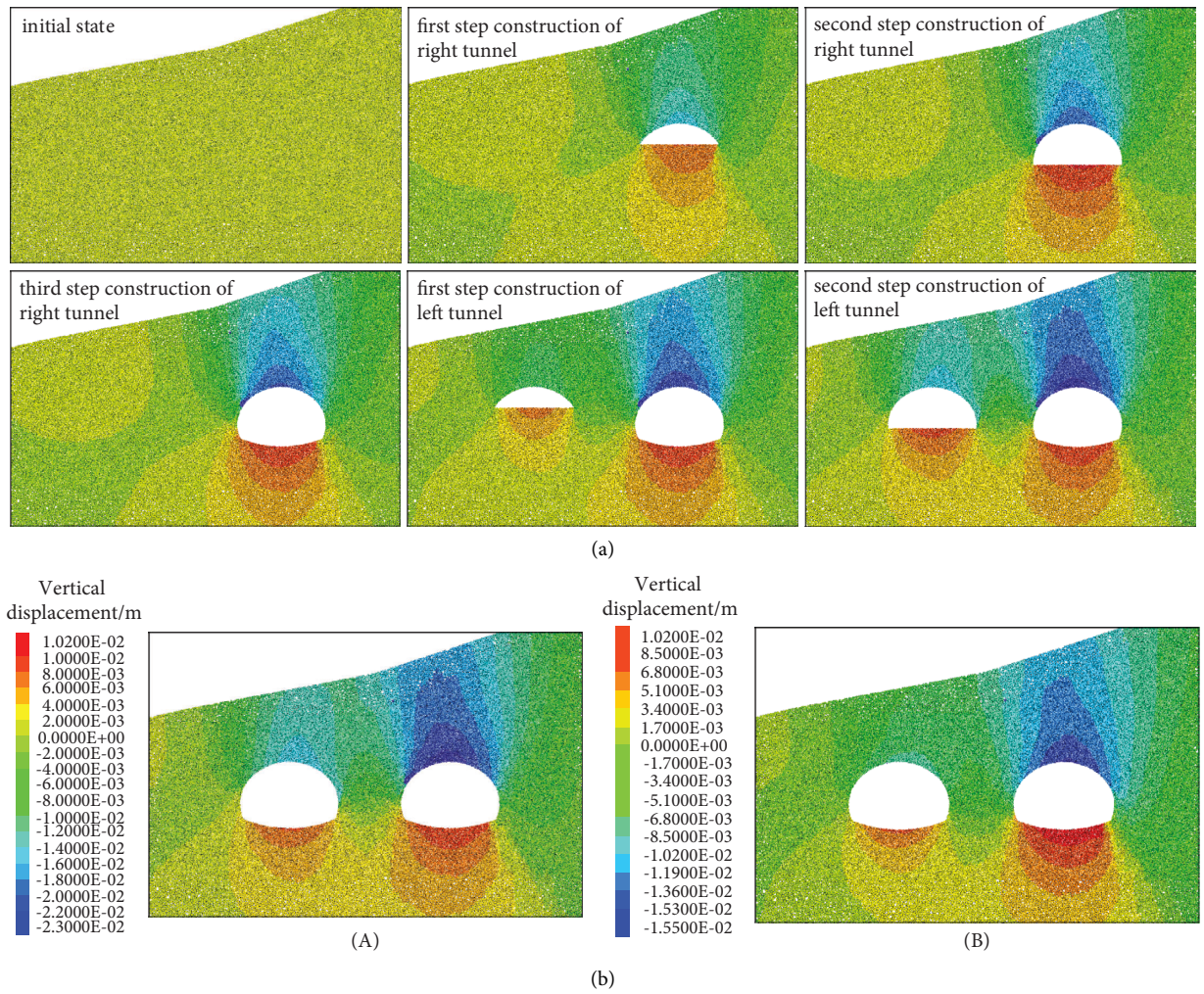

Figure 9: Distribution of vertical displacement of the three-step method: (a) displacement contours of different excavation stages of the three-step method (without systematic bolt); (b) distribution of vertical displacement for final excavation stage of the three-step method: work condition 1 (A), work condition 2 (B).

surrounding rock. The subsidence of tunnel vault and arch waist without systematic bolt support is 1.26~1.51 and 0.95~1.53 times greater than cases with systematic bolt. Notably, systematic bolt can reduce vault subsidence of the shallow buried bias tunnel but has deficiency in reducing deformation of side wall, which may even cause the deformation of side wall occurring earlier.

Thus, the entrance section of the tunnel is preferred to use the single side heading method with systematic bolt in real construction to guarantee the stability of surrounding rock and decrease surface settlement. In sections far from the opening, the three-step method with bolt support is suggested to reduce cost and improve efficiency, since the integrity of surrounding rock will be increased and the terrain bias will recede due to the increase of thickness of overlaying soil. It is also noticed that the support at arch footing, arch shoulder, side wall, and mid-rock pillar should be enhanced, and lining should be closed as soon as possible, and the monitoring frequency of mid-rock pillar should be enhanced to guarantee stability of surrounding rock.

4.2.3. Surface Deformation Results. Vertical and horizontal displacements of ground surface of different work conditions are shown in Figures 12 and 13, respectively.

It can be observed from Figure 12 that the surface settlement is in the shape of "*W*." The surface settlement presents evidently unsymmetrical characteristic, which is larger at the deep buried side due to terrain bias and uneven distribution of rock and soil strata. The positions of maximum settlement for all cases are all located above the right tunnel, and some ground heave occurs on the toe of slope. The maximal surface settlement of the three-step method without systematic bolt and the single side heading method without systematic bolt is 17.5 mm and 10.5 mm, respectively. The maximal surface settlement of the three-step method with systematic bolt and the single side heading method with systematic bolt is 11.1 mm and 7.81 mm, respectively. Notably, the single side heading method has a good effect on controlling surface subsidence, and the system bolt support can effectively reduce surface subsidence.

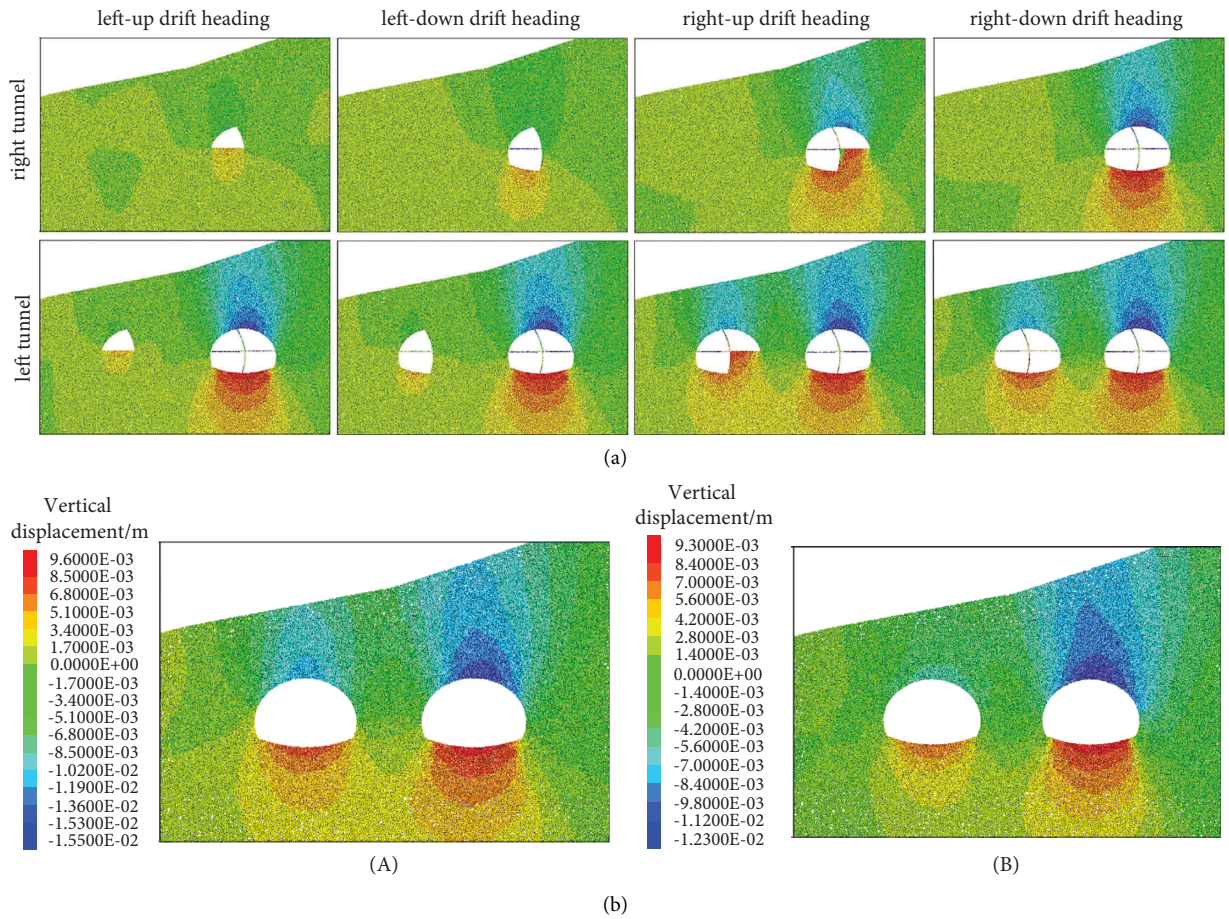

Figure 10: Distribution of vertical displacement of the single side heading method: (a) displacement contours of different excavation stages of the single side heading method (without systematic bolt); (b) distribution of vertical displacement for final excavation stage of the single side heading method: work condition 3 (A), work condition 4 (B).

Table 4: Micromechanical parameters for numerical simulation.

Work condition	Left tunnel			Right tunnel		
	Vault	Left side wall	Right side wall	Vault	Left side wall	Right side wall
1	14.6	3.12	11.05	22.4	9.69	9.84
2	6.77	2.19	5.02	14.8	7.36	9.69
3	10.9	1.94	5.12	14.4	3.38	6.95
4	4.82	1.27	3.19	11.4	3.55	6.65

In Figure 13, horizontal displacement of ground surface moves right at left side of left tunnel and symmetrical axis between left and right tunnels, while moves left at other sites. The maximal horizontal surface displacement is located in the slope top of right-up side of right tunnel. It can be found that the systematic bolt support decreases the horizontal surface displacement.

5. Microscopic Results and Discussion

5.1. Analysis of Fracture of Surrounding Rocks. Figure 14 shows the fracture development of surrounding rocks of the three-step method. According to Figure 14, the number of fractures of work condition 1 is the largest, where the cracks of arch waist of right tunnel extend 12 m upwards and 12 m downwards. The influence distance of crack to the depth of surrounding rock is about 5.5 m. Systematic bolt support effectively reduces the number of cracks, and the number of fractures in work condition 2 decreased by 28.15% compared with that in work condition 1. Meanwhile, the number of cracks is also influenced by excavation methods. The crack development law of the single side heading method is similar, while the number of cracks is less than the three-step method.

5.2. Analysis of Pressure Arching Effect. Excavation of tunnel broke the equilibrium state of surrounding rock. In order to resist nonuniform deformation, the tangential stress inside the rock mass increases, and the stress path is deflected.

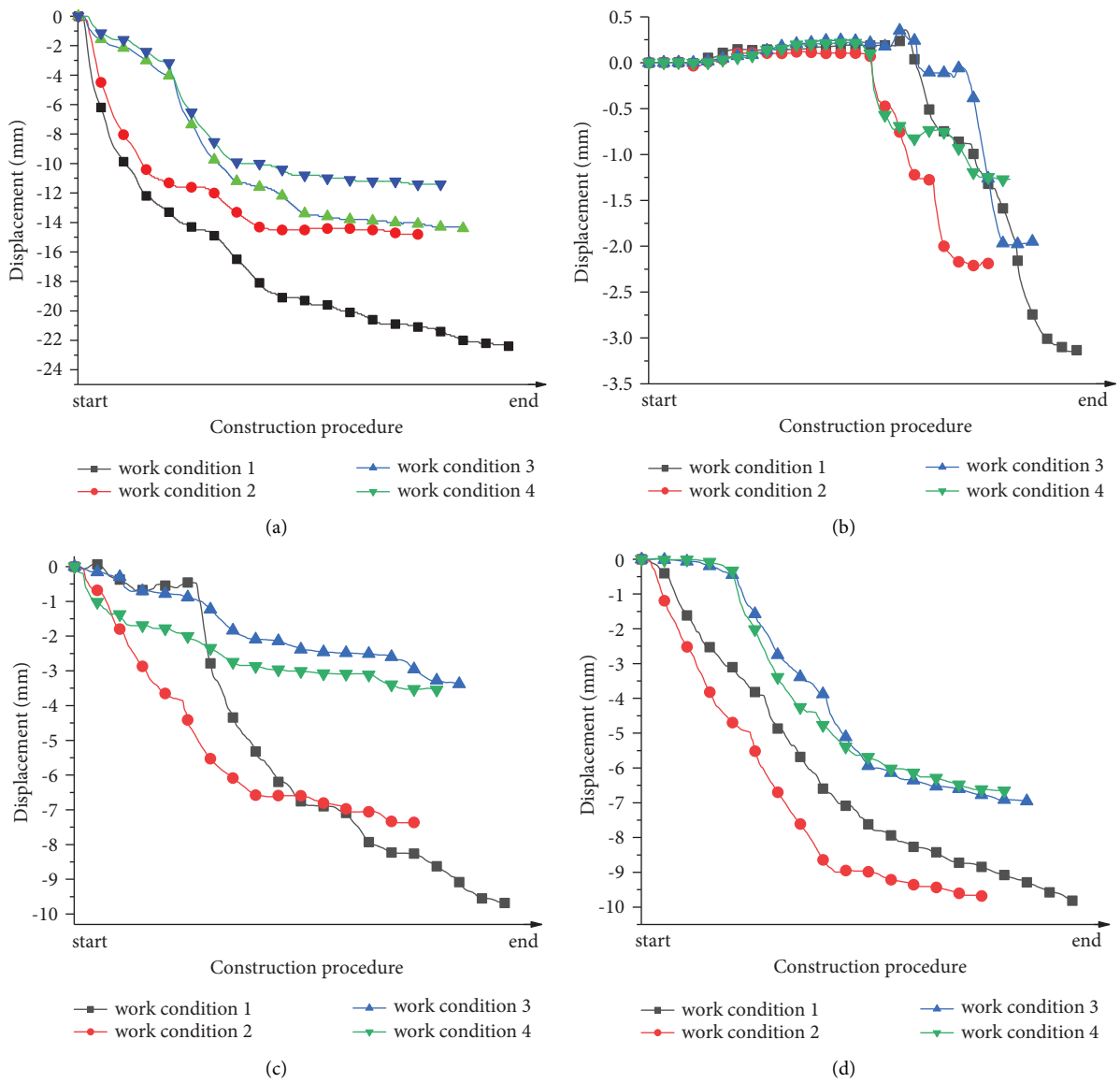

Figure 11: Deformation of surrounding rock with different construction methods: (a) vault subsidence of right tunnel; (b) left side wall subsidence of left tunnel; (c) left side wall subsidence of right tunnel; (d) right side wall subsidence of right tunnel.

Thus, a special bearing structure formed, called pressure arch. The development state of pressure arch can be reflected by the arching coefficient k [40]:

$$k = \frac{\sigma_\theta - \sigma_{\theta 0}}{\sigma_{\theta 0}}, \tag{1}$$

where σ_θ and $\sigma_{\theta 0}$ are the tangential stress of surrounding rock after and before excavation, respectively. $k < 0$ indicates that the tangential stress is lower than original rock stress and the position is located outside the pressure arch; while $k > 0$ represents that the position is located in the pressure arch; when $k = 0$, the position is the inner boundary and outer boundary of pressure arch.

The layout of measure points of pressure arch is shown in Figure 15. The inner and outer boundaries of pressure arch under different support methods are calculated by linear interpolation of arching coefficient calculated by (1). The shape of pressure arch after tunnel excavation is shown in Figure 16.

As shown in Figure 16, the inner boundary of the pressure arch is far from the tunnel section in work condition 1, and the inner boundary of the pressure arch coincide with the lining of tunnel, indicating that there are unstable surrounding rocks under the arch. The arching effect is promoted by systematic bolt support; thus, the stability of tunnel is improved.

5.3. Analysis of Systematic Bolt Mechanism. Using FISH programming language to count the magnitude of contact force in each direction in the range of bolt and grouting area, the result of microscopic contact force is shown in Figure 17. The position of the line segment in the figure represents the magnitude of the contact force in each direction.

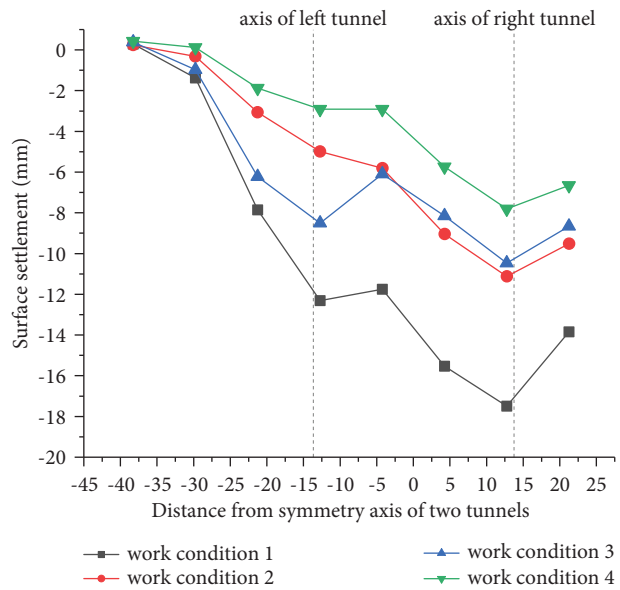

Figure 12: Surface settlement with different construction methods.

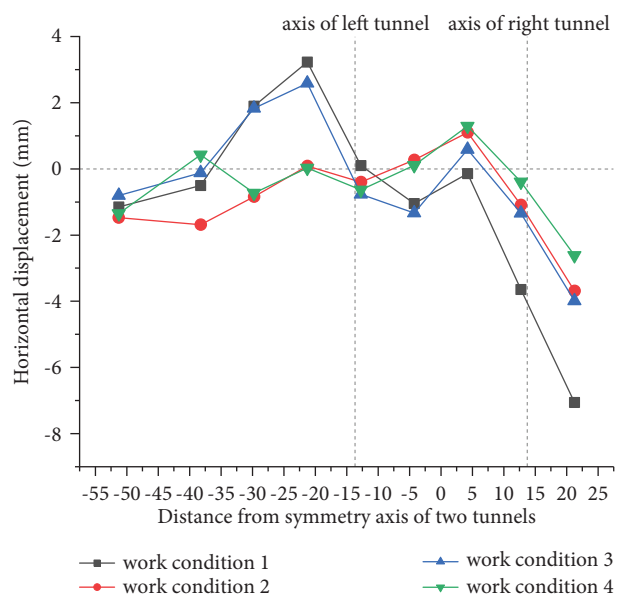

Figure 13: Horizontal surface displacement with different construction methods.

As shown in Figure 17, there are some differences in distributions of contact force of surrounding rock at bolt and grout region of different work conditions:

(1) The contact force in the initial state is in a "peanut-like" distribution. After excavation, the contact force in work conditions without bolt support increased, and its distribution is basically consistent with that of initial state. Under the work condition with bolt support, the contact force increased sharply and the distribution changes obviously.

(2) Among all work conditions, large contact force occurred in direction 60°and 300°, due to the terrain bias. In work conditions with bolt support, contact force in direction of 0° and 180° increased, and the distribution of contact force is more rounded, which indicates the surrounding rock stress is more uniform in all directions.

(3) The reasons why the distribution of contact force changes are as follows: the mechanical parameters of bolt reinforcement region increased by systematic bolt and grouting support and the arching effect is improved by the extrusion reinforcement effect of bolt support (Figure 16(b)). Thus, the contact force distribution changed, leading to variation of stress concentration region.

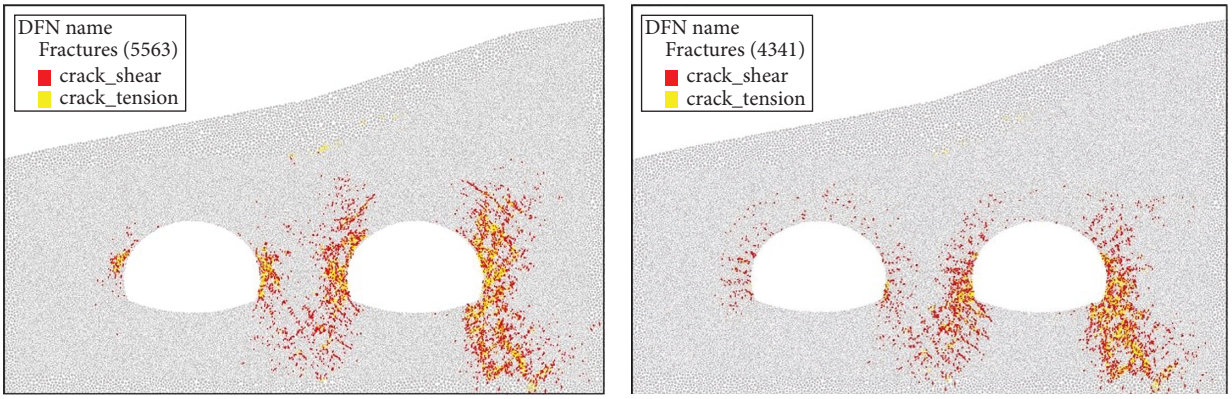

(a) (b)

Figure 14: Distribution of crack in surrounding rock with different construction methods: (a) work condition 1: the three-step method without systematic bolt; (b) work condition 2: the three-step method with systematic bolt.

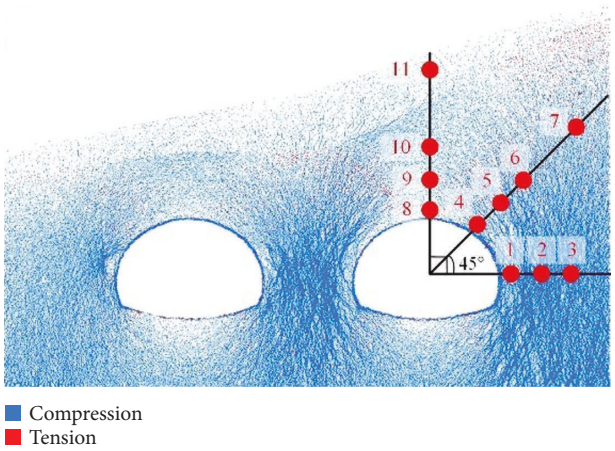

Figure 15: Layout of measure point of pressure arch.

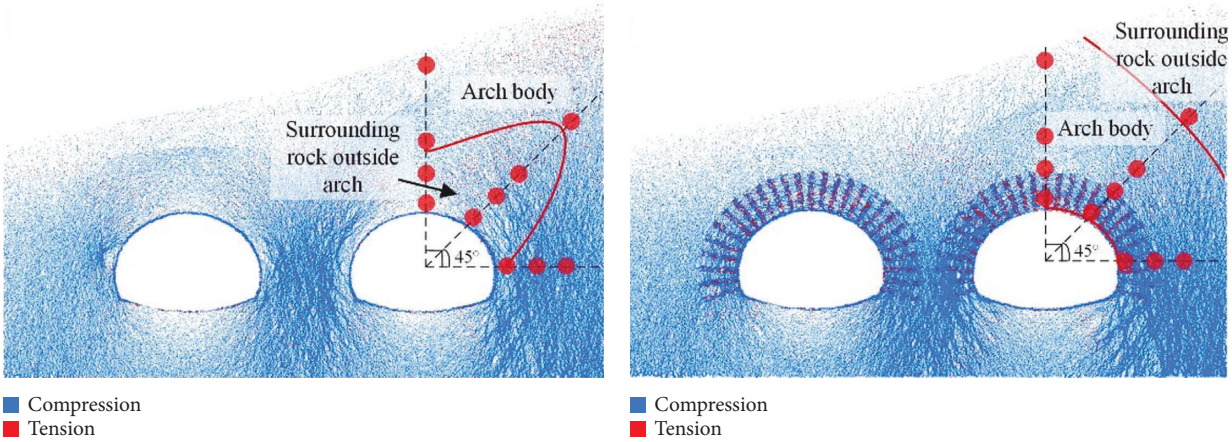

(a) (b)

Figure 16: Pressure arch distribution diagram: (a) work condition 1: the three-step method without systematic bolt; (b) work condition 2: three-step method with systematic bolt.

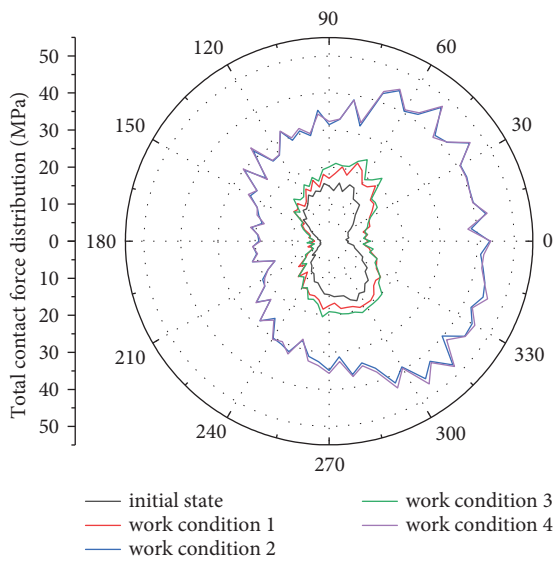

Figure 17: Contact force results of bolt reinforcement area.

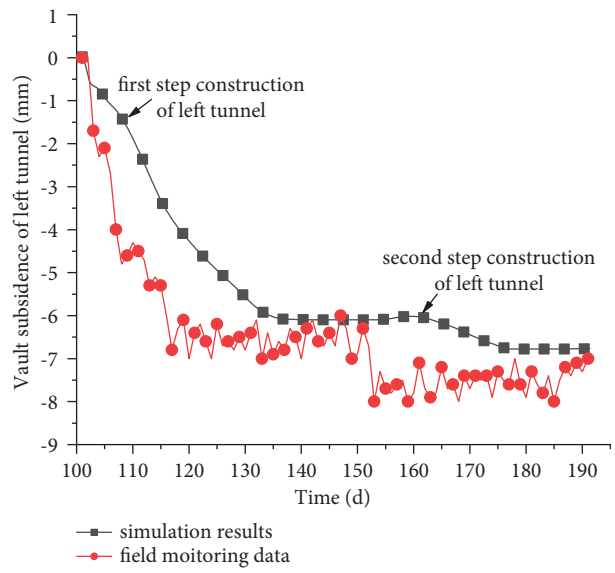

Figure 19: Variation curve of accumulated settlement of the vault of left tunnel.

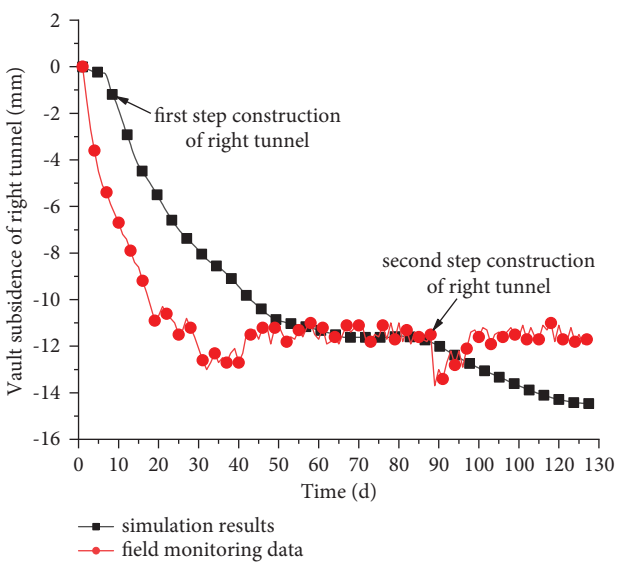

Figure 18: Variation curve of accumulated settlement of the vault of right tunnel.

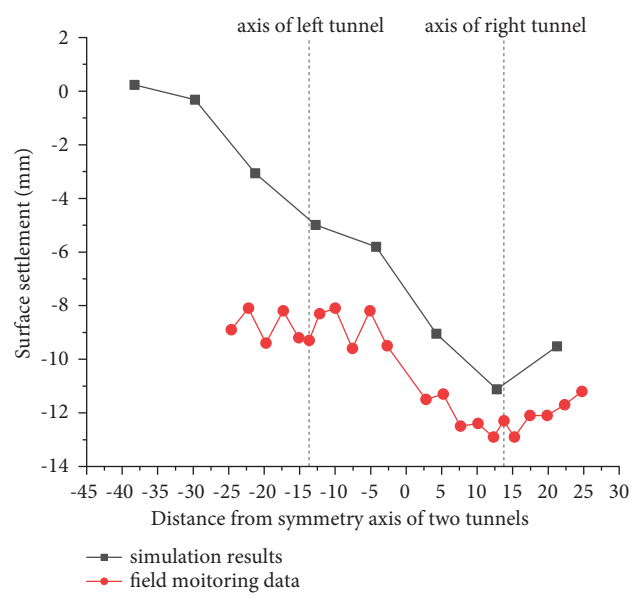

Figure 20: Settlement curves of surface.

Therefore, the existence of systematic bolt lead to the formation of active bearing structure at the nearby surrounding rock, which enhanced the bearing capacity of surrounding rocks and improved its ability of sustain upper loading and resist nonuniform deformations.

6. Field Monitoring

The displacement of surrounding rock and ground surface are measured during construction of portal part of the tunnel, and the data of displacement of portal part are analyzed [41]. Comparison of measured and simulated vault settlement curves for left and right tunnels is shown in Figures 18 and 19, respectively. Comparison of surface settlements between field monitoring and simulation results is shown in Figure 20.

As shown in Figures 18 and 19, the vault subsidence curves obtained by numerical simulation and field monitoring are consistent, which grow in "steps" pattern. The vault subsidence of right tunnel increases rapidly at the first step excavation stage and be stable about the 50th day. The vault subsidence fluctuates about the 90th day due to the influence of second step construction. The simulation results matched the monitoring data. The vault subsidence of left tunnel increases rapidly at the first 20 days, and the simulation results agreed with the monitoring data well after the displacement being stable.

Figure 20 shows that the numerical simulation results matched the field monitoring data, and the data of field monitoring are larger.

7. Conclusions

Numerical simulations were carried out towards Qijiazhuang tunnel by using the discrete element method. The rule of stress, vertical displacement of surrounding rock, surface displacement, microscopic fractures, and contact force were analyzed in detail. Then, the field monitoring data were compared and analyzed. The following conclusions can be drawn.

(1) Due to the terrain bias, stress concentration, deformation of surrounding rock, and surface displacement of deep buried side are larger than those of shallow buried side, despite the difference of the excavation method and support method

(2) The single side heading method can gradually release the load and deformation, which is beneficial to make the support and control the magnitude of deformation. The single side heading method should be adopted as far as possible in the shallow buried bias tunnel.

(3) The vault subsidence and subsidence of arch waist without systematic bolt are 1.26–1.51 times and 0.95–1.53 times as large as those with systematic bolt. Systematic bolt can reduce the vertical displacement of surrounding rock and the displacement of ground surface greatly. The system bolt support method can be used in the shallow buried bias tunnel to ensure safety in construction. The shape of pressure arch indicates that the existence of systematic bolt increases the shear capacity of surrounding rock; thus, the ability of bearing nonuniform load and deformation of surrounding rock is improved.

(4) The results of numerical simulation match the data of field monitoring well. The entrance section of the tunnel preferred to use the single side heading method with systematic bolt in real construction. In sections far from the opening, the three-step method with bolt support is suggested because of the relatively lower cost and higher efficiency. Meanwhile, monitoring frequency and support should be enhanced of key positions that influence the stability of the tunnel.

Data Availability

The data used to support the findings of this study are available from the corresponding author upon request.

Conflicts of Interest

The authors declare that they have no conflicts of interest.

Authors' Contributions

Chenyu Ge performed the data analyses and wrote the manuscript; Liping Su contributed significantly to data analysis and manuscript preparation; Lin Wang established the numerical model and analyzed the results; Shuo Xu reviewed and edited the manuscript; Pengqiang Yu contributed to the conception and methodology of the study. All authors have read and agreed to the published version of the manuscript.

References

[1] X. L. Yang and Z. R. Sui, "Numerical simulation of construction sequence for shallow embedded bias tunnels with small clear distance," *Journal of Central South University*, vol. 38, pp. 764–770, 2007.

[2] X. G. Jin, W. Liu, X. G. Zheng, and H. Ding, "Optimization of excavating sequence for closely spaced bias double-tube tunnels," *Journal of Highway and Transportation Research and Development*, vol. 22, pp. 61–64, 2005.

[3] X. J. Liu and Y. X. Zhang, "Analysis of reasonable excavation sequence and stress characteristics of portal section of shallow tunnel with unsymmetrical loadings," *Chinese Journal of Rock Mechanics and Engineering*, vol. 30, pp. 3066–3073, 2011.

[4] M. F. Lei, L. M. Peng, C. H. Shi, W. L. Chuan, and Z. C. Liu, "Model research on failure mechanism and lining stress characteristics of shallow buried tunnel under unsymmetrical pressure," *Journal of Central South University*, vol. 44, pp. 3316–3325, 2013.

[5] W. X. Gao, W. L. Sun, W. X. Zhou, P. Fu, H. L. Deng, and Y. Y. Zhang, "Numerical simulation and monitoring analysis for construction process of shallow tunnel under unsymmetrical pressure," *Construction Technology*, vol. 40, pp. 48–50, 2011.

[6] L. H. Xu and M. Ma, "Dynamic response of the multilayered half-space medium due to the spatially periodic harmonic moving load," *Soil Dynamics and Earthquake Engineering*, vol. 157, Article ID 107246, 2022.

[7] H. Jin, Q. R. Tian, and Z. Li, "Crack development of rebar rust in rubberized concrete using mesoscale model," *Construction and Building Materials*, vol. 321, Article ID 126409, 2022.

[8] B. X. Yuan, Z. J. Li, W. J. Chen et al., "Influence of groundwater depth on pile–soil mechanical properties and fractal characteristics under cyclic loading," *Fractal and Fractional*, vol. 6, no. 4, p. 198, 2022.

[9] B. X. Yuan, W. J. Chen, J. Zhao et al., "Addition of alkaline solutions and fibers for the reinforcement of kaolinite-containing granite residual soil," *Applied Clay Science*, vol. 228, pp. 106644–112022.

[10] B. X. Yuan, M. J. Chen, W. J. Chen, Q. Z. Luo, and H. Z. Li, "Effect of pile-soil relative stiffness on deformation characteristics of the laterally loaded pile," *Advances in Materials Science and Engineering*, vol. 2022, Article ID 4913887, 2022.

[11] M. F. Lei, L. M. Peng, and C. H. Shi, "Model test to investigate the failure mechanisms and lining stress characteristics of shallow buried tunnels under unsymmetrical loading," *Tunnelling and Underground Space Technology*, vol. 46, pp. 64–75, 2015.

[12] M. F. Lei, D. Y. Lin, W. C. Yang, C. H. Shi, L. M. Peng, and J. Huang, "Model test to investigate failure mechanism and loading characteristics of shallow-bias tunnels with small clear distance," *J. Cent. South Univ,* vol. 23, no. 12, pp. 3312–3321, 2016.

[13] J. Y. Teng, J. X. Tang, C. Zhang, and Y. N. Zhang, "Distribution and control of surrounding rock pressure of shallow buried tunnel under the condition of terrain bias," *Chinese*

Journal of Underground Space and Engineering, vol. 14, pp. 761–769, 2018.

[14] B. Bai, Y. Wang, D. Rao, and F. Bai, "The effective thermal conductivity of unsaturated porous media deduced by pore-scale SPH simulation," *Frontiers of Earth Science*, vol. 10, Article ID 943853, 2022.

[15] B. Bai, Q. Nie, Y. Zhang, X. Wang, and W. Hu, "Cotransport of heavy metals and SiO2 particles at different temperatures by seepage," *Journal of Hydrology*, vol. 597, pp. 125771–132021.

[16] B. Bai, R. Zhou, G. Cai, W. Hu, and G. Yang, "Coupled thermo-hydro-mechanical mechanism in view of the soil particle rearrangement of granular thermodynamics," *Computers and Geotechnics*, vol. 2021, Article ID 104272, 137 pages, 2021.

[17] X. D. Bai, W. C. Cheng, B. B. Sheil, and G. Li, "Pipejacking clogging detection in soft alluvial deposits using machine learning algorithms," *Tunnelling and Underground Space Technology*, vol. 113, Article ID 103908, 2021.

[18] Y. S. Li, K. N. Zhang, X. Yang, and C. B. Huang, "Numerical simulation for the excavation in tunnel construction," *Applied Mechanics and Materials*, vol. 90-93, pp. 90–93, 2011.

[19] C. Y. Dong, "Construction deformation control of shallow bias tunnel entrance section," *Traffic Engineering and Technology for National Defence*, vol. 19, pp. 46–49, 2021.

[20] L. B. Cai, *Research on the Mechanical Behavior of Unsymmetrical Loading Twin-Arched Tunnels Located on the Shallow Weak Rock Mass*, Tongji University, Shang Hai, 2008.

[21] H. Jin, J. Su, and C. Zhao, "Relationship between invert-filling disengaging and deformation of shield tunnel using staggered assembled segment," *KSCE Journal of Civil Engineering*, vol. 26, no. 4, pp. 1966–1977, 2022.

[22] Y. G. Zhao, S. J. Shao, and C. L. Han, "Simulation on different excavation construction of the shallow-buried tunnel under the uneven rock pressure," *Rock and Soil Mechanics*, vol. 30, pp. 509–513, 2009.

[23] W. Pan, F. Wu, C. He et al., "Construction methods and asymmetric design optimization for shallow-buried tunnels subjected to unsymmetrical loads," *Tunnel Construction*, vol. 41, pp. 352–361, 2021.

[24] G. Z. Lu, B. Zhou, F. Xu, G. W. Shang, G. Wang, and S. B. Zhang, "Stability analysis and construction mechanics of shallow buried bias tunnel openings," *Journal of Shandong University*, vol. 51, pp. 61–70, 2021.

[25] Y. Liu, J. Hu, and K. J. Wu, "Particle flow code numerical simulation of loess shallow-buried tunnel with different excavation and reinforcement method," *Journal of Basic Science and Engineering*, vol. 24, pp. 126–138, 2016.

[26] C. Yang, Z. X. Hu, D. Huang, and F. Guo, "Failure mechanism of primary support for a shallow and asymmetrically loaded tunnel portal and treatment measures," *Journal of Performance of Constructed Facilities*, vol. 34, no. 1, 2020.

[27] X. X. Wang, Y. Liu, and P. Q. Yu, "Upscaling critical state considering the distribution of meso-structures in granular materials," *International Journal for Numerical and Analytical Methods in Geomechanics*, vol. 45, no. 11, pp. 1624–1646, 2021.

[28] Y. Liu, D. Zhang, S. C. Wu, and P. Q. Yu, "DEM investigation on the evolution of fabric under true triaxial conditions in granular materials," *International Journal of Geomechanics*, vol. 20, no. 8, 2020.

[29] T. Wang, "Research on Simulation of Rupture of Rock Mass of Tunnel Based on Particle Flow Method," in *Proceedings of the The 9th National Conference on Rock Mechanics and Engineering, Shen Yang*, January 2006.

[30] M. J. Jiang, "New paradigm for modern soil mechanics: geo mechanics from micro to Macro," *Chinese Journal of Geotechnical Engineering*, vol. 41, pp. 195–254, 2019.

[31] P. Yuan, S. F. Wang, T. Wang, and Q. Liu, "Construction technology and particle flow code modelling of diversion tunnel support in xigeda stratum," *Engineering Journal of Wuhan University*, vol. 54, pp. 205–211, 2021.

[32] R. Xue, "Stability analysis of surrounding rock of tunnel with small clear distance based on discrete element method," *Fujian Transportation Technology*, pp. 61–65, 2021.

[33] M. J. Jiang, H. N. Wang, G. S. Li, Y. B. Liao, Y. L. Chen, and C. Q. Wei, "DEM investigation on tunnel excavation of deeply-situated composite rock mass with different strength ratios," *Chinese Journal of Geotechnical Engineering*, vol. 42, pp. 20–25, 2020.

[34] M. J. Jiang, H. X. Pang, H. N. Wang, Y. L. Chen, and Y. B. Liao, "Discrete element analysis on excavation failure mechanism of deep-buried tunnel in composite rock mass," *Chinese Journal of Underground Space and Engineering*, vol. 16, pp. 702–709, 2020.

[35] B. Bai, S. Jiang, L. Liu, X. Li, and H. Wu, "The transport of silica powders and lead ions under unsteady flow and variable injection concentrations," *Powder Technology*, vol. 387, pp. 22–30, 2021.

[36] B. Bai, T. Xu, Q. Nie, and P. Li, "Temperature-driven migration of heavy metal Pb2+ along with moisture movement in unsaturated soils," *International Journal of Heat and Mass Transfer*, vol. 153, 2020.

[37] B. Bai, G. c. Yang, T. Li, and G. s. Yang, "A thermodynamic constitutive model with temperature effect based on particle rearrangement for geomaterials," *Mechanics of Materials*, vol. 139, Article ID 103180, 2019.

[38] *Ministry of housing and urban rural development of the people's Republic of ChinaGBT50218-2014 Standard for Engineering Classification of Rock Mass*, China Planning Press, Beijing, 2014.

[39] X. D. Liang, J. Zhao, and H. W. Song, "Experimental and numerical analysis on the arching action from stress adjusting in surrounding rocks," *Journal of Engineering Geology*, vol. 20, pp. 96–102, 2012.

[40] H. W. Song and X. L. Du, *Pressure Arch in Vicinity of Geotechnical Openning and its Characteristics*, Coal Industry Press, Beijing, 2012.

[41] Q. W. Xu, P. P. Cheng, P. S. Su, J. T. Dong, and G. Z. Chen, "Study on construction mechanical properties of the shallow tunnel entrance under unsymmetrical pressure," *Chinese Journal of Underground Space and Engineering*, vol. 13, pp. 1311–1318, 2017.

Hindawi
Advances in Civil Engineering
Volume 2022, Article ID 3313013, 11 pages
https://doi.org/10.1155/2022/3313013

Research Article

The Seepage-Destruction Mechanism of Water Inrush Channel of Sandstone Fault Filling Using the EDEM-Fluent Method

Wenya Cai,[1] Yan Wang,[2] Fujun He,[2] Pengyuan Zhang,[2] and Shuo Sun[3]

[1]*Beijing Guodaotong Highway Design & Research Institute Co., Ltd, Beijing 100055, China*
[2]*Beijing Uni.-Construction Group Co., Ltd, Beijing 101200, China*
[3]*School of Civil Engineering, Beijing Jiaotong University, Beijing 100044, China*

Correspondence should be addressed to Shuo Sun; 20125912@bjtu.edu.cn

Received 15 August 2022; Accepted 9 September 2022; Published 5 October 2022

Academic Editor: Chao Zou

By the EDEM-Fluent coupling calculation method, the formation mechanism of the seepage failure water inrush channel and the migration of particles in the sandstone fault filling body are studied. Under the condition of variable hydraulic gradient, the whole seepage process can be divided into three stages: slow seepage stage, sudden seepage stage, and stable seepage stage. In the stage of slow seepage, the mass of lost particles is small. In the stage of sudden seepage, particles are lost on a large scale. In the stable seepage stage, the model is basically in a stable state. During the seepage process, the particles in the outlet zone will move before the particles in the inlet zone under the action of the seepage force. The overall movement trend of particles can be predicted, while the movement trajectory of a single particle is irregular. The change trend of the contact quantity between particles is basically consistent with the change in the quality of the lost particles. Moreover, the change in the contact quantity of particles is caused by the loss of the filler particles.

1. Introduction

During the construction of mountain tunnels, geological disasters of different degrees will be suffered and water inrush is common [1–3]. Its frequent occurrence and harmfulness bring great resistance to tunnel survey, design, and construction [4–8]. When crossing karst caves and fault fracture zones under water-rich conditions, karst-type water inrush usually occurs [9–11]. Besides, the fissure type water inrush occurs under the influence of water storage structure and rainfall, and the water inrush pressure even exceeds 2 MPa [12–14]. Fault-type water inrush occurred during the excavation of two regional rock fault planes under severe weathering conditions, and the water flow was very huge, even reaching 1800 m^3/h [15].

With the increasing demand for safety in the process of tunnel construction, a series of empirical standards and analysis models are proposed for the occurrence mechanism of water inrush, the prediction of water inrush volume, water inrush location, and water inrush characteristics. Guo et al. [16] used UDEC software based on the discrete element method, which was combined with laboratory tests, and analyzed the occurrence mechanism of water inrush in karst tunnels from macroperspectives and microperspectives. It was clarified that the secondary stress redistribution of surrounding rock and karst water pressure with a high head easily caused water inrush in karst tunnels. Using the finite difference program, Jiang et al. [17] calculated the instantaneous and stable water inflow during deep and long tunnel excavation in bedrock fissure aquifers and established a reliable and practical hydrogeological model. Based on the finite element method, Li [18] explored the seepage characteristics of groundwater and identified the location of inrush water as the vault and the arch waist on both sides and proposed the cement-water glass double slurry water-blocking measures. Zhao and Yang [19] analyzed the characteristics of water inflow when the tunnel passes through the fault fracture zone. When the tunnel collapses, the water inflow pressure will drop sharply and the existence of surface water will increase the water inflow and grouting thickness of the tunnel.

However, the traditional analysis method cannot be suitable for the complex fault fracture zone conditions, and the simulation of fluid movement is also relatively effective. The SPH method can be applied to solve complex fluid dynamics [20]. Bai et al. [21] proposed an SPH-FDM boundary method to analyze heat transfer in homogeneous media with discontinuous interfaces [22]. It should be noted that hydrogeological conditions are not the only determinant of water inrush type and seepage path [5, 23–25]. Bai et al. [26, 27] established a nonlinear coupled transport equation of water movement driven by temperature in unsaturated soil. The water distribution under the action of the temperature gradient is uneven, which verified the hysteresis effect of water movement caused by the thermal cycle. A thermo-mechanical composition model is established for the particle rearrangement problem caused by the thermodynamics of porous granular materials, which can be used to describe the path problem in the process of water migration [28]. Bai et al. [29] explored the dynamic characteristics of suspended particles in porous media under variable temperature and proposed that water viscosity, adsorption effect, electric double layer effect, and particle kinetic energy will all affect particle motion.

The Zhaitang Mountain Tunnel of the G109 expressway has sandstone geological conditions. The fault fracture zone will be exposed during the construction process, the fault runs through the Zhaitang Tunnel and Zhaitang reservoir, and the shortest horizontal distance is only 320 meters. Based on the geotechnical dominant surface theory, it belongs to the dangerous water-conducting section [30, 31]. With the tunnel excavation, the permeability coefficient of the fault fracture zone increases and the water source in the Zhaitang reservoir may carry the filling material in the fault to gush water into the tunnel along the fault fracture zone, thus forming a relatively through seepage channel, which is prone to seepage damage type water inrush of the filling body [9, 32–35]. Based on the DEM-CFD coupling calculation method, Zhou et al. [36] used a 100 mm × 50 mm × 100 mm rock mass model to simulate the engineering scale water inrush process with a real time of 1.8 s, showing the formation and expansion process of the dominant channel of water inrush. Through the self-designed test system, Wang et al. [37] made samples with a diameter of 100 mm and a height of 500 mm to qualitatively study the mechanism of water inrush caused by the migration of fault-filling particles. Xu et al. [38] used PFC3D software to build a fault fractured rock mass model with a diameter of 60 mm and a height of 120 mm and simulated the disaster process of water inrush in a microscopic view. Through the laboratory test method, Chen and Lyu [39] made a 30 mm × 30 mm × 110 mm sample of the broken rock mass to discuss the change law and influencing factors of the particle migration on the hydraulic properties of the sandstone in the fault fracture zone during the occurrence of water inrush.

During the formation of seepage failure type water inrush channel in sandstone fault filling body, there is the interaction between particle phase and fluid phase. Not only the independent migration and stress of solid particles and fluid but also the exchange of energy, momentum, and mass between solid particles and fluid should be considered. Based on the fluid-solid coupling theory, this paper adopts the coupling method of discrete element software EDEM 2018 and computational fluid dynamics software Fluent 18.0, which is more accurate than the traditional method (i.e., PFC method), to establish a small-scale broken sandstone model and carry out three-dimensional numerical simulation. The formation mechanism of the water inrush channel and the migration law of particles in the seepage process are explored.

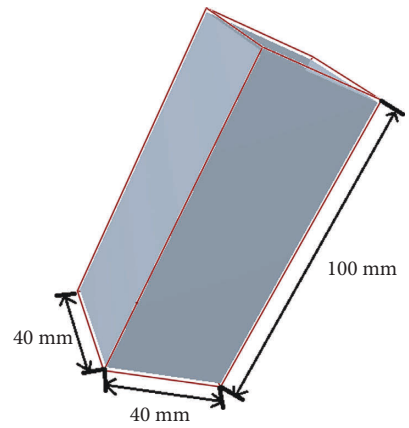

Figure 1: Geometric model.

2. Modeling of Broken Sandstone

2.1. EDEM Geometric Model. The fault fracture zone of tunnel excavation is a dangerous section for water diversion. Using EDEM software and the discrete element method, the model of broken sandstone inside the fault is established, which is expressed by several particle combinations. However, it is difficult to establish a stratum model which is equivalent to the actual engineering size in the process of numerical simulation due to the limitation of computer capabilities. Therefore, combined with actual working conditions, a 40 mm × 40 mm × 100 mm rectangular broken sandstone millimeter scale model [40, 41] with an initial porosity of 18.27% was studied to discuss the formation mechanism of seepage failure type water inrush channel of sandstone fault backfill under the action of reservoir seepage force.

As shown in Figure 1, the dark gray area is the geometric area where particles are generated, and the red border is the calculation domain. That is, if the particle movement exceeds the calculation domain, it will be deleted automatically. The highest water level of the Zhaitang reservoir is lower than the design elevation of the tunnel, so the flow in this model is seepage from bottom to top. The six faces of the broken sandstone model are all walls. The bottom and top faces are, respectively, set as fluid inlets and outlets. The physical properties of the surrounding walls are consistent with those of the sandstone, and none of them has water permeability. The top face of the model was deleted so that the particles inside the model can gush outward under the action of single

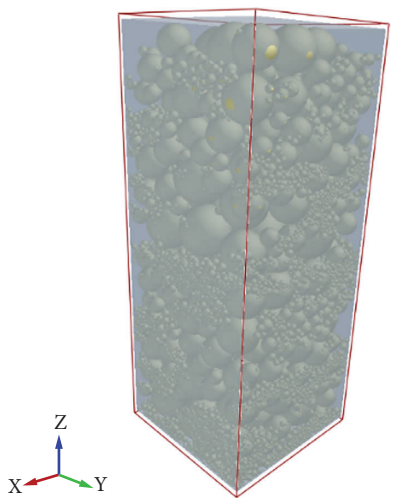

Figure 2: Sandstone model generated by EDEM.

bottom-up water seepage. Among them, the initial hydraulic gradient at the inlet is 0.1, increasing by 0.1 every 0.1 s in a stepped manner, and the fluid outlet pressure is constant at 0.

Broken rock mass is considered to be composed of rock mass skeleton and filling medium. In combination with the actual conditions of the tunnel, two particles with different particle size ranges are used to represent the skeleton particles (2–15 mm) and filling particles (0.25–2 mm), respectively, to simulate the broken sandstone. The ratio of filling particles to skeleton particles is 1 : 3, all particle shapes are simplified to spheres, and they are rigid elements that cannot be deformed. EDEM software based on the discrete element principle is used to generate broken sandstone particles. The particle sizes of filling particles and skeleton particles are randomly generated within their desirable range, and a total of 18985 particles were generated. Figure 2 shows the broken sandstone model generated by EDEM with a gravity of 9.8 KN/m^3 and a negative direction along the Z axis.

It should be noted that fault fractured rock mass is formed by bonding a series of discontinuous particles, and different particle contact models will produce different contact forces. Based on this, the contact between skeleton particles is set as Hertz–Mindlin with the bonding model to simulate the adhesion between particles. Skeleton particles with certain adhesion constitute a skeleton network. Once the adhesion between particles is destroyed, the particles will change to Hertz–Mindlin (No Slip) model when they contact again. According to field measurement and theoretical analysis, the physical parameters of particles are shown in Table 1.

Due to the difference between the mesh generation in EDEM software and the mesh size of fluid computing, when using EDEM-Fluent for coupling calculation, it is necessary to divide the mesh of EDEM and fluid computing, respectively. The mesh size of EDEM is directly related to the minimum particle size, which is usually about twice the minimum particle radius. The selected EDEM grid size is 2.5 times of the minimum particle radius, and the minimum radius of generated particles is 0.125 mm. Hence, the grid size is 0.3125 mm, including a total of 5611647 grids. To ensure the grid quality and the accuracy of calculation results, a single fluid calculation grid must contain at least three solid particles, and the size of the fluent fluid grid is 10 mm × 10 mm × 10 mm, including a total of 160 fluid computing grid cells.

Table 1: Particle parameter setting.

Particle parameter	Numerical value
Poisson's ratio	0.2
Density	2.08×10^3 kg/m^3
Modulus of elasticity	3.3e + 10 Pa
Static friction coefficient	0.5
Rolling friction coefficient	0.05
Filling particle size	0.25–2 mm
Skeleton particle size	2–15 mm
Particle shape	Sphere
Model size	40 mm × 40 mm × 100 mm
Skeleton particle contact model	Hertz–Mindlin with bonding model

2.2. EDEM Calculation Principle. In the discrete element method, the particle motion follows Newton's second law of motion [42], and the interaction between particles is a transient process. Within a sufficiently small time step, it can be assumed that the velocity and acceleration of a single particle are fixed values and only the particles or boundaries in direct contact with it play a role without being affected by the indirect action of other particles. The basic equation of motion for a single particle is as follows:

$$m\frac{\mathrm{d}^2u}{\mathrm{d}t^2} + f_d + f_c + f = 0,$$
$$I\frac{d^2\theta}{dt^2} = \sum r_c f_c, \tag{1}$$

where m is the particle mass, u is the linear displacement, θ is the angular displacement, $f_\mathrm{d}, f_\mathrm{c}$, and f are the damping force contact force and volume force on the particles, respectively, I is the moment of inertia, and r_c is the force arm of the contact force on the particles.

During EDEM calculation, the particle and boundary position will be obtained. Taking the relative displacement between particles as the basic physical variable, the normal force and tangential force of particles will be obtained according to the relationship between force and displacement in the contact model, so as to obtain the resultant force and resultant moment. Then, the physical quantities such as displacement, velocity, and acceleration of particles will be calculated according to Newton's second law of motion, and the continuous cycle calculation will be carried out. Fluent calculation ensures that the fluid motion follows the continuity equation and momentum conservation equation.

3. Numerical Simulation and Discussion

3.1. Particle Movement. The total duration of seepage failure of the simulated sandstone fault filling body is 1 s, the time step of EDEM is set as 1×10^{-7} s, and the data saving interval

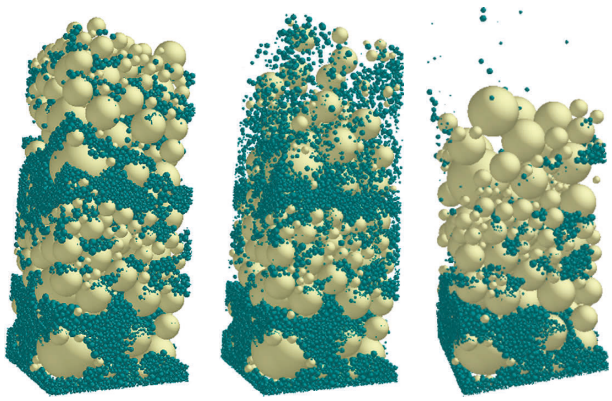

Figure 3: Particle movement at different times.

is 0.01 s. The time step ratio of EDEM and Fluent is 1 : 100, and the time interval ratio of data saving is 1 : 10. Within the calculation time, EDEM needs to calculate 10 million steps in total and Fluent needs to calculate 100000 steps in total.

Figure 3 shows the particle state in the model when $t = 0$, $t = 0.5$ and $t = 1.0$ s in the seepage process [22]. The dark green particles are filling particles and the yellow-green particles are skeleton particles. Different time points correspond to different hydraulic gradients [27]. By observing the particle state at different time points, based on the loss speed and amount of particles, the movement law of particles under the action of fluid seepage force with gradient increase can be obtained.

When the seepage force is small, the filling particles in the outlet area along the direction of seepage force and some skeleton particles outside the skeleton network will gush out before the particles in the inlet area [43], and the particle position in the inlet area has no obvious change and is in a stable state. With the increase of hydraulic gradient, the resultant force of fluid drag force, gravity, and indirect contact force of particles in the middle section occurs gradually upward and the contact relationship between particles also changes. The flow will carry a large number of filling particles and some small skeleton particles from the high water pressure to the low water pressure area. At this stage, the filling particles gush out on a large scale, some small skeleton particles will also be lost, and the large skeleton particles will move unsteadily with the change of contact relationship. As most of the filling particles have gushed out, the remaining filling particles will gradually stabilize, but there are still a small part of filling particles and small skeleton particles slowly gushing out. Due to the change of the contact relationship between particles, the particles moving from the middle and lower part to the outlet area under the action of seepage force will also gush out. The filling particles in the inlet area cannot gush out because of the large skeleton particles and form a stable structure with the remaining skeleton particles.

When $t = 1$ s, the seepage simulation process ends, and most of the filling particles and a small part of the skeleton particles have gushed out, which further increases the porosity, permeability coefficient, and water velocity of the fault fracture zone, forming a relatively smooth water inrush channel. In addition, the loss of particles is obviously nonuniform. Although the particles migrate first in the outlet area, the particles do not gush out layer by layer, indicating that the water velocity in the particle pores is different in the same horizontal plane, and the seepage path is irregular [44]. However, under the action of the drag force of the water flow, it drives the filling particles and some skeleton particles to gush out, thus forming a relatively smooth water inrush channel.

According to the motion law of a single particle, the motion trajectories of three particles in the outlet area, the middle section, and the inlet area are randomly selected (Figure 4). In the process of gushing, a single particle moves under the combined action of gravity, water drag force, normal contact force, and tangential contact force between different particles. The upward migration and gushing of filling particles and some small skeleton particles along the direction of seepage force need to pass through the pores between skeleton networks. The particle sizes of single particles randomly selected may be different, and the gravity of particles with different sizes is different [45, 46]. Because the pore size and the flow velocity and direction are different between the skeleton particles, the size and direction of the flow drag force on different particles are different. The contact relationship between a single particle and other particles is not exactly the same [47–49], and the sizes and directions of normal, tangential, and angular velocities of particles affected by water flow are also different. Similarly, there are differences in the moment of inertia of particles with different particle sizes [50]. Therefore, the sizes and directions of normal and tangential contact forces on a single particle at different times are different, which leads to different resultant forces of a single particle under the action of water flow.

Actually, the movement of particles is irregular and will not strictly follow the action direction of seepage force. For example, the single particle movement tracks in the middle section selected in Figure 4 move downward first and then upward. Figure 5 more intuitively shows the trajectory of the particle, in which the purple particle is the characteristic particle, the dark green particle is the filling particle, and the yellow-green particle is the skeleton particle. The motion track of the characteristic particle starts because the particle is a skeleton particle free from the skeleton network. Under the action of initial water pressure, the force of seepage force on the skeleton particle is not enough to make it move upward and gush out, but the drag force of water flow can carry the filling particles around the particle upward, thus changing the contact relationship between the particle and other filling particles. With the increase of seepage force, the surrounding filling particles continuously gush out and the contact force between particles decreases. The gravity of the characteristic particles gradually plays a leading role in the resultant force, and the resultant force direction of the particles is gradually downward, so the particles move downward first. As the seepage force continues to increase, the drag force of the water flow on the characteristic particles continues to increase and the resultant force on the particles gradually moves upward. The drag force begins to dominate

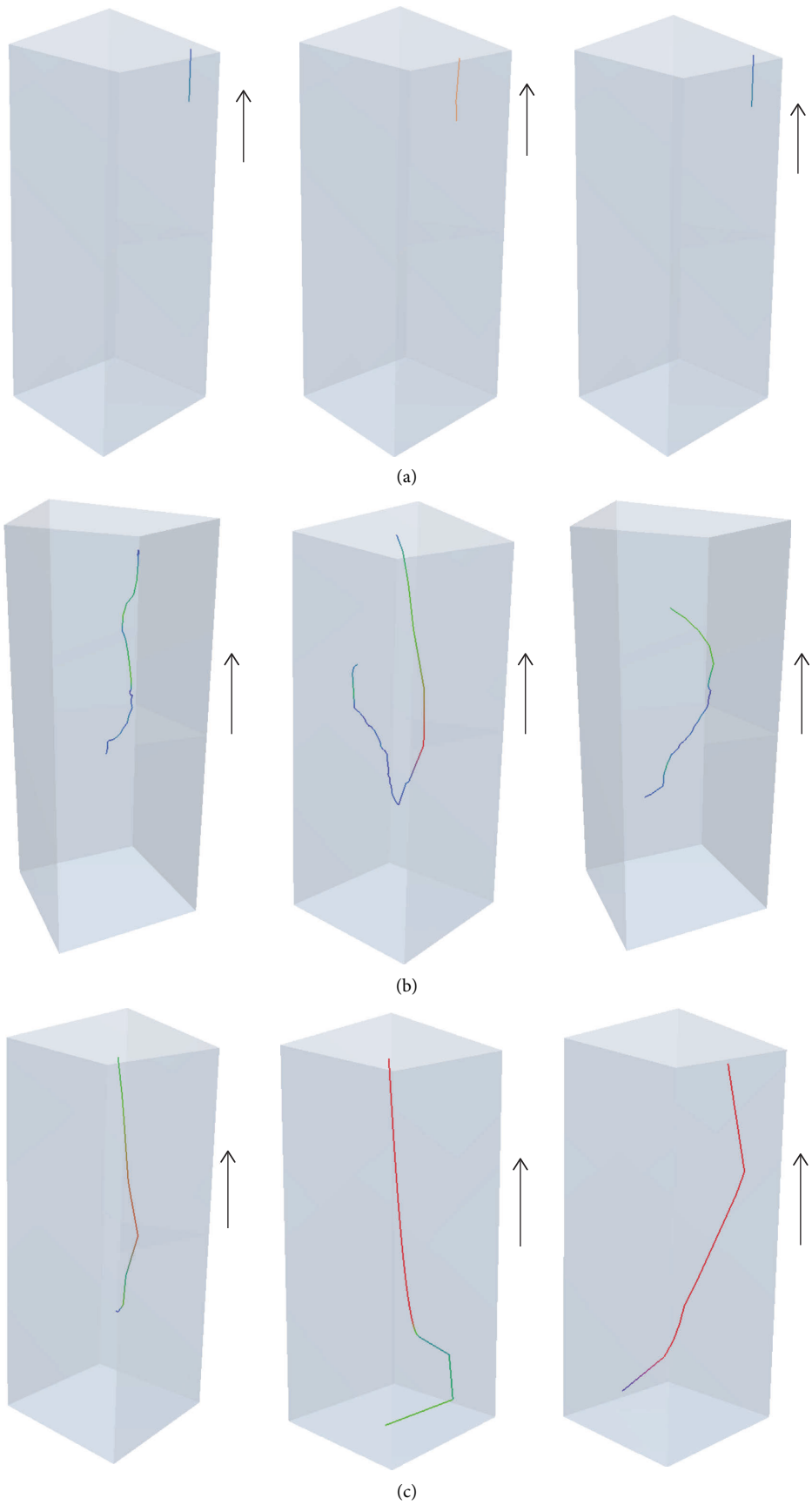

Figure 4: Particle trajectory. (a) Outlet area particles, (b) middle section particles, and (c) inlet area particles.

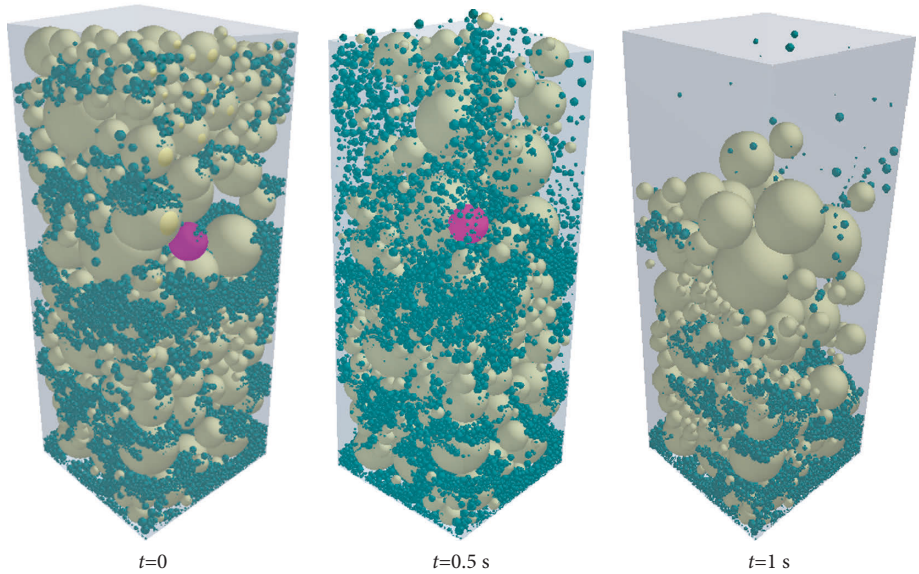

Figure 5: The trajectory of particle 1.

the movement direction of the particles, and the particles move upward.

To clarify the influence of the particle indirect contact force on the motion trajectory of the characteristic particle, the change of the particle indirect contact force of particle 1 in the whole seepage process is output in the EDEM postprocessing (Figure 6). Within 0–0.2 s, the filling particles begin to move under the action of the drag force of water flow, and the contact relationship between the characteristic particles and the surrounding filling particles changes, so the contact force on the particles begins to decrease gradually. At this time, particle 1 does not move, and at the same time, the pores around the particle increase. After 0.2 s, gravity plays a leading role, and the characteristic particles begin to move downward, but the drag force of the water flow on the particles increases with the increase of the hydraulic gradient, and the particles begin to move upward until they gush out of the channel at 0.6 s. During the movement of the particle, it is subjected to a short and slight contact force at some time because the particle collides with other particles during the movement.

The trajectory of a single particle is also different in the middle section shown (Figure 4). In the process of particle emission, some particles do not move upward along the direction of seepage force but remain stationary after a period of upward movement until the end of seepage. The reason for the particle trajectory is that at the beginning, the filling particles move upward under the action of the water drag force, get stuck between the skeleton network formed by the large skeleton particles after a certain distance, and then reach a stable state. Because the characteristic particle is located inside the model and it is difficult to observe directly, other particles are hidden and only the characteristic particle is displayed (Figure 7). The characteristic particle moves upward slowly under the initial water pressure, and it moves violently at 0.8 s and finally stops the upward trend.

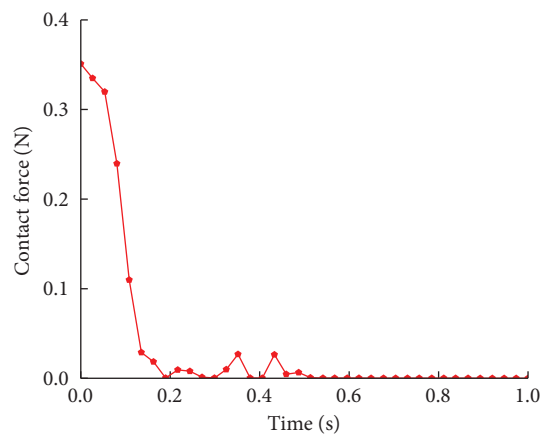

Figure 6: The contact force variation of characteristic particle 1.

3.2. Mass Change of Lost Particles. To explore the particle emission during the seepage process, using the post-processing function of EDEM software, the change of residual particle mass with time is shown in Figure 8, which can directly reflect the particle loss speed and mutation point at different time points and the particle emission in a certain period of time. Figure 9 shows the variation of lost particle mass with time during the whole seepage process. It can be seen that within 0–0.3 s, the slope of the curve is relatively flat, and the particle loss speed is relatively slow. At 0.3 s, the slope of the curve increases sharply, the particles begin to lose on a large scale and the particle loss speed and amount increase. After 0.8 s, the curve slope tends to be flat again, the particle loss speed gradually decreases, and the particle loss quality tends to be stable.

The particle loss process can be divided into three stages. In the first stage (slow seepage stage, 0–0.3 s), the particle loss mass in this stage is 5.0 g, accounting for 5.41% of the total mass loss in the whole seepage process. The initial hydraulic

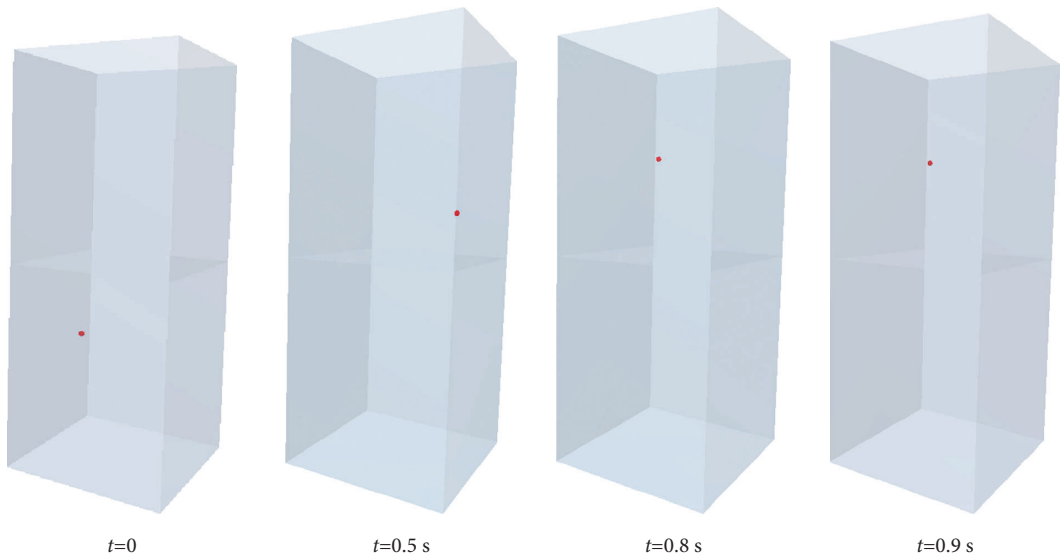

Figure 7: Characteristic particle trajectory.

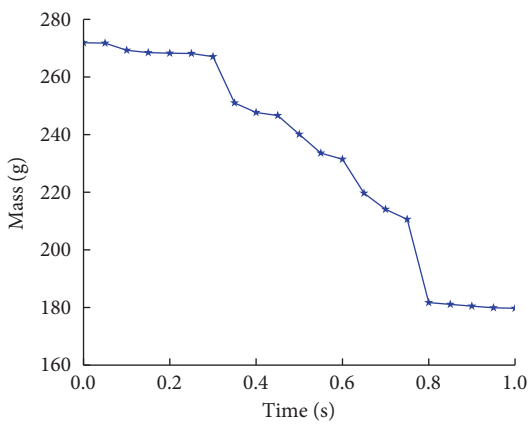

Figure 8: Broken line diagram of residual mass variation with numerical simulation time.

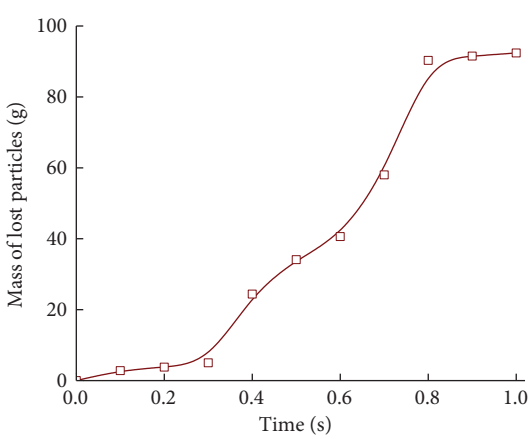

Figure 9: Variation curve of lost particle mass with time.

gradient is 0.1, the drag capacity of the flow is low, the filling particles in the outlet area will move upward slowly, and the skeleton particles will not move because of their own gravity and the large contact force between the particles. The loss mass of particles in 0–0.1 s is 2.8 g, accounting for 56% of the total mass of particles lost in the slow seepage stage. This is because the upward movement of particles in the outlet area is not hindered by other particles. After this part of the particles gushes out, the rest of the filling particles and some of the small skeleton particles free from the skeleton network begin to move upward. However, due to the drag force of water flow, the outflow velocity and outflow volume of particles are relatively small. In practical engineering, the seepage volume is small, and the water flow is relatively clear. This stage is the best time to take corresponding measures. Grouting and water plugging at appropriate positions can avoid the formation of water inrush channels. In the second stage (sudden seepage stage, 0.3 s–0.8 s), the critical hydraulic gradient corresponding to the starting point is 0.4 and the total mass loss of particles is 85.3 g, accounting for 92.32% of the total mass loss in the whole seepage process. With the emission of particles gathered in the outlet area in the slow seepage stage, the pores between the skeleton particles gradually increase and the particle loss speed and amount suddenly change, forming a relatively through seepage channel. This stage is the main stage of particle loss in the whole seepage process. In fact, the seepage volume increases and the water quality is turbid. In the third stage (stable seepage stage, 0.8–1 s), the total mass loss of particles in this stage is 2.1 g, accounting for 2.27% of the total mass loss in the whole seepage stage. As most of the filling particles and some of the skeleton particles that are free from the skeleton network have gushed out, only a few particles will slowly gush out after 0.8 s. The remaining filling particles interact with the large skeleton particles to form a new skeleton. The seepage reaches a stable state and forms a smooth seepage channel.

3.3. Change of Particle Contact Quantity. In the process of seepage, particles move upward and gush out, because the contact relationship between particles is changing and the

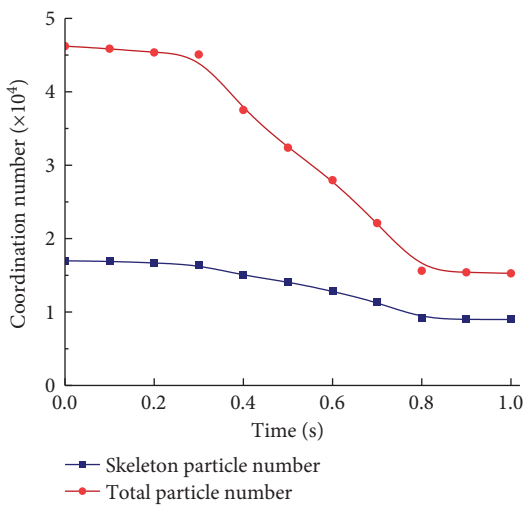

Figure 10: Curve of particle coordination number change.

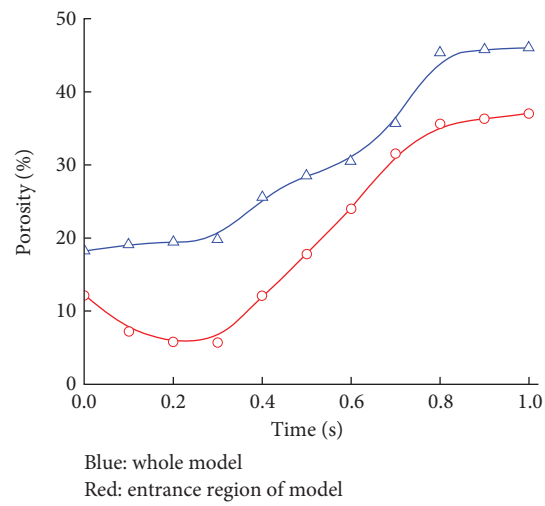

Figure 11: Variation curve of porosity with time.

normal contact force and tangential contact force are changing. The contact number between particles is described by the change of coordination number in EDEM with time. The coordination number is greater than the contact number between particles, but the larger the coordination number, the more the contact number between particles. As shown in Figure 10, the particle coordination number versus the time curve is shown. The red curve represents the change of total coordination number between particles, and the blue curve represents the change in coordination number of skeleton particles.

Within 0–0.3 s, the coordination number of skeleton particles did not change much, while the total coordination number of particles decreased slightly to a certain extent. After 0.3 s, the coordination number of skeleton particles began to decrease because the continuous loss of filling particles led to the change of contact force on skeleton particles under the action of seepage force, which made skeleton particles free from the skeleton network move, However, the contact relationship between the skeleton particles in the skeleton network has not changed.

The change of contact quantity between particles is consistent with the seepage stage, and the decrease rate of contact quantity between particles is relatively slow in the process of slow seepage. In the stage of sudden seepage, the contact quantity between filling particles and between filling particles and skeleton particles changes abruptly. During the steady seepage stage, the contact quantity between particles reaches a steady state. After the seepage process, the particles in the model are basically in a stable state, and only a small number of particles will continue to lose. Therefore, the contact number between particles will not change significantly.

3.4. Change of the Porosity. The increasing porosity in the process of seepage is the fundamental reason for the formation of water inrush channels. Because the particle loss in the inlet area is smaller than the total loss, the porosity changes in the inlet area and the total are studied, respectively. By adding "Geometry Bin" in EDEM post-processing, the change of porosity in the inlet area is analyzed, where the size is set to 40 mm × 40 mm × 50 mm. The evolution curve of porosity with time cannot be directly generated by EDEM. Therefore, the change of porosity is calculated through the change of particle volume or mass in the region. The calculation is shown as follows:

$$P = \left(1 - \frac{\rho_0}{\rho_s}\right) \times 100\% = \left[1 - \frac{m_s}{\rho_s V}\right] \times 100\%, \tag{2}$$

where P is the porosity, V is the total volume of the model, m_s is the particle mass in the model,ρ_0 is the bulk density of the material, and ρ_s is the material density.

Figure 11 (red curve) shows that the porosity in the entrance region decreases first and then increases rapidly and finally becomes stable with time. In the stage of slow seepage, the hydraulic gradient is relatively small. For larger particles in the outlet area, gravity plays a leading role. Under the downward condition of the resultant force, it moves slowly downward and continuously flows into the "Geometry Bin." Therefore, in this stage of seepage, the porosity in the inlet area decreases. As the hydraulic gradient reaches the critical hydraulic gradient and enters the sudden seepage stage, the filling particles in the inlet area will move upward rapidly under the drag force of water flow, so the porosity will increase rapidly. After entering the stable seepage stage, there is still a small amount of filling particles moving to the outlet area, but most of the particles have been in a relatively stable state, so the porosity will slowly increase and tend to be stable.

For the overall porosity, the porosity versus time curve (Figure 11, blue curve) can be obtained according to Figure 8. The change of overall porosity is a direct manifestation of particle loss. The time change curve of overall porosity is consistent with the time change curve of lost particle mass in Figure 9. In the slow seepage stage, because a small amount of particles gush out, the overall porosity increases slowly. In the stage of sudden seepage, the hydraulic gradient reaches the critical hydraulic gradient and the overall porosity

increases rapidly with the large amount of particles gushing out. After reaching the stable seepage stage, as the particles have basically remained stable, the overall porosity of the model also tends to be stable.

4. Conclusions

In the process of seepage, the particles will migrate under the action of the flow seepage force and the particles in the outlet area will move before the particles in the inlet area. As the particles in the outlet area gush out, the particles in the inlet area will move and gush out, forming a relatively smooth water inrush channel. Under the condition of variable hydraulic gradient, based on the loss speed and quality of particles, the whole seepage process can be divided into three stages: slow seepage stage, sudden seepage stage, and stable seepage stage. There are critical hydraulic gradients in the slow seepage stage and sudden seepage stage.

The particle loss speed is slow under the condition of the low hydraulic gradient. After reaching the critical hydraulic gradient, the particle loss speed increases significantly. After most of the filling particles gush out, the particle loss speed slows down and tends to be stable. In the process of water inrush, the overall movement trend of particles can be roughly predicted, but the movement trajectory of a single particle is irregular.

The change of contact quantity is mainly caused by the loss of filling particles. The change trend of contact quantity between particles is basically consistent with the change in particle loss quality. In the stage of slow seepage, the contact quantity between particles decreases slowly. The contact quantity between particles decreases rapidly after entering the stage of sudden seepage. In the steady seepage stage, the contact quantity between particles is basically in a stable state.

Data Availability

The original contributions presented in the study are included in the article, and further inquiries can be directed to the corresponding author.

Conflicts of Interest

The author WC is employed by Beijing Guodaotong Highway Design and Research Institute Co., Ltd. The authors YW, FH, and PZ are employed by Beijing Uni.-Construction Group Co., Ltd. The remaining authors declare that they have no conflicts of interest.

Authors' Contributions

The main contribution of SS in this paper is methodology, and the other authors (WC, YW, FH, and PZ) contributed to investigation and analysis.

Acknowledgments

This research was funded by the Beijing Natural Science Foundation (8222023).

References

[1] Y. Zhao, P. Li, and S. Tian, "Prevention and treatment technologies of railway tunnel water inrush and mud gushing in China," *Journal of Rock Mechanics and Geotechnical Engineering*, vol. 5, no. 6, pp. 468–477, 2013.

[2] D. Ma, H. Duan, X. Li, Z. Li, Z. Zhou, and T. Li, "Effects of seepage-induced erosion on nonlinear hydraulic properties of broken red sandstones," *Tunnelling and Underground Space Technology*, vol. 91, Article ID 102993, 2019.

[3] Z. Huang, W. Zeng, Y. Wu, S. Li, and K. Zhao, "Experimental investigation of fracture propagation and inrush characteristics in tunnel construction," *Natural Hazards*, vol. 97, no. 1, pp. 193–210, 2019.

[4] W. Zeng, Z. Huang, Y. Wu, S. Li, R. Zhang, and K. Zhao, "Experimental investigation on mining-induced strain and failure characteristics of rock masses of mine floor," *Geomatics, Natural Hazards and Risk*, vol. 11, no. 1, pp. 491–509, 2020.

[5] C. Zou, J. A. Moore, M. Sanayei, Z. Tao, and Y. Wang, "Impedance model of train-induced vibration transmission across a transfer structure into an over track building in a metro depot," *Journal of Structural Engineering*, vol. 148, no. 11, 2022.

[6] L. Li, S. Sun, J. Wang, W. Yang, S. Song, and Z. Fang, "Experimental study of the precursor information of the water inrush in shield tunnels due to the proximity of a water-filled cave," *International Journal of Rock Mechanics and Mining Sciences*, vol. 130, Article ID 104320, 2020.

[7] C. Roques, L. Aquilina, O. Bour et al., "Groundwater sources and geochemical processes in a crystalline fault aquifer," *Journal of Hydrology*, vol. 519, pp. 3110–3128, 2014.

[8] Z. Huang, W. Zeng, and K. Zhao, "Experimental investigation of the variations in hydraulic properties of a fault zone in Western Shandong, China," *Journal of Hydrology*, vol. 574, pp. 822–835, 2019.

[9] H. Jin, J. Su, and C. Zhao, "Relationship between invert-filling disengaging and deformation of shield tunnel using staggered assembled segment," *KSCE Journal of Civil Engineering*, vol. 26, no. 4, pp. 1966–1977, 2022.

[10] M. Ma, M. Li, X. Qu, and H. Zhang, "Effect of passing metro trains on uncertainty of vibration source intensity: monitoring tests," *Measurement*, vol. 193, Article ID 110992, 2022.

[11] X. Wang, S. Li, Z. Xu, J. Hu, D. Pan, and Y. Xue, "Risk assessment of water inrush in karst tunnels excavation based on normal cloud model," *Bulletin of Engineering Geology and the Environment*, vol. 78, no. 5, pp. 3783–3798, 2019.

[12] F. Qian, "Mechanism analysis and treatment technology of gushing water in Guanjiao tunnel," *Railway Engineering*, vol. 10, pp. 52–58, 2014.

[13] Y. Ma, J. Yang, L. Li, and Y. Li, "Analysis on ultimate water pressure and treatment measures of tunnels operating in water rich areas based on water hazard investigation," *Alexandria Engineering Journal*, vol. 61, no. 8, pp. 6581–6589, 2022.

[14] Y. Jiang, P. Zhou, F. Zhou et al., "Failure analysis and control measures for tunnel faces in water-rich sandy dolomite formations," *Engineering Failure Analysis*, vol. 138, Article ID 106350, 2022.

[15] X. Li, P. Zhang, Z. He, Z. Huang, M. Cheng, and L. Guo, "Identification of geological structure which induced heavy water and mud inrush in tunnel excavation: a case study on Lingjiao tunnel," *Tunnelling and Underground Space Technology*, vol. 69, pp. 203–208, 2017.

[16] J. Q. Guo, L. W. Ren, and X. L. Liu, "Study on safe thickness of comparatively intact rock ahead of karst tunnel face," *Applied Mechanics and Materials*, vol. 90-93, pp. 2456–2459, 2011.

[17] S. Jiang, Y. Wang, X. Li, and N. Zhou, "3D numerical simulation for predicting water inflow volume in deep and long tunnels," *Modern Tunnelling Technology*, vol. 379, pp. 78–83, 2016.

[18] R. Li, "Analysis and treatment measures of pouring water in Cenxi large highway tunnel," *Bridge and Tunnel Engineering*, vol. 90, pp. 33–37, 2013.

[19] X. Zhao and X. Yang, "Experimental study on water inflow characteristics of tunnel in the fault fracture zone," *Arabian Journal of Geosciences*, vol. 12, no. 13, p. 399, 2019.

[20] M. Liu and Z. Zhang, "Smoothed particle hydrodynamics (SPH) for modeling fluid-structure interactions," *Science China Physics, Mechanics & Astronomy*, vol. 62, Article ID 984701, 2019.

[21] B. Bai, D. Rao, T. Xu, and P. Chen, "SPH-FDM boundary for the analysis of thermal process in homogeneous media with a discontinuous interface," *International Journal of Heat and Mass Transfer*, vol. 117, pp. 517–526, 2018.

[22] B. Bai, F. Long, D. Rao, and T. Xu, "The effect of temperature on the seepage transport of suspended particles in a porous medium," *Hydrological Processes*, vol. 31, no. 2, pp. 382–393, 2017.

[23] W. C. Cheng, X. D. Bai, B. B. Sheil, G. Li, and F. Wang, "Identifying characteristics of pipejacking parameters to assess geological conditions using optimisation algorithm-based support vector machines," *Tunnelling and Underground Space Technology*, vol. 106, Article ID 103592, 2020.

[24] B. Bai, "Fluctuation responses of saturated porous media subjected to cyclic thermal loading," *Computers and Geotechnics*, vol. 33, no. 8, pp. 396–403, 2006.

[25] B. Yuan, Z. Li, W. Chen et al., "Influence of groundwater depth on pile–soil mechanical properties and fractal characteristics under cyclic loading," *Fractal and Fractional*, vol. 6, no. 4, p. 198, 2022.

[26] B. Bai, G. C. Yang, T. Li, and G. S. Yang, "A thermodynamic constitutive model with temperature effect based on particle rearrangement for geomaterials," *Mechanics of Materials*, vol. 139, Article ID 103180, 2019.

[27] B. Bai, R. Zhou, G. Cai, W. Hu, and G. Yang, "Coupled thermo-hydro-mechanical mechanism in view of the soil particle rearrangement of granular thermodynamics," *Computers and Geotechnics*, vol. 137, Article ID 104272, 2021.

[28] B. Bai and Z. Su, "Thermal responses of saturated silty clay during repeated heating-cooling processes," *Transport in Porous Media*, vol. 93, pp. 1–11, 2012.

[29] B. Bai, Q. Nie, Y. Zhang, X. Wang, and W. Hu, "Cotransport of heavy metals and SiO_2 particles at different temperatures by seepage," *Journal of Hydrology*, vol. 597, Article ID 125771, 2021.

[30] W. Hu, W. C. Cheng, S. Wen, and K. Yuan, "Revealing the enhancement and degradation mechanisms affecting the performance of carbonate precipitation in EICP process," *Frontiers in Bioengineering and Biotechnology*, vol. 9, Article ID 750258, 2021.

[31] L. Guoyu, Y. Changhong, L. Xiaozhao, J. Jianping, and M. Ji, "Exploration of water resource and multiple model for water resource development in karst areas with the preferred plane theory," *Acta Geologica Sinica - English Edition*, vol. 77, no. 1, pp. 129–135, 2010.

[32] B. Bai and T. Li, "Irreversible consolidation problem of a saturated porothermoelastic spherical body with a spherical cavity," *Applied Mathematical Modelling*, vol. 37, no. 4, pp. 1973–1982, 2013.

[33] B. Bai, L. Guo, and S. Han, "Pore pressure and consolidation of saturated silty clay induced by progressively heating/cooling," *Mechanics of Materials*, vol. 75, pp. 84–94, 2014.

[34] B. Yuan, M. Chen, W. Chen, Q. Luo, and H. Li, "Effect of pile-soil relative stiffness on deformation characteristics of the laterally loaded pile," *Advances in Materials Science and Engineering*, vol. 13, p. 1, 2022.

[35] B. Yuan, W. Chen, J. Zhao, F. Yang, Q. Luo, and T. Chen, "The effect of organic and inorganic modifiers on the physical properties of granite residual soil," *Advances in Materials Science and Engineering*, vol. 13, p. 1, 2022.

[36] Z. Zhou, L. Li, S. Shi et al., "Study on tunnel water inrush mechanism and simulation of seepage failure process," *Rock and Soil Mechanics*, vol. 41, pp. 3621–3631, 2020.

[37] Y. Wang, F. Geng, S. Yang, H. Jing, and B. Meng, "Numerical simulation of particle migration from crushed sandstones during groundwater inrush," *Journal of Hazardous Materials*, vol. 362, pp. 327–335, 2019.

[38] Z. Xu, M. Xian, X. Li, and W. Zhou, "Risk assessment of water inrush in shallow karst tunnel with stable surface water supply: case study," *Geomechanics and Engineering*, vol. 25, pp. 495–508, 2021.

[39] X. Chen and R. Lyu, "Experimental study on effects of particle migration on hydraulic Characteristics of crushed sandstone during water inrush," *China Mining Magazine*, vol. 30, pp. 184–188, 2021.

[40] M. Wang, W. Yang, Z. Zhou et al., "Experimental research on the effect of particle migration of a filling medium in a fault during water and mud inrush," *Arabian Journal of Geosciences*, vol. 14, no. 21, p. 2206, 2021.

[41] B. Bai, T. Xu, Q. Nie, and P. Li, "Temperature-driven migration of heavy metal Pb^{2+} along with moisture movement in unsaturated soils," *International Journal of Heat and Mass Transfer*, vol. 153, Article ID 119573, 2020.

[42] J. Kozicki and F. V. Donzé, "A new open-source software developed for numerical simulations using discrete modeling methods," *Computer Methods in Applied Mechanics and Engineering*, vol. 197, no. 49-50, pp. 4429–4443, 2008.

[43] B. Bai, S. Jiang, L. Liu, X. Li, and H. Wu, "The transport of silica powders and lead ions under unsteady flow and variable injection concentrations," *Powder Technology*, vol. 387, pp. 22–30, 2021.

[44] B. Bai, Q. Nie, H. Wu, and J. Hou, "The attachment-detachment mechanism of ionic/nanoscale/microscale substances on quartz sand in water," *Powder Technology*, vol. 394, pp. 1158–1168, 2021.

[45] W. Hu, W. C. Cheng, S. Wen, and M. Mizanur Rahman, "Effects of chemical contamination on microscale structural characteristics of intact loess and resultant macroscale mechanical properties," *Catena*, vol. 203, Article ID 105361, 2021.

[46] Z. F. Xue, W.-C. Cheng, L. Wang, and G. Song, "Improvement of the shearing behaviour of loess using recycled straw fiber reinforcement," *KSCE Journal of Civil Engineering*, vol. 25, no. 9, pp. 3319–3335, 2021.

[47] H. Jin, Q. Tian, and Z. Li, "Crack development of rebar rust in rubberized concrete using mesoscale model," *Construction and Building Materials*, vol. 321, Article ID 126409, 2022.

[48] Z. F. Xue, W. C. Cheng, L. Wang, and W. Hu, "Effects of bacterial inoculation and calcium source on microbial-induced carbonate precipitation for lead remediation," *Journal of Hazardous Materials*, vol. 426, Article ID 128090, 2022.

[49] L. Xu and M. Ma, "Dynamic response of the multilayered half-space medium due to the spatially periodic harmonic moving load," *Soil Dynamics and Earthquake Engineering*, vol. 157, Article ID 107246, 2022.

[50] S. Shi, X. Xie, L. Bu, L. Li, and Z. Zhou, "Hazard-based evaluation model of water inrush disaster sources in karst tunnels and its engineering application," *Environmental Earth Sciences*, vol. 77, no. 4, p. 141, 2018.

Hindawi
Advances in Civil Engineering
Volume 2022, Article ID 5306923, 14 pages
https://doi.org/10.1155/2022/5306923

Research Article

Numerical Simulation of the Stability of a Cutting Slope and Study on Its Reinforcement Scheme

Song Chen,[1,2] **Zhao Yang**,[3] **Wenpeng Zhang**,[2,4] **Liufang Li**,[5] **Yibo Zheng**,[1,2] **and Ying Yuan**[2,4]

[1]*Hebei Key Laboratory of Optoelectronic Information and Geo-detection Technology, Hebei GEO University, Shijiazhuang 050031, China*
[2]*College of Urban Geology and Engineering, Hebei GEO University, Shijiazhuang 050031, China*
[3]*Guangdong Hualu Transport Technology Co., Ltd., Guangzhou 510420, China*
[4]*Hebei Technology Innovation Center for Intelligent Development and Control of Underground Built Environment, Hebei GEO University, Shijiazhuang 050031, China*
[5]*College of Civil Engineering and Mechanics, Lanzhou University, Lanzhou 730000, China*

Correspondence should be addressed to Liufang Li; lliufun@126.com

Received 14 July 2022; Accepted 3 September 2022; Published 5 October 2022

Academic Editor: Ziyu Tao

Analyzing the stability of the slope and studying the reinforcement scheme can reduce ecological disasters, improve the ecological environment, and protect people's lives and property. In this paper, taking the left side slope of ZK100 + 860~+975 cutting of the Huizhou-Qingyuan section of the Shantou-Zhanjiang Expressway as an example, based on the strength reduction method (SRM), the stability of the slope under different conditions (natural conditions, unsupported excavation conditions, rainstorm conditions, and reinforcement conditions) is analyzed by using finite element software. The results show that the slope was almost stable before excavation, and the safety factor of slope stability decreases due to excavation, so it is in an unstable state. Rainwater has a great influence on the stability of the slope. The damage to the slope is deepened, and the stability safety factor is decreased under the rainstorm condition. The stability safety factor of the slope has increased by 24.3% after the reinforcement of the anchor rod and anchor cable, and the slope is in a stable state. It can be seen that the anchor rod and anchor cable can effectively control the deformation of the slope and have a good reinforcement effect.

1. Introduction

At present, there are many common methods to analyze slope stability, including the slice method, rigid body limit equilibrium method, plastic limit analysis method [1], stereographic projection method, and strength reduction method (SRM). However, the ideal method to truly analyze slope stress, deformation, and stability is the strength reduction method (SRM) [2]. The strength reduction method (SRM) was introduced into slope stability analysis in the 1960s. Later, in order to make it more suitable for engineering practice and study the failure mechanism and characteristics of the slope, many scholars in China conducted in-depth research on this basis. Yuan et al. proposed a new nonlinear SRM method based on the generalized Hoek-Brown (GHB) criterion, which provides a reduction strategy with precise physical significance for seeking the optimal parameter set of rock slope failure [3]. Wang et al. put forward a discrete element modeling method (DSDM) for the stability of jointed rock slopes based on displacement statistics on the basis of the strength reduction method (SRM), which can be coupled with anti-SRM to effectively analyze the stability of jointed slopes with potential sliding surfaces [4]. Yang et al., considering the nonlinear failure characteristics of rock mass, proposed 3D-NSRNMM based on the nonlinear GHB failure criterion to conduct a 3D analysis of rock slope to study the stability of slope [5]. Nie et al. used the constant boundary element method to discretize sliding mass to study SRM-related slope instability criteria and got a relatively reliable conclusion [6]. Sun et al.,

based on the incremental method of elastic-plastic mechanics and bilinear projection operator method, combined the strength reduction method with φ-ν inequality and proposed a virtual element strength reduction technique to analyze the stability of slope [7]. Zhou and Hua combined rock mechanics theory, nonlinear finite element analysis technology, and the strength reduction coefficient method to put forward the strength parameter reduction finite element method, which can effectively analyze the stability of bedding rock cutting slope [8]. Chen et al. put forward a dynamic stability evaluation method for slopes based on the dynamic and overall strength reduction method and carried out stability evaluation and support analysis of slopes [9]. Some scholars combine the strength reduction method with the limit equilibrium method to quantitatively analyze the slope and evaluate its stability [10–12]. Based on the above research findings, with the in-depth study of slope problems, the finite element strength reduction method has become the mainstream method to analyze the stress, displacement, and stability of slopes, and a series of new slope research methods have been derived based on its basic principles.

In the existing cases of slope stability analysis based on the finite element strength reduction method (SRM), some scholars only consider the impact of excavation on slope stability [13–15] while ignoring the impact of heavy rainfall. Studies have shown that heavy rainfall is also one of the most important factors affecting slope stability [16]. Based on this statement, many scholars have carried out extensive research. Sun et al. used the saturated-unsaturated strength and infiltration theory of silty sand slopes to study the influence of rainfall infiltration on slope stability by numerical simulation [17]. Tian et al. obtained the soil mechanical parameters of the slope through triaxial compression, saturated infiltration and other geotechnical tests and, based on this, established a finite element model to study the stability of the slope with rainfall intensity and duration [18]. Song and Tan conducted a large number of indoor rainfall tests combined with DIC image technology to explore the failure mechanism of the soil slope under heavy rainfall and finally obtained the failure characteristics of the slope in different scenarios [16]. In terms of rock and soil material properties, Bai et al. [19–21] have studied the particle interaction and mutual coupling mechanisms of rock and soil, which play a certain key role in slope stability.

The research in this paper is based on the principle of the finite element strength reduction method (SRM). Taking a specific slope project as an actual case, the natural and excavation conditions of the slope are quantitatively analyzed by Midas software. At the same time, take heavy rainfall into account, study the impact of rainfall on the slope, and put forward the slope support design scheme according to the actual engineering needs. This provides a basis for studying the stability of slopes under different working conditions, solving practical construction problems, and optimizing support design schemes.

2. Project Background

The Huizhou-Qingyuan section of the Shantou-Zhanjiang Expressway is located in the central part of Guangdong Province. The project route starts at Hengcha Village, Longhua Town, Longmen County, Huizhou City, crosses the T-shape of the Guanghe Expressway, and ends at Taihe Town, Qingxin District, Qingyuan City, connecting with the Qingyuan-Yunfu section of the Shantou-Zhanjiang Expressway, with a total length of 126200.0 m. The project is located on the left side of ZK100 + 860 ~ ZK100 + 975 cutting, with a slope length of 115.0 m and a maximum slope height of 50.0 m. This place is located in the hills, where the terrain fluctuates greatly. The ground elevation of the slope is about 154.2~186.2 m, and the natural slope angle is about 25~30°. The mainline map and slope topographic map are shown in Figure 1.

According to the drilling data and field geological mapping results, the slope rocks are mainly quaternary colluvial silty clay, Yanshanian granite and its weathered layer. The quaternary overburden and all strongly weathered layers of the slope are thick, the vegetation is well developed, and no joints are measured in the slope area. The section of structural plane occurrence is shown in Figure 2. The climate in this area is mild, the rainfall is abundant, and the surface runoff has a great impact on the foot of the slope. Atmospheric precipitation is the main source of groundwater supply. According to the drilling data, the buried depth of the underground stable water level is about 21m, measured locally in the drilling depth, while others are not found. Relevant parameters of slopes and stages at all levels after excavation on the left side are shown in Table 1.

3. Numerical Simulation of Slope Stability

3.1. Finite Element Software and Method. MIDAS GTS NX is a commonly used finite element numerical simulation software in geotechnical engineering, which is usually suitable for modeling tunnels, slopes, and other projects. It can be used for linear dynamic analysis, seepage and consolidation analysis, etc., and can simulate many special working conditions for complex operations. The finite element model of the slope is established in Midas, and the stability safety factor of the slope is calculated by the strength reduction method. The strength reduction method (SRM) is a common method to calculate F_s (the safety factor) of slope stability. The basic principle is that the shear strength indexes c and φ of soil continuously reduce until the slope is in the critical state of limit equilibrium. The specific calculation formula is as follows:

$$c' = \frac{c}{F_s},$$
$$\tan\varphi' = \frac{\tan\varphi}{F_s}, \tag{1}$$
$$\tau' = c' + \sigma\tan\varphi'.$$

Matters that need attention are as follows: (1) the initial value of the reduction coefficient and the increment of F_s should be small enough to ensure the numerical calculation result and (2) the value of the reduction coefficient before divergence is the stability safety factor of the slope.

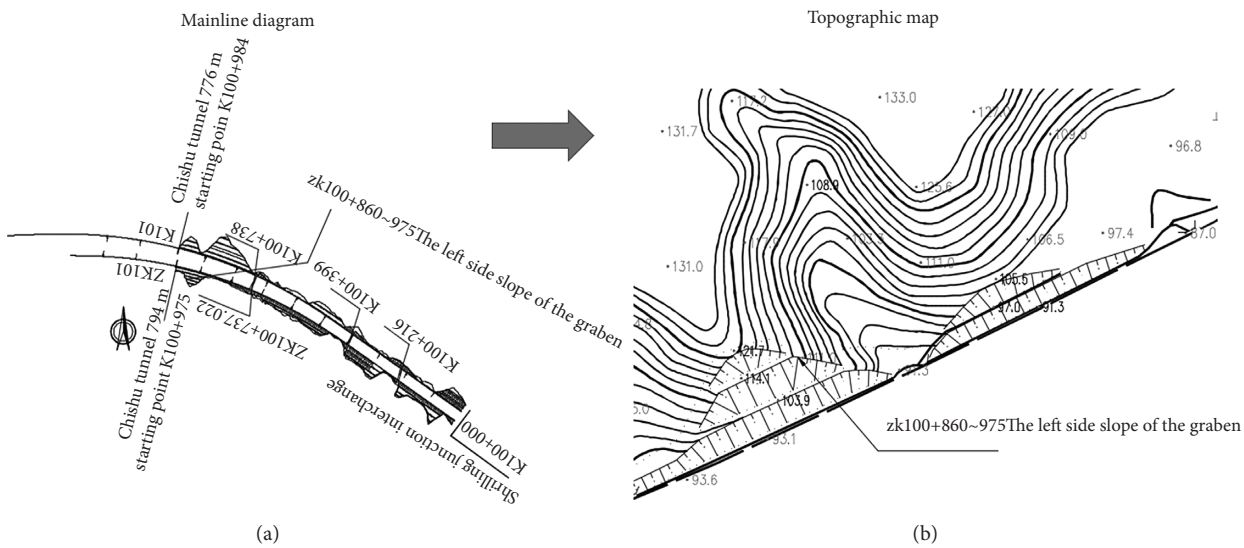

Figure 1: Mainline map (a) and topographic map of the left side slope of cutting (b).

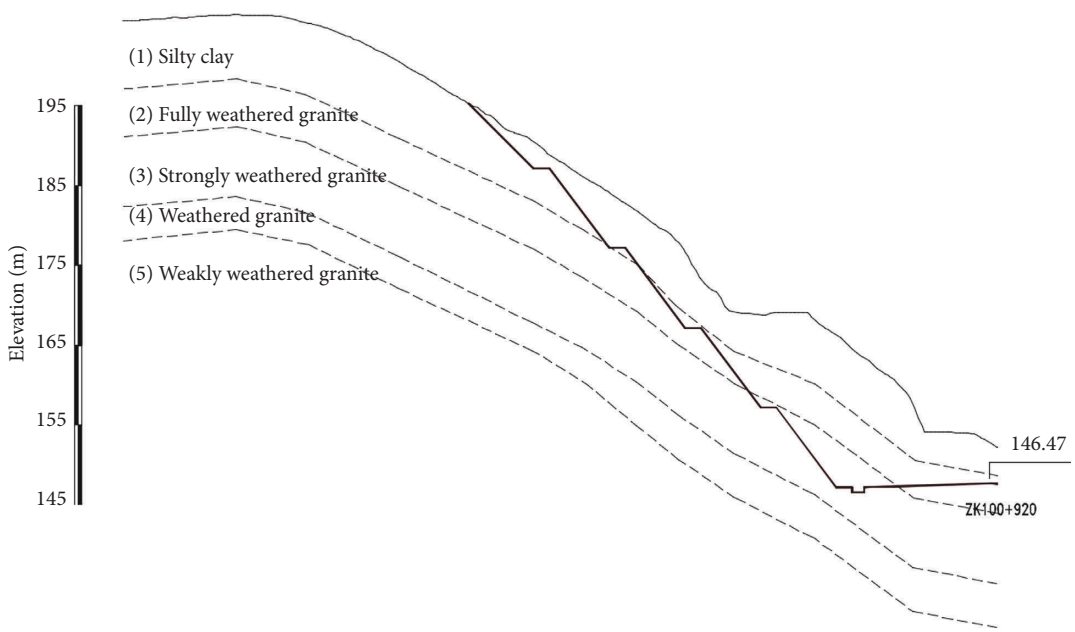

Figure 2: Geological profile of slope.

3.2. Selection of Instability Criterion. There are three main criteria for judging slope instability by finite element strength reduction method:

(1) The plastic zone of the slip surface is completely connected [22]

(2) The displacement and strain on the slip surface suddenly change, resulting in a very large and unlimited plastic flow [23]

(3) Double convergence criterion of force and displacement; judging from the convergence criterion of force and displacement, the model calculation is not convergent

3.3. Numerical Model and Parameters. According to the geological profile and construction excavation scheme, the finite element calculation model is established. There are two types of models: one is the model under natural conditions, and the other is the stratum model after excavation, as shown in Figure 3.

The two models are 151 meters long and 100 meters high. According to automatic mesh generation, the natural model is divided into 12116 units and 12364 nodes. The excavation model is divided into 11178 units and 11389 nodes. The boundary condition of the tectonic geostress field should be considered at the bottom and left and right sides of the model and the whole model should be loaded with self-

Table 1: Table of parameters related to slope excavation.

Slope stage	Slope ratio	Height (m)	Width (m)
The 1st slope stage	1 : 0.75	10	2
The 2nd slope stage	1 : 0.75	10	2
The 3rd slope stage	1 : 0.75	10	2
The 4th slope stage	1 : 0.75	10	2
The 5th slope stage	1 : 1.00	Varies	—

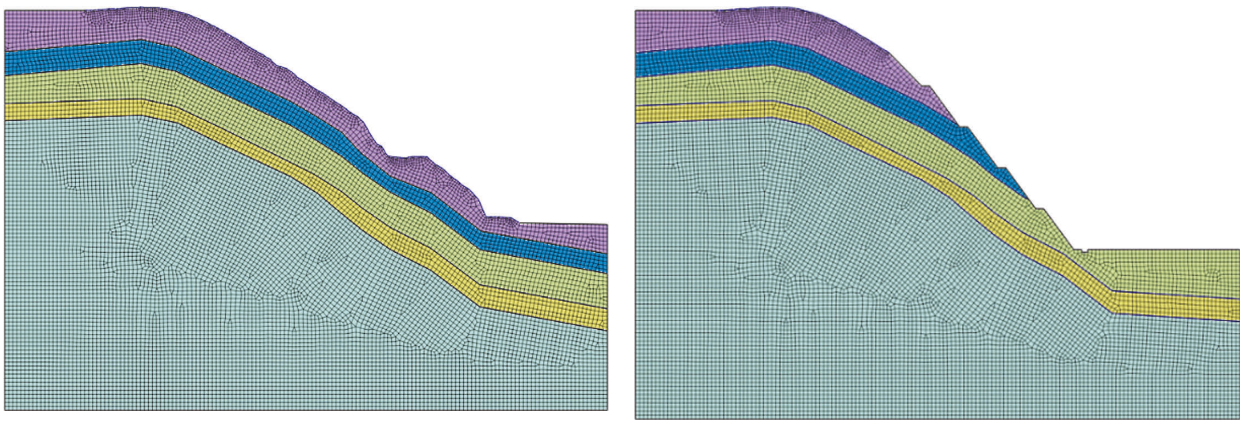

(a) (b)

Figure 3: Numerical calculation model. (a) Model in natural state. (b) The model after excavation.

weight stress. Considering the rock mass attribute characteristics of strata, Mohr–Coulomb constitutive model is selected as the model grid material, and the specific physical and mechanical parameters of rock mass materials are shown in Table 2.

3.4. Result Analysis

3.4.1. The Condition under Natural Conditions. The strength reduction method (SRM) is used to calculate the safety and stability coefficient of the slope model under natural conditions. The results show that the value is 1.05, the slip surface is not penetrated, and the slope is in an unstable state.

As shown in Figure 4, according to the displacement-stress contour, the displacement in the middle and upper parts of the slope is the largest, with the maximum displacement reaching 0.0932 m, where the rock strata are severely deformed and often heave. At this position, the downward deformation along the slope shows a decreasing trend until the bottom of the slope, the displacement of the rock stratum is minimal, and almost no deformation occurs. The effective plastic strain contour is shown in Figure 5, and the results show that the maximum strain in the plastic region is 0.0246, and the slip surface in the slope extends from the top to the foot of the slope, but there is no penetration. The length of the slip surface is about to 86 m, and it exists in an arc shape at the interface between silty clay and granite strata. The overall slip-crack effect is very obvious, and the shear outlet is located at the foot of the slope.

3.4.2. The Condition of Excavation Without Support. According to the Revit stratum map, after excavation, a finite element model is established, and boundary conditions are imposed. On this basis, the strength reduction method is used to calculate the slope stability. The results show that the safety factor of slope stability decreases to 0.97 after grade 5 excavation, and the plastic zone of the slip surface has been completely penetrated. At this time, the slope is unstable.

Figure 6 shows the displacement contour. It can be seen from the figure that the large displacement and deformation of the slope after excavation are mostly concentrated at the fourth and fifth slopes, and the maximum displacement is about 0.113 m, while the displacement and deformation of the first, second, and third slopes are relatively small, which can be ignored by comparison.

The effective plastic strain contour is shown in Figure 7. According to the analysis, the slip zone is about 45 m long, distributed between 4.5 and 8 m below the slope, and the maximum plastic strain of the slope is 0.0322. Compared with the natural condition, the slip surface is shorter in length, and the shear outlet position becomes the platform between the fourth and fifth slopes.

3.5. Influence of Rainfall Infiltration on Slope Stability. The slope is located in an area with abundant rain and rainy days all year round. In order to study the degree of influence of rain on slope stability, numerical simulation software is used to simulate and analyze the influence of rain on slope stability.

Table 2: Physical parameters of rock mass materials.

Name	C (kPa)	φ (°)	Young's modulus (MPa)	Poisson's ratio	Natural gravity (kN/m^3)
Silty clay	19	18	40	0.3	18
Completely weathered granite	25	25	31000	0.15	19
Highly weathered granite	28	29	40000	0.22	21
Moderately weathered granite	31	32	55000	0.36	22
Weakly weathered granite	32	33	60000	0.37	23

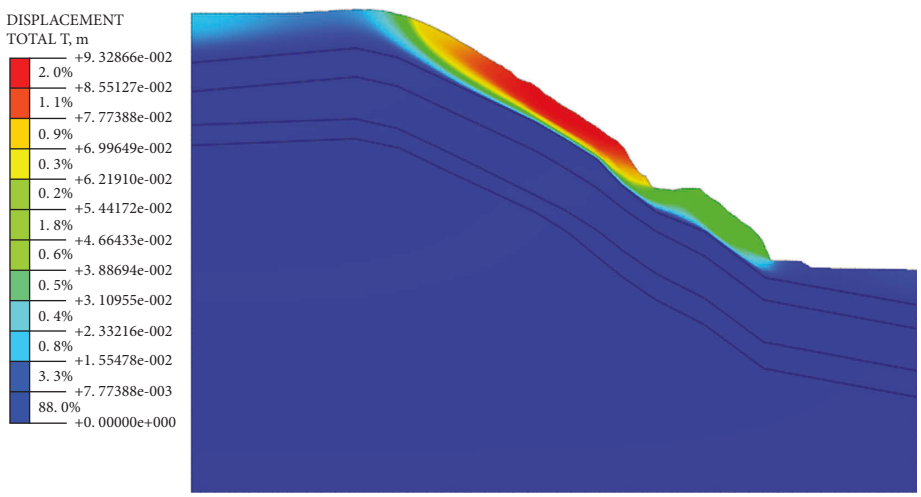

Figure 4: Contour of displacement under natural conditions.

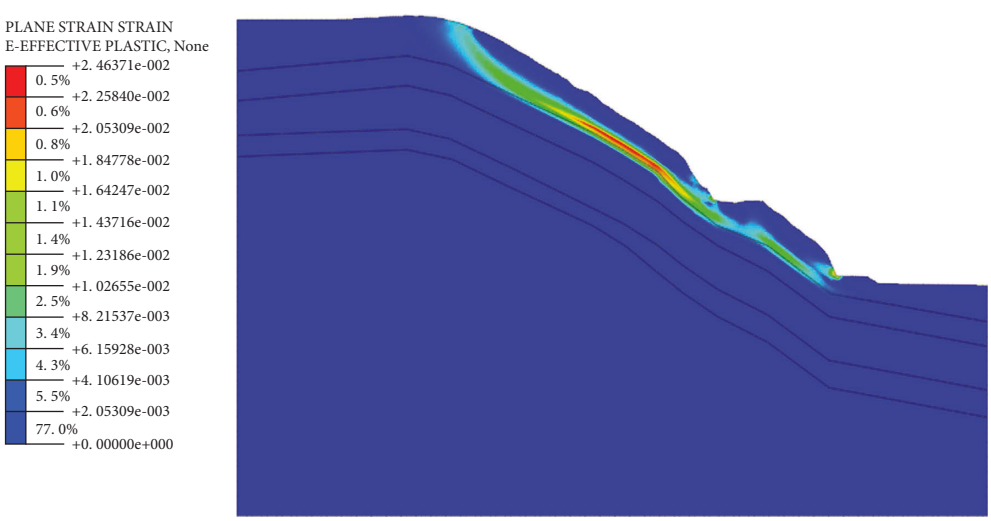

Figure 5: Contour of effective plastic strain under natural conditions.

In this paper, based on the excavated slope model, when establishing the model, according to the soil data in Table 2, the corresponding material attributes are given to each stratum. The permeability and water-bearing function of the material is defined by the van Genuchten model, and the specific characteristic curves are shown in Figures 8 and 9. The expression is

$$\theta = \theta_r + \frac{\theta_s - \theta_r}{\left[1 + (a \times h)^n\right]^m}, \quad m = 1 - \frac{1}{n}, \tag{2}$$

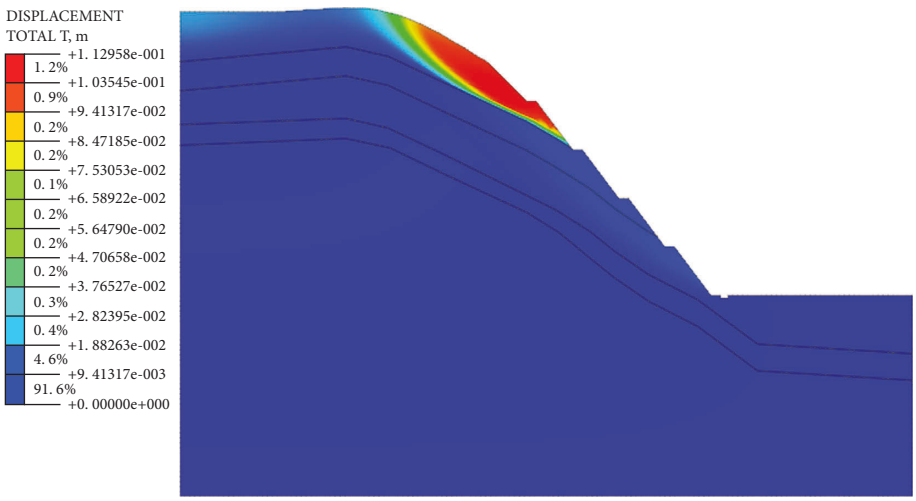

Figure 6: Displacement contour under the condition of excavation without support.

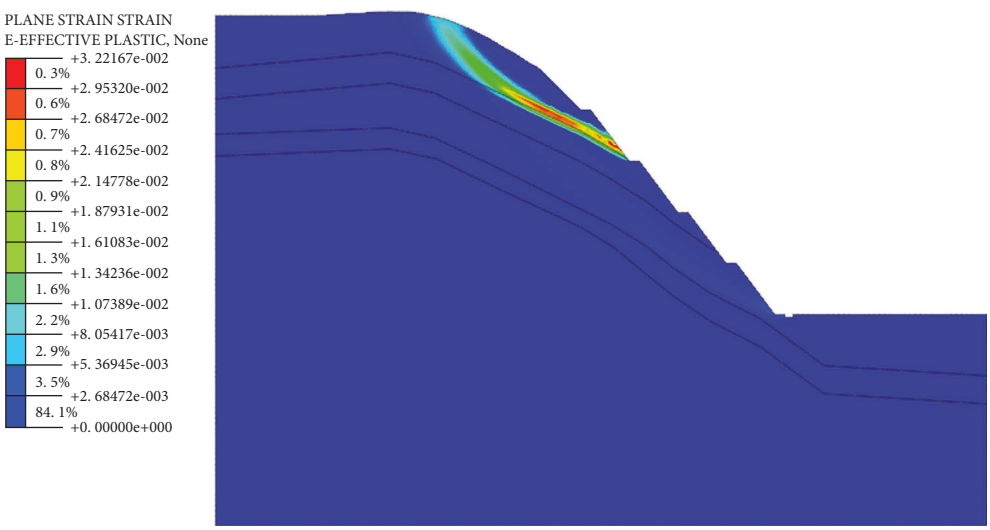

Figure 7: Contour of effective plastic strain under excavation and unsupported conditions.

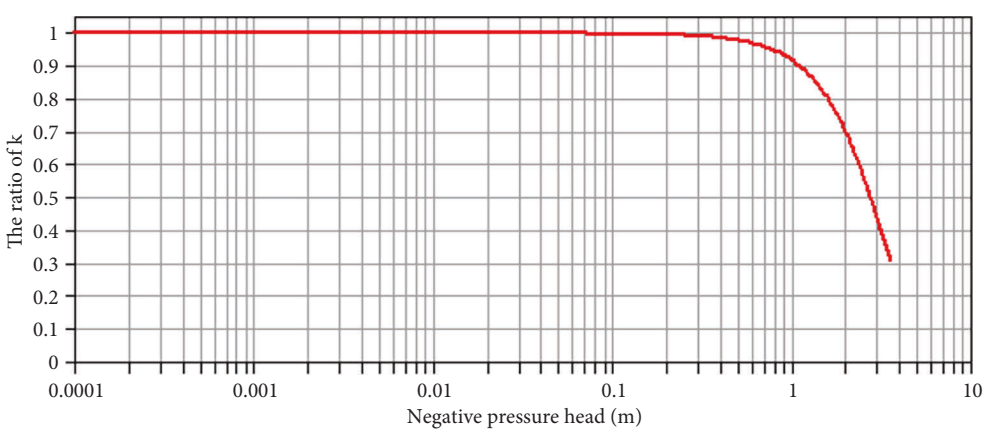

Figure 8: The permeability curve.

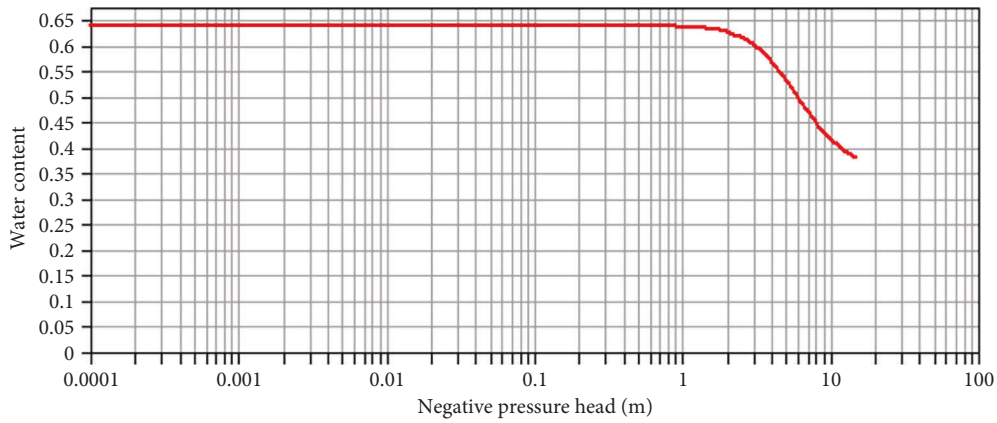

Figure 9: Curve of soil and water characteristics.

where θ is the volume water content of soil; h is the pressure head; and θ_r and θ_s represent residual volume water content and saturated volume water content of the soil, respectively. a, n are empirical fitting parameters. In this paper, $\theta_r = 0.35$, $\theta_s = 0.64$; $a = 0.2$, $n = 3$, $m = 0.66$.

When establishing the rainfall conditions of the model, the influence of the initial groundwater level should be fully considered. In this paper, the pressure head is set to 0 by the operation of the node head. The whole slope surface of the model is set as the rainfall infiltration surface, and the heavy rain lasting 24 hours is taken as the short-term heavy rainfall condition. For the setting of rainfall intensity, the curved flow rate is adopted, and the rainfall intensity is 300 mm/d. Finally, the 8-hour period is divided into three stages for calculation and analysis. The model is shown in Figure 10.

The results show that the slope safety factor decreases to 0.95 after 24 hours of rainfall infiltration, and the slope is extremely unstable. The deformation characteristics of the slope are basically the same as those without rainfall. As far as the deformation degree is concerned, as shown in Figure 11, the initial displacement of the slope has nearly doubled compared with that without rainfall, and the maximum displacement at the slope has reached 0.222 m. The position of the circular slip surface has no significant change compared with that without rainfall, but the damage to the plastic zone has deepened. As shown in Figure 12, the maximum plastic strain changes from 0.0322 to 0.0768, with an increase of 138%. The contour map of pore water pressure before and after rainfall is set by the ISO standard value surface, and the contour map before and after rainfall is shown in Figure 13. Compared to the pore water pressure before and after rainfall, it is found that after 24 h, the water level in the slope increases obviously, and the pore water pressure also increases.

Generally speaking, rainfall infiltration will seriously affect the deformation of rock and soil mass, thus affecting the stability of the slope. The influence of rainfall should be fully considered in slope excavation design and reinforcement optimization.

4. Slope Reinforcement and Results

4.1. Selection of Slope Reinforcement Scheme

4.1.1. Design of Reinforcement Measures. Through calculation, it is found that the safety factor of the slope after excavation is less than 1, the displacement and deformation of the slope are large, and the state is extremely unstable. After the rainfall, the stability safety factor of the slope decreased, the slope damage deepened, and the deformation became more serious. In view of the above situation, reinforcement measures should be taken for the slope. According to the above analysis of the deformation mechanism and failure characteristics of the slope, it is decided to adopt measures such as anchor lattice beam, anchor cable frame beam, and shotcrete for reinforcement. See Table 3 for specific reinforcement measures and Figure 14 for reinforcement effects.

4.1.2. Reinforcement and Protection Structure Design

(1) Roof bolt. The diameter of the bolt hole is 110 mm, and the bolt is made of an HRB400 steel bar of ϕ28 mm. The anchor is 8.5 m long, and the designed pullout resistance is 60 kN. The anchor is 11.5 m long, and the designed pullout force is 90 kN. The grouting body adopts M30 cement slurry. The grouting method is adopted at the bottom of the hole. It is forbidden to pull up the bound PVC grouting pipe in the grouting process. The grouting pipe must not be reused. After grouting is finished, grout should be replenished at the orifice. M30 cement slurry is used for grout replenishment, and a rust inhibitor is added to the M30 cement slurry. Figure 15 shows the reinforcement schematic diagram.

(2) Prestressed anchor cable. The prestressed anchor cable body is made of ordinary prestressed steel strands with ϕ15.2 mm standard tensile strength of 1860 MPa and high strength and low relaxation. The anchor cable body adopts 4 strands of steel strands, and the anchor cable drilling hole is ϕ130 m in diameter, with a designed tensile force of 400 kN and a locking tension of 480 kN; 5~6 bundles of steel strands are used for the anchor cable body,

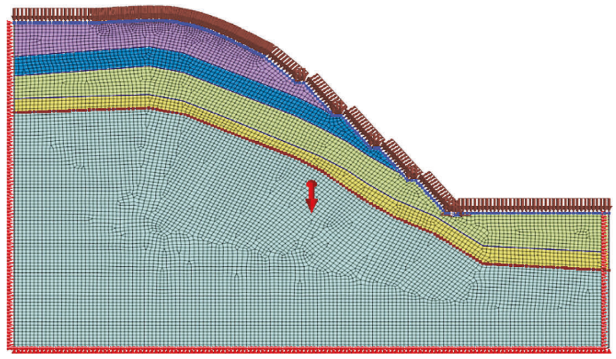

Figure 10: Model diagram under rainfall conditions.

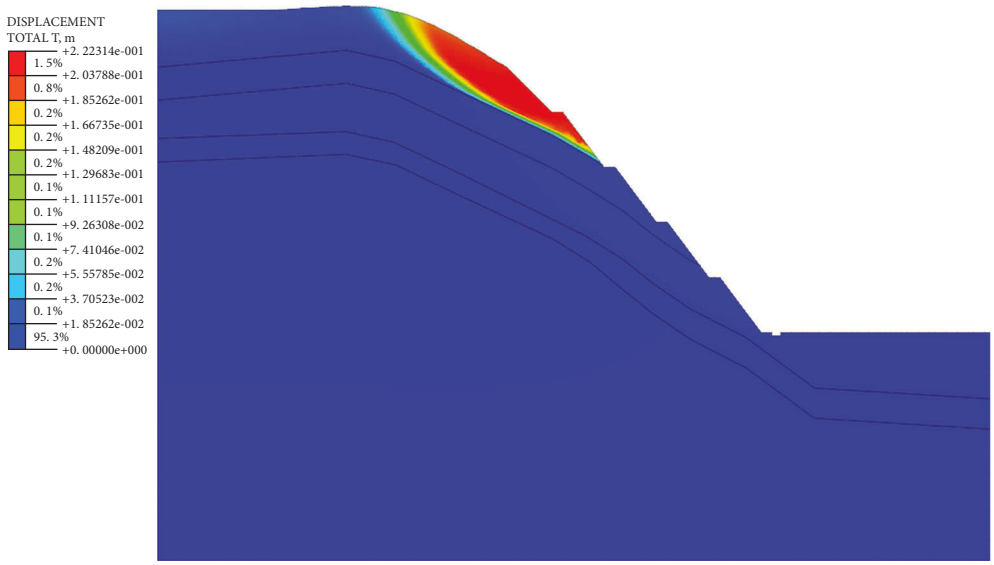

Figure 11: Slope displacement contour under unsupported rainfall conditions.

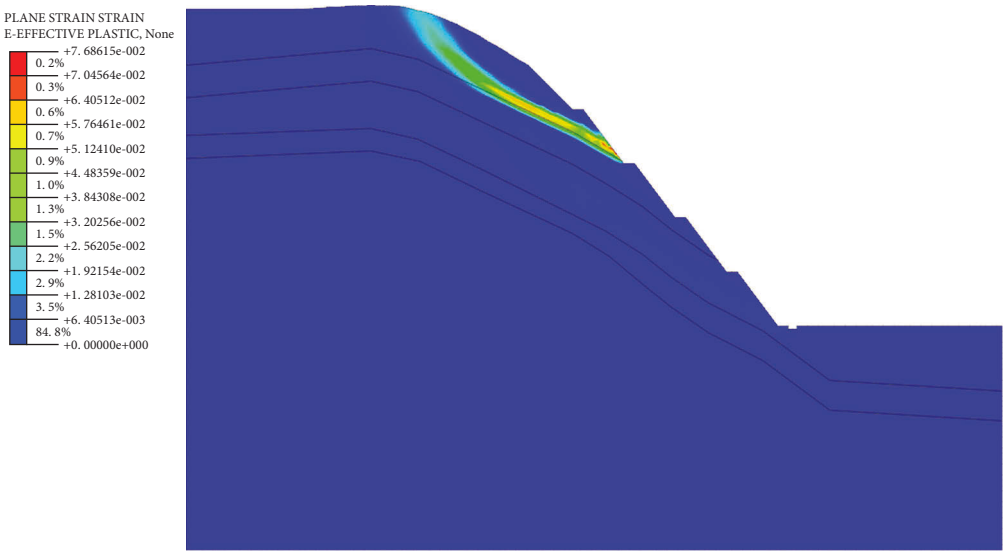

Figure 12: Contour of the effective plastic strain of slope under unsupported rainfall conditions.

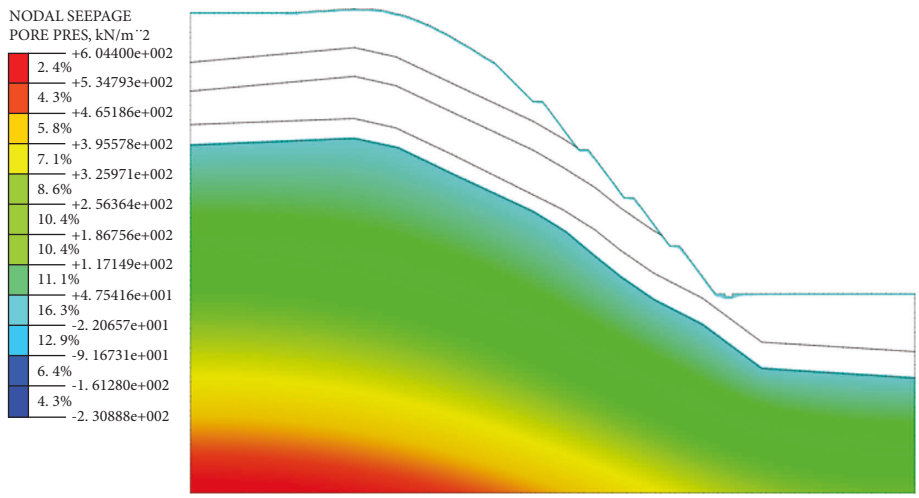

(a)

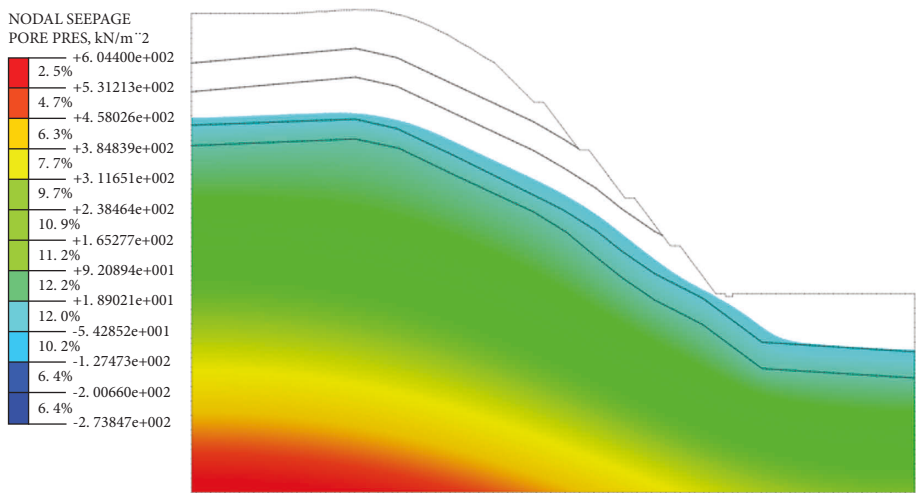

(b)

Figure 13: Isograph of pore water pressure of slope before and after rainfall. (a) Before the rainfall. (b) After 24 hours of rain.

Table 3: Slope reinforcement measures.

Slope level	Reinforcement measures
The 1st slope stage	Four anchor bars are used for reinforcement, and the length of the anchor bars is 8.5 m;
The 2nd slope stage	Three prestressed anchor cable frame beams are used for reinforcement, with an anchor cable length of 22 m and anchor cable length of 10 m;
The 3rd slope stage	Three prestressed anchor cable frame beams are used for reinforcement, with an anchor cable length of 26 m and anchor cable length of 10 m;
The 4th slope stage	Three prestressed anchor cable frame beams are used for reinforcement, the anchor cable is 28 m long, and the anchor length is 10 m long;
The 5th slope stage	Four anchor bars are used for reinforcement, and the length of the anchor bars is 11.5 m;

the diameter of the anchor cable drilling hole is ϕ150 mm, the design tension of the anchor cable is 500 kN, and the locking tension is 600 kN. The anchorage length is 10m, secondary grouting is adopted, and cement slurry with a strength of M40 is poured. The primary grouting pressure is not less than 0.5~1.0 MPa, and the secondary grouting pressure is not less than 1.5~2.0 MPa. The reinforcement effect is shown in Figure 16.

(3) Others. The cross-section size of the anchor beam is 0.3×0.3 m, and that of the anchor cable frame beam is 0.4×0.4 m. C30 concrete is used for pouring, and each beam is 6 m long. Expansion joints are set between beams during

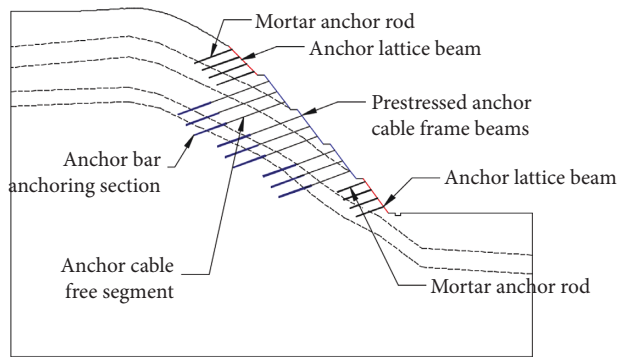

Figure 14: Slope support diagram.

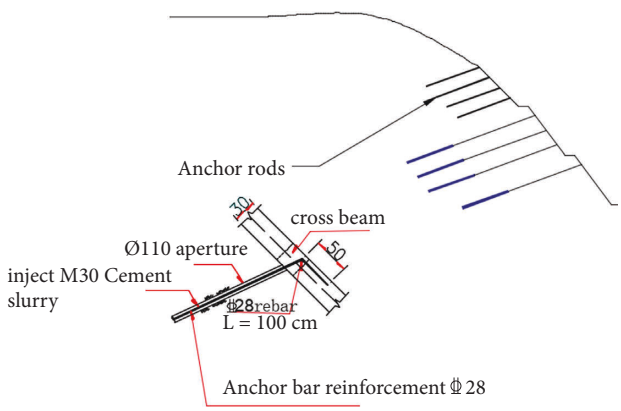

Figure 15: Effect diagram of bolt support.

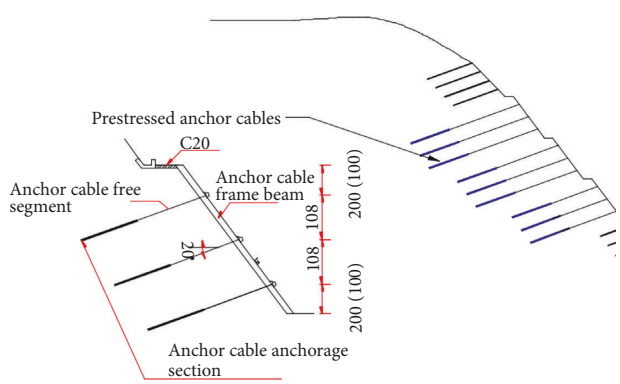

Figure 16: Anchor cable support diagram.

construction. Figure 17 and Figure 18 show the reinforcement effect.

4.2. Application of the Finite Element Method in Slope Reinforcement. The Midas simulation support measures are adopted, and the modified Mohr–Coulomb constitutive model is still adopted for rock and soil. The elastic constitutive model is adopted for the supporting material. The concrete unit type is 1 d slab, the cross-section is a solid rectangle, the anchor rod and anchor cable are 1 d embedded truss, the cross-section is round, and the supporting material attribute parameters are shown in Table 4. An anchor grid beam and an anchor cable frame beam cannot be simulated separately, so they are converted into concrete in the process of numerical simulation.

After grid division, the new model is divided into 11404 units and 11558 nodes, and the whole in-situ stress constraint, dead weight, and prestress are added. Through the anchor modeling assistant, support measures such as anchor rods and anchor cables are added to the model. The angle between the anchor rod and anchor cable and the horizontal

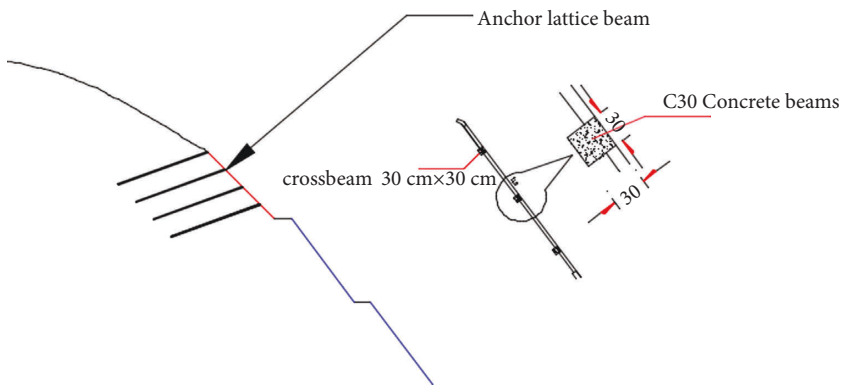

Figure 17: Anchor grid beam support diagram.

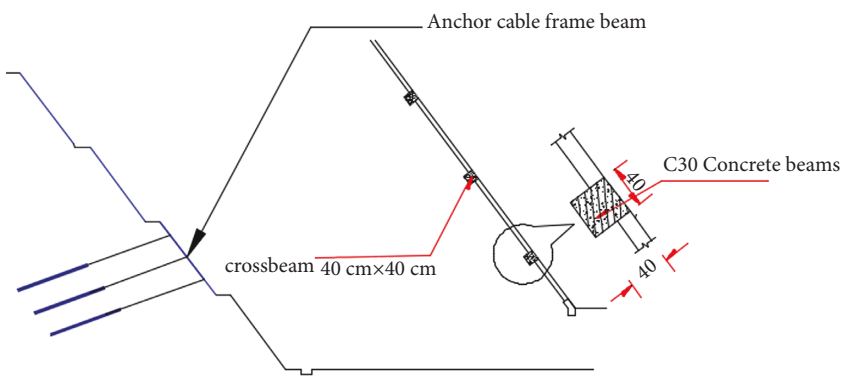

Figure 18: Anchor cable frame beam support diagram.

Table 4: Property parameters of supporting materials.

Material type	Constitutive model	Young's modulus (kN/m^2)	Poisson's ratio	unit weight (kN/m^3)
C30	Elastic	3.0e + 07	0.21	23
C20	Elastic	2.55e + 07	0.2	23
Anchor and anchor cable	Elastic	2.0e + 08	0.3	78

plane is 200°. The grid diagram after support is shown in Figure 19. After the model is established, SRM is used for calculation in the construction stage.

4.3. Stability Analysis of Reinforcement Scheme

4.3.1. Stability Analysis of a Rainless Slope. Numerical simulation based on the SRM principle calculates that the stability safety factor of the slope under support measures is 1.18. Figure 20. The anchoring effect of the slope is obvious; the slip zone almost disappears. As shown in Figure 21, the displacement deformation is reduced to the allowable range, and the landslide deformation is controlled. The maximum displacement deformation is located at the slope shoulder, and the displacement value is 0.034 m.

4.3.2. Analysis of the Influence of Rainfall Stability on Slope. Applying the above boundary conditions related to rainfall to the reinforced model and repeating the above operations, the safety factor of slope stability is calculated to be 1.15.

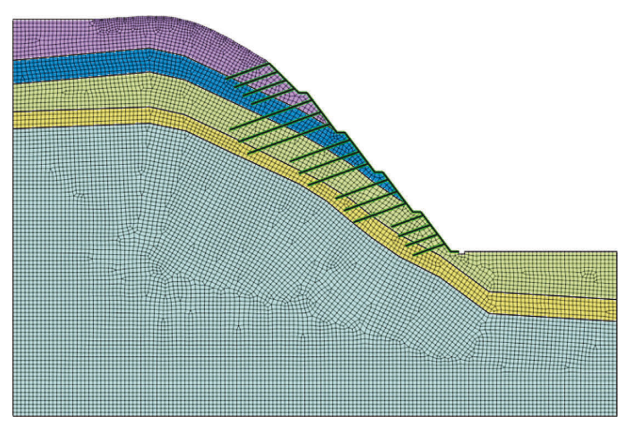

Figure 19: The model after support.

According to the research, it is found that the slope soil is strengthened after support, and the influence of rainfall on the stability of the slope is reduced. After support, the

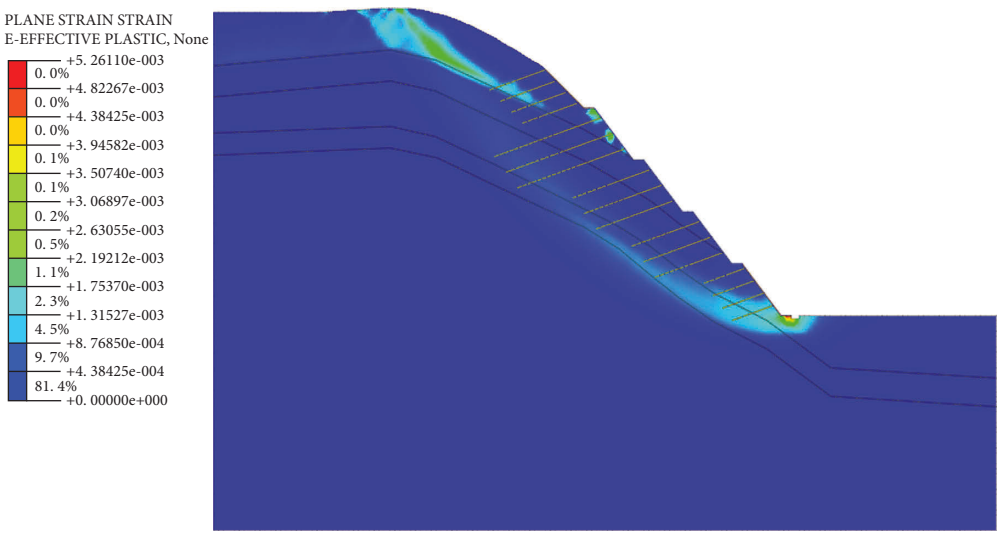

Figure 20: Contour of the effective plastic strain of slope behind support.

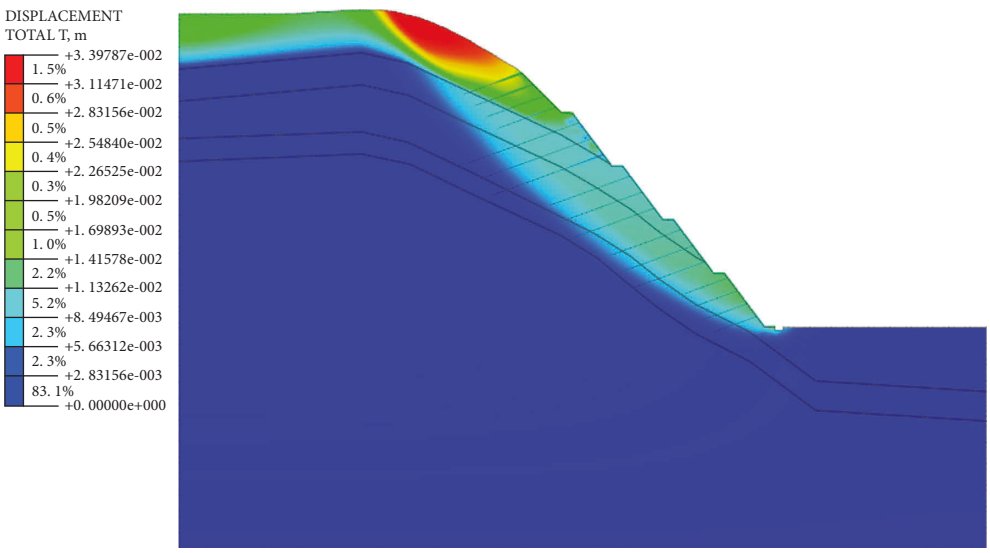

Figure 21: Contour of slope displacement after support.

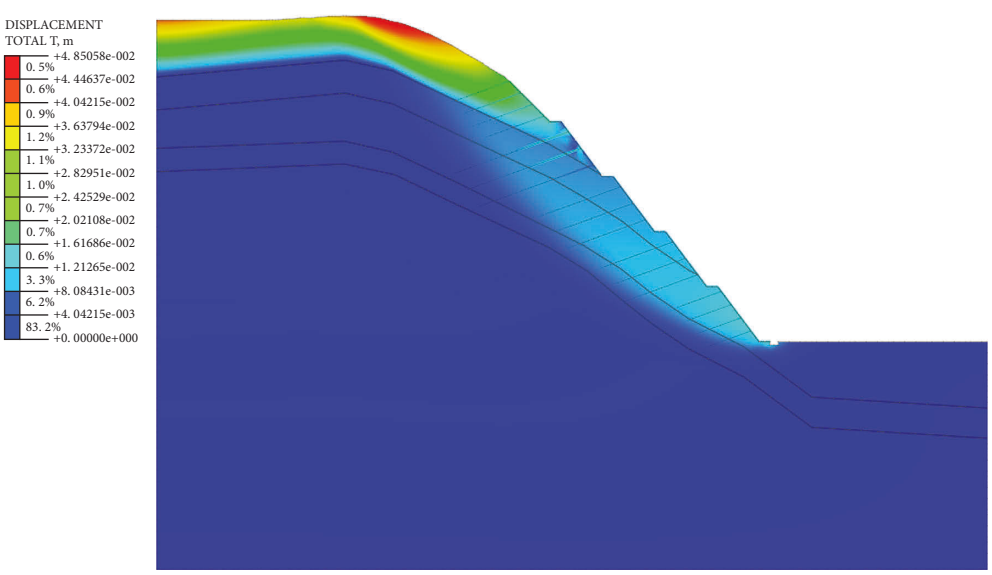

Figure 22: Contour of slope displacement under rainfall condition after support.

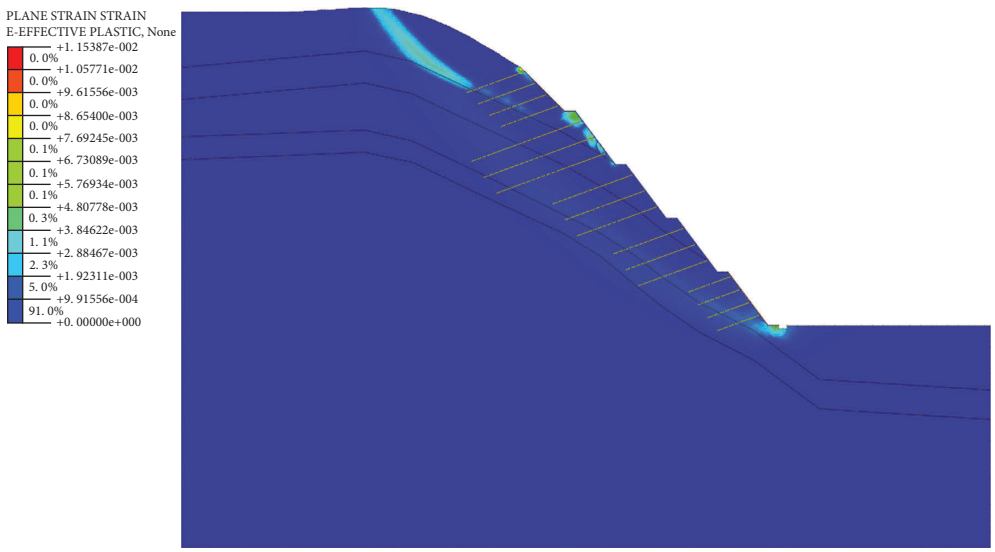

Figure 23: Contour of the effective plastic strain of slope under rainfall condition after support.

maximum displacement of the slope under rainfall conditions is 0.0485 m, which is 78.1% lower than that of the slope without support, which is 0.222 m. Figure 22 provides detailed note. In Figure 23, it can be seen that there is still no slip zone after the slope is reinforced, even under the rainstorm condition, which shows that the reinforcement effect is very ideal.

5. Conclusions

The main conclusions of the thesis are as follows:

(1) The stability safety factor of the slope under natural conditions is 1.05, and the slope is basically stable. After the excavation of the slope, due to the large excavation volume and the large adjustment of the Earth stress after the excavation of the slope body, it is easy to form a large relaxation zone, which leads to the reduction of the stability of the slope, and the stability safety factor is reduced to 0.97, making the whole slope in an unstable state.

(2) The rainstorm conditions have a great influence on the stability of the slope, and the safety factor decreases to 0.95 under the rainstorm conditions after excavation, the slope displacement deformation increases by 98%, the damage to the plastic zone is also deepened, and the maximum plastic strain value increases by 138%. Under these conditions, the plastic area is prone to slope diseases such as collapse and ditching along the structural surface, so it is necessary to strengthen the rainfall slope in time.

(3) With reference to the deformation mechanism, failure characteristics, and geological conditions of the slope, it is proposed to adopt an anchor grid beam and an anchor cable frame beam to reinforce the slope surface.

(4) Through numerical simulation of the reinforced slope, it can be found that the anchorage effect is obvious, the deformation and displacement of the slope are significantly reduced, the slope safety factor is 1.18, and the slope is in a stable state. The safety factor of the slope is 1.15 by simulating the slope under the rainstorm condition after reinforcement. It can be found that even under the rainstorm condition, there is no large deformation, and the slope is still in a stable state.

Data Availability

The data used to support the findings of the study can be obtained from the corresponding author upon request.

Conflicts of Interest

The authors declare that they have no conflicts of interest.

Acknowledgments

This research is sponsored by the doctoral research start-up fund of Hebei GEO University and Hebei University Youth Fund Project (QN202105) and Key Research and Development Projects in Hebei Province (22371701D) and Hebei Province Innovation Ability Promotion Program (21567628H).

References

[1] Z. Li and J. Wang, "Lower bound limit study on plastic limit analysis of rock slope using finite elements based on nonlinear programming," *Chinese Journal of Rock Mechanics and Engineering*, vol. 04, pp. 747–753, 2007.

[2] X. Qiao, "Stability analysis and treatment measures of high slope based on limit equilibrium method," *Railway Engineering*, vol. 57, no. 8, pp. 89–93, 2017.

[3] Y. Wei, L. Jiaxin, L. Zonghong, W. Wei, and S. Xiaoyun, "A strength reduction method based on the Generalized Hoek-Brown (GHB) criterion for rock slope stability analysis," *Computers and Geotechnics*, vol. 117, Article ID 103240, 2020.

[4] H. Wang, B. Zhang, G. Mei, and N. Xu, "A statistics-based discrete element modeling method coupled with the strength reduction method for the stability analysis of jointed rock slopes," *Engineering Geology*, vol. 264, Article ID 105247, 2019.

[5] Y. Yang, G. Sun, H. Zheng, and Y. Qi, "Investigation of the sequential excavation of a soil-rock-mixture slope using the numerical manifold method," *Engineering Geology*, vol. 256, pp. 93–109, 2019.

[6] Z. Nie, Z. Zhang, and H. Zheng, "Slope stability analysis using convergent strength reduction method," *Engineering Analysis with Boundary Elements*, vol. 108, pp. 402–410, 2019.

[7] G. Sun, S. Lin, H. Zheng, Y. Tan, and T. Sui, "The virtual element method strength reduction technique for the stability analysis of stony soil slopes," *Computers and Geotechnics*, vol. 119, Article ID 103349, 2020.

[8] Y. B. Zhou, R. G. Ye, and Y. J. Li, "Targeting the CD134-CD134L interaction using anti-CD134 and/or rhCD134 fusion protein as a possible strategy to prevent lupus nephritis," *Rheumatology International*, vol. 29, no. 4, pp. 417–425, 2008.

[9] G. Chen, R. Huang, Y. Shi, and Q. Xu, "Stability analysis of slope based on dynamic and whole strength reduction methods," *Chinese Journal of Rock Mechanics and Engineering*, vol. 33, no. 02, pp. 243–256, 2014.

[10] P. Su, P. Qiu, B. Liu, W. Chen, and S. Su, "Stability prediction and optimal angle of high slope in open-pit mine based on twodimension limit equilibrium method and three-dimension numerical simulation," *Physics and Chemistry of the Earth*, vol. 127, 2022.

[11] T. Yang, Y. Rao, N. Ma, J. Feng, H. Feng, and H. Wang, "A new method for defining the local factor of safety based on displacement isosurfaces to assess slope stability," *Engineering Geology*, vol. 300, Article ID 106587, 2022.

[12] K. Yang and Y. Zhu, "Soil slope stress state and stability analysis based on unloading effect of slope surfaces," *Engineering Mechanics*, vol. 38, no. 11, pp. 95–104, 2021.

[13] S. Chen, Y. Zhu, Z. Li, L. Huang, and H. Zhang, "Analysis of lateral slope stability during construction of a loess tunnel with a large section," *Modern Tunnelling Technology*, vol. 51, no. 1, pp. 82–89, 2014.

[14] Yu. Zhao, T. Wang, W. Li, and F. Dai, "Stability evaluation and treatment simulation of an expressway landslide," *Chinese Journal of Rock Mechanics and Engineering*, vol. 27, no. 11, pp. 2340–2346, 2008.

[15] Q. Xu, D. Zhang, and G. Zheng, "Failure mode and stability analysis of leet bank abutment high slope at Jinping I hydropower station," *Chinese Journal of Rock Mechanics and Engineering*, vol. 28, no. 6, pp. 1183–1192, 2009.

[16] X. Song and Y. Tan, "Experimental study on failure of temporary earthen slope triggered by intense rainfall," *Engineering Failure Analysis*, vol. 116, pp. 104718–104812, 2020.

[17] C. Sun, A. Li, and H. Zhang, "Numerical simulation on slope stability under rainfall infiltration," *Port Engineering Technology*, vol. 50, no. 4, pp. 67–70, 2013.

[18] J. Tian, L. Han, X. Jin, L. Xu, X. Wang, and Y. Dong, "Effect of rainfall on slope stability of Picea crassifolia forest based on finite element method in Qinghai," *Science of Soil and Water Conservation*, vol. 17, no. 6, pp. 11–18, 2019.

[19] B. Bai, Y. Wang, D. Y. Rao, and F. Bai, "The effective thermal conductivity of unsaturated porous media deduced by pore-scale SPH simulation," *Frontiers of Earth Science*, vol. 10, 2022.

[20] B. Bai, R. Zhou, G. Q. Cai, W. Hu, and G. C. Yang, "Coupled thermo-hydro-mechanical mechanism in view of the soil particle rearrangement of granular thermodynamics," *Computers and Geotechnics*, vol. 137, no. 8, Article ID 104272, 2021.

[21] B. Bai, G. C. Yang, T. Li, and G. S. Yang, "A thermodynamic constitutive model with temperature effect based on particle rearrangement for geomaterials," *Mechanics of Materials*, vol. 139, Article ID 103180, 2019.

[22] L. Chen and X. Jin, "Study on the applicability of three criteria for slope instability using finite element strength reduction method," *China Civil Engineering Journal*, vol. 45, no. 9, pp. 136–146, 2012.

[23] S. Zhao, Y. Zheng, and Y. Zhang, "Study on slope failure criterion in strength reduction finite element method," *Rock and Soil Mechanics*, vol. 26, no. 2, pp. 332–336, 2005.

Hindawi
Advances in Civil Engineering
Volume 2022, Article ID 7796204, 18 pages
https://doi.org/10.1155/2022/7796204

Research Article

Reduction of Vibrations in Long-Span Continuous Girder Bridges with Pounding Tuned Mass Dampers

Juncheng Yao,[1,2] Hekuan Zhou,[3] Jiahua Zhu,[4] Liang Huang,[1] Jianguo Xu,[1] and Weiguo Li[3]

[1]*School of Water Conservancy and Civil Engineering, Zhengzhou University, Zhengzhou 450001, China*
[2]*CCCC Second Highway Consultants Co., Ltd., Wuhan 430056, China*
[3]*Highway Engineering Bureau Group Co., Ltd. of Henan Province, Zhengzhou 450052, China*
[4]*CCCC Infrastructure Maintenance Group Co., Ltd., Guangzhou Branch, Guangzhou 510220, China*

Correspondence should be addressed to Liang Huang; zzuhuangliang@163.com

Received 12 July 2022; Accepted 3 September 2022; Published 3 October 2022

Academic Editor: Chao Zou

Earthquakes often cause bridges to vibrate to different degrees; moreover, in the case of poor road conditions, the vibration amplitude of bridges caused by vehicles often exceeds a reasonable range, thus causing different degrees of damage to bridges. Therefore, this article studies the vibration reduction effect of the pounding tuned mass dampers (PTMD) on long-span continuous bridges under earthquake and vehicle loads. The PTMD used in this study can reduce the vibration in both lateral and vertical directions. The PTMD provides a stronger vibration dampening effect compared to the TMD since it increases collision to use energy. The LS-DYNA software is used for numerical modeling to optimize the parameters of the PTMD and to determine the size and installation position of the PTMD. Then, the bridge is subjected to two recorded ground motions, and the bridge response with and without the PTMD is compared and analyzed, which shows how PTMD might lessen bridge vibration in its transverse direction. To assess how efficiently the PTMD dampens vibrations induced by vehicle loads on bridges, a vehicle/bridge/PTMD system is simulated using a refined vehicle model. The findings demonstrate that the PTMD may significantly lessen the bridge's lateral and vertical vibration while enhancing driving comfort. Thus, this research study is of great significance for vertical and lateral vibration control of long-span continuous girder bridges.

1. Introduction

The bridge structure is an important part of the uninterrupted operation lifeline. At present, there are many existing bridges that mainly consider gravity load and vehicle load in the design, so they are not enough to withstand earthquakes. In previous reports, earthquakes often caused different degrees of damage to bridge structures, so bridge seismic research has been continuously developed [1–4]. As a result, lowering the bridge's seismic response is critical. In the case of poor road conditions, the amplitude of bridge vibration caused by vehicle driving often exceeds a reasonable range. Vehicle weight, speed, and the state of the road's surface all have an impact on how much the bridge vibrates [5–8]. This study's findings indicate that when the road is uneven and the car is heavy, the vibration created by the vehicle on the bridge will frequently be more intense than is appropriate. Therefore, it is necessary to use dampers to control bridge vibration.

Many academics have studied the vibration of structures in-depth [9, 10]. Studying the impact of subway trains on tunnel vibration was performed by Ma et al. [11]. From a theoretical perspective, Xu and Ma investigated the dynamic response of a multilayer half-space under spatial periodic harmonic stresses [12]. A novel impedance model was suggested by Zou et al. to investigate how subway vibration affects nearby structures [13]. Wu et al. presented the "Kriging model + swarm intelligence updating technique" for the finite element model of complex bridges and applied it to the finite element model of complex bridges [14]. Seismic isolation technology is an effective damping measure. Numerous computer calculations and experimental tests have verified the damping effect of seismic isolation technology [9, 10]. Seismic isolation technology usually uses

flexible supports to isolate the upper structure from its foundation, when seismic excitations propagate upward from the foundation, the energy is greatly weakened. Another common control method for reducing bridge vibration is TMD [15]. Many scholars have conducted various optimization studies on TMD according to the actual situation. TMD is widely used in bridge structure vibration reduction [16].

TMD is a passive control device, usually installed in the most responsive position of the structure. If the TMD is constructed properly, it may efficiently absorb energy and lessen the displacement of the bridge when the fundamental frequencies of the TMD and the bridge coincide [17]. Rana and Soong studied the characteristics of TMD parameters and proposed the application of TMD in a multidegree of freedom structures [18]. However, the energy dissipation capability of TMD has certain limitations, and the vibration frequency range of TMD is relatively small. Although TMD was applied to vibration reduction of various engineering structures decades ago, various optimization designs of TMD are still very active [19–31]. In order to further reduce structural vibration, many improved TMDs have been proposed, such as unconventional TMD, granular TMD, and eddy current TMD [32–35].

Recently, Yin et al. used pounding tuned mass dampers (PTMD) to suppress bridge vibration caused by vehicle motion [36]. PTMD is mainly composed of two parts: moving mass and delimiter. The L-shaped steel beam is connected with the mass block and passes through the inner surface of the delimiter. Furthermore, a layer of viscoelastic material is attached to the inner surface of the delimiter. The L-shaped steel beam collides with the viscoelastic material when the structure vibrates, dissipating structural kinetic energy.

Therefore, compared with conventional TMD, PTMD increases energy consumption through collision and therefore has a better vibration control effect. In addition, PTMD can also improve the robustness of the system [37–40]. Because PTMD has a good effect on reducing vibration and is easy to install and maintain, it is often used for vibration reduction in various engineering structures [35–38, 40–44]. Many scholars have applied PTMD in the field of bridge vibration reduction.

Wang et al. studied the damping effects of multiple PTMDs on bridge structures, mainly considering the combined effects of vehicle loads and wind loads [39]. Li et al. proposed single-sided PTMD (SS-PTMD) and further optimized various design parameters. Experiments and computer simulations show that the SS-PTMD can greatly minimize the bridge deck's vortex-induced vibration [40]. Zhang et al. proposed an asymmetric PTMD. The response of cable-stayed bridges under various seismic excitations has been comparatively studied. APTMD has a perfect vibration damping effect [45]. However, there are not many studies on PTMD in suppressing the vibration of continuous beam bridges.

According to [36, 41, 42, 44], this study uses PTMD technology to lessen the lateral and vertical vibration of a long-span continuous girder bridge. This research focuses on the use of PTMD to reduce vibration on bridges subjected to earthquakes and moving vehicle loads. First, the main design parameters of PTMD are optimized. Secondly, two recorded ground motions from the El-Centro and Taft earthquakes are applied laterally to the bridge system with or without PTMD. The impact of the PTMD vibration reduction is then confirmed by comparing and analyzing the dynamic response data. Finally, based on the refined vehicle model, a refined numerical simulation of the bridge-vehicle-PTMD system is carried out. Subsequently, it is assessed how PTMD will impact driving comfort and how much of the system's vertical vibration will be reduced. The research in this study is of great significance for vertical and lateral vibration control of long-span continuous girder bridges. In addition, a refined vehicle model is used in this study, which further improves the accuracy of vehicle-induced bridge vibration studies.

2. Modeling and Basic Theory

2.1. Pounding Tuned Mass Dampers. Figure 1 depicts the composition of the PTMD, which also includes a moving mass, an L-shaped steel beam, and a viscoelastic delimiter. A layer of viscoelastic material is attached to the inner surface of the delimiter. The L-shaped steel beam and mass block are consolidated. The L-shaped steel beam will flex somewhat and will crash onto the inner surface of the delimiter when the structure shakes, thereby dissipating energy and reducing structural vibration [42, 44]. There is an opening inside the delimiter, and a viscoelastic material is attached to the opening of the delimiter. The delimiter is fixed to the main structure. PTMD can reduce the dynamic response in both the vertical direction and the radial direction of the delimiter because the L-shaped rod can only bend in these two directions.

2.2. The Nonlinear Pounding Force Model. When the structure vibrates, the PTMD will run into the limitation. So, it is important to construct a matching numerical model of the collision force in the cause of examining the interaction between the PTMD and the bridge structure. The nonlinear model used in this work combines the Hert contact element and the damper, which has been proved to be one of the most suitable models in previous studies [42].

$$F = \begin{cases} \beta\delta^{3/2} + c\dot{\delta}, \dot{\delta} > 0, \\ \beta\delta^{3/2}, \dot{\delta} < 0, \end{cases} \tag{1}$$

$$\delta = \begin{cases} x_1 - x_2 - g_p, x_1 - x_2 > g_p, \\ \left|x_1 - x_2 - g_p\right|, x_1 - x_2 < -g_p, \\ 0, otherwise, \end{cases} \tag{2}$$

$$\dot{\delta} = \dot{x}_1 - \dot{x}_2,$$
$$c = 2\xi\sqrt{\beta\delta^{1/2}\frac{m_1 m_2}{m_1 + m_2}}. \tag{3}$$

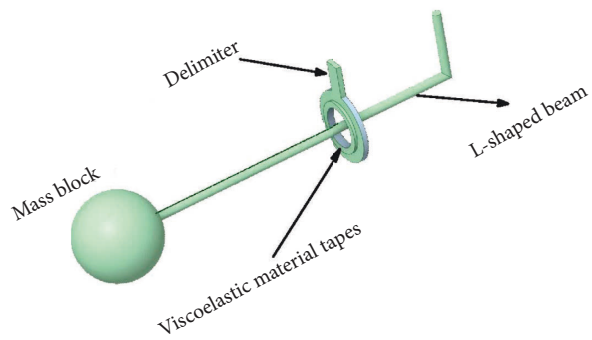

Figure 1: Components of a PTMD system.

The collision force can be obtained from equation (1). c = the pounding damping, c can be obtained from equation (3). Here, δ = the viscoelastic material's deformation; $\dot{\delta}$ = the velocity of deformation; β = pounding stiffness coefficient; x_1 = displacements of the L-shaped steel beam; $\dot{x}_1$ = velocity of the L-shaped steel beam; x_2 = displacements of the delimiter; and $\dot{x}_2$ = velocity of the delimiter and g_p = distance between them.

$$u = \sqrt{\frac{h_1}{h_0}}, \tag{4}$$

where u = the restitution coefficient, which is related to the properties of viscoelastic materials. It can be calculated from experimental data. By freely dropping the ball towards the viscoelastic material, h_0 = the initial height and h_1 = rebound height, e can be calculated using equation (4).

2.3. Motion Equation of Bridge Structure Using PTMD under Earthquake Action.

$$[m_b]\{\ddot{x}_b\} + [c_p]\{\dot{x}_b\} + [k_b]\{x_b\} = -[m_b]\ddot{x}_g + \{F_p\}, \tag{5}$$

$$\begin{aligned} &\cdot \begin{pmatrix} m_b & \\ & m_p \end{pmatrix} \begin{Bmatrix} \ddot{x}_b \\ \ddot{x}_p \end{Bmatrix} + \begin{pmatrix} c_p & 0 \\ 0 & 0 \end{pmatrix} \begin{Bmatrix} \dot{x}_b \\ \dot{x}_p \end{Bmatrix} \\ &+ \begin{pmatrix} k_b + k_p & -k_p \\ -k_p & k_p \end{pmatrix} \begin{Bmatrix} x_b \\ x_p \end{Bmatrix} \\ &= -\begin{pmatrix} m_b & \\ & m_p \end{pmatrix} \begin{Bmatrix} 1 \\ 1 \end{Bmatrix} \ddot{x}_g + \begin{pmatrix} 1 \\ -1 \end{pmatrix} F_p. \end{aligned} \tag{6}$$

The structural diagram of using PTMD to control bridge vibration is shown in Figure 2. According to the collision force model in Section 2.2, equation (5) is the motion equation of bridge structure with PTMD under earthquake. The bridge structure and PTMD motion equation are shown in equation (6), where m = mass, c = damping, and k = stiffness and x = the displacement, $\dot{x}$ = velocity, and $\ddot{x}$ = the acceleration. Subscript "b" represents the bridge and "p" represents the PTMD. In equations (5) and (6), $\ddot{x}_g$ is the acceleration response caused by the earthquake and F_p is the collision force, which can be obtained by using equation (1).

2.4. Motion Equation of Bridge with PTMD under Vehicle Load

$$[m_b]\{\ddot{x}_b\} + [c_p]\{\dot{x}_b\} + [k_b]\{x_b\} = \{F_b + F_{b-p}\}, \tag{7}$$

$$[m_v]\{\ddot{x}_v\} + [c_v]\{\dot{x}_v\} + [k_v]\{x_v\} = \{F_G\} + \{F_{v-b}\}. \tag{8}$$

Equations (7) and (8) are matrices that provide the equations of motion for bridges and automobiles, respectively, where $[m]$ = mass matrice, $[c]$ = damping matrice, $[k]$ = stiffness matrice, $\{x\}$ = displacement, $\{\dot{x}\}$ = velocity, and $\{\ddot{x}\}$ = acceleration. The subscript "b" stands for the bridge and "v" stands for the vehicle. F = force, the subscript "b" denotes the external force acting on the bridge structure. "G" represents gravity, "$b-p$" represents the force generated by PTMD on the bridge, and "$v-p$" represents the vehicle-bridge interaction force.

$$m_p\ddot{x}_{pv}(t) + c_{pv}\dot{x}_{pv}(t) + k_{pv}x_{pv}(t) = -F^{v}_{p-b}(t) - HF^{vp}_{p-b}(t), \tag{9}$$

$$m_p\ddot{x}_{pl}(t) + c_{pl}\dot{x}_{pl}(t) + k_{pl}x_{pl}(t) = -F^{l}_{p-b}(t) - HF^{lp}_{p-b}(t), \tag{10}$$

$$m_p\{\ddot{X}_p\} + [c_p]\{\dot{X}_p\} + [K_p]\{X_p\} = \{F_{p-b}\} + RT\{F^{p}_{p-b}\}. \tag{11}$$

Equations (9)–(11) represent the equations of motion for the PTMD-bridge interaction [36], where m = mass, c = damping, and k = stiffness. The subscript "p" stands for PTMD, "v" stands for the vertical direction, and "l" stands for lateral direction. $F_{\mathrm{p-b}}(t)$ = force of interaction between PTMD and bridge and $F^{p}_{\mathrm{p-b}}$ = pounding forces. Superscript "l" stands for the lateral direction and "v" stands for the vertical direction. $F^{p}_{\mathrm{p-b}}$ can be computed by using equation (1), R = direction of the pounding force, and T = location of the pounding forces.

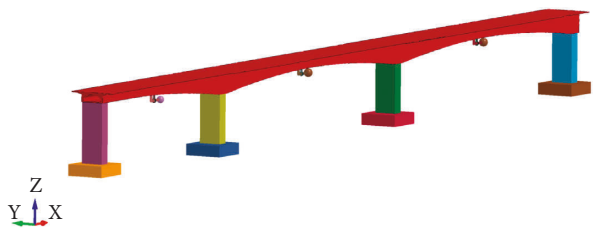

Figure 2: bridge model with PTMD.

$$\begin{pmatrix} m_b & & \\ & m_p & \\ & & m_v \end{pmatrix} \left\{ \ddot{X}_b \, \ddot{X}_p \ddot{X}_v \right\} + \begin{pmatrix} C_b + C_b^v + C_b^p & C_{b-p} & C_{b-v} \\ C_{p-b} & C_p + C_{p-p} & 0 \\ C_{v-b} & 0 & C_v \end{pmatrix} \begin{Bmatrix} \dot{X}_b \\ \dot{X}_p \\ \dot{X}_v \end{Bmatrix} + \begin{pmatrix} K_b + K_b^v + K_b^p & K_{b-p} & K_{b-v} \\ K_{p-b} & K_p + K_{p-p} & 0 \\ K_{v-b} & 0 & K_v \end{pmatrix} \begin{Bmatrix} X_b \\ X_p \\ X_v \end{Bmatrix} = \begin{Bmatrix} F_{b-r} + F_{b-p} \\ F_{p-b} + RTF_{p-b}^p \\ -F_{v-r} + F_G \end{Bmatrix}. \tag{12}$$

Through the aforementioned analysis, combined with the vehicle-bridge motion equation, equation (12) illustrates the PTMD-vehicle-bridge system's equation of motion [36, 46], where m = mass, c = damping, and k = stiffness; subscripts "b," "p," and "v" denote the bridge, PTMD, and vehicles, respectively; superscripts "p" and "v" represent contributions from PTMD and vehicles, respectively; subscripts "$b-v$" and "$v-b$" denote the vehicle-bridge interaction. F_{b-r} = the force formed by the uneven road surface on the bridge structure; F_{v-r} = the force formed by the uneven road surface on the vehicles; and F_G = the gravity of the vehicle.

3. The Numerical Analysis Model

3.1. Bridge Prototype. The prototype bridge (Figure 3) is a three-span continuous structure with an effective span of 120 m + 120 m + 80 m. The upper structure is composed of a variable cross-section prestressed concrete box girder. A cross-sectional view of the bridge midspan and the top of the pier is shown in Figure 4. The piers are hollow box piers.

The bridge's midspan exhibits the most displacement along the direction of seismic excitations movement. Therefore, the positions of these three PTMDs are all placed in the middle of the three spans.

3.2. Bridge's Multiscale Finite Element Model. Figure 5 illustrates the numerical model created with LS-DYNA, which shows the numerical calculation model of the prototype bridge and each component. The entire structure is divided into bridge piers, caps, concrete box girder, and PTMD, Figures 5(a)–5(c) represent the bridge deck, piers, caps, and PTMD, respectively. The concrete box girder is made up of solid elements; the bridge piers and caps adopt beam elements, the PTMD limiter and mass block adopt solid elements, and the L-shaped steel beam adopts beam elements. There are 94,830 solid elements and 341 beam elements in the total model. Among them, the concrete box girder has 89380 units, the bridge piers and caps have 226 units, and the PTMD has 5565 units. The boundary conditions are set as follows. The bottom surfaces of caps are consolidated, and horizontal and vertical constraints are added at the connections between the bridge's upper structure and the piers. Moreover, the nodes at the junctions of the piers and the caps adopt consolidation constraints. One end of the L-shaped steel beam is connected with the mass block and the other end is consolidated with the bridge superstructure.

C 55 concrete is used for variable section box girders; the bridge piers and caps are made of C 40 concrete. Both the limiter of the PTMD and L-shaped rod are made out of steel, and the limiter is attached with viscoelastic material. The material parameters of C 40 concrete are the following: $E_1 = 32500$ MPa, $\mu_1 = 0.2$, $G_1 = 13000$ MPa, $f_{c1} = 18.4$ MPa, and $f_{t1} = 1.65$ MPa; and the material parameters of C50 concrete include the following: $E_2 = 32500$ MPa, $\mu_2 = 0.2$, $G_2 = 13000$ MPa, $f_{c2} = 18.4$ MPa, and $f_{t2} = 1.65$ MPa. PTMD is composed of steel and viscoelastic material, their main parameters are $\rho_1 = 7850\,\text{kg/m}^3$, $E_1 = 200000$ MPa, $\mu_1 = 0.3$, $\rho_2 = 1150\,\text{kg/m}^3$, $E_2 = 2000$ MPa, and $G = 0.6$ MPa, respectively. Among them, E = the elastic modulus, μ = Poisson's ratio, G = the shear modulus, ρ = density, f_c = concrete compressive strength, and f_t = the tensile strength of concrete.

3.3. Vehicles' Finite Element Model. This study uses Ford's simplified model (21724 elements) single-unit truck (SUT) (Figure 6) as the vehicle load. The truck model can be downloaded from the NCAC website. The accuracy of each model is verified through frontal collision experiments [37]. Both models highly correlated with experimental results. The entire vehicle modulus consists of 21,724 elements, including 123 beam elements, 20,109 shell elements, and 1,492 solid elements.

3.4. Modal Analysis of the Bridges. Using the finite element model in 3.2 for modal analysis, the first two-order frequencies and mode shape descriptions of the bridge are shown in Table 1, and the formation diagram is shown in Figure 7.

The bridge's lateral angular frequency in the absence of a control is $\omega_1 = 12.3$ rad/s and $\omega_2 = 22.3$ rad/s. In addition, $\xi = 0.05$, when the values are substituted in Rayleigh's formula, it produces the following results $a = 0.79$ and $b = 0.003$, and with PTMD installed, we get $a = 0.64$ and $b = 0.004$. Similar to this, the bridge's vertical calculation results are the following: without any control, $a = 0.57$ and $b = 0.004$; and with PTMD installed, $a = 0.48$ and $b = 0.005$. The numerical computations that follow will make use of the results.

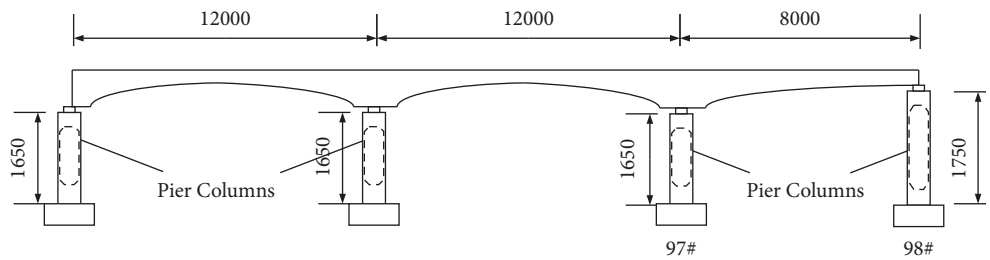

Figure 3: Elevation of a three-span continuous bridge (unit: cm).

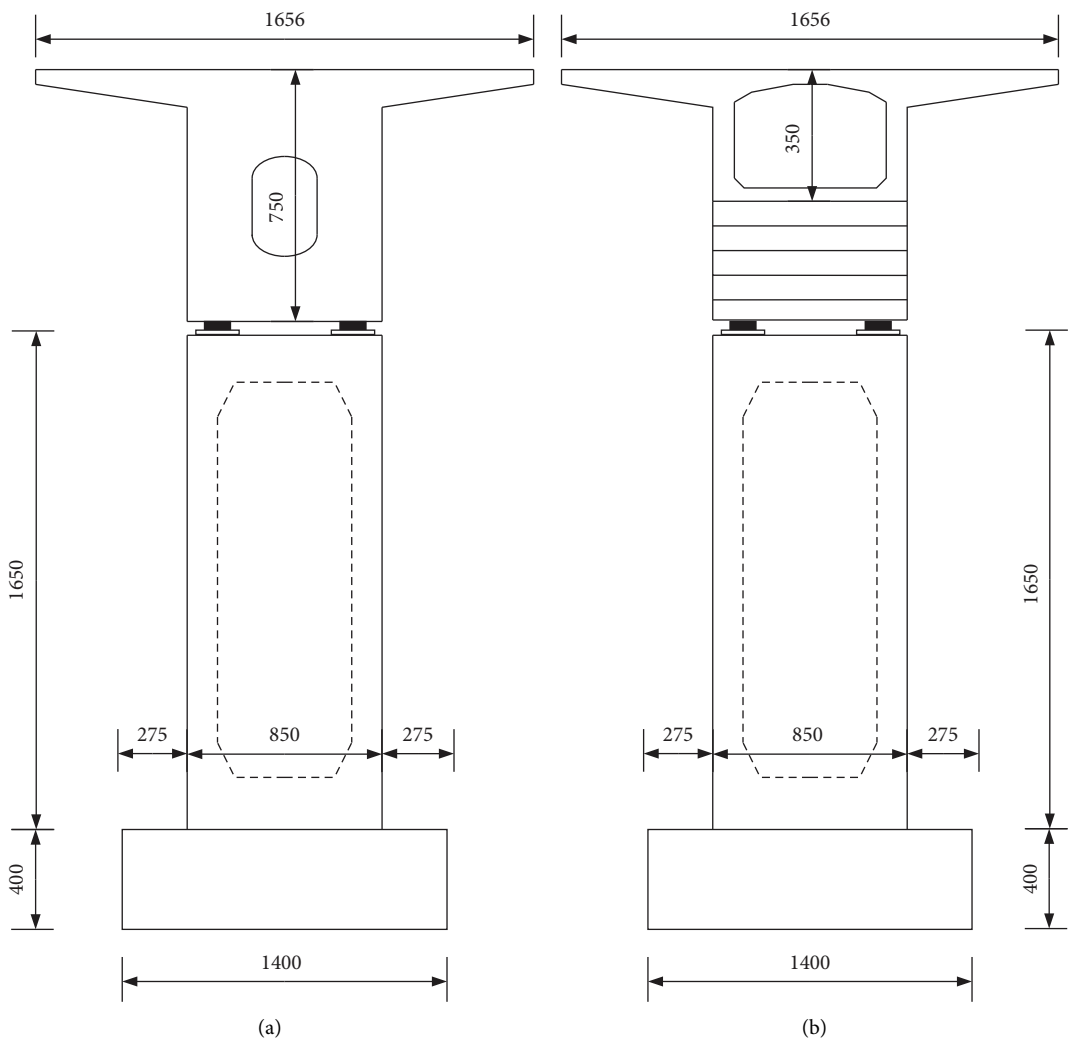

Figure 4: Transverse views of the bridge (unit: cm): (a) cross-section of the top of the pier and (b) cross-section at the midpoint of the span.

4. Optimization of PTMD Parameters

The bridge's location is relatively weak in seismic activity and the site category is Category III. The record from the El-Centro earthquake (suitable for Category II and III sites) is selected as the seismic excitation. Figure 8 depicts t as the acceleration time histories of the record from El-Centro, with a hight of 0.4 g.

4.1. Initial Determination of PTMD Parameters. Figure 9 shows the various parameters of PTMD and Table 2 lists their precise values. The parameters of PTMD affect the vibration reduction effect of PTMD so that it can be optimized for the main parameters.

Where g_p = the collision gap.

$$\lambda = \frac{L_1}{L}, \tag{13}$$

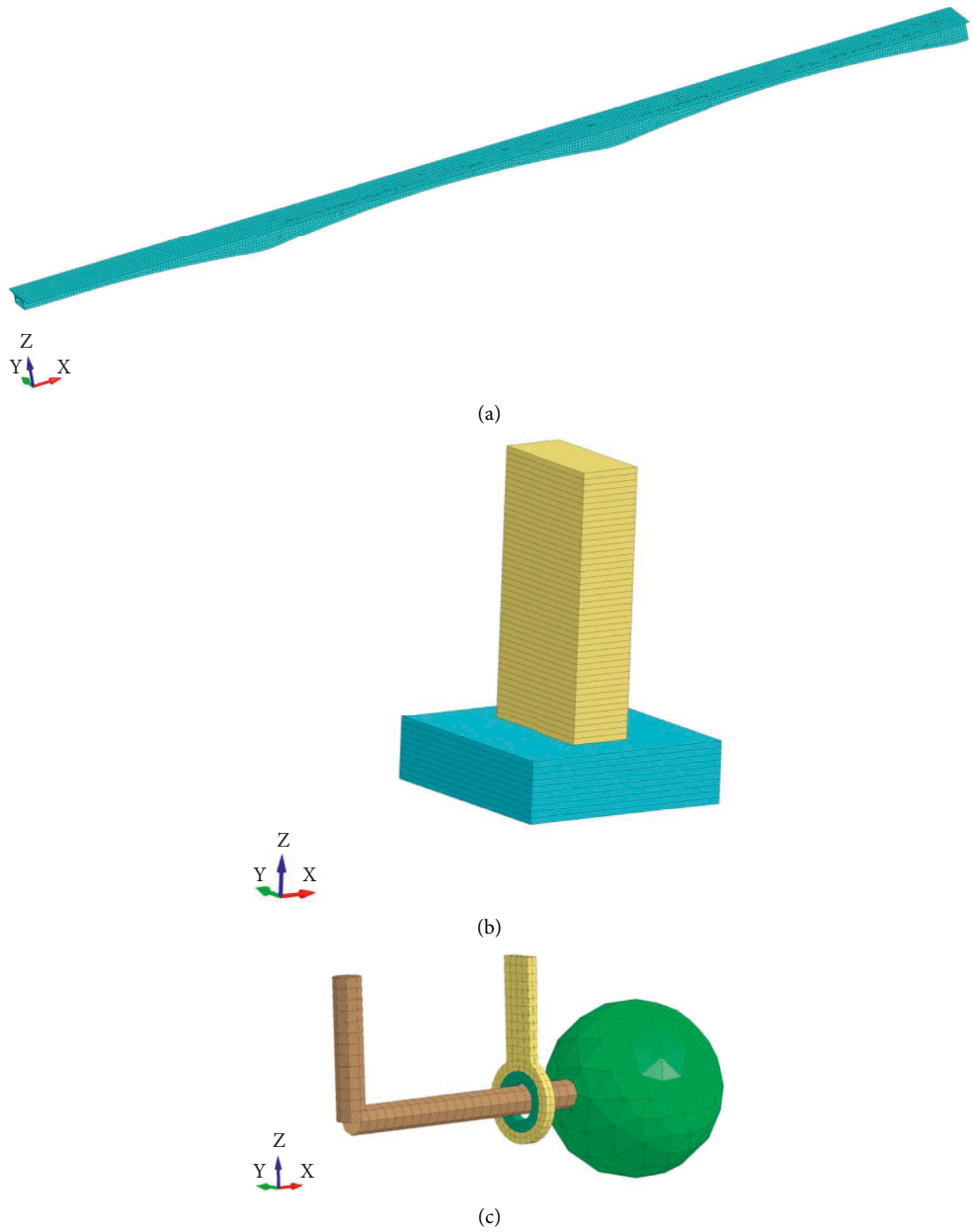

Figure 5: The finite element model of the bridge: (a) main beam, (b) pier columns and caps, and (c) PTMDs.

where λ = length ratio.

$$g_p = R_1 - R_4, \tag{14}$$

The mass ratio u is defined by

$$u = \frac{m}{M_b}, \tag{15}$$

where u = mass ratio, m = the mass block's mass, and M_b = the mass of the superstructure of the bridge span where the PTMD is located. We use the damping rate to evaluate the damping effect of the damper.

$$\mu = \frac{D - D_C}{D} \times 100\%. \tag{16}$$

In the formula, D represents the displacement peak without PTMD, D_C represents the displacement peak value of the PTMD damping device installed, and μ represents the damping rate.

4.2. The Effect of Length Ratio. λ is an important parameter of PTMD, which determines the installation position of the L-shaped steel beam and also affects the vibration reduction effect of PTMD. The length ratio of 0.2–0.7 is selected for optimal design, and Figure 10 displays the vibration reduction rate's fluctuation curve with λ. When the length ratio of the three spans is 0.6, the vibration reduction rate is the highest. The vibration reduction rate of the 80-meter side

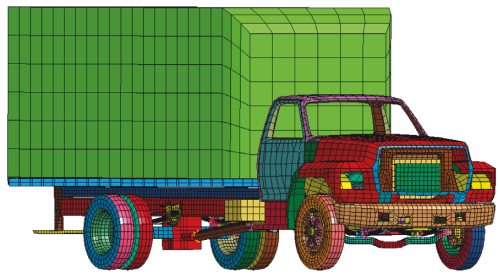

Figure 6: The finite element model of the truck.

Table 1: The first two modal analysis results of the bridge.

Mode shape	Frequency, f (Hz)		Angular frequency, ω (rad/s)		Period (s)	
	Uncontrolled	With PTMD	Uncontrolled	With PTMD	Uncontrolled	With PTMD
First-order cross bend	1.96	1.65	12.3	10.4	0.5	0.6
Second-order cross bend	3.55	2.69	22.3	16.9	0.3	0.4
First-order vertical bend	1.69	1.35	10.6	8.5	0.6	0.7
Second-order vertical bend	1.93	1.75	12.1	11.0	0.5	0.6

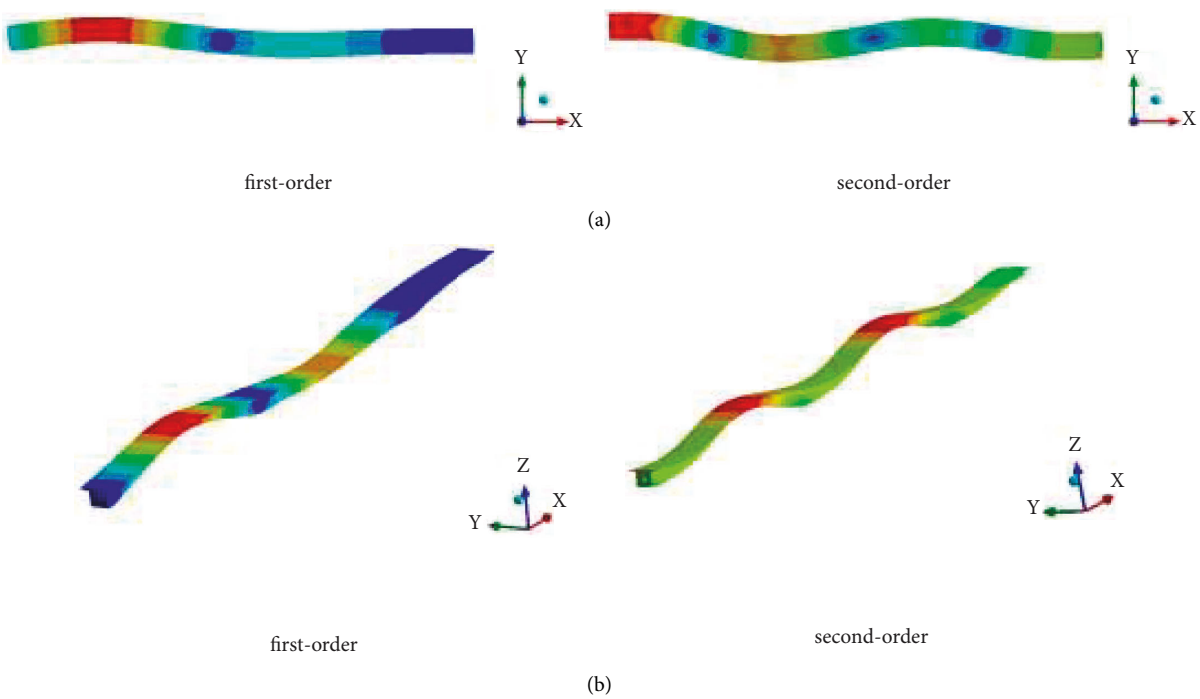

Figure 7: Bridge mode shapes: (a) lateral: X direction; and (b) vertical: Z direction.

span, the 120-meter midspan, and the 120-meter side span reaches 15.1%, 44.6%, and 28.5%, respectively.

4.3. Length Ratio Impact. The vertical length is an important parameter of PTMD. The vertical length of 2 meters, 2.5 meters, and 3.5 meters was selected for comparative analysis. The length ratio λ is 0.6, and other parameters of PTMD are still the same as shown in Table 2. The vibration reduction rate is best when H_1 is 2 meters, as shown in Table 3 and Figure 11. This is because, the shorter the vertical length, the closer the collision site is to the main beam, and the more noticeable is the reduction in the dynamic response to the bridge structure.

Among them, when the vertical length is 2.5 meters, the shock absorption effect of PTMD is not much different from that of 2 meters. Simultaneously, a vertical length of 2.5 m is chosen to prevent PTMD's vertical vibration from colliding with the bridge's superstructure. In the actual project, the value of H_1 should be comprehensively considered according to the installation space and the vibration amplitude.

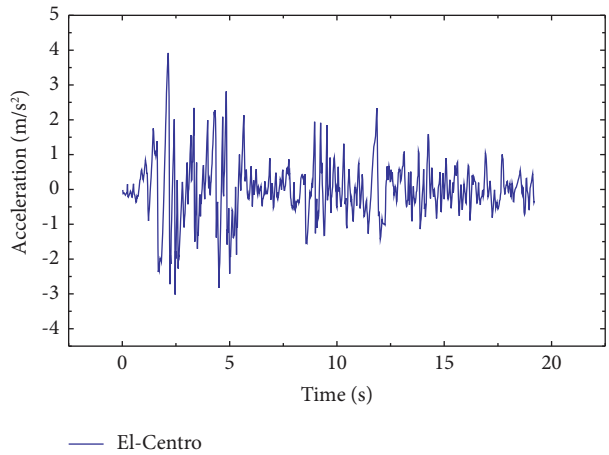

Figure 8: Acceleration time histories of the record from the El-Centro earthquake.

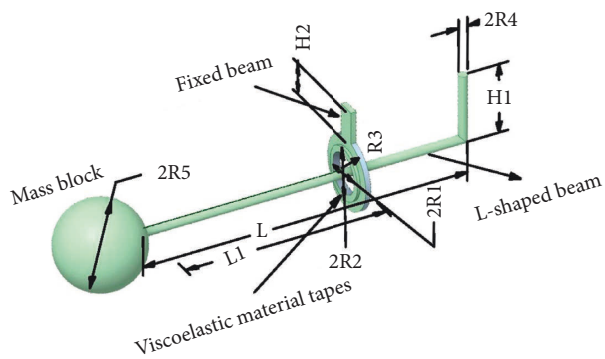

Figure 9: A schematic diagram of PTMD parameters.

Table 2: Parameters of PTMD.

Span (m)	The mass ratio (%)	Quality (t)	H_1 (m)	L (m)	R_1 (cm)	R_2 (cm)	R_3 (cm)	R_4 (cm)
120	2	121.2	2.5	5	33	53	73	25
80	2	67.8	2.5	5	33	53	73	25

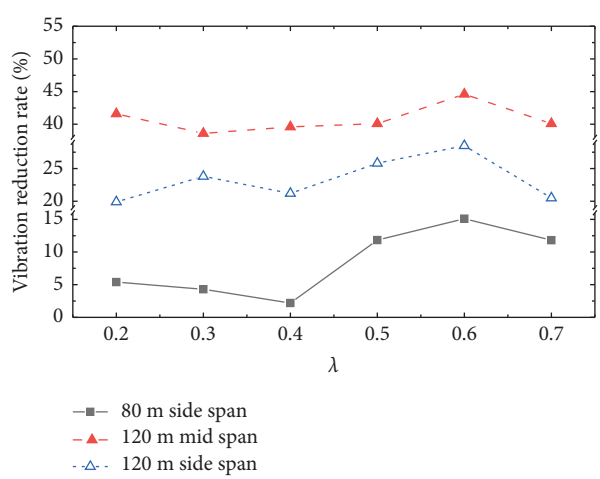

Figure 10: Vibration reduction ratios with various length ratios.

Table 3: Dynamic responses of bridges with different PTMDs.

Span (m)	H1 (m)	Displacement (m)	Displacement of uncontrolled bridges (mm)	Vibration reduction rate
80	2	78	93	16.1
	2.5	80	93	14.0
	3.5	83	93	10.8
120 (midspan)	2	110	202	45.6
	2.5	112	202	44.6
	3.5	120	202	40.6
120 (side span)	2	112	151	25.8
	2.5	112	151	25.8
	3.5	116	151	23.2

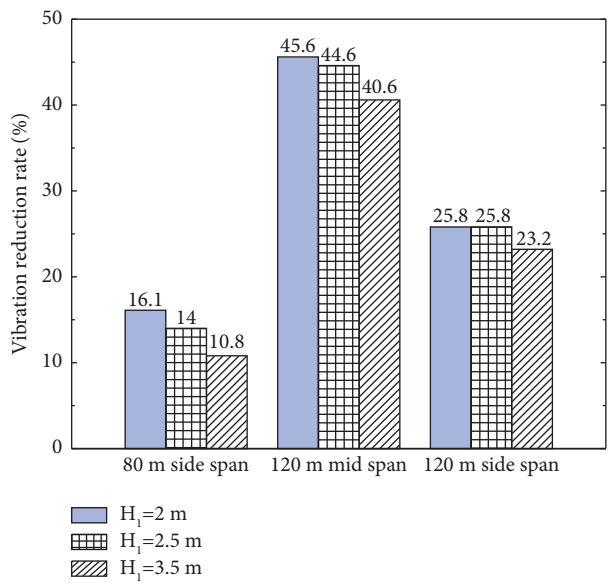

Figure 11: A parametric study of vertical length on the vibration reduction rate.

Table 4: Parameters of PTMD with different collision gaps.

Span (m)	U (%)	m (t)	H_1 (m)	L (m)	R_1 (cm)	R_2 (cm)	R_3 (cm)	R_4 (cm)	g_p (cm)
120	2	121.2	2.5	5	31	51	71	25	6
					33	53	73	25	8
					35	55	75	25	10
					37	57	77	25	12
80	2	67.8	2.5	5	31	51	71	25	6
					33	53	73	25	8
					35	55	75	25	10
					37	57	77	25	12

Table 5: Comparison of PTMD vibration reduction effects under different collision gaps.

Span (m)	Collision gap (cm)	Displacement peak (mm)	The vibration reduction rate (%)	Speed peak	The vibration reduction rate (%)
80	No control	93	—	0.85	—
	6	80	14.0	0.61	28.2
	8	79	15.1	0.61	28.2
	10	79	15.1	0.6	29.4
	12	82	11.8	0.63	25.9
120 (midspan)	No control	202	—	1.51	—
	6	117	42.1	1.02	32.5
	8	112	44.6	0.96	36.4
	10	110	45.5	1.0	33.8
	12	119	41.1	1.02	32.5

Table 5: Continued.

Span (m)	Collision gap (cm)	Displacement peak (mm)	The vibration reduction rate (%)	Speed peak	The vibration reduction rate (%)
120 (side span)	No control	151	—	1.19	—
	6	114	24.5	0.83	30.3
	8	108	28.5	0.74	37.8
	10	115	23.8	0.77	35.3
	12	120	20.5	0.9	24.4

Table 6: PTMDs' parameters with various mass ratios.

Span (m)	U (%)	m (t)	H_1	L_1	L	L_1/L	Collision gap (cm)
120	1	80.8	2.5	3	5	0.6	8
	1.5	121.2	2.5	3	5	0.6	8
	2	161.6	2.5	3	5	0.6	8
80	1	45.2	2.5	3	5	0.6	8
	1.5	67.8	2.5	3	5	0.6	8
	2	90.5	2.5	3	5	0.6	8

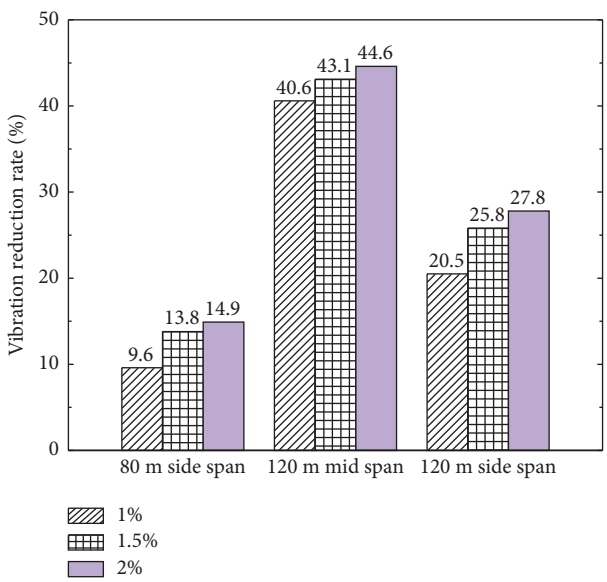

Figure 12: A parametric study of mass ratio on the vibration reduction rate.

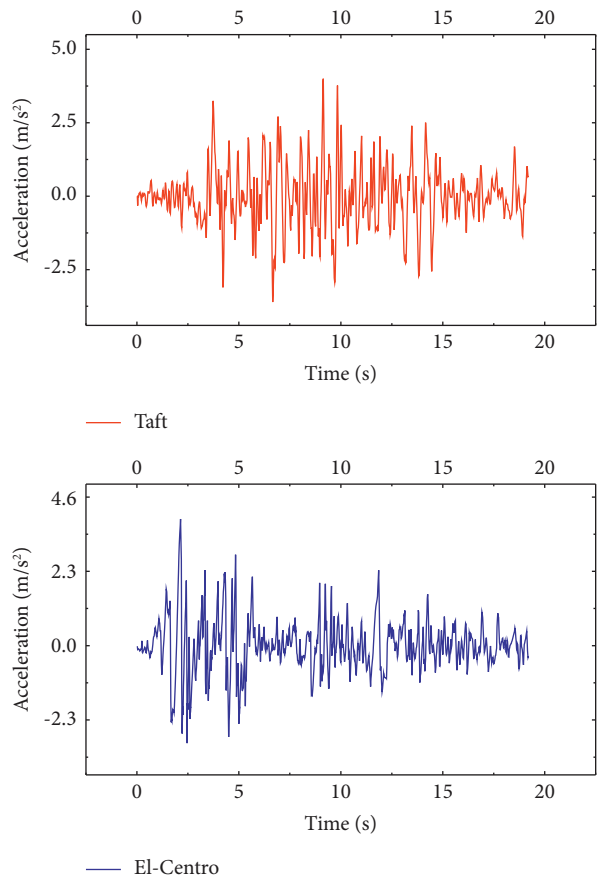

Figure 13: Acceleration time histories of the two records from the El-Centro and Taft earthquakes.

Table 7: Parameters of PTMDs.

Span (m)	u (%)	m (t)	H_1	L_1	L	L_1/L	Collision gap (cm)
120	1.5	121.2	2.5	3	5	0.6	8
80	1.5	67.8	2.5	3	5	0.6	8

4.4. Impact of Collision Gap. The collision gap refers to the distance between the L-shaped steel beam and the viscoelastic material. The size of the collision gap determines the speed of the steel beam before the collision and determines the deformation of the viscoelastic material. In this section, four kinds of collision gaps, 6 cm, 8 cm, 10 cm, and 12 cm, are selected for comparative analysis. Besides, the impact of various collision gaps on the PTMD's vibration control effect is investigated. Table 4 shows the PTMD's unique specifications, and Table 5 displays the bridge-PTMD system's dynamic reaction for various collision gaps. Considering the dynamic response of the three spans, the most suitable collision gap is 8 cm.

Table 8: Seismic response of the bridge under the record from the El-Centro earthquake with and without PTMD.

Span (m)	Structural response	Peak value		Decrease rate
		No control	PTMD	
120 (side span)	Displacement (m)	0.151	0.112	25.8%
	Velocity (m/s)	1.2	0.74	38.3%
120 (midspan)	Displacement (m)	0.202	0.115	43.1
	Velocity (m/s)	1.5	1.0	33.3
80	Displacement (m)	0.93	0.81	12.9
	Velocity (m/s)	0.85	0.60	29.4

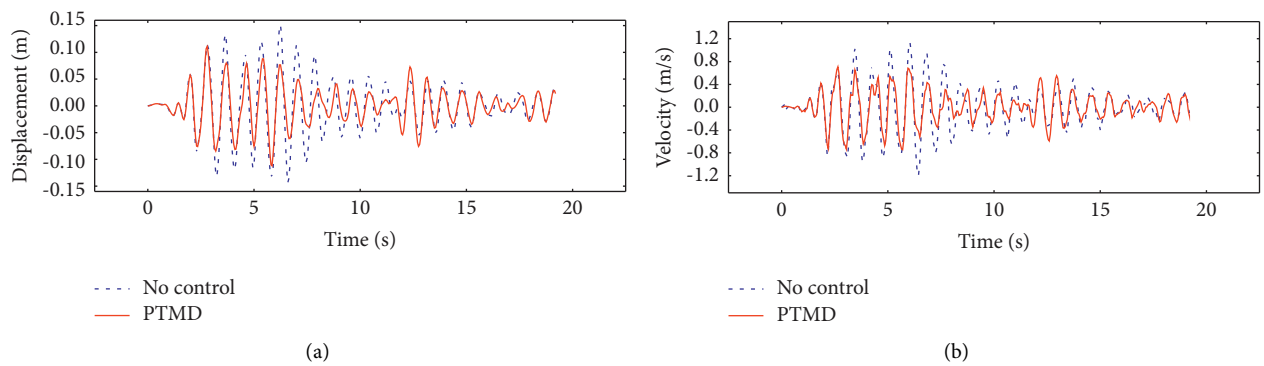

Figure 14: Dynamic response of 120-m side span under the record from the El-Centro earthquake: (a) displacement and (b) velocity.

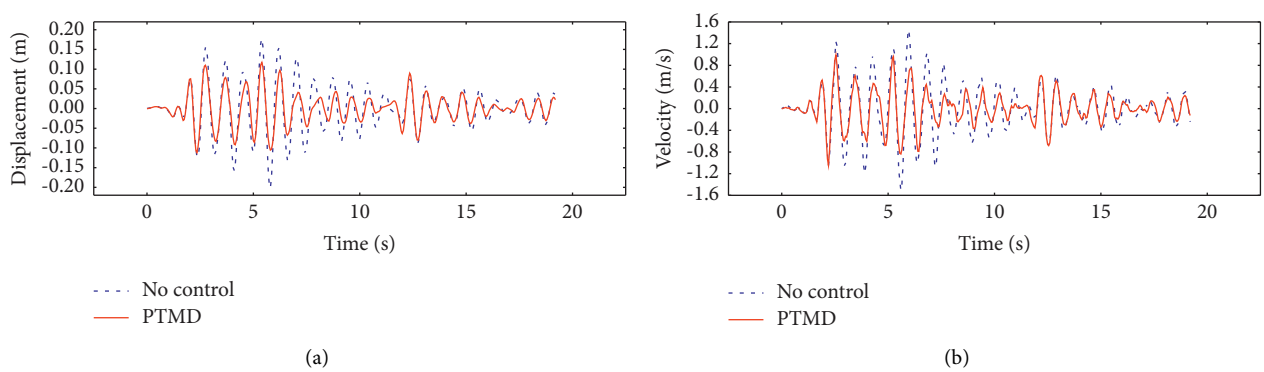

Figure 15: Dynamic response of 120-m midspan under the record from the El-Centro earthquake: (a) displacement and (b) velocity.

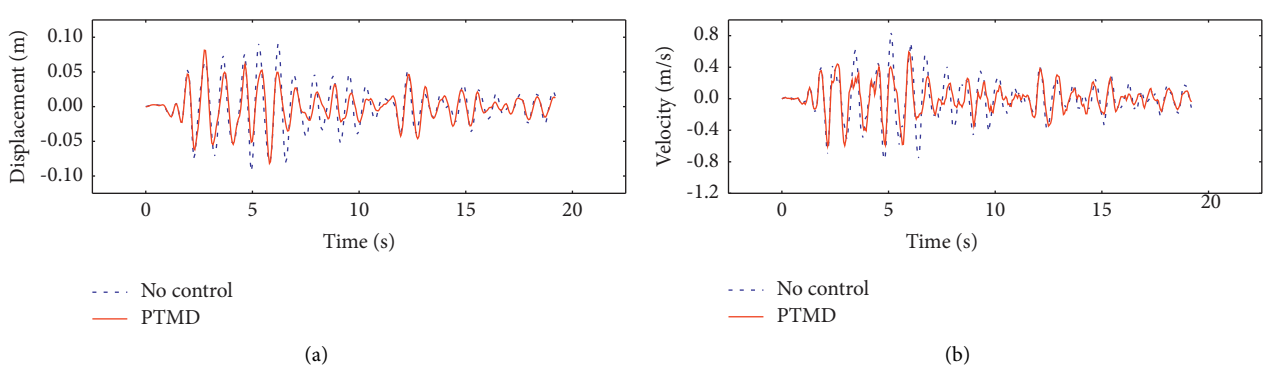

Figure 16: Dynamic response of 80-m side span under the record from the El-Centro earthquake: (a) displacement and (b) velocity.

4.5. The Effect of Mass Ratio. The mass ratio (u) is an important parameter of PTMD. Three distinct values of mass ratio, 1.0%, 1.5%, and 2.0%, were chosen for computation in order to evaluate the impact of mass ratio on the vibration reduction effect of PTMD. To evaluate its damping performance, the reduction rate of the three-span midspan node's lateral displacement and velocity is used. The design parameters of PTMD under four mass ratio conditions are shown in Table 6.

Figure 12 depicts the vibration reduction rate of PTMD at various mass ratios, the vibration reduction rate is greatest at the mass ratio of 2%. 80-meter side span, 120-meter midspan, and 120-meter side span, all have vibration reduction rates of 14.9%, 27.8%, and 44.6%, respectively. The mass ratio of 1.5 percent has a slightly less than two percent impact on vibration reduction. However, the vibration reduction rate of 1% is greatly decreased. A complete analysis reveals that the mass ratio of 1.5% is ideal for reducing the bulk of the mass ball and preventing the midspan stress concentration.

Through the analysis of 4.1~4.5, the optimized PTMD parameters for bridge vibration control are shown in Table 7.

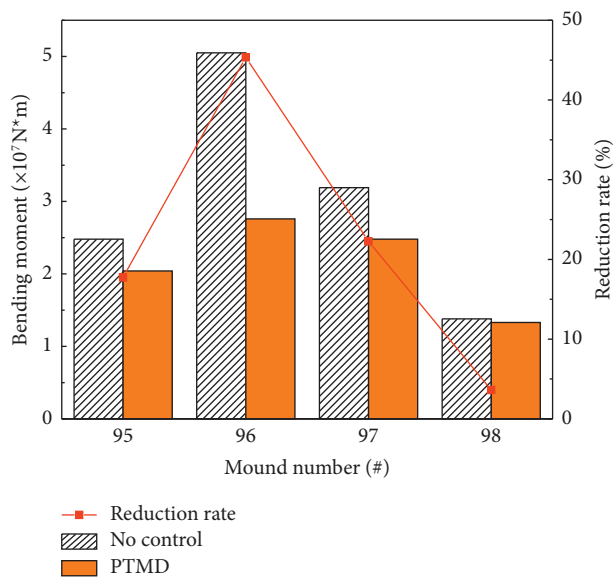

Figure 17: Bending moment around the longitudinal bridge at the base of the pier.

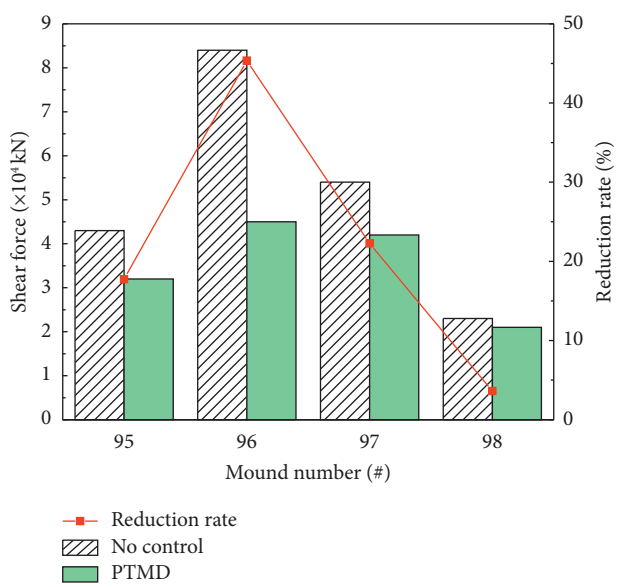

Figure 18: Transverse shear force at the pier bottom.

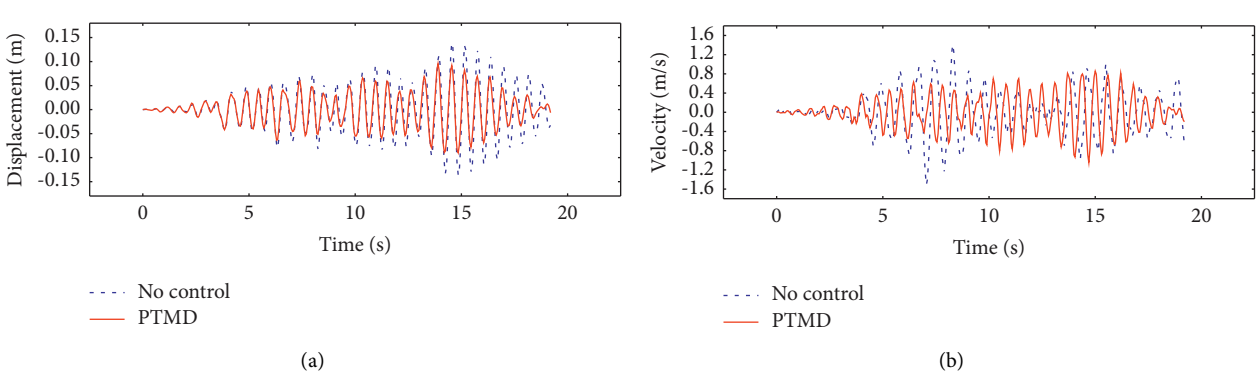

Figure 19: Dynamic response of 120-m side span under the record from the Taft earthquake: (a) displacement and (b) velocity.

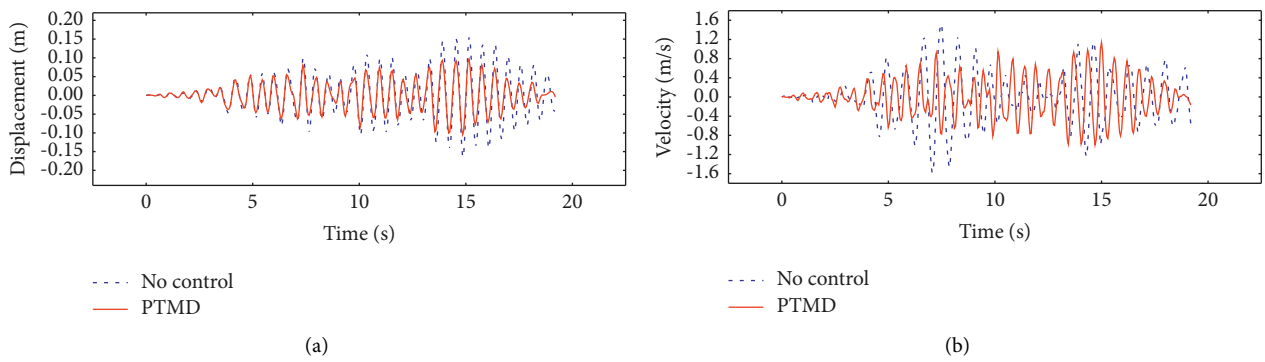

Figure 20: Dynamic response of 120-m midspan under the record from Taft earthquake: (a) displacement and (b) velocity.

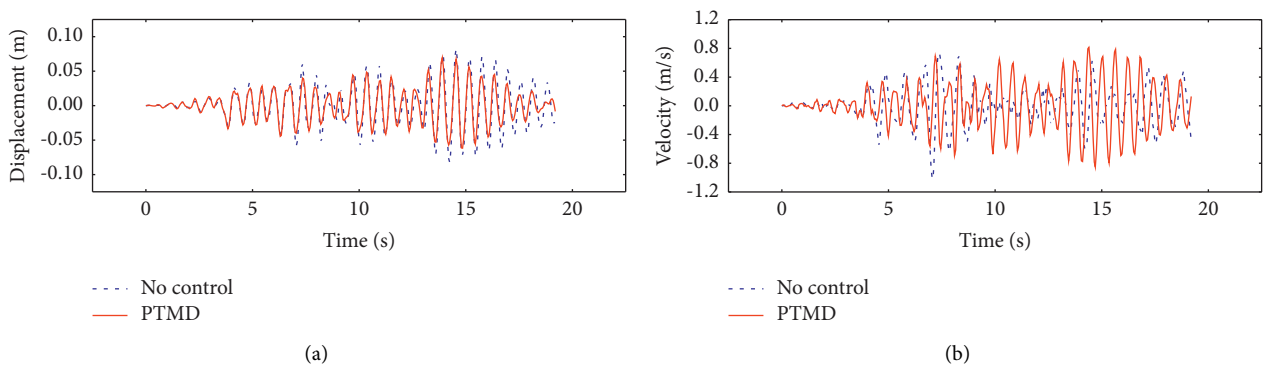

Figure 21: Dynamic response of 80-m side span under the record from the Taft earthquake: (a) displacement and (b) velocity.

Table 9: Seismic response of the bridge under the record from the Taft earthquake with and without PTMD.

Span (m)	Structural response	Peak value		Decrease rate (%)
		No control	PTMD	
120 (side span)	Displacement (m)	0.139	0.096	30.9
	Velocity (m/s)	1.56	1.04	33.3
120 (midspan)	Displacement (m)	0.165	0.104	37.0
	Velocity (m/s)	1.7	1.13	33.5
80	Displacement (m)	0.082	0.07	14.6
	Velocity (m/s)	0.85	0.78	8.2

5. Result Analysis

5.1. The Transverse Bridge Vibration Reduction Effect of PTMD under Earthquakes. Two recorded ground motions from the El-Centro (0.4 g) and Taft (0.4 g) earthquakes, were utilized for transverse direction excitation. A time history study was subsequently completed to confirm the effect of PTMD on lateral vibration control of the bridge. Figure 13 displays the acceleration time histories of two recordings.

5.1.1. Excitation of the Record from the El-Centro Earthquake

(1) Displacement and Velocity of Midspan Nodes. The record from the El-Centro earthquake was chosen as a seismic stimulation. The bridge's seismic reaction is displayed in Table 8 both with and without the PTMD. Figures 14–16 display the dynamic response (velocities and displacements at midspan) of the bridge for three spans. The picture demonstrates how useful it might be to employ PTMD to lessen the peak velocity and displacement at midspan. The uncontrolled bridge's 120-meter side span, 120-meter center span, and 80-meter side span all have peak displacements of 0.151 m, 0.202 m, and 0.93 m, respectively. The peak displacement values were lowered to 0.112 m, 0.115 m, and 0.81 m after the installation of the PTMD control device, with corresponding reduction rates of 25.8%, 43.1%, and 12.9%.

(2) Bending Moment of Pier Bottom. There are a variety of explanations for bridge damage induced by earthquakes, one of which is bridge pier damage caused by high bending moments at the piers' bottoms. The bending moment of the pier bottom around the longitudinal bridge is much greater

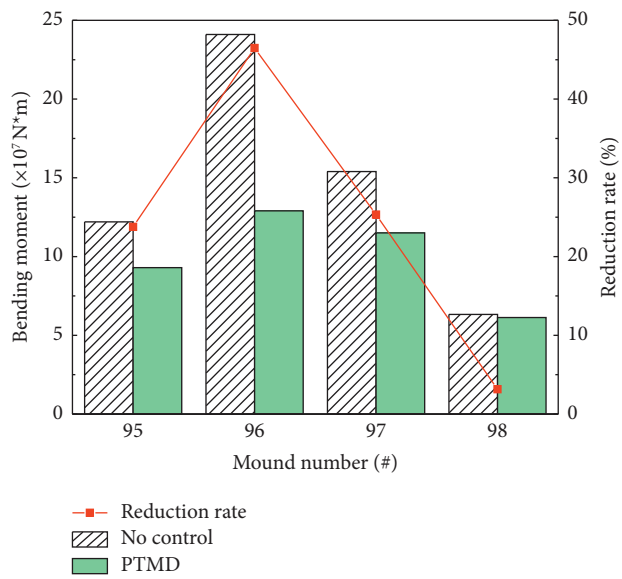

Figure 22: Bending moment around the longitudinal bridge at the base of the pier.

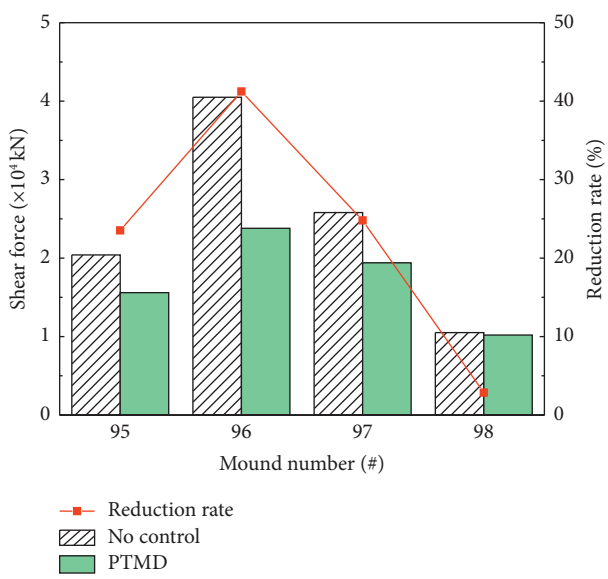

Figure 23: Transverse shear force at the pier bottom.

than that around the transverse bridge due to the transverse loading of seismic excitations. Figure 17 depicts, both without control and using PTMD, the maximum longitudinal bending moment at the bottom of the bridge's pier. As shown in Figure 17, piers 96 and 97 have the best bending moment reduction effect, reaching 45% and 22%, respectively. In addition, the maximum bending moments of the remaining piers also were reduced. Therefore, it is clear that the PTMD device may increase the seismic performance of the bridge while also reducing the bending moment at the base of the pier.

(3) Shear Force at the Bottom of the Pier. Shear force is a major cause of bridge damage caused by earthquakes. Figure 18 depicts the maximum shear force at the bottom of bridge piers with and without PTMD. As can be seen in the diagram, PTMD may effectively lower the shear force at the bridge pier's bottom. Among them, the shear force of No. 96 pier has the most obvious reduction effect, which is reduced by 46%. The shear force of the other piers has been significantly reduced as well. PTMD may greatly reduce shear stress at the bottom of bridge piers, as well as earthquake-related damage to bridge piers.

5.1.2. Excitation of the Record from the Taft Earthquake

(1) Displacement and Velocity of Midspan Nodes. The Taft (0.4g) earthquake record is used as the source of seismic excitation. The lateral displacement and velocity time-history curve of the three-span midspan node of the main bridge are shown in Figures 19–21. Besides, the seismic response comparison of bridges with and without the PTMD system under the record from the Taft earthquake is shown in Table 9. The findings suggest that PTMD can successfully minimize the maximum velocity and displacement in the midspan. The peak displacements of the 120-m side span, 120-m midspan, and 80-m side span of the uncontrolled bridge are 0.139 m, 0.165 m, and 0.082 m, respectively. After installing the PTMD control device, the peak midspan displacement was reduced to 0.096 m, 0.15 m, and 0.1 m, respectively, and the reduction rates were 30.9%, 37%, and 14.6%, respectively. It is clear that PTMD can lessen bridge reaction during the excitation of the record from the Taft earthquake.

(2) Bending Moment of Pier Bottom. Figure 22 illustrates the maximum bending moment at the pier bottom with and without PTMD control around the longitudinal bridge. Piers 96 and 97 exhibit the highest pier bottom bending moments, which were decreased by 46.5% and 25.3%,

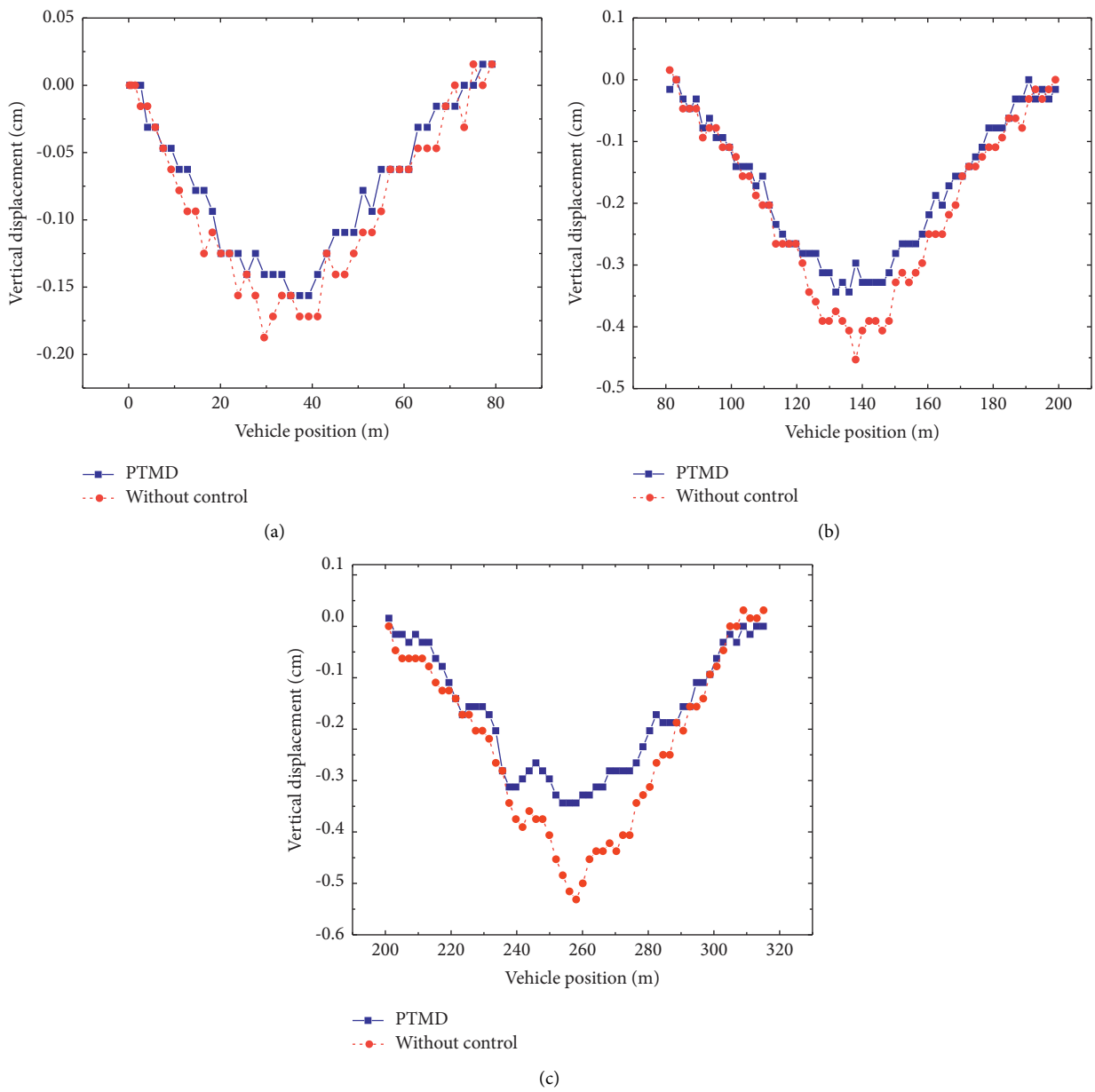

Figure 24: The dynamic displacement of the three-span bridge under the truck movement: (a) side span (80 m), (b) midspan (120 m), and (c) side span (120 m).

Table 10: Response of bridges without and with PTMD.

Span (m)	Structural response	Peak value		Decrease rate (%)
		No control	PTMD	
80 (side span)	Midspan displacement (cm)	−0.19	−0.16	15.8
120 (midspan)	Midspan displacement (cm)	−0.45	−0.34	24.4
120 (side span)	Midspan displacement (cm)	−0.53	−0.34	35.8

respectively, once PTMD devices were installed. Consequently, the PTMD device can decrease bridge piers' bending moment caused by the recorded ground motion from the Taft earthquake and can improve the safety of the bridge.

(3) Shear force at the bottom of the pier. Figure 23 displays the maximum shear force of the bridge's four piers both with and without PTMD. It is obvious that PTMD can greatly lessen the shear stress at the bridge pier's bottom. No. 96's pier bottom shear force has been reduced by 41.2%, and that

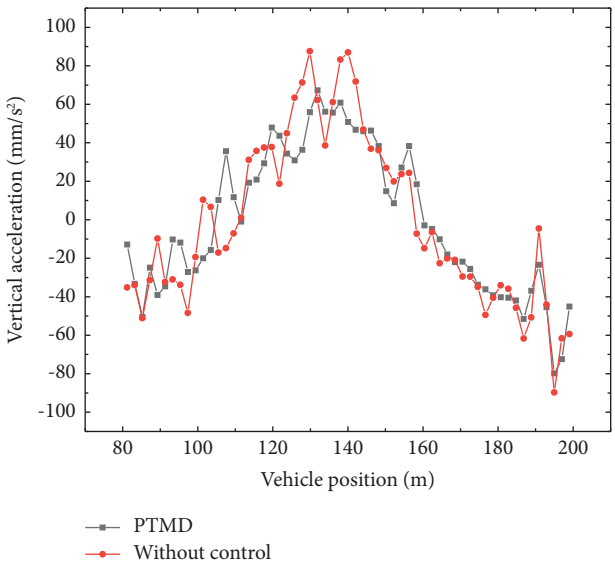

Figure 25: Acceleration of a single vehicle moving on midspan (120 m) of the bridge.

of the other bridge piers has also been significantly reduced. The bridge piers' shear force may be greatly lowered by using PTMD, which lessens the earthquake's damage to the pier.

5.2. Analysis of the Vertical Vibration Reduction Effect of PTMD under Vehicle Load

5.2.1. Comparison of Bridge Vibration with or without PTMD under Vehicle Load. The vehicle in this research is traveling at an average speed of 80 km/h on the bridge. Figure 24 plots the dynamic deflection time history of a three-span bridge without a vibration suppression system and with a PTMD system. Figure 24 shows how PTMD may minimize the vertical displacement of the bridge structure greatly. For example, the maximum midspan displacement of a 120 m long bridge without control and with PTMD control is 0.37 cm and 0.31 cm, respectively, and the reduction rate is 13.9%. As shown in Table 10, the midspan displacement of the other two spans of 80 m and 120 m of the bridge with the PTMD system decreased by 15.8% and 35.8%, respectively. As a result, the PTMD system may significantly minimize the bridge's vertical vibration caused by vehicle loads.

5.2.2. Comparison of Car Driving Comfort. For the driver, the change of acceleration directly reflects the driving comfort and reflects the vibration of the vehicle. Due to the large difference in the acceleration of each node of the vehicle, the vehicle engine as a whole is selected as the research object. When the vehicle travels to the midspan of 120 meters, its vertical acceleration varies with the position of the vehicle, as shown in Figure 25. PTMD is particularly successful in reducing the vehicle's vertical acceleration. In Figure 25, the peak acceleration of the vehicle without the control system is 0.087 m/s^2, while the peak acceleration of the midspan node of the PTMD bridge is 0.051 m/s^2. Acceleration was reduced by 41.4%. The vertical vibration of the bridge structure may be reduced using PTMD, which reduces vehicle vibration and improves driving comfort.

6. Conclusion

PTMD is employed in this work to regulate earthquake-induced lateral transverse bridge vibrations as well as vertical vehicle-induced vibrations. The motion equations of the bridge-PTMD system under earthquake and the vehicle-bridge-PTMD system are established, and parameters are optimized for PTMD. Furthermore, numerical analysis is carried out under different seismic excitations and vehicle loads. Numerical simulations show the following:

(1) In this study, length ratio, vertical length, collision gap, and mass ratio are selected as design parameters. Subsequently, the parameters are optimized by numerical simulation, and PTMDs' vibration reduction impact is improved.

(2) Under the impact of an earthquake, the vibration of the bridge in its transverse direction can be significantly reduced using the PTMD. The PTMD may effectively minimize bridge seismic response, as well as the midspan node velocity, displacement, shear force, and bending moment of the pier bottom. Therefore, the PTMD improves the bridge's seismic performance.

(3) Based on the PTMD system of a three-span bridge under the action of a single vehicle, the PTMD can lower the vertical vibration amplitude of the bridge, according to numerical estimates. The displacement of the 80-m side span, 120-m midspan, and 120-m side span of the bridge with PTMDs system decreased by 15.8%, 24.4%, and 35.8% respectively. The PTMD technology lessens the vehicle's vertical acceleration, lessens its vibration, and enhances driving comfort.

In this study, the PTMD is applied to the vibration control of large-span continuous girder bridges, and the numerical simulations have obtained very good results. But there are still some problems that need to be further studied and improved, mainly in the following aspects:

(1) In order to further study the vibration control effect of PTMD, the PTMD system can be fabricated and installed on a scale bridge to study its vibration control effect.

(2) Under the action of random traffic flow, the dynamic response of bridges with or without PTMD needs further study.

Data Availability

The data supporting the current study are given in the article.

Conflicts of Interest

The authors declare that they have no conflicts of interest.

Acknowledgments

The authors would like to thank the National Natural Science Foundation of China: No. 52079128; and Science and Technology Project of Henan Province, No. 212102310289, for their support.

References

[1] W. Guo, Y. Hu, H. Liu, and D. Bu, "Seismic performance evaluation of typical piers of China's high-speed railway bridge line using pushover analysis," *Mathematical Problems in Engineering*, Advance online publication, vol. 2019, , 2019.

[2] X.-X. Liu and Y. Wang, "A novel seismic risk analysis method for structures with both random and convex set mixed variables: case study of a RC bridge," *Mathematical Problems in Engineering*, Advance online publication, vol. 2019, , 2019.

[3] K. Meng, C. Cui, Z. Liang, H. Li, and H. Pei, "A new approach for longitudinal vibration of a large-diameter floating pipe pile in visco-elastic soil considering the three-dimensional wave effects," *Computers and Geotechnics*, vol. 128, Article ID 103840, 2020.

[4] K. Meng, C. Cui, and H. Li, "An ontology framework for pile integrity evaluation based on analytical methodology," *IEEE Access*, vol. 8, pp. 72158–72168, 2020.

[5] T.-L. Wang, D. Huang, and M. Shahawy, "Dynamic response of multigirder bridges," *Journal of Structural Engineering*, vol. 118, no. 8, pp. 2222–2238, 1992.

[6] L. Deng and C. Cai, "Identification of dynamic vehicular axle loads: demonstration by a field study," *Journal of Vibration and Control*, vol. 17, no. 2, pp. 183–195, 2011.

[7] Y. B. Yang, M. C. Cheng, and K. C. Chang, "Frequency variation in vehicle–bridge interaction systems," *International Journal of Structural Stability and Dynamics*, vol. 13, no. 02, Article ID 1350019, 2013.

[8] M. Wu, Y. Li, and W. Zhang, "Impacts of wind shielding effects of bridge tower on railway vehicle running performance," *Wind and Structures*, vol. 25, no. 1, pp. 63–77, 2017.

[9] H. Li, Z. Yu, J. Mao, and B. F. Spencer, "Effect of seismic isolation on random seismic response of High-Speed railway bridge based on probability density evolution method," *Structures*, vol. 29, pp. 1032–1046, 2021.

[10] M.-H. Tsai, S.-Y. Wu, K.-C. Chang, and G. C. Lee, "Shaking table tests of a scaled bridge model with rolling-type seismic isolation bearings," *Engineering Structures*, vol. 29, no. 5, pp. 694–702, 2007.

[11] M. Ma, M. Li, X. Qu, and H. Zhang, "Effect of passing metro trains on uncertainty of vibration source intensity: monitoring tests," *Measurement*, Article ID 110992, 2022.

[12] L. Xu and M. Ma, "Dynamic response of the multilayered half-space medium due to the spatially periodic harmonic moving load," *Soil Dynamics and Earthquake Engineering*, Article ID 107246, 2022.

[13] C. Zou, J. A. Moore, M. Sanayei, and Y. Wang, "Impedance model for estimating train-induced building vibrations," *Engineering Structures*, vol. 172, pp. 739–750, 2018.

[14] J. Wu, F. Cheng, C. Zou et al., "Swarm intelligent optimization conjunction with kriging model for bridge structure finite element model updating," *Buildings*, vol. 12, no. 5, p. 504, 2022.

[15] M. Brennan, "Some recent developments on adaptive tuned vibration absorbers/neutralisers (Invited Keynote Study)," in *Proceedings of the XI DINAME*, Ouro Preto, MG, Brazil, July 2005.

[16] C. C. Lin, G. L. Lin, and J. F. Wang, "Protection of seismic structures using semi-active friction TMD," *Earthquake Engineering & Structural Dynamics*, vol. 39, no. 6, pp. 635–659, 2010.

[17] A. R. Magnuson, "Mitigation of traffic-induced bridge vibrations through passive and semi-active control devices," Doctoral dissertation, Massachusetts Institute of Technology, Cambridge, MA, USA, 2011.

[18] R. Rana and T. Soong, "Parametric study and simplified design of tuned mass dampers," *Engineering Structures*, vol. 20, no. 3, pp. 193–204, 1998.

[19] J. J. Connor, *Structural Motion Control*, Pearson Education, Inc, New York, NY, USA, 2003.

[20] S. M. Nigdeli and G. Bekdaş, "Optimum tuned mass damper design in frequency domain for structures," *KSCE Journal of Civil Engineering*, vol. 21, no. 3, pp. 912–922, 2017.

[21] S. M. Nigdeli and G. Bekdas, "Optimum tuned mass damper approaches for adjacent structures," *Earthquakes and Structures*, vol. 7, no. 6, pp. 1071–1091, 2014.

[22] J. Salvi, F. Pioldi, and E. Rizzi, "Optimum tuned mass dampers under seismic soil-structure interaction," *Soil Dynamics and Earthquake Engineering*, vol. 114, pp. 576–597, 2018.

[23] G. Bekdaş and S. M. Nigdeli, "Metaheuristic based optimization of tuned mass dampers under earthquake excitation by considering soil-structure interaction," *Soil Dynamics and Earthquake Engineering*, vol. 92, pp. 443–461, 2017.

[24] G. Bekdaş, S. M. Nigdeli, and X.-S. Yang, "A novel bat algorithm based optimum tuning of mass dampers for improving the seismic safety of structures," *Engineering Structures*, vol. 159, pp. 89–98, 2018.

[25] H. Zhang and L. Zhang, "Tuned mass damper system of high-rise intake towers optimized by improved harmony search algorithm," *Engineering Structures*, vol. 138, pp. 270–282, 2017.

[26] Z. Lu, K. Li, Y. Ouyang, and J. Shan, "Performance-based optimal design of tuned impact damper for seismically excited nonlinear building," *Engineering Structures*, vol. 160, pp. 314–327, 2018.

[27] S. M. Nigdeli and G. Bekdaş, "Optimum design of multiple positioned tuned mass dampers for structures constrained with axial force capacity," *The Structural Design of Tall and Special Buildings*, vol. 28, no. 5, 2019.

[28] G. Bekdaş, A. E. Kayabekir, S. M. Nigdeli, and Y. C. Toklu, "Tranfer function amplitude minimization for structures with tuned mass dampers considering soil-structure interaction," *Soil Dynamics and Earthquake Engineering*, vol. 116, pp. 552–562, 2019.

[29] W. Shen, S. Zhu, Y. L. Xu, and H. p. Zhu, "Energy regenerative tuned mass dampers in high-rise buildings," *Structural Control and Health Monitoring*, vol. 25, no. 2, 2018.

[30] W.-a. Shen, S. Zhu, and Y.-l. Xu, "An experimental study on self-powered vibration control and monitoring system using electromagnetic TMD and wireless sensors," *Sensors and Actuators A: Physical*, vol. 180, pp. 166–176, 2012.

[31] R. Jabary and S. Madabhushi, "Structure-soil-structure interaction effects on structures retrofitted with tuned mass dampers," *Soil Dynamics and Earthquake Engineering*, vol. 100, pp. 301–315, 2017.

[32] M. De Angelis, S. Perno, and A. Reggio, "Dynamic response and optimal design of structures with large mass ratio TMD," *Earthquake Engineering & Structural Dynamics*, vol. 41, no. 1, pp. 41–60, 2012.

[33] Q. Wang, X. Dong, L. Li, and J. Ou, "Study on an improved variable stiffness tuned mass damper based on conical

magnetorheological elastomer isolators," *Smart Materials and Structures*, vol. 26, no. 10, Article ID 105028, 2017.

[34] Z. Lu, X. Chen, D. Zhang, and K. Dai, "Experimental and analytical study on the performance of particle tuned mass dampers under seismic excitation," *Earthquake Engineering & Structural Dynamics*, vol. 46, no. 5, pp. 697–714, 2017.

[35] Z. Lu, B. Huang, Q. Zhang, and X. Lu, "Experimental and analytical study on vibration control effects of eddy-current tuned mass dampers under seismic excitations," *Journal of Sound and Vibration*, vol. 421, pp. 153–165, 2018.

[36] X. Yin, Y. Liu, G. Song, and Y. L. Mo, "Suppression of bridge vibration induced by moving vehicles using pounding tuned mass dampers," *Journal of Bridge Engineering*, vol. 23, no. 7, Article ID 04018047, 2018.

[37] J. Jiang, P. Zhang, D. Patil, H. N. Li, and G. Song, "Experimental studies on the effectiveness and robustness of a pounding tuned mass damper for vibration suppression of a submerged cylindrical pipe," *Structural Control and Health Monitoring*, vol. 24, no. 12, Article ID e2027, 2017.

[38] X. Yin, G. Song, and Y. Liu, "Vibration suppression of wind/traffic/bridge coupled system using multiple pounding tuned mass dampers (MPTMD)," *Sensors*, vol. 19, no. 5, p. 1133, 2019.

[39] W. Wang, X. Wang, X. Hua, G. Song, and Z. Chen, "Vibration control of vortex-induced vibrations of a bridge deck by a single-side pounding tuned mass damper," *Engineering Structures*, vol. 173, pp. 61–75, 2018.

[40] H. Li, P. Zhang, G. Song, D. Patil, and Y. Mo, "Robustness study of the pounding tuned mass damper for vibration control of subsea jumpers," *Smart Materials and Structures*, vol. 24, no. 9, Article ID 095001, 2015.

[41] P. Zhang, G. Song, H.-N. Li, and Y.-X. Lin, "Seismic control of power transmission tower using pounding TMD," *Journal of Engineering Mechanics*, vol. 139, no. 10, pp. 1395–1406, 2013.

[42] L. Tian and X. Gai, "Wind-induced vibration control of power transmission tower using pounding tuned mass damper," *Journal of Vibroengineering*, vol. 17, no. 7, pp. 3693–3701, 2015.

[43] W. Lin, Q. Wang, J. Li, S. Chen, and A. Qi, "Shaking table test of pounding tuned mass damper (PTMD) on a frame structure under earthquake excitation," *Computers and Concrete, An International Journal*, vol. 20, no. 5, pp. 545–553, 2017.

[44] G. B. Song, P. Zhang, L. Y. Li et al., "Vibration control of a pipeline structure using pounding tuned mass damper," *Journal of Engineering Mechanics*, vol. 142, no. 6, Article ID 04016031, 2016.

[45] P. Zhang, J. Tan, H. Liu, G. Yang, and C. Cui, "Seismic vibration mitigation of a cable-stayed bridge with asymmetric pounding tuned mass damper," *Mathematical Problems in Engineering*, Advance online publication, vol. 2021, 2021.

[46] S. Chen and J. Wu, "Performance enhancement of bridge infrastructure systems: long-span bridge, moving trucks and wind with tuned mass dampers," *Engineering Structures*, vol. 30, no. 11, pp. 3316–3324, 2008.

Hindawi
Advances in Civil Engineering
Volume 2022, Article ID 2976271, 19 pages
https://doi.org/10.1155/2022/2976271

Research Article

Research on the Vibration Isolation Characteristics of Floor Vibration Isolation Slab System under Train Operation

Jinbao Yao, Han Wu, and Shaoyin Tao

School of Civil Engineering, Beijing Jiaotong University, Beijing 100044, China

Correspondence should be addressed to Jinbao Yao; jbyao@bjtu.edu.cn

Received 10 June 2022; Revised 20 July 2022; Accepted 12 August 2022; Published 12 September 2022

Academic Editor: Quanmin Liu

This study takes the vibration isolation measures of building floor vibrations induced by trains as the starting point and carries out both theoretical derivation and numerical simulation. A four-degree-of-freedom (DOF) multi-dimensional vibration isolation platform (VIP) dynamics model is established based on the theoretical research of single-level, single-degree-of-freedom vibration isolation systems. Under multi-point excitation, the model can deduce the horizontal and vertical vibration responses of the VIP system. A comprehensive analysis of the vibration isolation performance of the VIP system on the floor and how the variation of the parameters influences the performance of the vibration isolation systems are presented. Several variables, such as the thickness, stiffness, damping ratio, and the number of isolators of the VIP system, are theoretically found to have a significant impact on the vibration isolation effect of the floor VIP system. Empirical results show that the VIP system significantly affects the vibration isolation of the building floor induced by a train and has the best vibration isolation effect on the acceleration response and the worst vibration isolation effect on the displacement response.

1. Introduction

With the rapid development of China's transportation industry, the environmental vibration problems caused by train operations have become increasingly prominent. At the same time, as people's demand for quality of life continues to increase, higher demands are being placed on the control of environmental vibrations, and research on the environmental problems caused by train vibrations and vibration isolation measures have attracted considerable attention from scholars [1]; Forrest and hunt, 2006; [2–4]. At present, there are three main types of control measures for the impact of train vibrations on the surrounding environment: control of the vibration source, control of the propagation path, and control of the vibrated body. Among them, the installation of secondary vibration isolation platforms (VIP) inside buildings has become a popular research topic for many scholars.

Ungar et al. [5] first classified the main sources of vibrations associated with high-technology equipment into three categories: external sources (microseismic and seismic, nearby road or rail traffic, and construction activities), internal sources (personnel walking, service activities, and production work), and service machinery (all electromechanical equipment in buildings). Hwang et al. [6] evaluated the applicability of seismic protection systems in high-technology industrial structures in Earthquake-prone areas and compared the protective performances of structures against microseismic activity before and after the implementation of microseismic protection systems. They proposed that there is nonnegligible coupling between the plant structure and its internal vibration isolation plate system in the horizontal direction, and by establishing a single/double hybrid platform coupled with the building structure, a combination of experiments and numerical simulations was used to control the microvibrations of high-technology equipment [7–10]. Yang et al. [11] conducted a numerical analysis of a large building near a metro network, proposed a two-stage time-frequency prediction method for predicting the superstructure's vibration response, and evaluated building vibration using two related criteria. Ibrahim [12] introduced the basic concepts and characteristics of

nonlinear vibration isolators and the inherent nonlinear phenomena. Specific types of nonlinear vibration isolators are then discussed, including ultralow frequency isolators. Lazar et al. [13] proposed to inert a novel passive vibration control system in a multi-story building and compared an inertial agent-based system with a tuned mass damper (TMD) system. It demonstrates that the potential performance of vibration control will be improved through the use of an inertial agent rather than a TMD.

Domenico et al. [14] proposed an enhanced base seismic isolation system, a TMD inertia device (TMDI). They found that when the inertia device is installed in series with a spring and damper element, a lower-mass and more efficient alternative to conventional TMDs is obtained, finding the optimum parameters of the TMDI based on a probabilistic framework by using the time history analysis of isolated multi-story buildings under several seismic excitations to assess the effectiveness of the optimal TMDI parameters. Yun et al. [15] proposed the novel design of a dual redundant parallel robot. It enabled the positioning of high or rough precision and realized 6-DOF active vibration isolation and excitation of payloads on a moving platform; Gardonio et al. [16] proposed a multi-degree-of-freedom system to evaluate the dynamics of active isolation systems for structural vibrations; Kumar and Whittaker [17] proposed cross-platform implementation, verification, and validation of advanced mathematical models for elastic vibration isolation bearings; Farsangi et al. [18] proposed a shaking isolation system called the "telescopic column" (TC) and investigated an elastic low-damage base isolation system under combined vertical and horizontal excitations; and Yang and Agrawal [19] conducted an extensive numerical study on whether hybrid control isolation systems can be applied to microvibrations.

The structure of this study is organized as follows: Section 2 is based on the theory of single-layer VIP systems, establishing a four-degree-of-freedom multi-dimensional VIP system model. In addition, Sections 3,4, and 5 show that the vibration isolation effect of floor VIP systems under external excitation is analyzed more comprehensively, and the influence of VIP structural parameters on the vibration isolation effect is also studied. The conclusions are presented in Section 6.

2. Theoretical Research on Vibration Isolation in VIP Systems

2.1. Theoretical Analysis of Single-Degree-of-Freedom Vibration Isolation. The performance evaluation criterion of a single-degree-of-freedom vibration isolation system is the transmission efficiency of the vibration isolation system T_r. The value of T_r directly reflects the attenuation level of vibrations through vibration isolation systems and can effectively measure the vibration isolation effect of vibration isolation systems. The formula for the vibration isolation efficiency of a single-layer passive vibration isolation system is

$$T_r = \sqrt{\frac{1 + \left[2\xi\left(\omega/\omega_n\right)\right]^2}{\left[1 - \left(\omega/\omega_n\right)^2\right]^2 + \left[2\xi\left(\omega/\omega_n\right)\right]^2}}. \tag{1}$$

In (1), the smaller the value of T_r for vibration isolation efficiency is, the better the vibration isolation effect; ω is the external interference circle frequency (rad/s), ω_n is the self-circular frequency of the vibration isolation structure (rad/s); and ξ is the vibration isolator damping ratio.

2.2. Dynamic Analysis of a Single-Layer Multi-Dimensional VIP System under Multi-Point Excitation. With the increase in the number of vibration isolators on the VIP arrangement, the number of points of external excitation that vibration isolators are subjected to increases, and the vibration response of the VIP system changes from a single degree to multiple degrees of freedom.

2.2.1. Multidimensional Vibration Isolator System Dynamics Model. A vibration isolation system has three axes of translational motion and rotation along these three directions. The vibration isolation system's horizontal and vertical vibration response is the main form of vibration that triggers the secondary structure. In this study, we only consider the coupled motion of the four degrees of freedom of the vibration isolation system, including the translational degrees of freedom in the direction of the three axes (X, Y, and Z) and the rotational degrees of freedom around the Y-axis.

Figures 1 and 2 show a simplified multi-dimensional vibration isolation plate system model, which, from top to bottom, shows the vibration isolation plate, spring isolator, and foundation base.

Some parameters of the vibration isolation plate system and the vibration isolator arrangement are set as follows: the length of the VIP is $2l$, the width of the platform is d, the thickness of the platform is H, the density is ρ; the bottom of the VIP is uniformly arranged with N vibration isolators. The horizontal Y direction of the platform is uniformly arranged with N spring vibration isolators, and the height of the vibration isolator arrangement is consistent with the center of gravity of the VIP. The horizontal X direction of the platform is uniformly arranged with n spring vibration isolators, assuming that the height of the vibration isolator arrangement is consistent with the center of gravity of the vibration isolation plate. The vertical height difference between the vibration isolator and the center of gravity of the VIP is h ($h \geq 0$). The stiffness and damping of the isolators arranged along the three translational directions are set as k_1, k_2, and k_3 and c_1, c_2 and c_3, respectively, and the disturbance excitations F_x, F_y, and F_z in the X, Y, and Z directions are shown in (2) according to Figure 1:

$$\begin{cases} F_x = p_m \sin\left(\omega_x t + \theta_m\right) \\ F_y = p_j \sin\left(\omega_y t + \gamma_j\right) \quad (i, j, m = 1 \ldots n). \\ F_z = p_i \sin\left(\omega_z t + \vartheta_i\right) \end{cases} \tag{2}$$

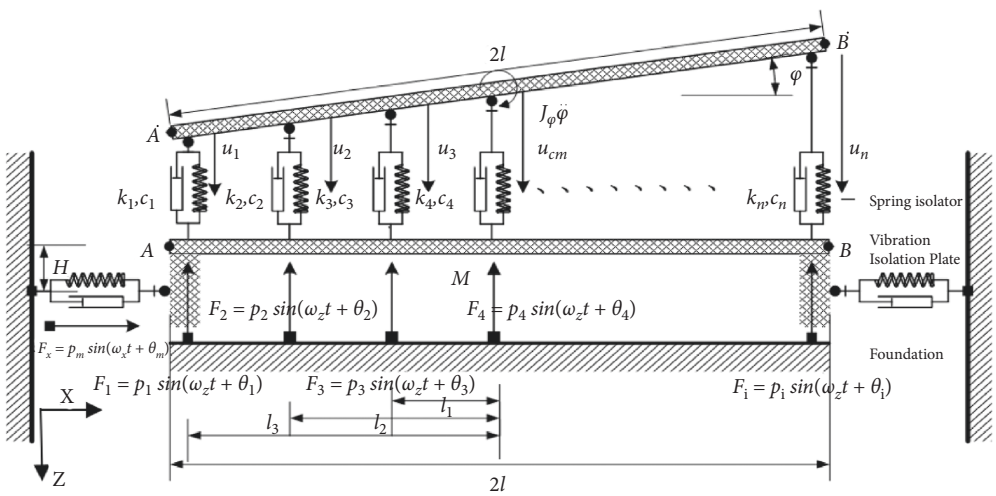

Figure 1: Multi-dimensional vibration isolation system (Front view).

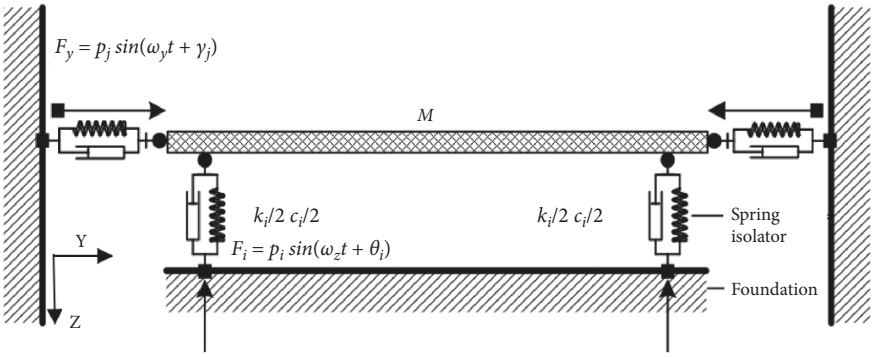

Figure 2: Multi-dimensional vibration isolation system (Side view).

When the stiffness and damping of the vibration isolators arranged under the vibration isolators are the same, $k_i = k_1$, and $c_i = c_1 (i = 1 \ldots n)$, the vertical degrees of freedom of the vibration isolators and the rotational degrees of freedom around the Y-axis are independent, are uncoupled and can be solved as single-degree-of-freedom systems, respectively.

u_{cm} and θ represent the generalized coordinates of the system; F_1 and F_2 represent the external disturbance forces; M represents the mass of the vibration isolator system; I_{c} represents the rotational inertia of the vibration isolator system; u_1 and u_n represent the vibration responses of the two ends of the vibration isolator system, where $u_1 = u_{\mathrm{cm}} - l_\theta$ and $u_{\mathrm{n}} = u_{\mathrm{cm}} + l_\theta$; θ indicates the rotational response of the vibration isolator.

2.2.2. Development of Differential Equations for the Vibration of a Multi-Dimensional Vibration Isolator System. For a complete constrained system of masses, the spatial position u_i of any mass m_i can be expressed as a function of its generalized coordinates $q_i (i = 1 \ldots n)$ and time, and for generalized coordinates $q_j = X, Y, Z, \varphi$; the corresponding generalized forces can be expressed by

$$\begin{cases} Q_x = \sum_{m=1}^{n} p_m \sin(\omega_x t + \theta_m), \\ Q_y = \sum_{j=1}^{n} p_j \sin(\omega_y t + \gamma_j), \\ Q_z = \sum_{i=1}^{n} p_i \sin(\omega_z t + \vartheta_i), \\ Q_\varphi = \sum_{i=1}^{n} p_i \sin(\omega_z t + \vartheta_i) l_i \zeta_i, \end{cases} \tag{3}$$

where Q_{y}, Q_{x}, Q_{z}, and Q_j represent the generalized forces corresponding to the four degrees of freedom of the isolation system; p_{m}, p_{j}, and p_{i} represent the amplitudes of the three directions of the external excitation in the isolation system; ω_{x}, ω_{y}, and ω_{z} represent the circular frequencies (rad/s) of the three directions of the external excitation in the isolation system; and θ_m, γ_j, and ϑ_i represent the phase angles of the three directions of the external excitation of the isolation system, ζ_i indicates the position coefficient of the spring isolator, value of ζ_i at the left and right sides of the center point of the plate is ± 1 respectively; l_i indicates the horizontal distance from the vibration isolator arranged at the

bottom of the vibration isolation plate to the center point of the plate.

The rotational inertia of the system along the direction is $I_y = \int (l^2 + h^2)dm$, as the thickness of the isolation plate, is much less than the length of the plate $2l$, so we can ignore the effect of the thickness of the isolation platform. The rotational inertia is expressed as $J_\varphi = 1/3Ml^2$. Bringing the energy formula derived in the previous summary into the Lagrange dynamics equations and replacing each degree of freedom of the VIP with the generalized coordinate q_j, the differential equations used for the dynamics of different degrees of freedom of the multi-dimensional vibration isolation system can be obtained, as shown in Equations (4)–(7).

(1) Vertical motion at the center of a multi-dimensional vibration isolator ($q_j = Z$) is represented as follows:

$$M\ddot{Z} + \sum_{i=1}^{n} k_i^3 Z + \sum_{i=1}^{n} c_i^3 \dot{Z} = \sum_{i=1}^{n} p_i \sin\left(\omega_z t + \vartheta_i\right). \tag{4}$$

(2) Rotation of multi-dimensional vibration isolators plate($q_j = \varphi$) is represented as follows:

$$J_\varphi \ddot{\varphi} + \sum_{i=1}^{n} k_i^1 \left(h^2 \varphi + hX\right) + \sum_{i=1}^{n} k_i^3 l_i^2 \varphi + \sum_{i=1}^{n} c_i^1 \left(h^2 \dot{\varphi} + h\dot{X}\right) + \sum_{i=1}^{n} c_i^3 l_i^2 \dot{\varphi} = \sum_{i=1}^{n} p_i \sin\left(\omega_z t + \vartheta_i\right) l_i \zeta_i. \tag{5}$$

(3) Horizontal movement of multi-dimensional vibration isolator plate($q_j = X$) is represented as follows:

$$M\ddot{X} + \sum_{i=1}^{n} k_i^1 \left(X + h\varphi\right) + \sum_{i=1}^{n} c_i^1 \left(\dot{X} + h\dot{\varphi}\right) = \sum_{m=1}^{n} p_m \sin\left(\omega_x t + \theta_m\right). \tag{6}$$

(4) Horizontal movement of multi-dimensional vibration isolator plate($q_j = Y$)is represented as follows:

$$M\ddot{Y} + \sum_{i=1}^{n} k_i^2 Y + \sum_{i=1}^{n} c_i^2 \dot{Y} = \sum_{j=1}^{n} p_j \sin\left(\omega_y t + \gamma_j\right). \tag{7}$$

$k_i^1, k_i^2, k_i^3$are the stiffness of the isolators in X, Y and Z directions respectively; c_i^1, c_i^2, c_i^3 are the damping of the isolators in X, Y and Z directions respectively.

2.3. Vibration Response of a Multi-Dimensional Vibration Isolator System under Multi-Point Excitation

2.3.1. Z-Directional Response of a Multi-Dimensional Vibration Isolator System under Multi-Point Excitation. Suppose that the external simple harmonic excitation $F_Z = p_i \sin(\omega_z t + \vartheta_i)$ is applied to the vibration isolator system by the arrangement of the vertical vibration isolator, thus causing the vertical vibration of the vibration isolator system. We take the central pickup point of the vibration isolator system as the research object, and then, the differential equation of the vertical response of the multi-dimensional vibration isolation system can be expressed by (4).

In equation (4), $k_i^3 = k_3$ represents the vertical vibration isolator spring stiffness, and $c_i^3 = c_3$ represents the vertical vibration isolator damping. The center point of the vertical displacement of the vibration isolator in the formula without the rotation angle φ and $\dot{\varphi}$item can be seen due to the influence of the vibration isolator, which is symmetrically arranged relative to the center point of the vibration isolator to the left and right; the position function ζ_i to the left and right sides show the opposite sign, so the parts of the formula containing φ and $\dot{\varphi}$ counteract each other. (4) can be expressed as follows:

$$M\ddot{Z} + nc_3\dot{Z} + nk_3 Z = \sum_{i=1}^{n} p_i \sin\left(\omega_z t + \vartheta_i\right). \tag{8}$$

The solution to the differential equation can be expressed as follows:

$$Z = u_i \sin\left(\omega_z t + \vartheta_i - \phi_i\right). \tag{9}$$

In the above formula, the following terms are utilized:

$$\begin{cases} u_i = u_{st} \dfrac{1}{\left[1 - \left(\omega_z/\omega_n\right)^2\right]^2 + \left[2\xi\left(\omega_z/\omega_n\right)\right]^2} \\ \phi_i = \arctan \dfrac{2\xi\left(\omega_z/\omega_n\right)}{1 - \left(\omega_z/\omega_n\right)^2} \end{cases}. \tag{10}$$

Considering the superposition ability of solutions to differential equations, the final solution to Equation (10) is therefore given as follows:

$$Z = \sum_{i=1}^{n} u_{st} \frac{1}{\left[1 - \left(\omega_z/\omega_n\right)^2\right]^2 + \left[2\xi\left(\omega_z/\omega_n\right)\right]^2} \sin\left(\omega_z t + \vartheta_i - \phi_i\right), \tag{11}$$

whereω_z represents the external disturbance circular frequency; $\omega_n$represents the vibration isolation structure's own circular frequency; ξ is the vibration isolator damping ratio; ϑ_i represents the initial phase angle of the external disturbance force; and $\vartheta_i - \phi_i$ represents the phase angle, reflecting the relationship between the system vibration displacement and the phase of the simple harmonic load.

2.3.2. Y-Directional Response of a Multi-Dimensional Vibration Isolator System with Multi-Point Excitation. According to (10), the horizontal Y-directional vibration response of this multi-dimensional vibration isolator system can also be reduced to the problem of a single-degree-of-freedom mass-spring system, similar to the z-directional response of vertical vibrations at the pickup point in the center of the vibration isolator, and can be solved in a similar manner and with similar results.

2.3.3. X-Direction and Y-Axis Rotation Response of a Multi-Dimensional Vibration Isolator System under Multi-Point Excitation. The horizontal X-directional degrees of freedom of the multi-dimensional vibration isolation system and the degrees of freedom of rotation around the Y-axis φ are coupled with each other, so the vibrations of the two degrees of freedom of the VIP are discussed together, and its dynamical differential equation matrix form can be introduced by (8) and (9) as follows:

$$\begin{bmatrix} M & \\ & J_\varphi \end{bmatrix}\left[\ddot{X}\ \ddot{\varphi}\right] + \sum_{i=1}^{n}\begin{bmatrix} c_i^1 & hc_i^1 \\ hc_i^1 & h^2c_i^1 + l_i^2c_i^3 \end{bmatrix}\begin{bmatrix} \dot{X} \\ \dot{\varphi} \end{bmatrix} + \sum_{i=1}^{n}\begin{bmatrix} k_i^1 & hk_i^1 \\ hk_i^1 & h^2k_i^1 + l_i^2k_i^3 \end{bmatrix}\begin{bmatrix} X \\ \varphi \end{bmatrix} = \begin{bmatrix} \sum_{m=1}^{n} p_m \sin\left(\omega_x t + \theta_m\right) \\ \sum_{i=1}^{n} p_i \sin\left(\omega_z t + \vartheta_i\right) l_i \zeta_i \end{bmatrix}, \tag{12}$$

where $k_i^1 = k_1$ is the horizontal vibration isolator spring stiffness and $c_i^1 = c_1$ is the horizontal vibration isolator damping.

It follows from the principle of the superposition of solutions to differential equations that the special solution to this equation consists of two parts, and we set the special solution to this equation as follows:

$$\begin{cases} X = H_{11}(\omega_x)F_1 + H_{12}(\omega_z)F_2, \\ \varphi = H_{21}(\omega_x)F_1 + H_{22}(\omega_z)F_2, \\ F_1 = \sum_{m=1}^{n} p_m \sin(\omega_x t + \theta_m), \\ F_2 = \sum_{i=1}^{n} p_i \sin\left(\omega_z t + \vartheta_i\right) l_i \zeta_i. \end{cases} \tag{13}$$

In this form, assume that the unique solution to the first part is as follows:

$$\begin{cases} X_{11} = H_{11}(\omega_x)e^{j\left(\omega_x t + \theta_m - \alpha\right)}, \\ \varphi_{21} = H_{21}(\omega_x)e^{j\left(\omega_x t + \theta_m - \alpha\right)}, \end{cases} \tag{14}$$

where ω_x is the circular frequency (rad/s) and θ_m-α is the initial phase angle; $j^2 = -1$.

By bringing in (15), we obtain the following:

$$\begin{bmatrix} nk_1 - M\omega_x^2 + in\omega_x c_1 & nh\left(k_1 + j\omega_x c_1\right) \\ nh\left(k_1 + j\omega_x c_1\right) & n\left(h^2k_1 + l^2k_3\right) - J_\varphi\omega_x^2 + jn\omega_x\left(h^2c_1 + l^2c_3\right) \end{bmatrix}\begin{bmatrix} H_{11}(\omega_x)e^{-j\alpha} \\ H_{21}(\omega_x)e^{-j\alpha} \end{bmatrix} = \begin{bmatrix} 1 \\ 0 \end{bmatrix}. \tag{15}$$

Equation (15) is expressed in the following form:

$$[Z]\begin{bmatrix} H_{11}(\omega_x)e^{-j\alpha} \\ H_{21}(\omega_x)e^{-j\alpha} \end{bmatrix} = \begin{bmatrix} 1 \\ 0 \end{bmatrix}. \tag{16}$$

Then, we obtain the following:

$$\begin{bmatrix} H_{11}(\omega_x)e^{-j\alpha} \\ H_{21}(\omega_x)e^{-j\alpha} \end{bmatrix} = [Z]^{-1}\begin{bmatrix} 1 \\ 0 \end{bmatrix} = \frac{1}{|Z|}\begin{bmatrix} n\left(h^2k_1 + k_3l^2\right) - J_\varphi\omega_x^2 + jn\omega_x\left(c_1h^2 + c_3l^2\right) \\ -nh\left(k_1 + j\omega_x c_1\right) \end{bmatrix}. \tag{17}$$

The final result is as follows:

$$\begin{cases} H_{11}(\lambda)e^{-j\alpha} = \dfrac{h^2 + l^2\lambda_2^2 - \mu\lambda_1^2 + j\lambda_1\left(2\xi_1h^2 + 2\xi_2l^2\lambda_2\right)}{\Delta\lambda nk_1}, \\ H_{21}(\lambda)e^{-j\alpha} = \dfrac{\left[h\lambda_1^2 + 2j\lambda_1\xi_1\right]}{\Delta\lambda nk_1}, \end{cases} \tag{18}$$

where

$$\lambda = \mu\lambda_1^4 - \lambda_1^2\left(l^2\lambda_2^2 + \mu\lambda_2^2 + 4\xi_1\xi_2\lambda_2^2 l^2 + h^2\right) + l^2\lambda_2^2 - 2j\left(-\xi_2\lambda_1\lambda_2 l^2 - \xi_1\lambda_1^2\lambda_2 l^2 + \mu\xi_1\lambda_1^3 + \xi_1\lambda_1^3 h^2 + \xi_2\lambda_1^3\lambda_2 l^2\right). \tag{19}$$

The following parameters are introduced:

$$\begin{aligned} &\mu = \frac{J_\varphi}{M}; \lambda_1 = \frac{\omega_x}{\omega_1}; \lambda_2 = \frac{\omega_3}{\omega_1} \\ &\omega_1^2 = \frac{nk_1}{M}; \omega_3^2 = \frac{nk_3}{M}; \xi_1 = \frac{nc_1}{2M\omega_1} \\ &\xi_2 = \frac{nc_3}{2M\omega_3}; \delta_1 = \frac{P_k}{nk_1}; \delta_2 = \frac{P_k}{nk_1} l_i \zeta_i \end{aligned} \tag{20}$$

From Equation (21), $h_{11}(\lambda_x)e^{-j\alpha}$ represents the characteristics of a system with an input of force, and $h_{21}(\lambda_x)e^{-j\alpha}$ represents the characteristics of a system that outputs displacement; thus, its magnitude is $1/K$. According to the rules of complex arithmetic calculations,

$$|H_{21}(\lambda)| = \sqrt{\frac{\left(h\lambda_1^2\right)^2 + \left[\left(2j\lambda_1\xi_1\right)\right]^2}{\left[\mu\lambda_1^4 - \lambda_1^2\left(l^2\lambda_2^2 + \mu\lambda_2^2 + 4\xi_1\xi_2\lambda_2^2 l^2 + h^2\right) + l^2\lambda_2^2\right]^2 + \left[\lambda_1^3(2)\mu\xi_1 + 2\xi_1 h^2 + 2\xi_2\lambda_2 l^2\right) - \lambda_1(2)\xi_2\lambda_2 l^2 + 2\xi_1\lambda_1\lambda_2 l^2)\right]^2}}. \tag{21}$$

Equation (19) is rewritten as follows:

$$\begin{aligned} &H_{11}(\lambda_x) = |H_{11}(\lambda_x)|e^{j\phi_{11}(\lambda)} = \left(\frac{D_{11}^2 + E_{11}^2}{A^2 + B^2}\right)^{\frac{1}{2}} e^{j\phi_{11}(\lambda)} \\ &j\phi_{21}(\lambda) \\ &A = \mu\lambda_1^4 - \lambda_1^2\left(l^2\lambda_2^2 + \mu\lambda_2^2 + 4\xi_1\xi_2\lambda_2^2 l^2 + h^2\right) + l^2\lambda_2^2 \\ &B = \lambda_1^3\left(2\mu\xi_1 + 2\xi_1 h^2 + 2\xi_2\lambda_2 l^2\right) - \lambda_1\left(2\xi_2\lambda_2 l^2 + 2\xi_1\lambda_1\lambda_2 l^2\right) \\ &D_{11} = \frac{h^2 + l^2\lambda_2^2 - \mu\lambda_1^2}{nk_1} \\ &E_{11} = \frac{\lambda_1\left(2\xi_1 h^2 + 2\xi_2 l^2\lambda_2\right)}{nk_1} \\ &D_{21} = \frac{h\lambda_1^2}{nk_1} \\ &E_{21} = \frac{2j\lambda_1\xi_1}{nk_1} \\ &H_{21}(\lambda_x) = |H_{21}(\lambda_x)|e^{j\phi_{21}(\lambda)} = \left(\frac{D_{21}^2 + E_{21}^2}{A^2 + B^2}\right)^{\frac{1}{2}} e \quad \phi_{11}(\lambda) = \arctan\frac{AE_{11} + BD_{11}}{AD_{11} - BE_{11}} \quad \phi_{21}(\lambda) = \arctan\frac{AE_{21} + BD_{21}}{AD_{21} - BE_{21}}. \end{aligned} \tag{22}$$

The special solution to the first part of the differential equation can be expressed as follows:

$$\begin{cases} X_{11} = H_{11}(\omega_x)F_1 = p_k|H_{11}(\lambda)|\sin(\omega_x t + \theta_m + \phi_{11}(\lambda)), \\ \varphi_{21} = H_{21}(\omega_x)F_1 = p_k|H_{21}(\lambda)|\sin(\omega_x t + \theta_m + \phi_{21}(\lambda)). \end{cases} \tag{23}$$

In (22), $|h_{21}(\lambda)|$ and $|h_{22}(\lambda)|$ are the power amplification factors, and $\varphi_{21}(\lambda)$ and $\varphi_{22}(\lambda)$ are the phase factors.

Similarly, the special solution to the second part of the equation is as follows:

$$\begin{cases} X_{12} = H_{12}(\omega_z)e^{j(\omega_z t + \vartheta_i - \beta)}, \\ \varphi_{22} = H_{22}(\omega_z)e^{j(\omega_z t + \vartheta_i - \beta)}, \end{cases} \tag{24}$$

where ω_z is the circular frequency and $\vartheta_i - \beta$ is the initial phase angle . $j^2 = 1$.

$$\begin{aligned} H_{12}(\lambda) &= |H_{12}(\lambda)|e^{j\phi_{12}(\lambda)} = \left(\frac{D_{12}^2 + E_{12}^2}{A^2 + B^2}\right)^{\frac{1}{2}} e^{j\phi_{12}(\lambda)}, \\ H_{22}(\lambda) &= |H_{22}(\lambda)|e^{j\phi_{22}(\lambda)} = \left(\frac{D_{12}^2 + E_{12}^2}{A^2 + B^2}\right)^{\frac{1}{2}} e^{j\phi_{22}(\lambda)}. \end{aligned} \tag{25}$$

Repeating the first part of the procedure yields the following:

$$\begin{cases} D_{12} = -\dfrac{h\lambda_1^2}{nk_1}, E_{12} = -2\lambda_1\xi_1/nk_1 \\ D_{22} = \dfrac{(1-\lambda_1^2)}{nk_1}, E_{22} = 2\lambda_1\xi_1/nk_1 \\ \phi_{21}(\lambda) = \arctan\dfrac{AE_{12} + BD_{12}}{AD_{12} - BE_{12}}, \phi_{22}(\lambda) = \arctan\dfrac{AE_{22} + BD_{22}}{AD_{22} - BE_{22}}. \end{cases} \tag{26}$$

The special solution to the second part of the differential equation can be written as follows:

$$\begin{cases} X_{12} = H_{12}(\omega)F_2 = p_i l_i \zeta_i |H_{12}(\lambda)| \sin(\omega_z t + \vartheta_i + \phi_{12}(\lambda)) \\ \varphi_{22} = H_{22}(\omega)F_2 = p_i l_i \zeta_i |H_{22}(\lambda)| \sin(\omega_z t + \vartheta_i + \phi_{22}(\lambda)). \end{cases} \tag{27}$$

According to the superposition principle of the differential equation solution and by combining the above solution results, the final solution to the differential equation for the horizontal and rotational response forces of the multi-dimensional vibration isolator system is as follows:

$$\begin{cases} X = X_{11} + X_{12} = \sum_{m=1}^{n} p_m|H_{11}(\lambda)|\sin(\omega_x t + \theta_m + \phi_{11}(\lambda)) + \sum_{i=1}^{n} p_i l_i \zeta_i |H_{12}(\lambda)|\sin(\omega_z t + \vartheta_i + \phi_{12}(\lambda)) \\ \varphi = \varphi_{21} + \varphi_{22} = \sum_{m=1}^{n} p_m|H_{21}(\lambda)|\sin(\omega_x t + \theta_m + \phi_{21}(\lambda)) + \sum_{i=1}^{n} p_i l_i \zeta_i |H_{22}(\lambda)|\sin(\omega_z t + \vartheta_i + \phi_{22}(\lambda)), \end{cases} \tag{28}$$

where $h_{12}(\lambda) = h_{21}(\lambda)$; u_{cm} is the vertical vibration response at the center of the vibration isolator system; and l_i represents the horizontal distance from the other position points on the vibration isolator to the center point.

Equation (27) shows that when the vibration isolation system is under the action of nonuniform excitation, the horizontal vibration response of the vibration isolation system is affected by the common effect of horizontal excitation and vertical excitation; the rotation response of the VIP is also affected by the common effect of horizontal excitation and vertical excitation; and the vertical displacement response at different positions on the VIP system can be expressed as $Z = u_{\mathrm{cm}} \pm l_i\varphi$.

3. Parametric Dynamic Characterization of Vibration Isolator Systems

The vibration isolation performance is defined in terms of the logarithmic power amplification factor, $\beta(\lambda) = lg|h_i(\lambda)|$, where $\beta(\lambda)$ is the defined logarithmic power amplification factor and $|h_i(\lambda)|$ is the absolute value of the power amplification factor; only three power amplification factor parameters, $h_{11}(\lambda)$, $h_{12}(\lambda)$ and $h_{22}(\lambda)$, need to be discussed here.

3.1. Theoretical Analysis of the Stability Parameters of Vibration Isolator Systems. To improve the stability of the vibration isolation system and reduce the adverse effects caused by the rotation of the vibration isolation system, the factors affecting the stability of the VIP system, such as the length of the VIP, the number of vibration isolator arrangements and the location of the horizontal vibration isolator arrangement, are analyzed.

3.1.1. Effect of the Length of the Vibration Isolator on the Stability of the Vibration Isolator System. The following fixed parameters were set for analysis: $N = 2$, $h = 0.2$ m, $\xi_1 = 0.065$, $\xi_2 = 0.05$, and $\lambda_2 = 1.5$. With the above-fixed parameters set, four working conditions were considered with vibration isolators of lengths $l = 3$ m, 5 m, 10 m, and 20 m. The variation in the logarithmic power amplification coefficient under different vibration isolator lengths is shown in Figure 3 below.

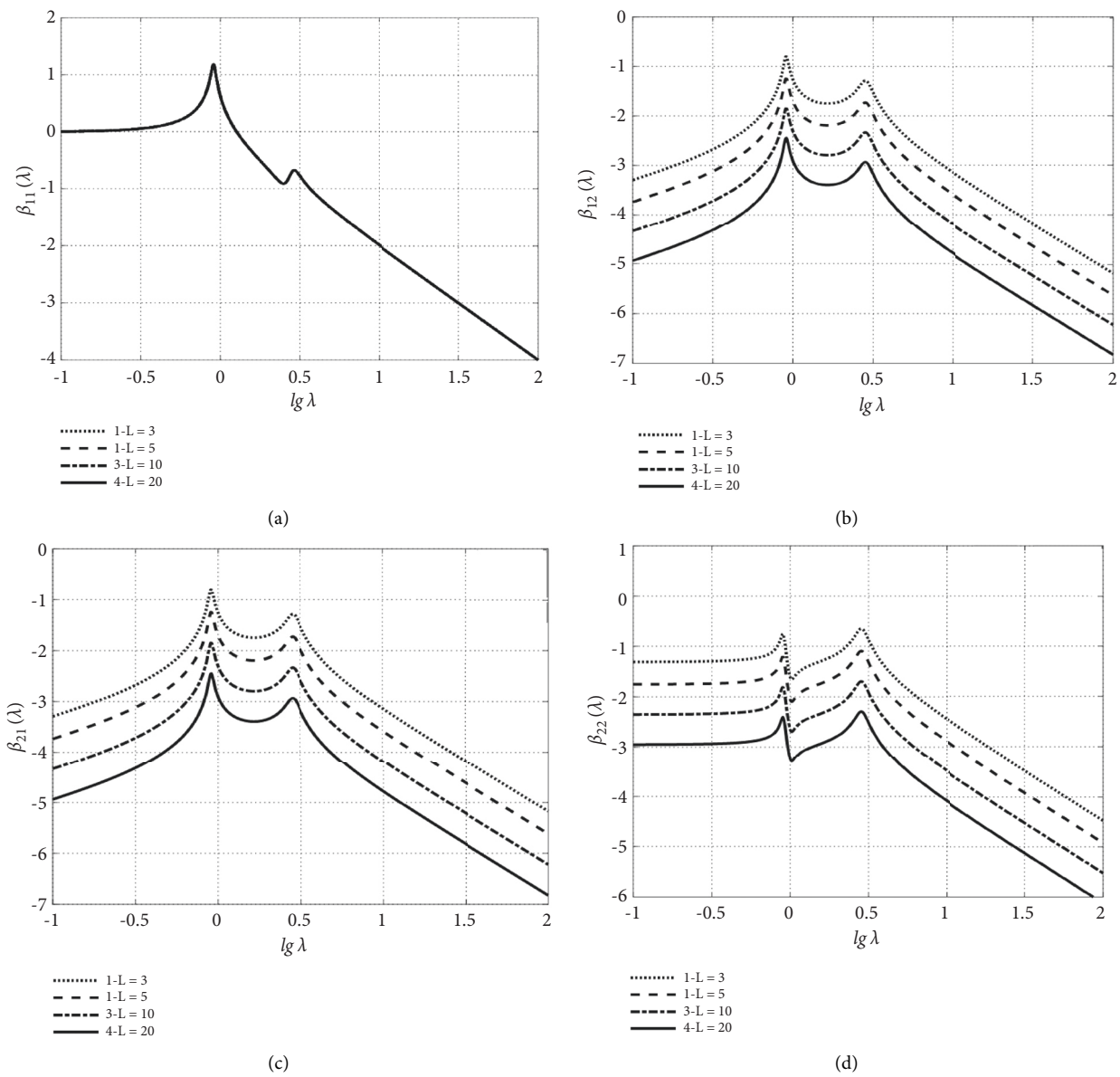

Figure 3: Logarithmic dynamic amplification factor under different vibration slab length changes.(a) logarithmic dynamic amplification factor β_{11} (b) logarithmic dynamic amplification factor β_{12}.(c) logarithmic dynamic amplification factor β_{21} (d) logarithmic dynamic amplification factor β_{22}.

Figure 3(a) shows that the logarithmic dynamic amplification factor β_{11} remains the same as the length of the vibration isolator increases; Figure 3(b)–3(d) show that the logarithmic dynamic amplification factors β_{12}, β_{21}, and β_{22} decrease as the length of the vibration isolator increases. This means that as the length of the vibration isolator increases, the rotation response of the vibration isolation system decreases, and the vibration isolator system is less affected by its own rotation; the horizontal vibration of the vibration isolator is less affected by the rotation of the system.

3.1.2. Effect of the Number of Vibration Isolator Arrangements on the Stability of the Vibration Isolator System. The fixed parameters set are as follows: $l = 3$ m, $h = 0.2$ m, $\xi_1 = 0.065$, $\xi_2 = 0.05$, and $\lambda_2 = 1.5$. Based on the fixed-parameter set, the number of vibration isolators arranged under the platform is considered to be $N = 2$, 4, 6, and 8 for the four working conditions. The variation law of the logarithmic dynamic amplification coefficient under different numbers of vibration isolators is shown in Figure 4.

Figure 4(a) shows that with the increase in the number of spring isolators of the vibration isolation system, the logarithmic dynamic amplification coefficient β_{11} remains stable; Figures 4(b), 4(c) and 4(d) shows that with the increase in the number of spring isolators in the vibration isolation system, the logarithmic dynamic amplification coefficients

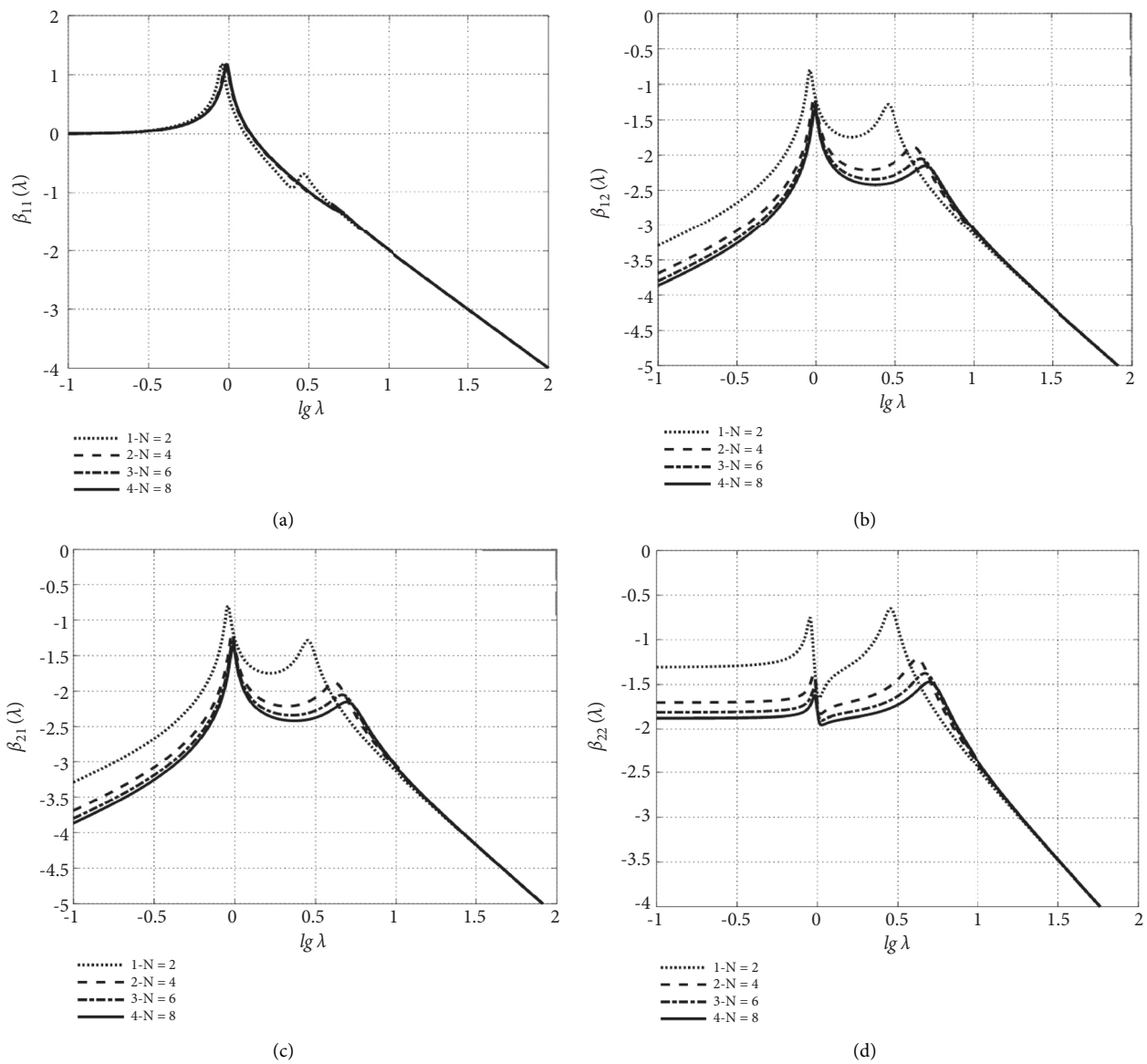

Figure 4: The variation law of the logarithmic dynamic amplification coefficient under different numbers of vibration isolators: (a) logarithmic dynamic amplification factor β^{11},(b) logarithmic dynamic amplification factor β^{12}, (c) logarithmic dynamic amplification factor β_{21}, and (d) logarithmic dynamic amplification factor $\beta_{2.}$

β_{12}, β_{21} and β_{22} gradually decrease. With the increase in the number of isolators, the rate of decrease in the logarithmic dynamic amplification coefficient gradually decreases. As a result, the horizontal response of the vibration isolation system is less affected by the rotation of the vibration isolator, and the impact on the stability of the VIP system is also gradually reduced.

3.1.3. Effect of the Position of the Horizontal Vibration Isolator on the Stability of the Vibration Isolation Plate System. The fixed parameters are set as follows: $l = 3$m, $\xi_1 = 0.065$, $\xi_2 = 0.05$, $\lambda_2 = 1.5$, and $N = 2$. Based on the fixed parameters, four working conditions are considered for the horizontal vibration isolator position: $h = 0.2$ m, 0.5 m, 0.8 m, and 1.0 m. The variation law of the logarithmic power amplification coefficient under different horizontal vibration isolator arrangement positions is shown in Figure 5.

Figure 5(a) shows the logarithmic power amplification coefficient. β_{11} does not change as the value of h increases. Figure 5(b) and 5(c) shows that β_{12} increases as the value of h increases. Figure 5(d) shows that β_{22} changes in a three-step pattern as h increases: before the first peak point, β_{22} increases as the value of h increases, after the second peak point, β_{22} increases as the value of h value increases, after the second peak point, β_{22} decreases with the increase in h value, and after the third peak point, β_{22} tends to be the same. Thus, considered together, reducing the value of the horizontal vibration isolator position h reduces the rotational response of the vibration isolator.

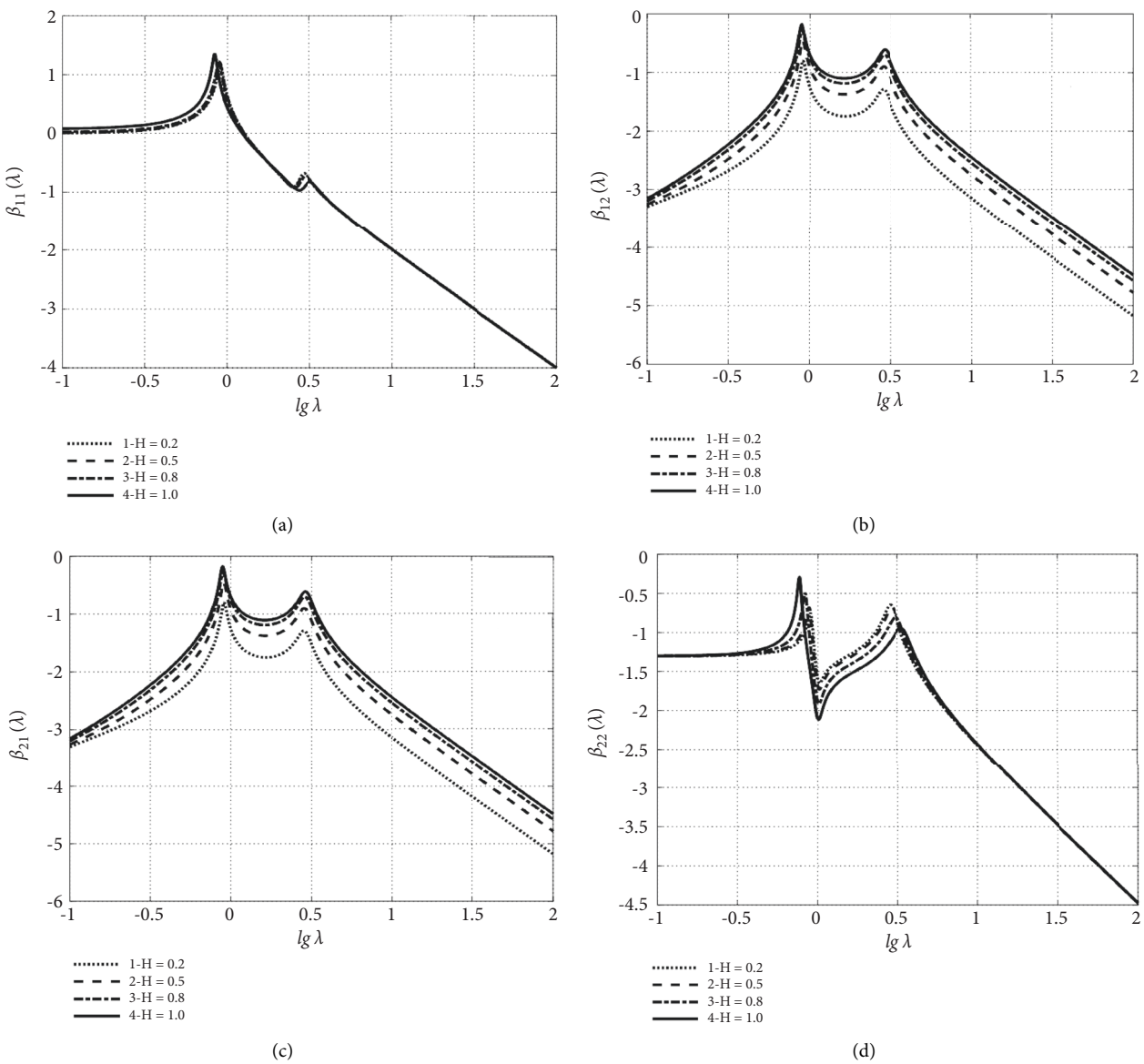

Figure 5: The variation law of the logarithmic power amplification coefficient under different horizontal vibration isolator arrangement positions: (a)logarithmic dynamic amplification factor $\beta_{11,}$ (b)logarithmic dynamic amplification factor β_{12}, (c)logarithmic dynamic amplification factor β_{21}, and (d)logarithmic dynamic amplification factor $\beta_{22.}$

Among the above parameters, the logarithmic power amplification coefficient β_{11} is unaffected; β_{21} and β_{22} decrease with the increase in the length of the VIP system and decrease with the increase in the number of spring vibration isolators; β_{21} increases with the increase in the horizontal vibration isolator position h value, and β_{22} shows a three-stage change form of first increasing, then decreasing, and finally keeping no edge with the increase in h value.

4. Verification of the Numerical Analysis of the Vibration Isolator System

A numerical model of the VIP is established to transiently analyze the vibration of the VIP system under the action of simple harmonic excitation. A finite-element model of the vibration isolator system is established, as shown in Figure 6. To simplify the analysis process, only the numerical simulation of the vibration of the VIP in the vertical and horizontal X directions is considered.

The model consists of a VIP, spring vibration isolators and a base platform, from top to bottom. The VIP has a length of 6 m, a thickness of 10 cm, a width of 3 m, a density of $\rho = 2700\,\mathrm{kg/m^3}$, and a modulus of elasticity $E = 3.0 \times 10^{10}$ Pa. The bottom and ends of the vibration isolator (X direction) are evenly arranged with different numbers of spring vibration isolators according to the study conditions, and the horizontal isolators are at the same height as the center of gravity of the VIP. The spring stiffness of the isolator is 8×10^6 N/m, and the damping coefficient is 0.05. The ShELL63 unit is used to simulate the VIP unit, and

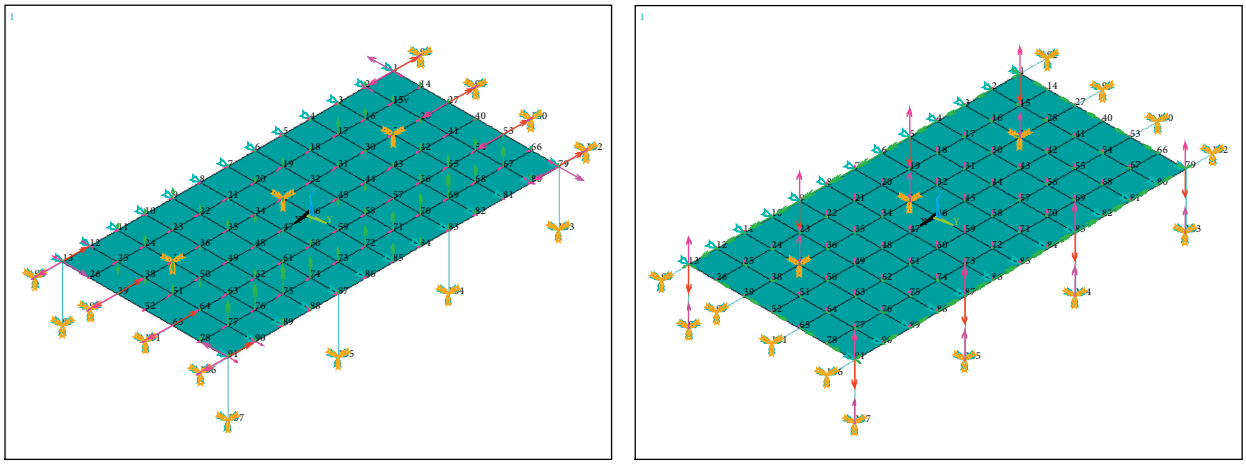

Figure 6: Finite element model of vibration isolation system.

a COMBIN14 unit is used to simulate the spring isolator unit, with the boundary conditions set with all constraints at the bottom of the base plate, all constraints set on both sides of the horizontal X direction of the VIP, and only DY constraints set on both sides of the horizontal Y direction of the VIP.

The frequency f_i values taken in this study are 1 Hz, 5 Hz, and 15 Hz at low frequencies, and the load excitation used in the numerical simulation is 800 N. The fitted load is loaded onto the model with an integration step of 0.005 s to obtain the vibration response of the vibration isolator system at different pickup points.

4.1. Vertical Response of a Vibration Isolator System under Uniform Excitation. Assuming that the initial phase of the simple harmonic excitation load is 0, the fixed parameters are set as follows: the horizontal and vertical directions of the VIP are uniformly arranged with eight vibration isolators, the horizontal vibration isolators are arranged with the center of gravity of the VIP at the same height, the damping ratio of the vibration isolators is 0.05, the spring stiffness is 8.0 MN/m, the thickness of the VIP is 10 cm, the support distance is 3@2 m, and the external excitation is assumed to be applied to the VIP by the arranged vertical vibration isolators. Comparing the vibration isolator to the VIP, the results are shown in Figure 7 and Table 1.

Figure 7 shows the vibration response of the vibration isolator system at 1, 5, and 15 Hz under simple harmonic excitation conditions through ANSYS numerical simulation and theoretical derivation of the vibration pickup point. The figure shows that the time course curve of the vertical acceleration at the pickup point obtained from the numerical simulation and the time course curve obtained from the theoretical derivation are basically the same, and Table 1 shows that the data obtained from the numerical simulation and the theoretical derivation are also very close to each other, which verifies the accuracy of the theoretical derivation.

Table 1 shows that the external excitation frequency of 1, 5, and 15 Hz, and the difference between the simulated values and the theoretically derived results gradually increase. As this study focuses on the vibration isolation characteristics of the VIP system under the low-frequency vibration response of the building floor caused by a train, the numerical simulation is still able to simulate the vibration of the VIP more accurately.

5. Vibration Isolation Analysis of VIP Systems under the Action of Running Trains

By establishing a three-dimensional finite element model of the train-track-soil-building-VIP system, the vibration isolation effect of the floor VIP system under train operation and the effect of structural parameter changes on the vibration isolation of the floor VIP are analyzed in two ways. The whole model is divided into two subsystem models for the convenience of calculation, i.e., the train-roadbed model and the foundation soil-buildings-VIP system model. As the building floor is dominated by vertical vibration [16], this study only analyses the vertical vibration isolation of the vibration platform system.

5.1. Train-Track System Model. The dynamic analysis model of the train-track system consists of the vehicle model and the track model, which are in line with the Hertz wheel-rail contact relationship. During the operation of the train, the moving axle weight produces both vertical and lateral forces on the bottom roadbed, and the vertical action is much larger than the lateral action; thus, only the vertical vibration needs to be considered in the analysis process, and the lateral vibration is ignored.

5.1.1. Train Models. A model train is normally made up of several locomotives. Each locomotive is a multi-degree-of-freedom vibration system consisting of a body, a bogie, a wheel-set, two-series springs, and dampers. Each locomotive and bogie has only two degrees of freedom, nod, and float, and the center of gravity of the locomotive is

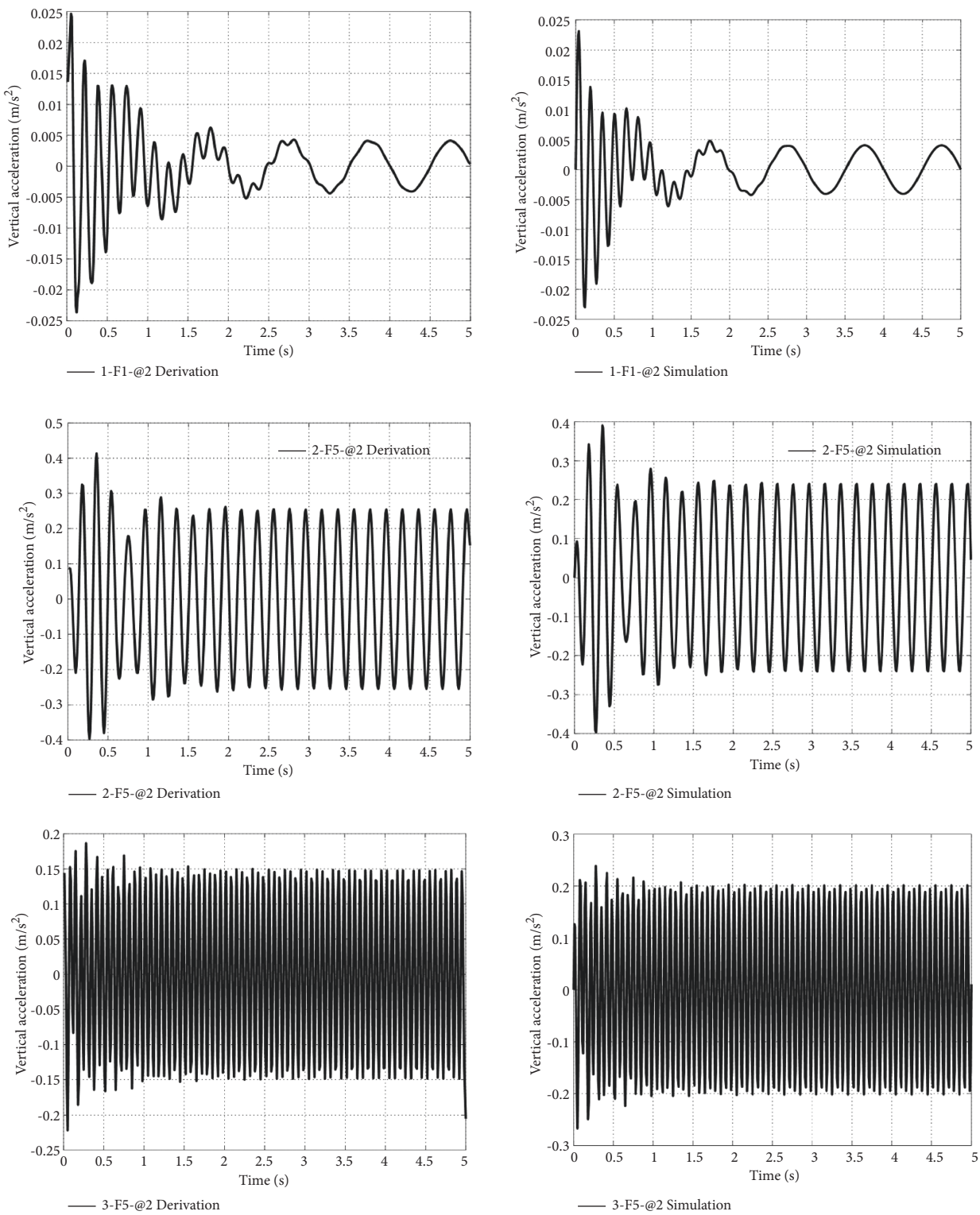

Figure 7: Comparison of theoretical derivation and numerical analysis of vibration point under multi-point excitation.

represented by the coordinates Z_c and φ_c; the center of gravity of the body is represented by the coordinates Z_T and φ_T; and the wheel pair has only one degree of freedom, which can be represented by Z_W.

5.1.2. Track Model. The rail model as a whole can be considered a triple mass-spring damper system. The main components of the system are the rail, plastic mat, rail sleeper, and bed reference mass. The rail is assumed to be an

Table 1: Comparison of simulation results and theoretical derivation of points under different frequency excitations.

External excitation frequency (Hz)	Displacement ($\times 10^{-4}$m)		Point acceleration($\times 10^{-1}$ m/s^2)		Vibration level(dB)	
	Numerical simulation	Theoretical derivation	Numerical simulation	Theoretical derivation	Numerical simulation	Theoretical derivation
1	1.036	1.024	0.0437	0.0406	72.81	72.17
5	2.677	2.447	2.578	2.426	108.23	107.70
15	0.233	0.235	1.500	2.028	103.52	106.14

Table 2: Soil properties.

Type of soil	Depth(m)	Modulus of elasticity/Mpa	Poisson's ratio	Damping ratio	Density/Kg/m^2	Shear wave speed s/m·s^{-1}	Compression wave speed s/m·s^{-1}
Mixed fill	1	191	0.36	0.03	1980	203	411
Powdered clay	3	268	0.33	0.03	1990	216	475
Coarse sand	4	394	0.23	0.03	1918	260.2	416.0
Gravelly sand	32	430	0.29	0.03	2122	351.8	879.5

infinitely long beam on elastic supports, but a suitable length is chosen for the specific analysis. In the numerical analysis, the mass of the rail forms the nodal mass matrix M_r in the finite element, the stiffness forms the nodal stiffness matrix K_r in the finite element, and the damping matrix can be represented by the Riley damping $Cr = \alpha M_r + \beta K_r$. A rail node has two degrees of freedom, i.e., vertical and corner, and one vertical displacement degree of freedom at each elastic support point. The rail system dynamics parameters are detailed in the literature [20].

5.2. Finite Element Model of the Soil-Building-Vibration Isolator System

5.2.1. Soil Model. Vibrations and microvibrations of the soil caused by rail traffic, the soil strain, are treated as an elastic deformation phase; the effect of nonlinear factors in the soil material is not considered.

The dimensions of the model are set as follows: the width of the foundation is 140 m in the vertical X direction of the track, the length of the foundation is 100 m along the Y direction of the track, and the depth of the foundation soil h is 40 m. The model soil parameters are shown in Table 2 below.

The simulated boundary is an artificial viscoelastic boundary, which is implemented by arranging the spring and damping system on the truncated boundary of the soil model, taking the form in (28):

$$\begin{cases} K_{BT} = \alpha_T \dfrac{G}{R}, C_{BT} = \rho c_s \\ K_{BN} = \alpha_N \dfrac{G}{R}, \quad C_{BN} = \rho c_p \end{cases}, \tag{29}$$

where K_{BT} and K_{BN} represent the spring normal stiffness and tangential stiffness, respectively; R is the distance from the wave source to the artificial boundary; c_s and c_p represent the shear and compressional wave velocities in the medium, respectively; G is the medium shear modulus; ρ is the density of the foundation soil; α_T and α_N represent the tangential and normal viscoelastic artificial boundary parameters, respectively; and the damping ratio $\xi_0 = 0.03$ in the soil body.

5.2.2. Finite Element Model of the Soil-Building-Vibration Isolator System. The building is a 12-story cast-in-place reinforced concrete frame structure, and the column network arrangement is shown in Figure 8 below. The building has 12 stories above ground with a floor height of 3 m and 1 story below ground with a floor height of 4 m. The column cross-sectional dimensions of the 1st to 4th stories are 600×600 mm, with a main beam cross-section of 350×600 mm and a secondary beam cross-section of 250×400 mm; the column cross-sectional dimensions of the 5th to 12th stories are 500×500 mm, with a main beam cross-section and secondary beam cross-section of 250×400 mm.

According to the design plan, the frame structure has a horizontal longitudinal three-span structure of 6 m-2 m-6 m dimensions, and the length of all seven openings along the horizontal transverse direction is 6 m. The building frame beams, columns, floor slabs, and continuous underground walls are all made of C30 concrete with a modulus of elasticity of 30 kN/mm^2 and a reinforced concrete material with a density of $\rho = 2700$ kg/m^3. The basement uses a box-shaped foundation with a basement floor slab of 400 mm and walls that are 180 mm thick.

The VIP system is set at the mid-span of each floor of the building. The finite element model parameters are as follows: a platform length of 6 m, a thickness of 0.1 m, a platform width of 3.0 m, several vibration isolators arranged under the plate, a density ρ of 2700 kg/m^3, and a concrete strength of C30; the VIP is simulated using SHELL63 units, and spring vibration isolators are simulated using COMBIN14 units. The modulus of elasticity of the platform is $E = 3.0 \times 10^{10}$ Pa, the vertical stiffness of the spring is $K = 8.0 \times 10^6$ N/m, and the damping ratio coefficient is 0.05.

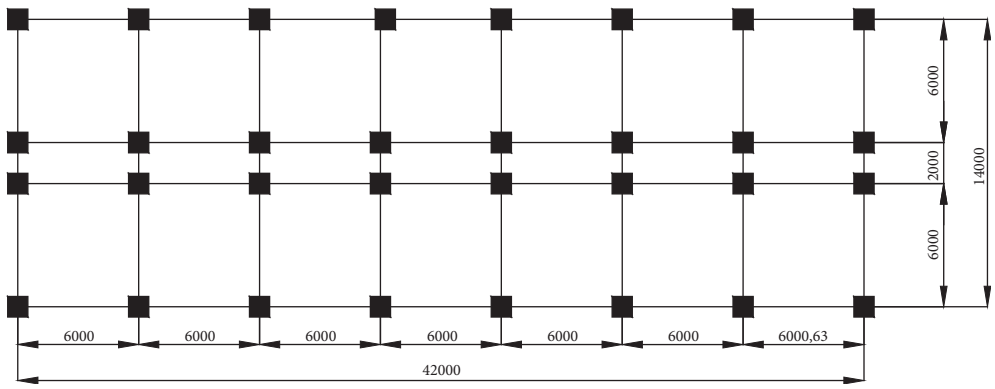

Figure 8: The schematic diagram of building plane (mm).

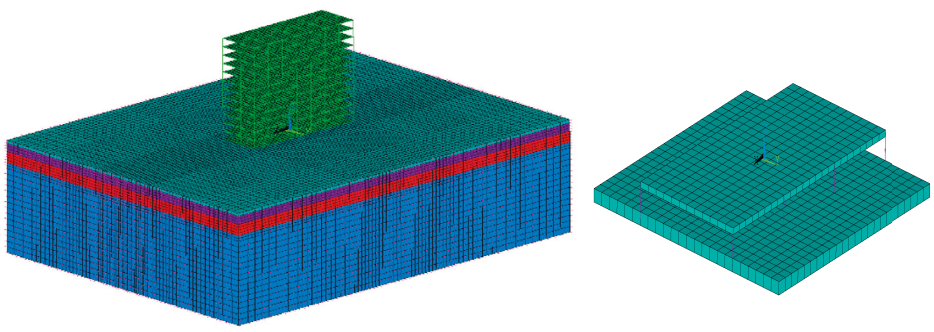

Figure 9: Soil-building-isolation slab finite element model.

The soil-building contact surfaces in this study mainly take the form of coordinated deformation contacts. The three-dimensional finite element model of the foundation soil-contact surface-building-vibration isolator interaction is shown in Figure 9.

5.3. Vibration Isolation Analysis of a VIP under the Action of Running Trains

5.3.1. Train Load Simulation. The train type is CRH2 rolling stock, and the CRH2 single-section vehicle parameters are detailed in the literature [4]. The train-track model program was used to input the parameters of this type of train and then obtain the wheel-track excitation loads for two operating conditions of 90 km/h and 150 km/h, as shown in Figure 10. Then, the excitation is input into the soil-building finite element model, and the vibration acceleration level VL is used as the evaluation criterion for building vibrations.

5.3.2. Comparative Analysis of the Vibration Responses of a Building Floor System with and without Vibration Isolators. The fixed parameters are set, and the working conditions are as follows: the train speed is 150 km/h, eight vibration isolators are evenly arranged under the platform, the spring stiffness is 0.2 MN/m, the vibration isolator damping ratio is 0.05, the thickness of the VIP is 10 cm, the support distance is 3@2 m, the VIP size is kept the same as above, and the distances between the train vibration source and the building are 15 m, 21 m and 27 m for the three working conditions. Due to space limitations, the vertical vibration responses of the first floor of the building with and without the VIP are only studied in this study, as shown in Figure 11.

Figure 12 shows the time courses of acceleration at the pickup point for the first floor of the building with and without vibration isolators at different source distances (15 m, 21 m, and 27 m) and train speeds of 150 km/h·m/s^2.

The acceleration time domain analysis shown in Figure 12 and Table 3 shows that the vibration isolation efficiency of the vibration isolation system for the acceleration response can reach approximately 85%, and the vibration isolation efficiency of the VIP system for the floor vibration response is not affected by the vibration source distance. Therefore, considered together, the VIP system is suitable for vibration isolation of low-frequency vibrations of building floors caused by trains, and the vibration isolation effect is very significant.

5.4. Influence of VIP Structural Parameters on the Vibration Isolation Effect.

Variations in the structural parameters of vibration isolators, such as the number of isolators, spring stiffness, isolator damping, thickness and other parameters, affect the vibration isolation effect. The vibration response of the vertical pickup point on the first floor of the building is analyzed for two vehicle speeds of 90 km/h and 150 km/h.

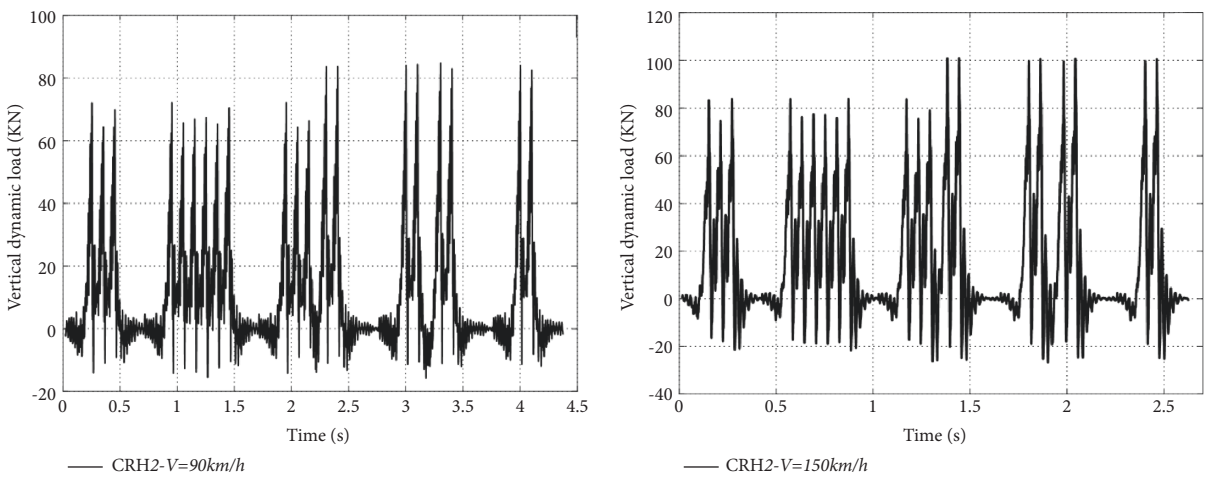

Figure 10: Wheel-rail excitation histories at different vehicle speeds.

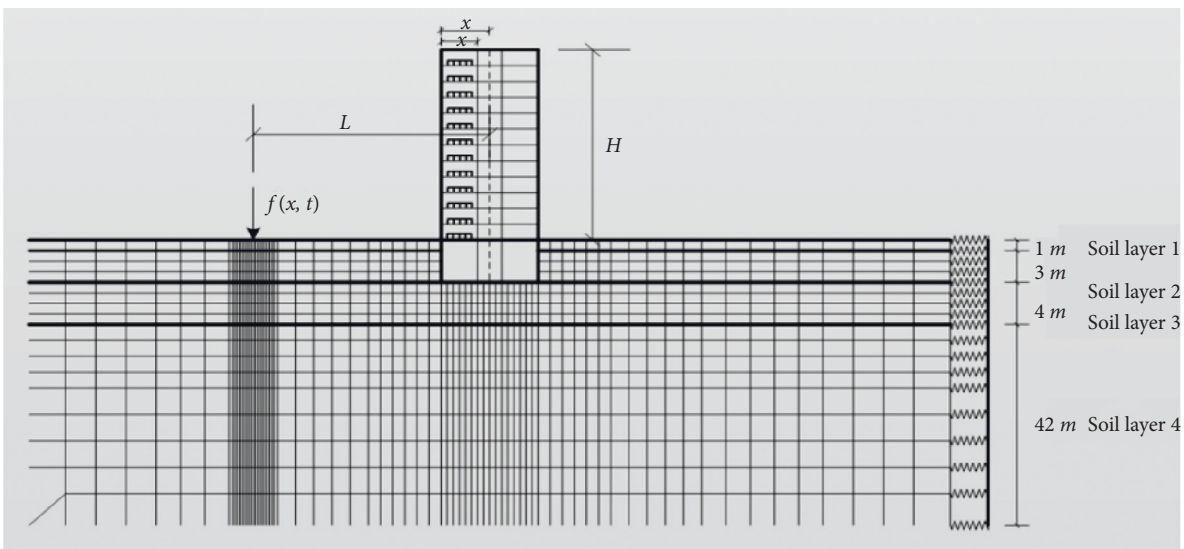

Figure 11: Schematic diagram of soil-building-isolation slab finite element analysis grid.

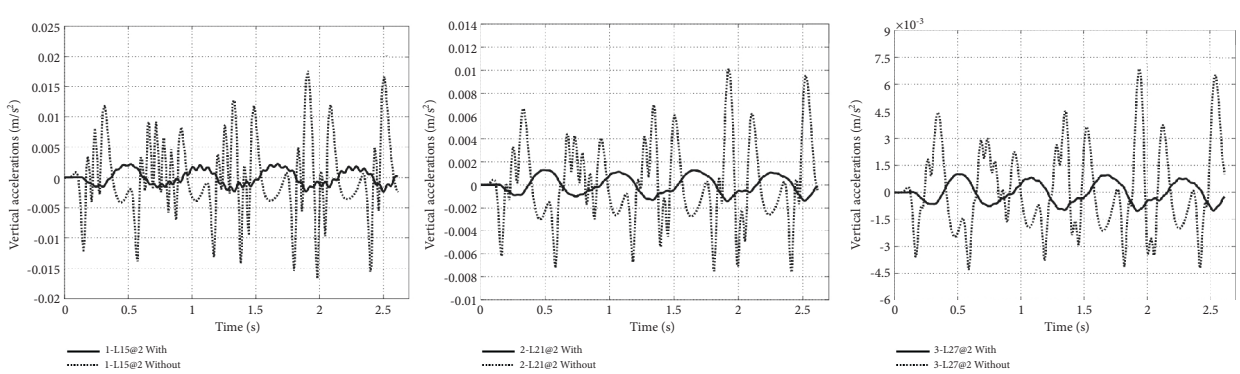

Figure 12: Vertical vibration isolation of the vibration isolation slab system 15m, 21m, and 27m from the center.

Table 3: Vibration comparison with and without vibration isolation system in different source distances.

Vibration source distance	($l = 15$ m)			($l = 21$ m)			($l = 27$ m)		
(Before/After) isolation	Before	After	T_r(%)	Before	After	T_r(%)	Before	After	T_r(%)
Acceleration($\times 10^{-3}$ m/)	17.620	2.390	13.56	10.122	1.409	13.92	6.56	1.023	14.92

Table 4: Number of vibration legislators conditions.

Condition number	Cases	Isolator thickness H(cm)	Support distance S(m)	Spring stiffness $k(MN/m)$	Number of isolators
1	N4@6	10	1@6	0.2	4
2	N8@2	10	3@2	0.2	8
3	N16@1	10	6@1	0.2	14

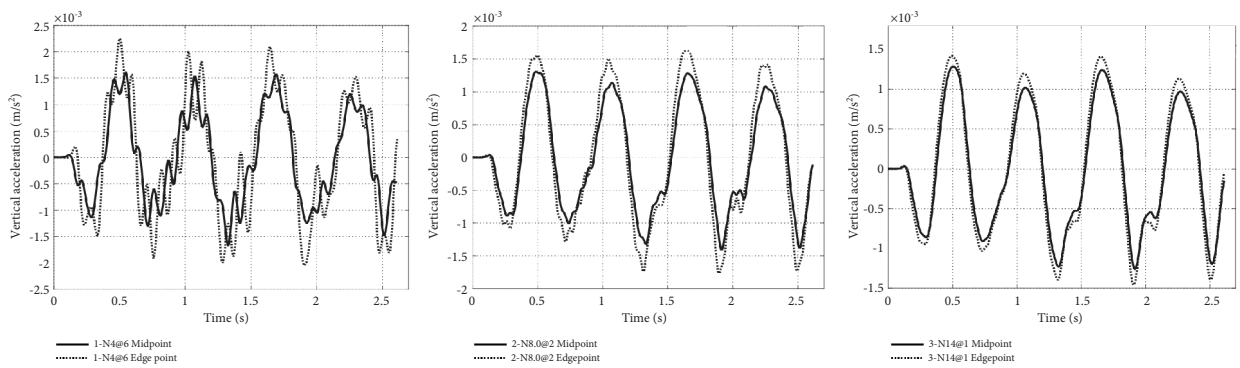

Figure 13: Vertical acceleration response of different pickup points when the number of isolators changes.

5.4.1. Influence of the Number of Vibration Isolators. Setting the fixed parameters shown in Table 4, the number of vibration isolators is $N = 4$, 8, 14. Figure 13 shows the acceleration time range of the vibration isolator center pickup point and edge pickup point under the three working conditions.

Figure 13 shows that when the number of isolators increases, the acceleration response at the midpoint and edge points of the vibration isolator decreases. An increase in the number of isolators is beneficial to reducing the vibration isolator acceleration response, but the reduction effect is less obvious.

5.4.2. Steel Spring Stiffness Effects. The damping coefficient of the vibration isolator is 0.05, the thickness of the vibration isolator is 10 cm, the vibration isolator distance is 3.0 m, and the vertical stiffness of the spring is $K = 0.32$ MN/m.

The results can be seen in Figure 14. When the spring stiffness increases, the acceleration response of the vibration isolator gradually increases. however, the change in spring stiffness has a greater effect on the vibration response of the vibration isolator; when the spring stiffness of the vibration isolator is beyond a specific range, the vibration of the vibration isolator is accompanied by an increase in vibration and acceleration response. When the spring stiffness of the vibration isolator exceeds a specific range, not only is there no vibration isolation effect, but there may also be a slight "amplification" phenomenon.

5.4.3. Effect of the Vibration Isolator Damping Ratio. The employed train speeds are 90 km/h and 150 km/h. Eight vibration isolators are arranged under the slab, and the spring stiffness of the vibration isolators is 0.6 M, the thickness of the vibration isolators is 10 cm, and the vibration isolation distance is 2.0 m. The damping ratios of the vibration isolators are set to 0.01, 0.05, 0.10, and 0.15. The damping ratio of the concrete vibration isolator is 0.05. The acceleration time range curve and spectrum curve of the vibration pickup point of the vibration isolator on the first floor of the building with different vibration isolator damping ratios are shown in Figure 15.

As shown in Figure 15, as the damping ratio increases, the time it takes for the vibration isolator system response to reach the steady state decreases, and the vibration decay time of the vibration isolator decreases as the damping ratio increases.

5.4.4. Effect of Vibration Isolator Thickness. The employed train speeds are 90 km/h and 150 km/h, with eight vibration isolators arranged under the platform. The vibration isolator damping coefficient is 0.05, and the spring stiffness is 0.2 MN/m. The thicknesses of the VIP re $h = 10$ cm, 15 cm,

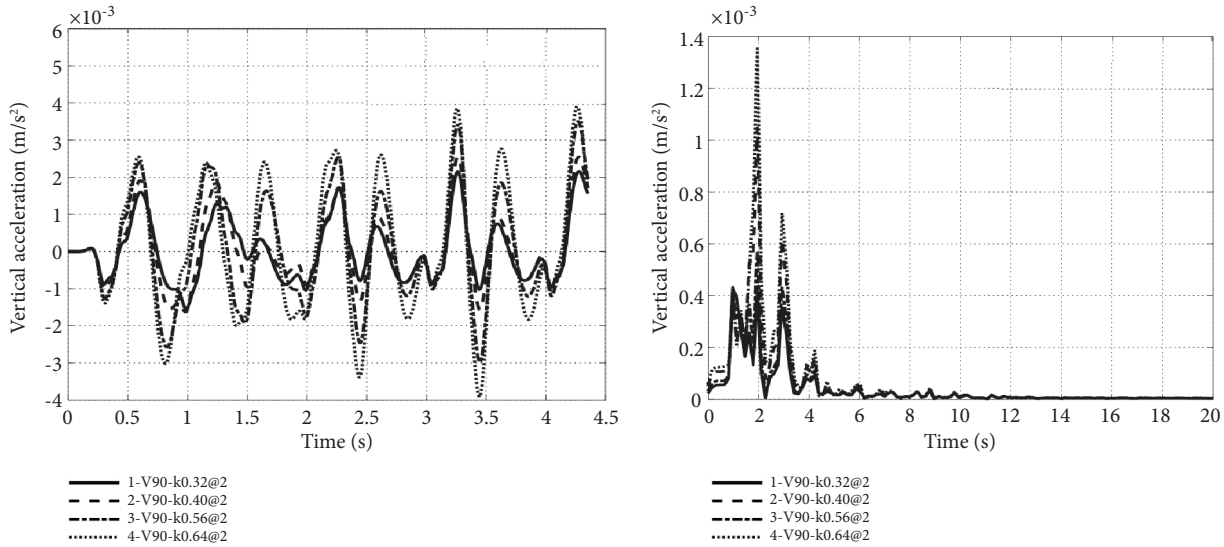

Figure 14: Vertical acceleration response of vibration pickup point under change of spring stiffness.

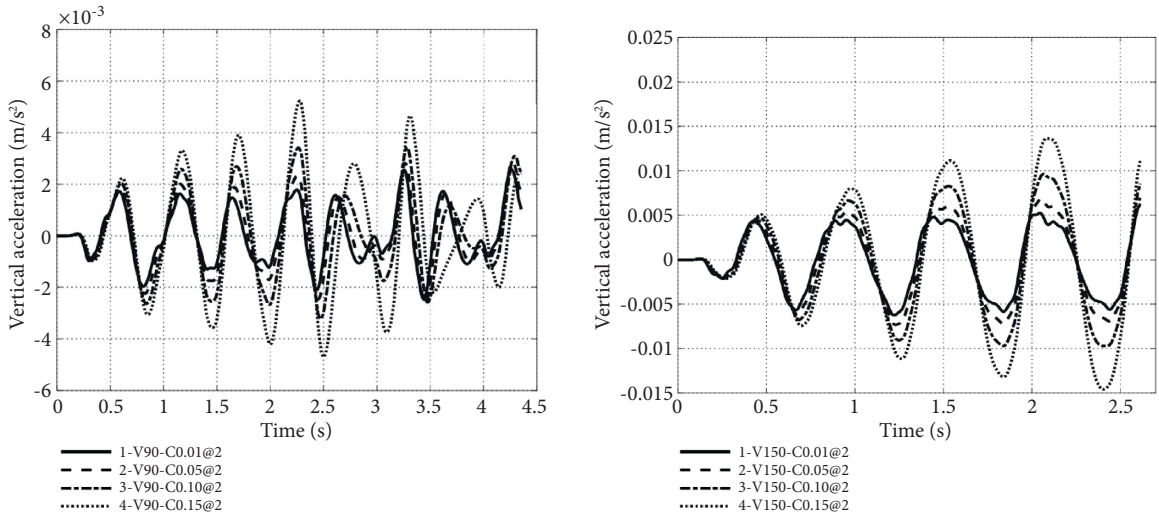

Figure 15: Vertical acceleration response of pickup point under change of damper ratio of vibration isolator.

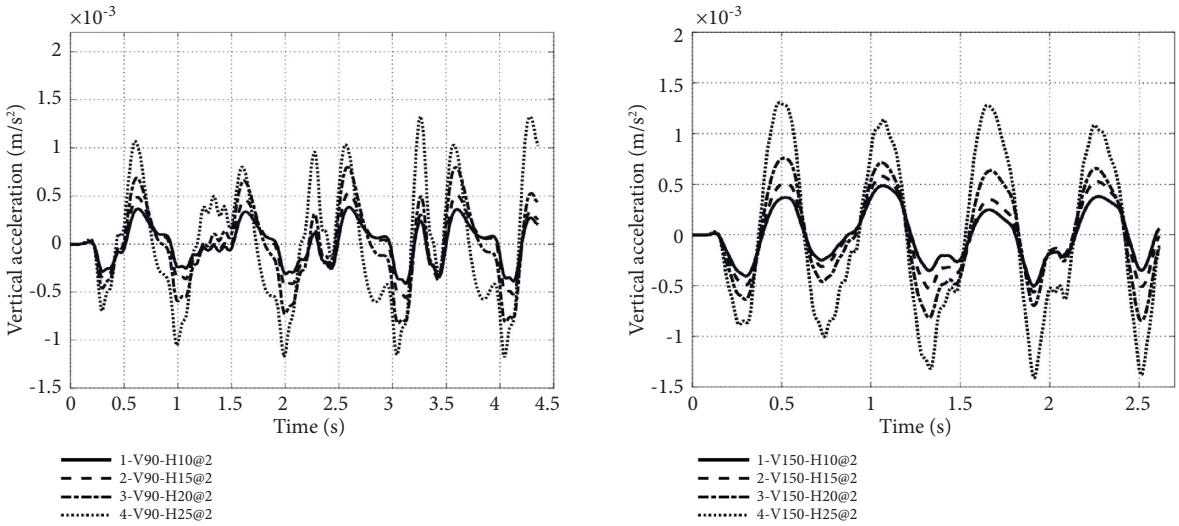

Figure 16: Vertical acceleration response of pickup point under thickness change of vibration isolation slab.

20 cm, and 25 cm for the four working conditions. Figure 16 shows the acceleration time curve at the pickup point of the vibration isolator on the first floor of the building with different vibration isolator thicknesses.

As shown in Figure 16, as the thickness of the vibration isolator increases, the acceleration response of the vibration isolator decreases, and the reduction is noticeable, which shows that increasing the thickness of the vibration isolator can reduce the vibration response of the vibration isolator more comprehensively.

6. Conclusions

This study focused on vibration isolation measures for building floor vibrations caused by running trains. Both theoretical derivation and numerical simulation were performed in this research, and the following conclusions were drawn. (1) The theoretical derivation and numerical analysis verified that the vibration response prediction model established in this study was feasible for the VIP system under the action of multi-point excitation. (2) Appropriate measures, such as increasing the number of vibration isolators, increasing the length of the vibration isolators and arranging the horizontal vibration isolators and the center of gravity of the vibration isolators at the same height, effectively improved the stability of the vibration isolator system. (3) VIP systems [21] were very effective [22] in reducing the [23] vibration of building floors caused by trains, and increasing the vibration isolator damping ratio and platform thickness and reducing the spring stiffness increasing the vibration isolation effect. (4) Variations in the distance between the running train and the building had a small effect on the vibration isolation efficiency of the secondary vibration response at the floor level.

Data Availability

The data that support the findings of this study are available from the corresponding author upon reasonable request.

Conflicts of Interest

No conflict of interest exists in the submission of this manuscript.

Acknowledgments

This research was supported by National Natural Science Foundation of China (52178101).

References

[1] L. Fang, J. Yao, and H. Xia, "Prediction on soil-ground vibration induced by high-speed moving train based on artificial neural network model," *Advances in Mechanical Engineering*, vol. 11, no. 5, Article ID 168781401984729, 2019.

[2] X. Sheng, C. J. C. Jones, and D. J. Thompson, "Prediction of ground vibration from trains using the wavenumber finite and boundary element methods," *Journal of Sound and Vibration*, vol. 293, no. 3-5, pp. 575–586, 2006.

[3] D. J. Thompson and C. J. C. Jones, "A review of the modelling of wheel/rail noise generation," *Journal of Sound and Vibration*, vol. 231, no. 3, pp. 519–536, 2000.

[4] J. Yao, R. Zhao, N. Zhang, and D. Yang, "Vibration isolation effect study of in-filled trench barriers to train-induced environmental vibrations," *Soil Dynamics and Earthquake Engineering*, vol. 125, 2019.

[5] E. E. Ungar, S. Dh, and C. H. Amick, "Vibration control design of high-technology facilities," *Sound and Vibration*, vol. 24, no. 7, pp. 20–27, 1990.

[6] J. S. hwang, Y. N. huang, Y. H. Hung, and J. C. huang, "Applicability of seismic protective systems to structures with vibration-sensitive equipment," *Journal of Structural Engineering*, vol. 130, no. 11, pp. 1676–1684, 2004.

[7] Y. L. Xu, H. J. Liu, and Z. C. Yang, "Hybrid platform for vibration control of high-tech equipment in buildings subject to ground motion. Part 1: experiment," *Earthquake Engineering & Structural Dynamics*, vol. 32, no. 8, pp. 1185–1200, 2003.

[8] Y. L. Xu and B. Li, "Hybrid platform for high-tech equipment protection against earthquake and microvibration," *Earthquake Engineering & Structural Dynamics*, vol. 35, no. 8, pp. 943–967, 2006.

[9] Y. Xu and A. X. Guo, "Microvibration control of coupled high tech equipment-building systems in vertical direction," *International Journal of Solids and Structures*, vol. 43, no. 21, pp. 6521–6534, 2006.

[10] Y. L. Xu, Z. F. Yu, and S. Zhan, "Experimental study of a hybrid platform for high-tech equipment protection against earthquake and microvibration," *Earthquake Engineering & Structural Dynamics*, vol. 37, no. 5, pp. 747–767, 2008.

[11] J. J. Yang, S. Y. Zhu, W. Zhai et al., "Prediction and mitigation of train-induced vibrations of large-scale building constructed on subway tunnel," *Science of the Total Environment*, vol. 668, pp. 485–499, 2019.

[12] R. A. Ibrahim, "Recent advances in nonlinear passive vibration isolators," *Journal of Sound and Vibration*, vol. 314, no. 3-5, pp. 371–452, 2008.

[13] I. F. Lazar, S. A. Neild, and D. J. Wagg, "Using an inerter-based device for structural vibration suppression," *Earthquake Engineering & Structural Dynamics*, vol. 43, no. 8, pp. 1129–1147, 2014.

[14] D. De Domenico and G. Ricciardi, "An enhanced base isolation system equipped with optimal tuned mass damper inerter (TMDI)," *Earthquake Engineering & Structural Dynamics*, vol. 47, no. 5, pp. 1169–1192, 2018.

[15] Y. A. Yun and Y. M. Li, "Design and analysis of a novel 6-DOF redundant actuated parallel robot with compliant hingesfor high precision positioning," *Nonlinear Dynamics*, vol. 61, no. 4, pp. 829–845, 2010.

[16] P. Gardonio, S. J. Elliott, and R. J. Pinnington, "Active isolation of structural vibration on a multiple-degree-of-freedom system .1. The dynamics of the system," *Journal of Sound and Vibration*, vol. 207, pp. 61–93, 1997.

[17] M. Kumar and A. S. Whittaker, "Cross-platform implementation, verification and validation of advanced mathematical models of elastomeric seismic isolation bearings," *Engineering Structures*, vol. 175, pp. 926–943, 2018.

[18] E. N. Farsangi, A. A. Tasnimi, T. Y. Yang, I. Takewaki, and M. Mohammadhasani, "Seismic performance of a resilient low-damage base isolation system under combined vertical and horizontal excitations," *Smart Structures and Systems*, vol. 22, pp. 383–397, 2018.

[19] JN. Yang and A. K. Agrawal, "Protective systems for high-technology facilities against microvibration and earthquake," *Structural Engineering & Mechanics*, vol. 10, no. 6, pp. 561–575, 2000.

[20] J. Yao, L. Fang, and R. Zhang, "Building vibration prediction induced by moving train with random forest," *Journal of Advanced Transportation*, vol. 2021, pp. 1–13, 2021.

[21] S. Deshpande, S. Mehta, and G. N. Jazar, "Optimization of secondary suspension of piecewise linear vibration isolation systems," *International Journal of Mechanical Sciences*, vol. 48, no. 4, pp. 341–377, 2006.

[22] J. Forrest and H. Hunt, "Ground vibration generated by trains in underground tunnels," *Journal of Sound and Vibration*, vol. 294, no. 4-5, pp. 706–736, 2006.

[23] N. Zhang, h. Xia, W. G. Yang, and S. Zhao, "Prediction and control of building vibration under metro excitations," in *Proceedings of the 8 Th International Conference on Structural Dynamics (EURODYN 2011)*, pp. 705–711, Leuven, Belgium, July 2011.

Hindawi
Advances in Civil Engineering
Volume 2022, Article ID 9291890, 15 pages
https://doi.org/10.1155/2022/9291890

Research Article

Effect of Mean Grain Size on the Small-Strain Dynamic Properties of Calcareous Sand

Liwei Wen [1,2,3]

[1] *Key Laboratory of Earthquake Engineering and Engineering Vibration, Institute of Engineering Mechanics, China Earthquake Administration, Harbin, Heilongjiang 150080, China*
[2] *Key Laboratory of Earthquake Disaster Mitigation, Ministry of Emergency Management, Harbin, Heilongjiang 150080, China*
[3] *School of Civil Engineering, Guangzhou University, Guangzhou, Guangdong 510006, China*

Correspondence should be addressed to Liwei Wen; liweiwen@gzhu.edu.cn

Received 7 May 2022; Accepted 29 June 2022; Published 18 July 2022

Academic Editor: Chao Zou

Calcareous sand was selected as the prior material for island reclamation in many coastal regions. The mechanical properties of the granular materials are greatly affected by their grain size distribution conditions. The shear modulus and damping ratio are two important parameters for earthquake ground response analysis and liquefaction evaluation. A series of resonant column tests had been performed on calcareous sands with varying median grain diameter and uniform coefficient. The dependence of the shear modulus and damping ratio of the calcareous sand on grain size has been confirmed in this examination. The test results reveal that the shear modulus decreases with a rise in shear strain for calcareous sand samples at a given confining pressure and relative density. The maximum shear modulus tends to increase with confining pressure and relative density. On the maximum shear modulus and void ratio plane, the trend lines of the measured results shift toward up and right position with a rise in grain diameter. The measured results indicate that the influence of uniform coefficient on the maximum shear modulus is neglectable. A revised empirical equation based on the Hardin model had been proposed considering the influence of grain diameter to estimate the maximum shear modulus of calcareous sand. The predicted values show satisfactory agreement with the measured results. The results manifest that the effect of grading condition on small-strain dynamic properties of calcareous sands cannot be neglected for the evaluation of seismic safety for reclamation engineering sites.

1. Introduction

Calcareous sands are biogenic medium and widely distributed in the coastal region all around the world. They are originated from marine shells and organisms. The major composition of such marine medium is calcium carbonate. The calcareous sands possess an intrapore structure, angular shape, and a rough surface. The calcareous sands are liable to be damaged at normal working stress [1–4]. Thus, calcareous sediments exhibit different mechanical response compared to the terrigenous sand. Recently, the calcareous sand is selected as the prior material for reclamation construction. The demand for fundamental understanding of the mechanical properties of calcareous sand is highly urgent.

Some costal island reclamation work in South China Sea had been constructed in past years [5–8]. Besides, the occurrence of earthquakes is frequently reported in that area. Therefore, well understanding of the dynamic characteristic of the sand deposition site is significantly important for the earthquake of reef reclamation site. Moreover, the small-level dynamic properties are parameters affecting the ground motion characteristics. Those indexes can also be adopted to estimate the settlement of reclamation ground subjected to earthquake.

The shear stiffness of the sand at the shear strain level less than 10–5 is generally defined as Go. Past studies verified that the shear modulus was the function of void ratio and confining stress. Additionally, the small-level dynamic properties of sand are also susceptible to many other factors including gradation, distribution, and particle characteristics. The bender element and resonant column tests are the two tradition laboratory approaches to measure the small-

level dynamic index of sands. The resonant column tests had been extensively carried out to measure the small-level dynamic properties of sands [9–12]. Phamet al. [13] found that the maximum shear modulus of the calcareous was larger than that of silica sand under the same test condition. Goudarzy et al. [14] noticed that the maximum shear modulus significantly reduced with increasing fines content and adopted the equivalent skeleton void ratio [15] to revise the Hardin model [16] to include the effect of fines particles on fabric and force chains of sand assembly. Jafarian and Javdanian [17] tested the dynamic properties of siliceous-carbonate sand and understood that the maximum shear modulus of the samples subjected to anisotropic condition was larger than the isotropically consolidated samples. The effect of uniform coefficient and mean grain size on the dynamic properties of sand at the small-strain level is mixed. Anastasiadis et al. [18] reported that the mean grain size affected the normalized shear modulus of the sand. However, some researchers held the opposite opinions [19, 20]. Therefore, the investigation on the effect of grain diameter on the small-level dynamic properties of the calcareous sand is still insufficient. Further research should be conducted to complement the existing literature.

This study carries out a series of resonant column tests to examine the influences of median diameter and uniform coefficient on the shear modulus and damping ratio of the calcareous sand at different confining pressures and densities. The dependence of the shear modulus of calcareous sand on the void ratio and confining pressure plane is also studied. The test results indicate that the effect of gradation condition on the small-strain dynamic properties of calcareous sand should be seriously considered when the earthquake ground response analysis and liquefaction evaluation of reclamation site are conducted. The well-proved Hardin model [16, 21] had been revised to consider the effect of gradation condition to estimate the maximum shear modulus of calcareous sand under different test conditions. The predicted values agree well with measured results for calcareous sand with varying gradation conditions.

2. Materials and Methods

The calcareous sand was collected from the Nansha island, South China Sea. The grain size distribution range for the calcareous sand of the Nansha island region is quite wide, and these biogenetic sediments contain large and small grains by arbitrary proportion. To investigate the influence of gradation property on the small-strain dynamic characteristics of calcareous sand, the grain size distribution curves of calcareous sand had been artificially adjusted. Figure 1 shows the grain size distribution curves of all samples. Three median diameters (d_{50}) of 0.75 mm, 1.5 mm, and 2.5 mm had been selected. For each grain diameter, the uniform coefficient Cu had been prepared as 1.2, 1.8, and 2.4. The larger the uniform coefficient Cu is, the wider the grain size distribution curve becomes. The grading curve basically covers the representative grain size distribution range in the reclamation reef island. It is noticed that less fines particle with a grain diameter smaller than 0.075 mm exist in tested materials [22–24]. Table 1 shows the representative physical parameters of the calcareous sand with varying median diameters and uniform coefficients. It is noted that the maximum and minimum void ratios of calcareous sand are affected by the gradation condition. For the same median diameter d_{50}, both the maximum and minimum void ratios decrease as coefficient uniform Cu increases. The maximum and minimum void ratios also increase as the median diameter increases. It is because more void space is created for the skeleton structure formed by large grains. The specific

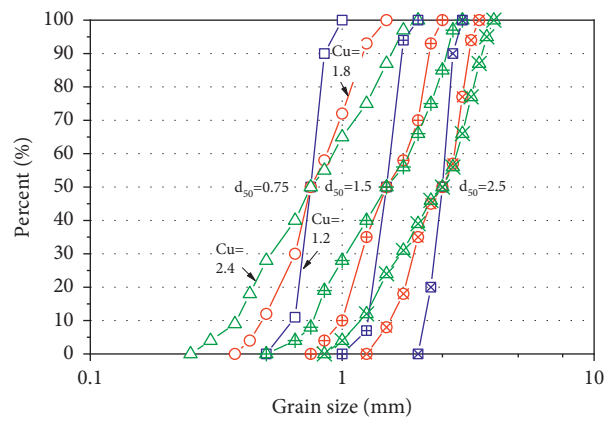

Figure 1: Grain size distribution curves of calcareous sand with varying gradation conditions.

Table 1: The physical parameters of calcareous sand with different gradation conditions.

Sample no.	e_{max}	e_{min}	d_{50} (mm)	C_u	G_s
1	1.264	0.902	0.75	1.2	2.76
2	1.279	0.854	0.75	1.8	2.76
3	1.214	0.774	0.75	2.4	2.76
4	1.273	0.968	1.5	1.2	2.76
5	1.139	0.896	1.5	1.8	2.76
6	1.072	0.835	1.5	2.4	2.76
7	1.390	1.084	2.5	1.2	2.76
8	1.295	1.006	2.5	1.8	2.76
9	1.233	0.970	2.5	2.4	2.76

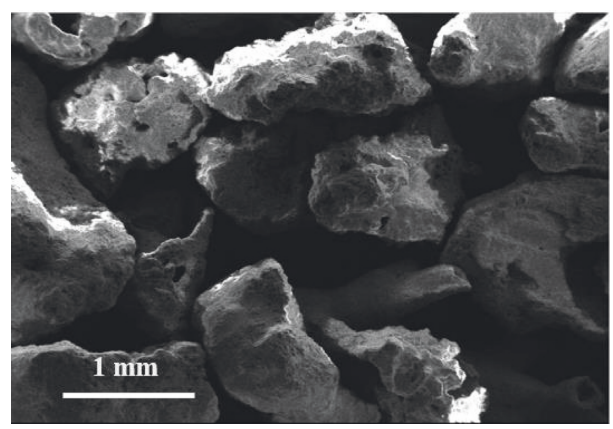

Figure 2: Scanning electron microscopy of calcareous sand.

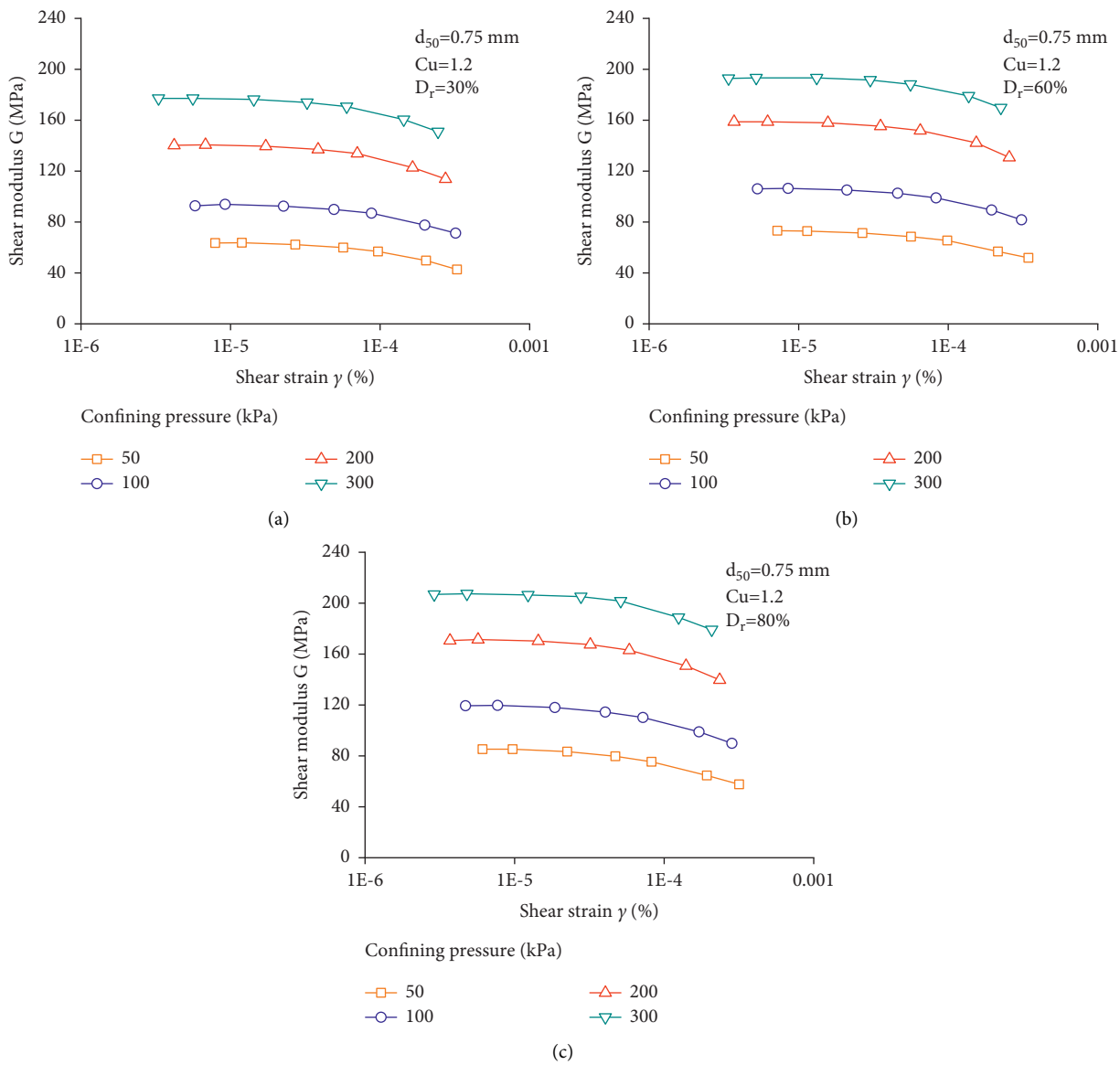

Figure 3: Shear modulus G and shear strain γ for calcareous sand with $d_{50} = 0.75$ mm and Cu = 1.2 at different confining pressures. (a) Loose state. (b) Medium dense state. (c) Dense state.

gravity G_s is less dependent on the median diameter and uniform coefficient.

Figure 2 shows the scanning electron microscopy of calcareous sand grains. The image shows that the particle shape of the calcareous sand is irregular and complex. The pores are distributed on the grain surface, and some pores are connected into the internal portion. The grain surfaces seem quite rough. The complex grain shape and microstructure of calcareous sand make its dynamic properties quite different from terrigenous sands.

The calcareous sand samples were prepared using the wetting tamping method [25–31]. The calcareous sand was mixed with an initial water content of 10%. The cylindrical sample is 50 mm in diameter and 100 mm in height. The moist calcareous sand was gradually poured into mold by five layers. The samples were prepared at different densities by specific tamping times. Three target relative densities of samples as 30% (loose state), 60% (medium-dense state), and 80% (dense state) were prepared. The saturation process for the calcareous sand sample is difficult due to its porositic nature. Initially, the calcareous sand is kept in vacuum for de-air. CO_2 is injected into the calcareous sand sample to replace the air, and this process lasts for 45 minutes. The saturation process for calcareous sand sample is accomplished by gradually elevating the back pressure. The Skempton B value for all samples is over 0.95 before testing. The isotropic consolidation pressures are set as 50 kPa, 100 kPa, 200 kPa, and 300 kPa before testing.

The GDS resonant column testing apparatus had been adopted to study the small-strain dynamic response of calcareous sand in this investigation. The resonant column testing apparatus is classified into the Stokoe type. The sample is excited in sinusoidal vibrations. The confining and back pressure range are 1.0 MPa, and the operating frequency

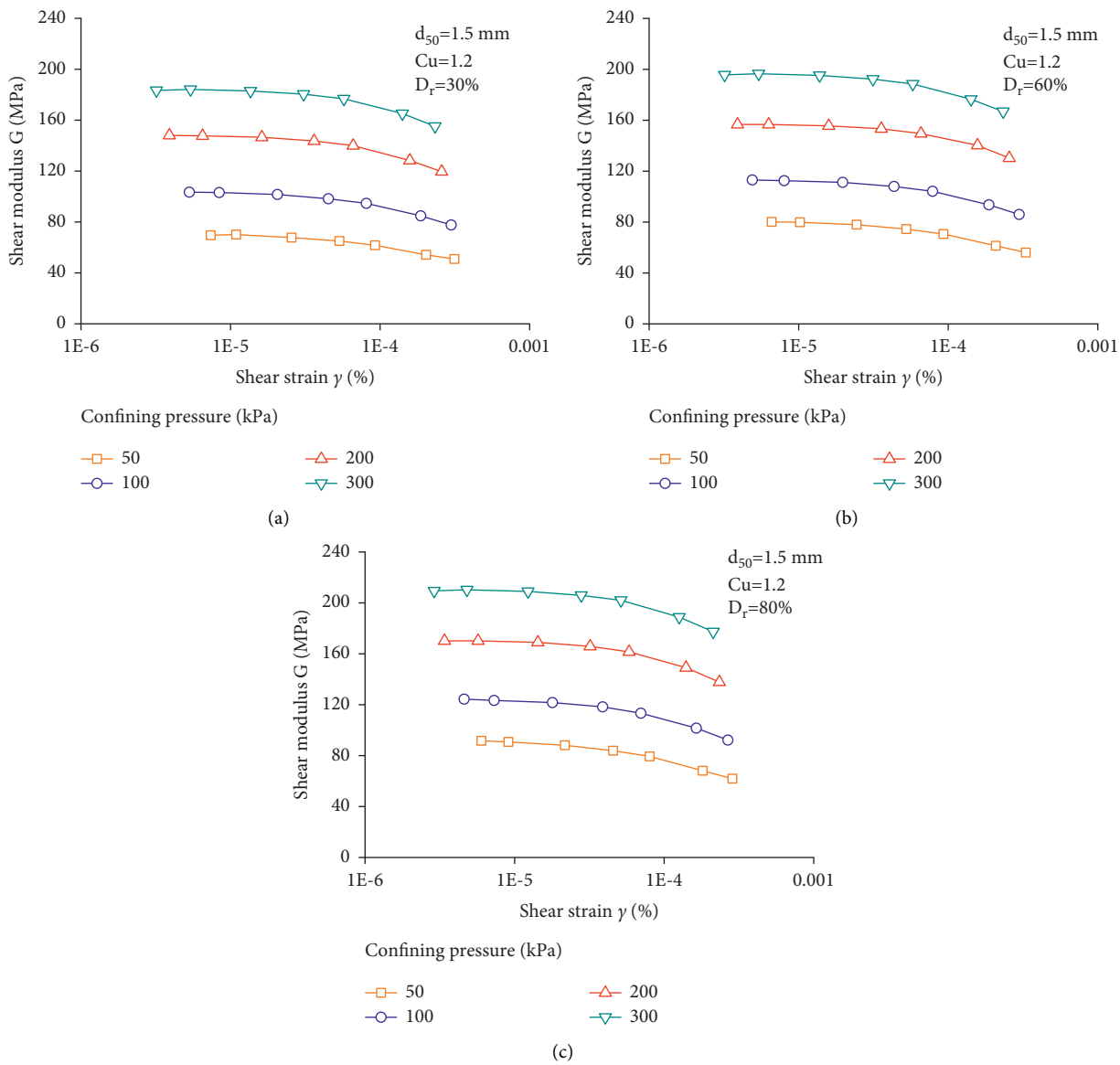

Figure 4: Shear modulus G and shear strain γ for calcareous sand with $d_{50} = 1.5$ mm and Cu = 1.2 at different confining pressures. (a) Loose state. (b) Medium dense state. (c) Dense state.

range is between 5 and 30 Hz. The cylindrical sample is installed in triaxial cell, and the cell base is embraced by water in an inner tube.

3. Test Results

Figure 3 shows the shear modulus G-shear strain γ curve of calcareous sand with a median diameter of 0.75 mm and a uniform coefficient Cu = 1.2 at three densities of 30%, 60%, and 80%. The varying range of shear modulus measured in this study is between $5 * 10^{-5}$ and 10^{-4}. The test results display that the shear modulus G tends to decline with a rise in the shear strain regardless of the initial relative density. The attenuating tendency of the shear modulus is steady at a small-level shear strain and intensifies as the shear strain increases. The confining stress-dependence of the shear modulus for calcareous sand is also clearly seen. At a specific confining pressure, the shear modulus-shear strain curves move upward with a rise in relative density. The varying range for the shear modulus of calcareous sand at loose, medium-dense, and dense states is between 40 MPa and 210 MPa.

Figures 4 and 5 present the plot of shear modulus G against the shear strain γ of calcareous sand with median diameters of 1.5 mm and 2.5 mm at varying confining pressures and densities. The shear modulus-shear strain curves expressed in Figures 4 and 5 exhibit quite similar varying tendency to the calcareous sand with a small median grain diameter shown in Figure 3. A rise in the confining pressure largely elevates the position of the G-γ curve. A rise in deposition state markedly enhances the shear modulus under the same test condition. It demonstrates that the densification of the calcareous sediment is an effective approach to increase the resilience of the reclamation ground when the earthquake occurs.

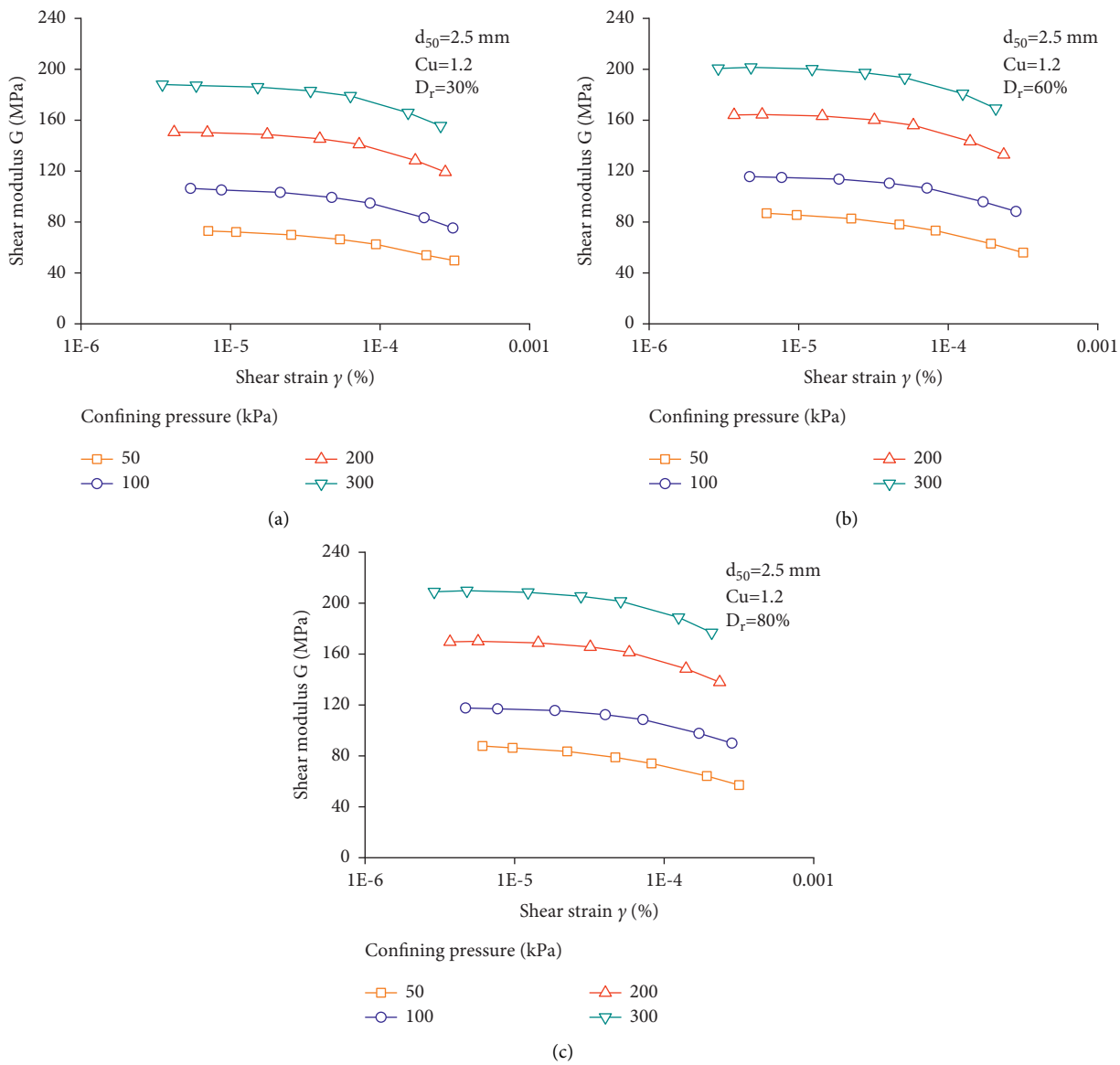

FIGURE 5: Shear modulus G and shear strain γ for calcareous sand with $d_{50} = 2.5$ mm and Cu = 1.2 at different confining pressures. (a) Loose state. (b) Medium dense state. (c) Dense state.

Figures 6(a) and 6(b) show the varying tendency of maximum shear modulus G_o with the level of confining stress for calcareous sand samples with median diameters of 0.75 mm and 2.5 mm, respectively. The maximum shear modulus G_o is determined as the intersection point of vertical axis and the fitting curve to measured data on shear modulus and shear strain γ plane. The dependence of maximum shear modulus G_o on the stress and density levels is distinctive. It is seen that the maximum shear modulus G_o linearly increases with a rise in confine pressure. An increasing confining pressure makes the calcareous sand grains closely contacted during the isotropic consolidation process. A rise in relative density enhances the maximum shear modulus for calcareous sand sample with small and large grains. Confining stress and deposition state are two influential parameters determining the maximum shear modulus for sandy material. It indicates that a denser calcareous ground owns a stronger modulus to resist small-level vibration loading. The results are consistent with past investigations on silica and calcareous sands [9, 32].

Figures 7(a) and 7(b) show the maximum shear modulus G_o plotted against the median diameter d_{50} for the calcareous sand. For calcareous sand with a uniform coefficient Cu = 1.2, the maximum shear modulus G_o is insensitive to the grain size at both loose and dense states. However, for calcareous sand with a relatively larger uniform coefficient, the maximum shear modulus G_o initially increases and reverses to reduce with diameter varying from 0.8 to 2.4. For a well-graded calcareous sand with a specific median diameter, the total grain number within a specimen and the major "force chain" subjected to torsion are larger than the other two cases. It is supposed that the mechanism about the influences of grain size and gradation condition on the small-level dynamic shear modulus is quite complicated.

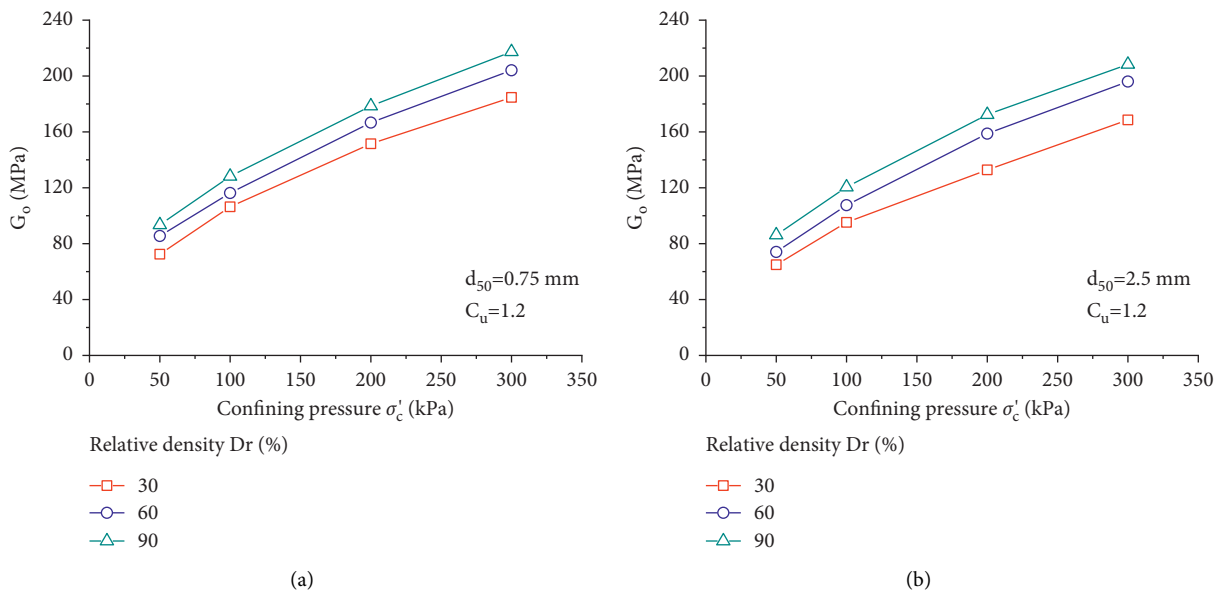

Figure 6: Maximum shear modulus G_o and confining pressure for calcareous sands with Cu = 1.2 at varying densities. (a) $d_{50} = 0.75$ mm and (b) $d_{50} = 2.5$ mm.

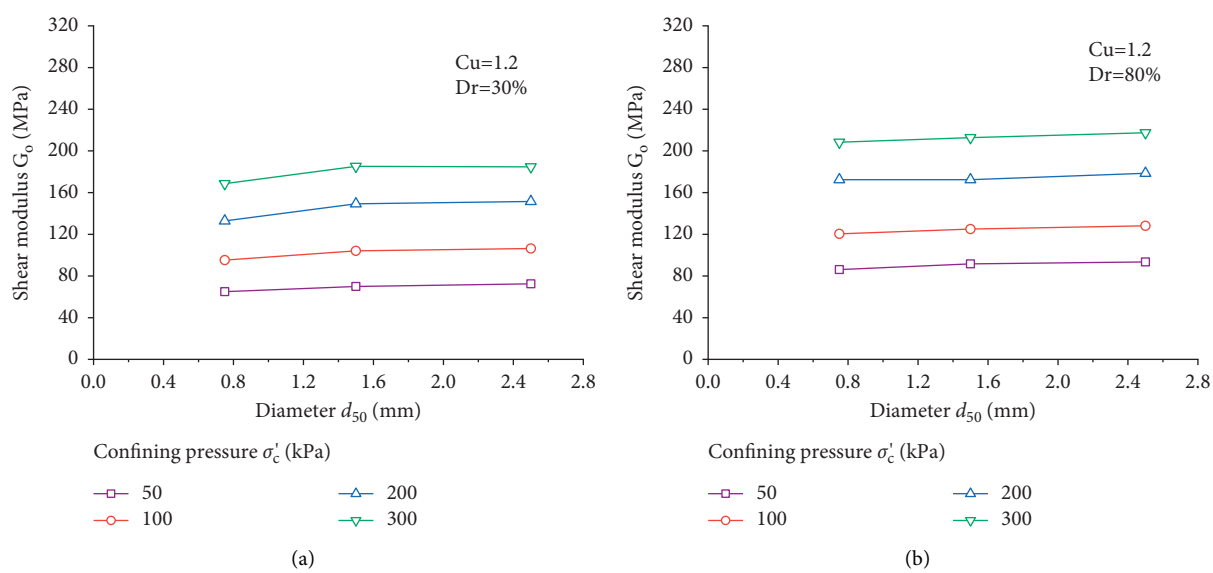

Figure 7: Continued.

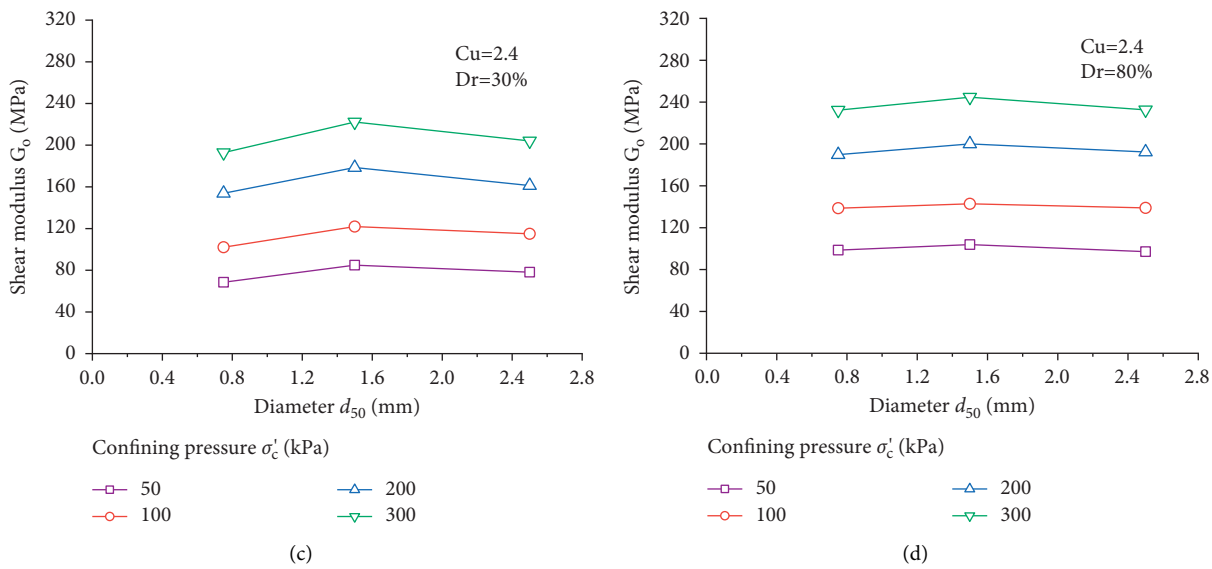

Figure 7: Maximum shear modulus G_o and median diameter d_{50}. (a) Cu = 1.2, Dr = 30%; (b) Cu = 1.2, Dr = 80%; (c) Cu = 2.4, Dr = 30%; (d) Cu = 2.4. Dr = 80%.

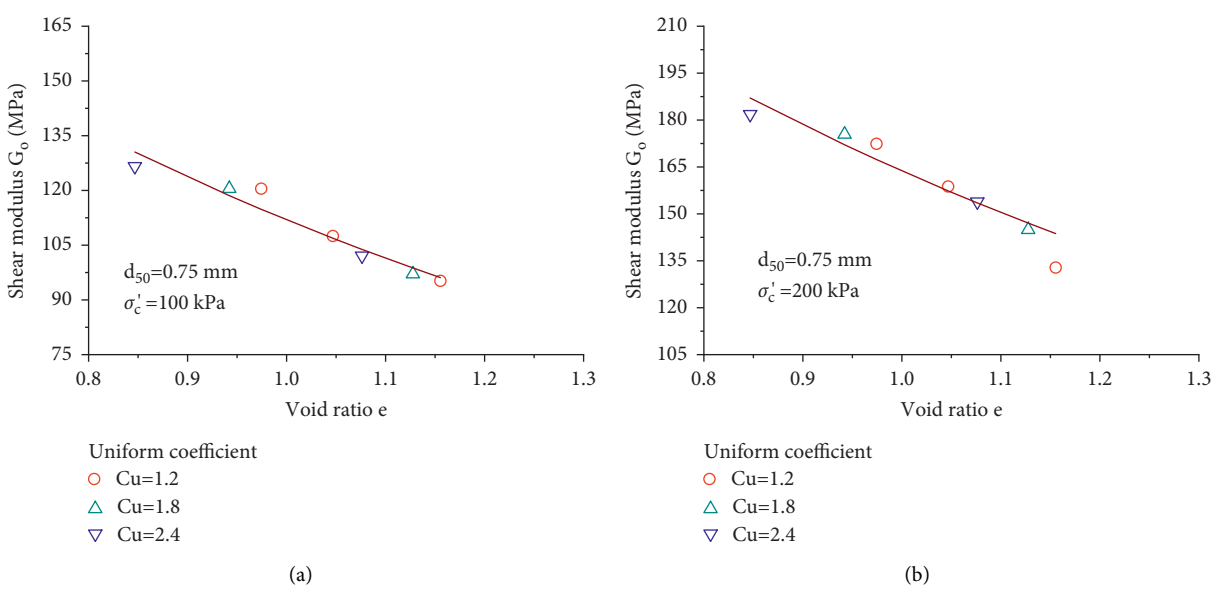

Figure 8: Continued.

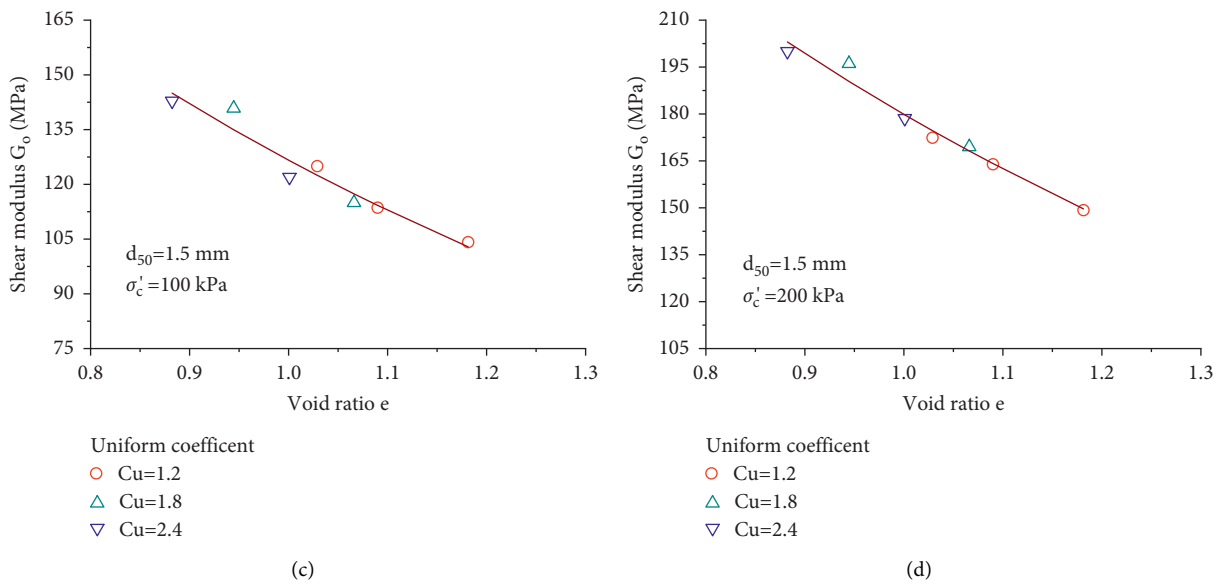

Figure 8: Shear modulus and void ratio for calcareous sand with varying uniform coefficient Cu. (a) $d_{50} = 0.75$ mm, 100 kPa; (b) $d_{50} = 0.75$ mm, 200 kPa; (c) $d_{50} = 1.5$ mm, 100 kPa; (d) $d_{50} = 1.5$ mm, 200 kPa.

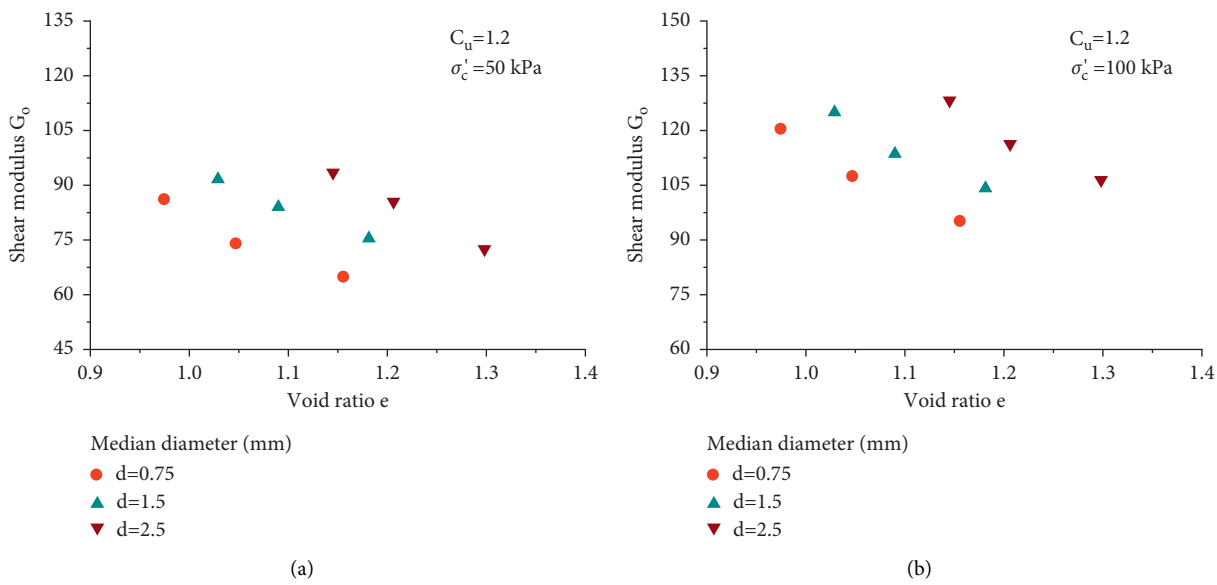

Figure 9: Continued.

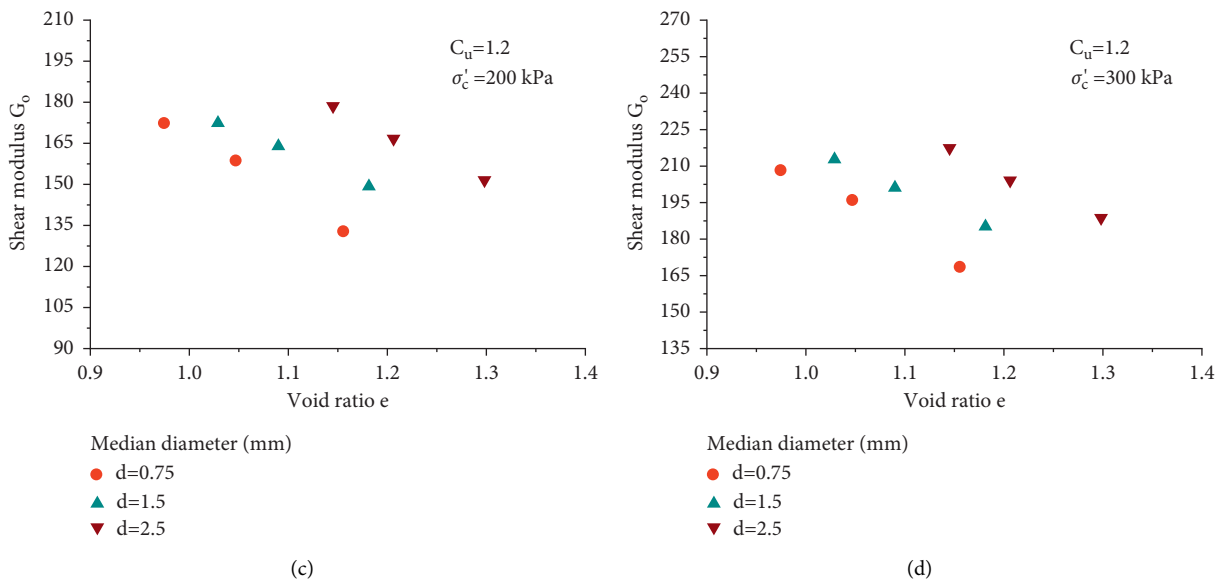

Figure 9: Maximum shear modulus and void ratio for calcareous sand with Cu = 1.2. (a) 50 kPa, (b) 100 kPa, (c) 200 kPa, and (d) 300 kPa.

Further investigation should be carried out to reveal the relevant micromechanism.

To directly understand the effect of uniform coefficient Cu on the maximum shear modulus, the test data under different test conditions are compared on the maximum shear modulus G_o-void ratio e plane. Figure 8 shows the relationship between the maximum shear modulus and void ratio for calcareous sand with varying uniform coefficient. The maximum shear modulus G_o tends to decrease with a rise in the void ratio. The calcareous sands subjected to dynamic loading loses its deformation resistance ability when it is at a loose state. It is noted that the effect of uniform coefficient on the G_o-e curve is neglectable. In Figure 8, all test results could be simulated using a curve on the maximum shear modulus and the void ratio plane when the median diameter and confining pressure are known. The test results acquired in this work are different to previous investigations on silica sand [11, 33]. The difference is probably originated from the grain morphology between the calcareous sand and silica sand.

Figure 9 expresses the maximum shear modulus G_o plotted against the void ratio e for calcareous sand with uniform coefficient Cu = 1.2 and different median diameters. The vertical axis for Figures 9(a)–9(d) is different because the applied confining pressure level is different. With similarity to Figure 8, the maximum shear modulus displays reducing tendency as the sample becomes loose. Under the same test condition, the effect of the grain diameter on the maximum shear modulus G_o is remarkable on the G_o-e plane. It is clearly seen that a decrease in grain diameter d makes the measured result points move downward. The difference in the grain diameter leads to the different fabric and coordination number among the grain particles. The complex contact condition in samples with small grain diameter leads to the reduction in maximum shear modulus for calcareous sand [34–38].

Figures 10 and 11 show the relationship between the maximum shear modulus G_o and void ratio e for calcareous sands at different confining pressures and two uniform coefficients. It indicates that the maximum shear modulus reduces as samples become loose. Besides, a rise in the grain diameter increases the maximum shear modulus at the same void ratio although only two measured points are acquired for a given median diameter. It is noted that the dependence of maximum shear modulus G_o on the grain size is applicable for samples with different Cu. Therefore, the effect of median diameter on the dynamic index of calcareous sand should be reasonably treated when the estimation equation of the maximum shear modulus is proposed.

4. Discussion

Past studies revealed that the shear modulus of the sand was greatly dependent on the density and confining stress [39–43]. Hardin and Richart [21] proposed an empirical formula to estimate the shear modulus G_o of sandy soil based on a database. The shear modulus G_o could be expressed as follows:

$$\mathrm{Go} = A\frac{(\mathrm{c}-\mathrm{e})^2}{1+e}\left(\frac{p}{p_a}\right)^n, \tag{1}$$

where A, n, and c are the material constant. p_a represents atmospheric pressure (100 kPa), and p indicates the consolidation stress. Additionally, parameter c is affected by the angularity of the grains and takes the value of 2.97 for angular sand. The item related with void ratio e is also expressed by other forms in some studies.

Figure 12 shows the $G_o/(p/p_a)^{0.5} - e$ curve of calcareous sand using three median diameters. The normalization form of vertical axis is adopted to eliminate the effect of confining stress. The points representing the test results with the same Cu at different confining pressures are closely distributed.

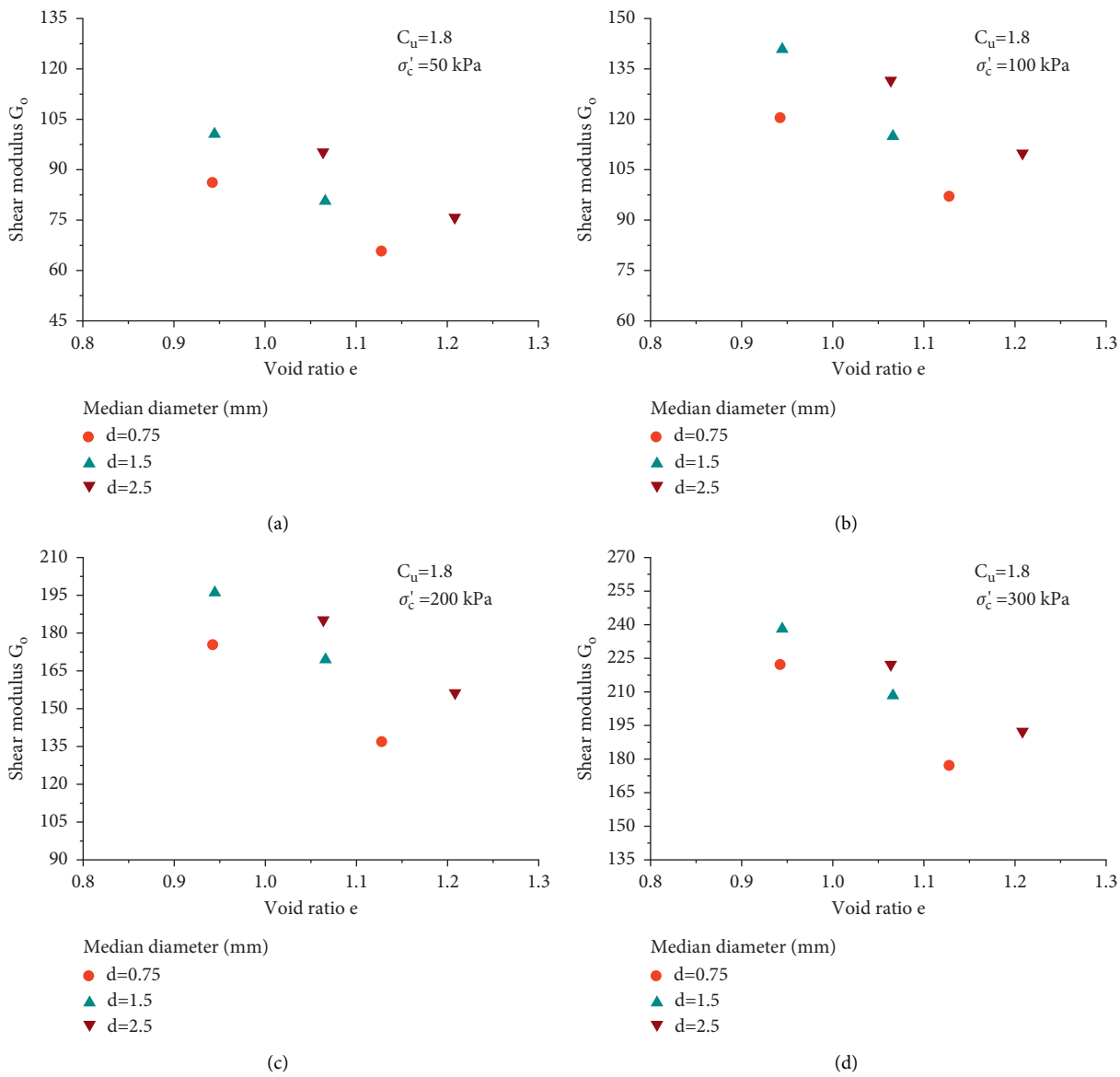

Figure 10: Maximum shear modulus and void ratio for calcareous sand with Cu = 1.8. (a) 50 kPa, (b) 100 kPa, (c) 200 kPa, and (d) 300 kPa.

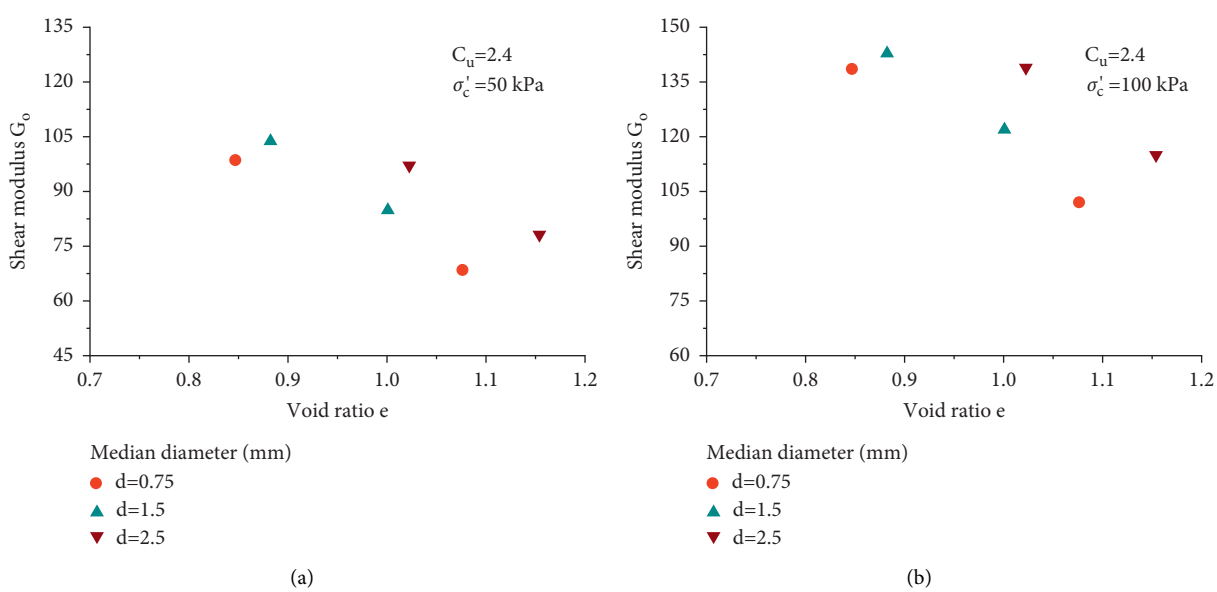

Figure 11: Continued.

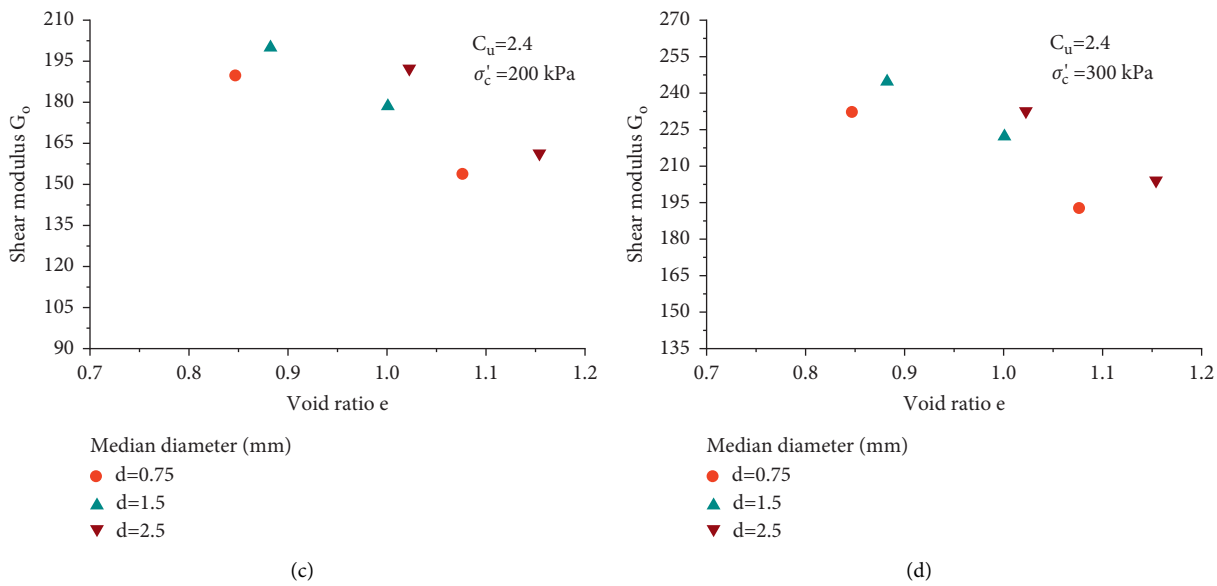

Figure 11: The maximum shear modulus and void ratio for calcareous sand with Cu = 2.4. (a) 50 kPa, (b) 100 kPa, (c) 200 kPa, and (d) 300 kPa.

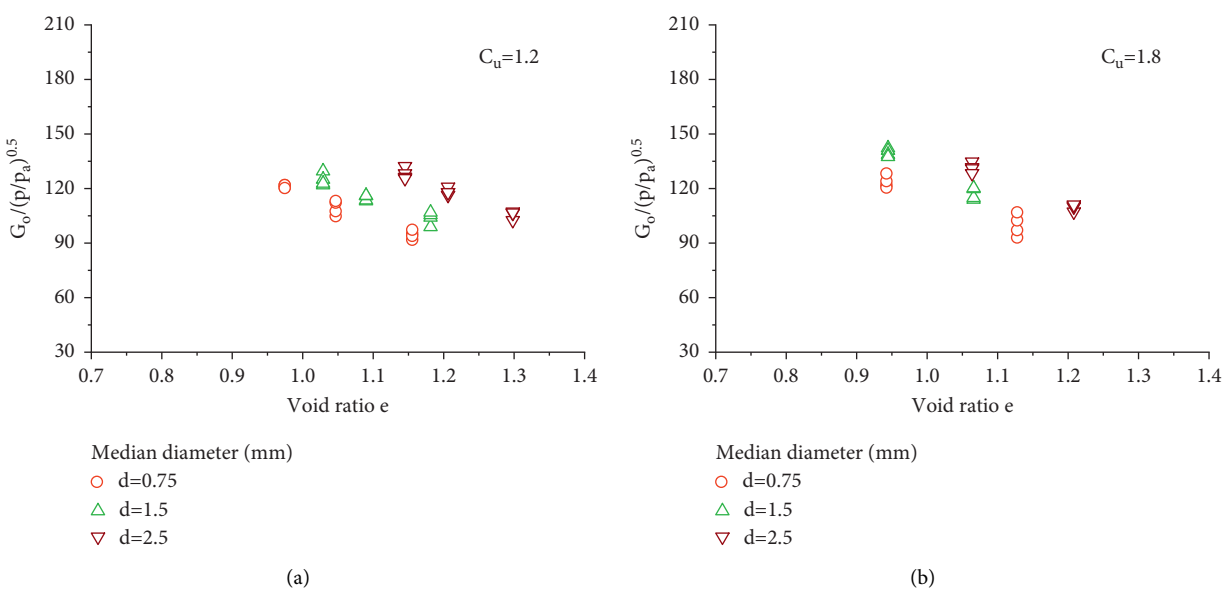

Figure 12: Continued.

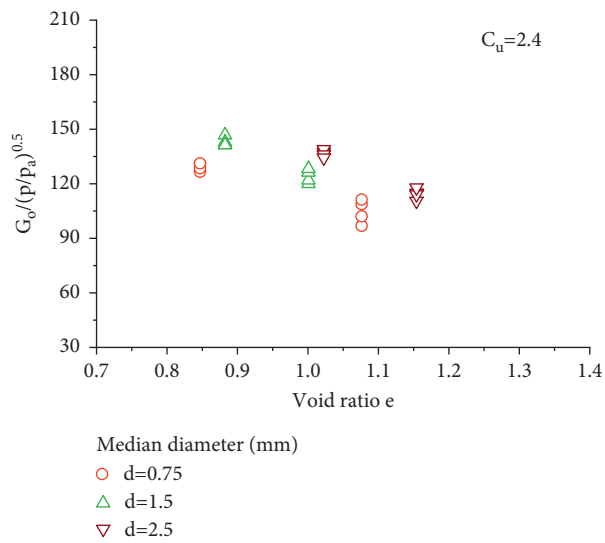

(c)

Figure 12: $G_o/(p/p_a)^n$ and void ratio for calcareous sand at different confining pressure. (a) Cu = 1.2, (b) Cu = 1.8, and (c) Cu = 2.4.

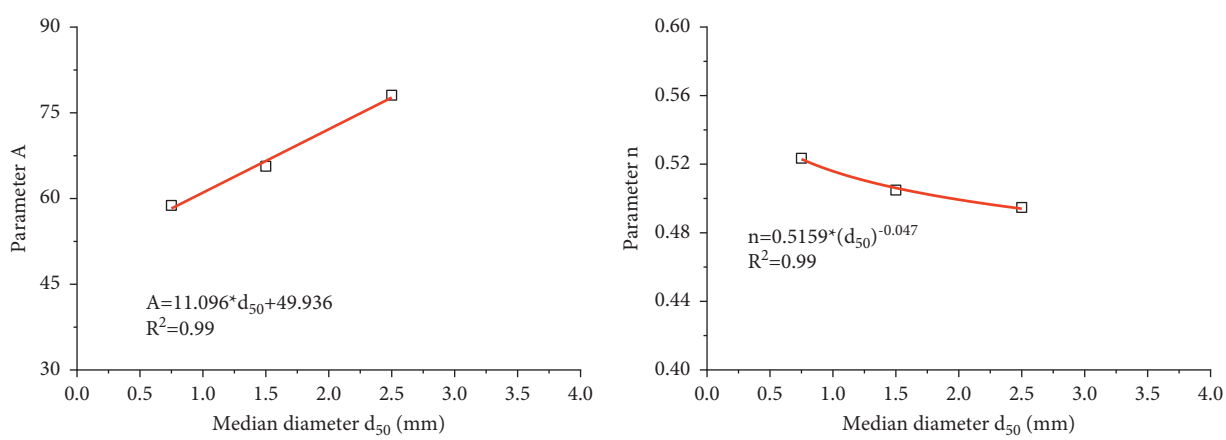

(a) (b)

Figure 13: The median diameter and parameters associated with experienced equations. (a) Parameter A and (b) parameter n.

The test results could be simulated using the Hardin model. However, the model parameters are greatly dependent on the median diameter d_{50}. Therefore, it is necessary to consider the effect of median diameter when the maximum shear modulus is estimated. For calcareous sands with a given median diameter d_{50}, a set of physical parameters including A and n could be obtained.

Figure 13 shows that model parameter A linearly increases with a median diameter of d_{50}. Besides, parameter n has an exponent power relationship with median diameter d_{50}. The goodness of fitting curves in Figure 13 is 0.99. These two parameters can be closely related and expressed using the median diameter d_{50}. Previous studies indicated that parameter c was insensitive to particle characteristics. Thus, parameter c is regarded to be a constant in the prediction.

Figure 14 represents all the test results for calcareous with three grain diameters at different confining pressures and densities. The varying tendency of normalization value of G_o with void ratio e could be described using the unique trend line. The trend line is determined using the revised Hardin model. The physical parameter d_{50} is directly introduced in the Hardin model to quantitatively describe the parameters A and n. Parameters A and n are determined using the best-fitting method to the measured results. The revised Hardin model considering the effect of grain diameter is capable of predicting the maximum shear modulus of calcareous with different gradation conditions at different densities and stresses.

Figures 15 and 16 show the predicted and measured maximum shear modulus of the calcareous sand with varying grading curves under different test conditions. The shear modulus estimated using the original Hardin model is displayed in Figure 15. It is noted that the points representing samples with a median diameter of 0.75 are above

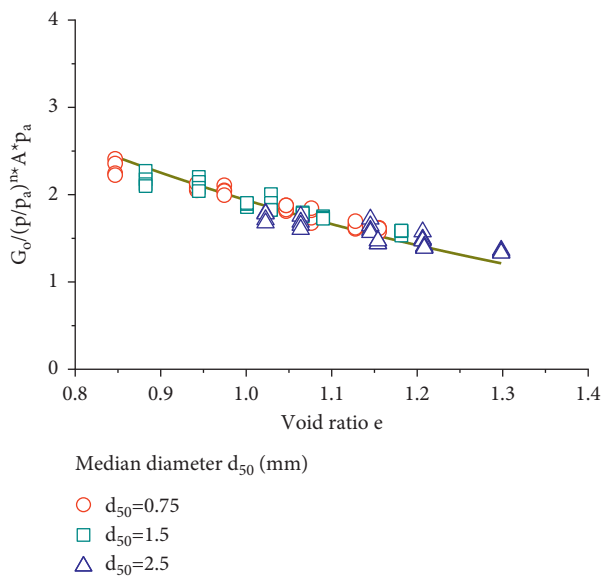

Figure 14: $G_o/(p/p_a)^n A p_a$ and void ratio for calcareous sands with three values of Cu.

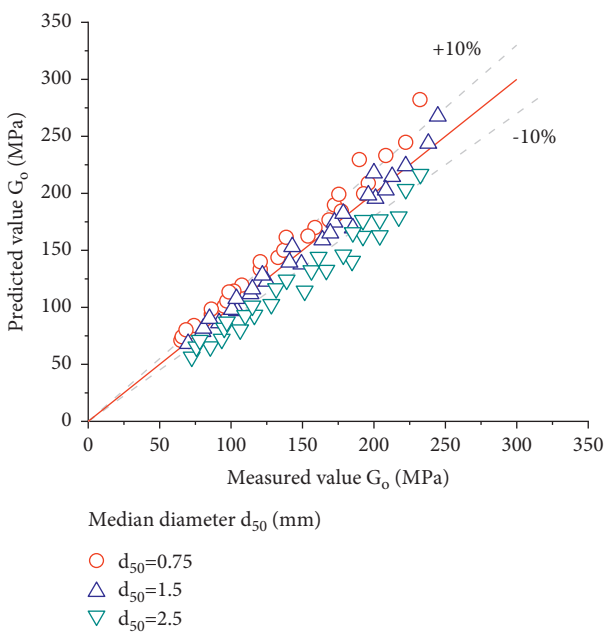

Figure 15: Measured and predicted maximum shear modulus G_o of the calcareous sand with different values of d_{50}.

the test results. It is also seen that the points are out of the zone indicating the relative error value within 10%.

Figure 16 shows that the predicted values match well with measured results with a relative error value of less than 10%. The maximum shear modulus is predicted using the revised Hardin model. The estimation capacity is largely enhanced by considering the influence of the grain size. The calcareous sand ground owns a wide range of grain size distribution curves. The revised Hardin model is expected to provide the predicted maximum shear modulus to accurately reflect the influence of gradation characteristics of calcareous sand ground in engineering practice.

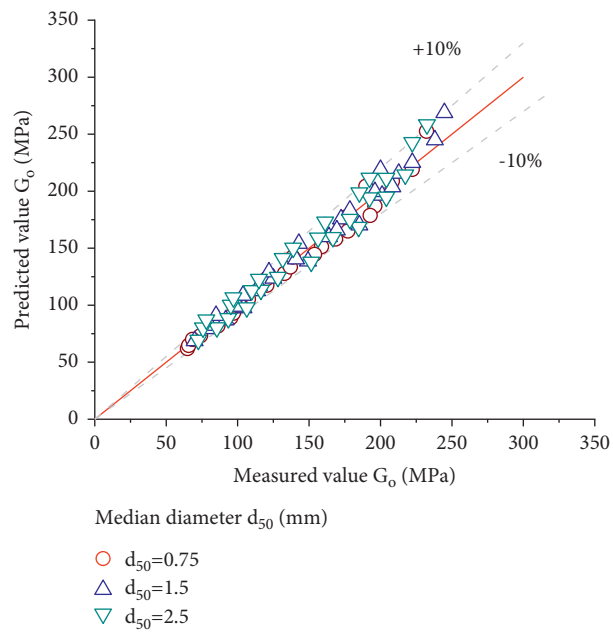

Figure 16: Measured and predicted maximum shear modulus G_o of the calcareous sand using the proposed estimated equation.

5. Conclusions

The grain median diameter is noticed to be an important parameter governing the monotonic and dynamic properties of the calcareous sand. A series of resonant column tests had been conducted to investigate the effect of gradation condition (median diameter and uniform coefficient) on the small-level dynamic property of the calcareous sand under different test conditions. The well-known Hardin model had been revised to include the influence of grain size on the small-level dynamic properties. The new findings of this work can be summarized as follows:

(1) The shear modulus of the calcareous sand tends to decrease with a rise in the shear strain at a given confining pressure and density. The confining stress-dependence and density-dependence of the shear modulus and damping ratio for calcareous sand had been confirmed in this investigation. The maximum shear modulus G_o linearly increases with the level of confining pressure at each relative density. On the maximum shear modulus and void ratio plane, the influence of uniform coefficient Cu on the measured maximum shear modulus is minimal.

(2) On the shear modulus and void ratio plane, at the same confining pressure and uniform coefficient, a rise in the median diameter enhances the maximum shear modulus. The maximum shear modulus displays a decreasing tendency with increasing void ratio. The looser the calcareous sand sample is, the smaller the capacity of the resisting torsion loading becomes.

(3) The physical parameter A in the Hardin model increases with median diameter, while parameter n in

the Hardin model exponentially decreases with the median diameter. The well-proved Hardin equation had been revised to consider the influence of median diameter. The proposed equation is capable of characterizing the small-level dynamic property of the calcareous sand with varying gradation conditions.

Data Availability

The data used to support the findings of this study are available from the corresponding author upon request.

Conflicts of Interest

The author declares no conflicts of interest regarding the publication of this paper.

Acknowledgments

A part of the work was funded by the Scientific Research Fund of Institute of Engineering Mechanics, China Earthquake Administration (Grant no. 2020D01), Guangdong Basic and Applied Basic Research Foundation (2021A1515012096 and 2021A1515110201), and Guangzhou City Technology and Science Program (202102010380 and 202201020204).

References

[1] M. R. Coop and J. H. Atkinson, "The mechanics of cemented carbonate sands," *Geotechnique*, vol. 43, pp. 53–67, 1993.

[2] S. Donohue, C. O' Sullivan, and M. Long, "Particle breakage during cyclic triaxial loading of a carbonate sand," *Geotechnique*, vol. 59, pp. 477–482, 2009.

[3] H. Shahnazari, Y. Jafarian, M. A. Tutunchian, and R. Rezvani, "Undrained cyclic and monotonic behavior of hormuz calcareous sand using hollow cylinder simple shear tests," *International Journal of Civil Engineering*, vol. 14, no. 4, pp. 209–219, 2016.

[4] G. Miao and D. Airey, "Breakage and ultimate states for a carbonate sand," *Géotechnique*, vol. 63, no. 14, pp. 1221–1229, 2013.

[5] Y. Wu, N. Li, X. Wang et al., "Experimental investigation on mechanical behavior and particle crushing of calcareous sand retrieved from South China Sea," *Engineering Geology*, vol. 280, Article ID 105932, 2021.

[6] T. Hyodo, Y. Wu, and M. Hyodo, "Influence of fines on the monotonic and cyclic shear behaviour of volcanic soil "Shirasu," *Engineering Geology*, vol. 301, 2022 https://doi.org/10.1016/j.enggeo.2022.106591, Article ID 106591.

[7] X.-Z. Wang, Y.-Y. Jiao, R. Wang, M.-J. Hu, Q.-S. Meng, and F.-Y. Tan, "Engineering characteristics of the calcareous sand in Nansha islands, South China Sea," *Engineering Geology*, vol. 120, no. 1-4, pp. 40–47, 2011.

[8] X. Wang, H. Shan, Y. Wu, Q. Meng, and C. Zhu, "Factors affecting particle breakage of calcareous soil retrieved from South China Sea," *Geomech. Eng.*vol. 22, pp. 173–185, 2020.

[9] T. Iwasaki and F. Tatsuoka, "Effects of grain size and grading on dynamic shear moduli of sands," *Soils and Foundations*, vol. 17, no. 3, pp. 19–35, 1977.

[10] E. Selig, R. Chung, F. Yokel, and V. Drnevich, "Evaluation of dynamic properties of sands by resonant column testing," *Geotechnical Testing Journal*, vol. 7, no. 2, p. 60, 1984.

[11] D. C. F. Lo Presti, M. Jamiolkowski, O. Pallara, A. Cavallaro, and S. Pedroni, "Shear modulus and damping of soils," *Géotechnique*, vol. 47, no. 3, pp. 603–617, 1997.

[12] K. Senetakis, A. Anastasiadis, and K. Pitilakis, "Normalized shear modulus reduction and damping ratio curves of quartz sand and rhyolitic crushed rock," *Soils and Foundations*, vol. 53, no. 6, pp. 879–893, 2013.

[13] H. H. G. Pham, V. I. Peter, V. I. William, M. Patrick, C. Veerle, and W. Haegeman, "3D particle shape of calcareous sand conducted by X-Ray computed tomography," in *Proceedings of the the 2nd World Congress on Civil, Structural, and Environmental Engineering*, CSEE'17, Barcelona, Spain, April 2017.

[14] M. Goudarzy, M. M. Rahman, D. König, and T. Schanz, "Influence of non-plastic fines content on maximum shear modulus of granular materials," *Soils and Foundations*, vol. 56, no. 6, pp. 973–983, 2016.

[15] M. M. Rahman, M. Cubrinovski, and S. R. Lo, "Initial shear modulus of sandy soils and equivalent granular void ratio," *Geomechanics and Geoengineering*, vol. 7, no. 3, pp. 219–226, 2012.

[16] B. O. Hardin and W. L. Black, "Sand stiffness under various triaxial stresses," *Journal of the Soil Mechanics and Foundations Division*, vol. 92, no. 2, pp. 27–42, 1966.

[17] Y. Jafarian and H. Javdanian, "Small-strain dynamic properties of siliceous-carbonate sand under stress anisotropy," *Soil Dynamics and Earthquake Engineering*, vol. 131, Article ID 106045, 2020.

[18] A. Anastasiadis, K. Pitilakis, K. Senetakis, and A. Souli, "Dynamic response of sandy and gravelly soils: effect of grain size characteristics on G-γ-D curves," in *Proceedings of the the 5th International Conference on Earthquake Geotechnical Engineering*, Santiago, Chile, January 2011.

[19] T. Wichtmann and T. Triantafyllidis, "Effect of uniformity coefficient on G/gmax and damping ratio of uniform to well-graded quartz sands," *Journal of Geotechnical and Geoenvironmental Engineering*, vol. 139, no. 1, pp. 59–72, 2013.

[20] P. H. Ha Giang, P. O. Van Impe, W. F. Van Impe, P. Menge, and W. Haegeman, "Small-strain shear modulus of calcareous sand and its dependence on particle characteristics and gradation," *Soil Dynamics and Earthquake Engineering*, vol. 100, pp. 371–379, 2017.

[21] B. O. Hardin and F. E. Richart, "Elastic wave velocities in granular soils," *Journal of the Soil Mechanics and Foundations Division*, vol. 89, no. 1, pp. 33–65, 1963.

[22] M. Hyodo, Y. Wu, S. Kajiyama, Y. Nakata, and N. Yoshimoto, "Effect of fines on the compression behaviour of poorly graded silica sand," *Geomech. Eng.*vol. 12, no. 1, pp. 127–138, 2017.

[23] N. Yoshimoto, Y. Wu, M. Hyodo, and Y. Nakata, "Effect of relative density on the shear behaviour of granulated coal ash," *Geomech. Eng.*vol. 10, no. 2, pp. 207–224, 2016.

[24] Y. Wu, N. Yoshimoto, M. Hyodo, and Y. Nakata, "Evaluation of crushing stress at critical state of granulated coal ash in triaxial test," *Géotechnique Letters*, vol. 4, no. 4, pp. 337–342, 2014.

[25] Y. Wu, J. Cui, J. Huang, W. Zhang, N. Yoshimoto, and L. Wen, "Correlation of critical state strength properties with particle shape and surface fractal dimension of clinker ash," *International Journal of Geomechanics*, vol. 21, no. 6, Article ID 4021071, 2021.

[26] Y. Wu, H. Yamamoto, and Y. Yao, "Numerical study on bearing behavior of pile considering sand particle crushing," *Geomech. Eng.*vol. 5, no. 3, pp. 241–261, 2013.

[27] M. Hyodo, Y. Wu, N. Aramaki, and Y. Nakata, "Undrained monotonic and cyclic shear response and particle crushing of silica sand at low and high pressures," *Canadian Geotechnical Journal*, vol. 54, no. 2, pp. 207–218, 2017.

[28] M. J. Winter, M. Hyodo, Y. Wu, N. Yoshimoto, M. B. Hasan, and K. Matsui, "Influences of particle characteristic and compaction degree on the shear response of clinker ash," *Engineering Geology*, vol. 230, pp. 32–45, 2017.

[29] Y. Wu, H. Yamamoto, J. Cui, and H. Cheng, "Influence of load mode on particle crushing characteristics of silica sand at high stresses," *International Journal of Geomechanics*, vol. 20, no. 3, Article ID 4019194, 2020.

[30] Y. Wu, M. Hyodo, and N. Aramaki, "Undrained cyclic shear characteristics and crushing behaviour of silica sand," *Geomech. Eng.*vol. 14, pp. 1–8, 2018.

[31] W. Zhang, J. Q. Zou, K. Bian, and Y. Wu, "Thermodynamic-based cross-scale model for structural soil with emphasis on bond dissolution," *Canadian Geotechnical Journal*, vol. 59, no. 1, pp. 1–11, 2022.

[32] Y. Jafarian, H. Javdanian, and A. Haddad, "Dynamic properties of calcareous and siliceous sands under isotropic and anisotropic stress conditions," *Soils and Foundations*, vol. 58, no. 1, pp. 172–184, 2018.

[33] S. Oztoprak and M. D. Bolton, "Stiffness of sands through a laboratory test database," *Géotechnique*, vol. 63, no. 1, pp. 54–70, 2013.

[34] C. Zou, J. A. Moore, M. Sanayei, Z. Tao, and Y. Wang, "Impedance model of train-induced vibration transmission across a transfer structure into an over track building in a metro depot," *Journal of Structural Engineering*, vol. 172, pp. 739–750, 2022.

[35] H. Jin, Q. Tian, and Z. Li, "Crack development of rebar rust in rubberized concrete using mesoscale model," *Construction and Building Materials*, vol. 321, Article ID 126409, 2022.

[36] L. H. Xu and M. Ma, "Dynamic response of the multilayered half-space medium due to the spatially periodic harmonic moving load," *Soil Dynamics and Earthquake Engineering*, vol. 157, Article ID 107246, 2022.

[37] H. Jin, J. Su, and C. Zhao, "Relationship between invert-filling disengaging and deformation of shield tunnel using staggered assembled segment," *KSCE Journal of Civil Engineering*, vol. 26, no. 4, pp. 1966–1977, 2022.

[38] M. Ma, M. H. Li, X. Y. Qu, and H. Zhang, "Effect of passing metro trains on uncertainty of vibration source intensity: monitoring tests," *Measurement*, vol. 193, Article ID 110992, 2022.

[39] B. Yuan, Z. Li, Y. Chen et al., "Mechanical and microstructural properties of recycling granite residual soil reinforced with glass fiber and liquid-modified polyvinyl alcohol polymer," *Chemosphere*, vol. 286, Article ID 131652, 2022.

[40] B. Yuan, Z. Li, W. Chen et al., "Influence of groundwater depth on pile–soil mechanical properties and fractal characteristics under cyclic loading," *Fractal and Fractional*, vol. 6, no. 4, p. 198, 2022.

[41] B. Yuan, M. Chen, W. Chen, Q. Luo, and H. Li, "Effect of pile-soil relative stiffness on deformation characteristics of the laterally loaded pile," *Advances in Materials Science and Engineering*, vol. 2022, p. 13, Article ID 4913887, 2022.

[42] B. Yuan, W. Chen, J. Zhao, F. Yang, Q. Luo, and T. Chen, "The effect of organic and inorganic modifiers on the physical properties of granite residual soil," *Advances in Materials Science and Engineering*, vol. 2022, Article ID 9542258, 13 pages, 2022.

[43] B. Yuan, Z. Li, Z. Zhao, H. Ni, Z. Su, and Z. Li, "Experimental study of displacement field of layered soils surrounding laterally loaded pile based on Transparent Soil," *Journal of Soils and Sediments*, vol. 21, no. 9, pp. 3072–3083, 2021.

Hindawi
Advances in Civil Engineering
Volume 2022, Article ID 4915820, 10 pages
https://doi.org/10.1155/2022/4915820

Research Article

Stability Analysis of Jointed Rock Cutting Slope Based on Discrete Element Method

Wei Zhu,[1] Liang Gao,[1] Yingai Zhao,[1] Chao Yang,[2] Wei Sun,[3] and Pengqiang Yu[3]

[1]*PowerChina Roadbridge Group Co., Ltd., Beijing 100044, China*
[2]*PowerChina Zhongnan Engineering Corporation Limited, Changsha, Hunan 410014, China*
[3]*University of Science and Technology Beijing, Beijing 100083, China*

Correspondence should be addressed to Pengqiang Yu; yu_pengqiang@163.com

Received 18 May 2022; Accepted 29 June 2022; Published 16 July 2022

Academic Editor: Ziyu Tao

The joints in the rock mass are essential for the stability of rocky slopes, and the destabilization damage of the slope is often directly related to the joints. In this study, in order to reveal the instability process and mechanism of rock slopes from a microscale perspective, the DEM simulations for rocky slopes of the K88 + 400~K88 + 540 section of Zhongkai Expressway are carried out considering the influence of joints. Based on the findings of the on-site jointed structural surfaces, a rocky slope model containing two sets of intermittent joints was constructed, and the linear parallel bond model and the smooth joint model are used to characterize the rock body and joints, respectively. The evolution of microfracture, contact force chain, and particle displacement are analyzed to explore the micromechanism of slope instability. Finally, the triple reinforcement scheme of anchor cable frame and grass planting is proposed. The research results can provide a reference for stability analysis and reinforcement of similar rocky slope projects.

1. Introduction

The deformation and failure of geotechnical materials has always been a key topic [1–6]. Especially, the deformation and failure of jointed rock slope is often caused by the development of joint fissures and the destruction of structural surfaces of the rock. Under the effect of weathering and erosion for a long time, the inherent physical and mechanical properties of the slope rock with a weak layer and structural surface deteriorate; especially, the rock strength index will show obvious attenuation over time; and the microstructure inside the rock will undergo damage and accumulation, leading to macroscopic time-dependent deformation of the rocky slope with weak structural surface and finally destabilization damage of the slope. Therefore, it is particularly important to study the structural surfaces and joints of rock masses for stability analysis of rocky slopes.

Zheng and Zhao [7] adopted the finite element strength reduction method in the stability analysis of rocky slopes and obtained the sliding surface and stability coefficient of rocky slopes, which set a precedent for solving the sliding surface and safety coefficient of jointed rock slopes. Wu et al. [8] analyzed the stability of densely jointed rocky slopes using the strength reduction method based on the ubiquitous-joint model, and the results showed that the potential failure surface occurred first in the weak rock mass or along the jointing surface or both at the same time. Zhong and Miao [9] investigated the relationship between the slope safety factor and sliding mode and the sequestration of the weak interlayer within the slope using the limit equilibrium method. Based on the elastoplastic constitutive model considering complex stress state, the stability of slopes with seepage flow is analyzed using FLAC [10]. According to the field investigation and Google Earth images, Hu et al. [11] analyzed the process of fracture propagation on the slope under underground mining and then investigated the failure mechanism of the slope by the numerical software RFPA3D. Taking the process of excavation of the open-pit mine as the background, Wang et al. [12] analyzed the slope stability factor of the end slopes

using the strength reduction method, which shows that the vertical stress and stability factor decreased with the process of excavation, while the horizontal stress initially increased and then decreased. Wang et al. [13] proposed a displacement-statistics-based discrete element method and then investigated the stability of the jointed rocky slopes by incorporating the shear strength reduction method into the proposed modeling method. Meng et al. [14] proposed a hierarchical multiscale strength reduction method with a coupled FEM and DEM approach to investigate the stability of a soil and rock mixture slope. Their research showed that the multiscale simulation approach can be used as a novel numerical tool for the analysis of slope stability of geomaterials. Zhou et al. [15] investigated the effects of discontinuous joint length, dip angle, friction angle, and cohesion on slope stability based on the theoretical mechanical model of cusp catastrophe for intermittent jointed rocky slope instability. Jiang et al. [16] studied the destabilization and collapse processes of jointed rocky slopes by means of a cohesive contact model and revealed the failure mechanism at the macroscopic level of the slope. Scholtès and Donze [17] investigated the damage mechanism of jointed rocky slopes and found that the initiating weak surface of slope instability is developed from its internal cracks. The discrete element modeling method based on displacement statistics proposed by Wang et al. [18] can be combined with the strength reduction method to analyze the stability of jointed rock slopes. Zhao et al. [19] used the granular flow method to simulate the destabilization damage process of rocky slopes and explored the influence of the distribution depth and dip angle of the weak structural surface on the damage form of the slope by presetting weak structural surfaces with different distribution forms. Victor and Tedius [20] established a numerical model considering key geological features such as joints and structural planes to simulate the stability of jointed rocky slopes affected by wedge failure mechanisms. Li et al. [21] analyzed the stability of a jointed rock slope under translational failure and toppling failure by combining the quasi-static method, multidegree of freedom of rigid block element discretization technology, mathematical programming method, and plastic limit analysis method. Song and Sun [22] measured the parameters of rock structure surface by various methods and searched for the connected structure surface with minimum shear strength so called the potential slip surface, based on the depth-learning search algorithm. Shen et al. [23] used the Sarma method combined with the optimization method to analyze the stability of the down-layer sliding and cut-layer sliding methods for a large horizontal layered rock slope in the Three Gorges reservoir area affected by the combination of soft level, joints, and lithology of the slope.

In summary, although numerous studies have been conducted on jointed rock slopes, there are relatively few studies on the micromechanism of failure of crossed intermittent jointed rock slopes. In this paper, a model of cross-sectional intermittent jointed rock mass and rock slope is constructed based on the discrete element method, and the evolution law of fracture and the micromechanism of slope failure are then studied at the microscale level, which can improve the understanding of the failure mechanism of rock masses and slopes.

2. Microfracture and Joint Surface in Rock

There are many random microfractures in the rock mass, and the crack tip is prone to cause high-stress concentration under loading. When the maximum stress near the crack tip reaches the material strength value, the crack will expand unsteadily, which leads to the brittle fracture of the rock mass. Cracks generated in rock masses under load can be mainly classified as wing crack and secondary crack. The wing crack arises at the end of primary joints and gradually expands under load. It is considered by Lajtai [24] and Bobet and Einstein [25] as a type of tensile crack that starts from the crack tip and expands along the direction of maximum load. Secondary crack, on the other hand, is the shear crack that is approximately coplanar with the crack. Secondary cracks usually propagate as shear cracks in the same plane, which also arise at the end of the fracture and are the main contributors to rock damage.

The rock mass is generally composed of structural surfaces and intact rocks, which often exhibits anisotropy, nonuniformity, and discontinuity due to the complex geological processes. The structural surface is the weak surface prone to damage in the rock mass. Recently, in addition to the experimental method [26, 27], continuous constitutive modeling and discrete element method are increasingly used to simulate the deformation and failure of geotechnical materials [28–37]. The discrete element method has significant advantages in simulating cracks and large deformations. It only needs to consider the contact properties between particles and does not need to define the overall complex constitutive relationship [38–40]. The instability model of rock slopes containing joints under gravity is simulated in PFC 6.0 by synthetic rock mass, as shown in Figure 1. The synthetic rock mass is composed of a model of cohesive particles and a network of discrete fractures. The particles are connected by adhesive bonds, which make each particle glued into a whole, and under the load, the adhesive bonds are broken. For stronger rock materials, the linear parallel bonding model is often chosen as the model for bonded particles. The linear parallel bonding model can connect both particles to particles as well as to planes. Parallel bonding can provide mechanical properties stored between two contacting parts, and parallel bonding parts are similar to linear parts and establish elastic interactions. The existence of parallel bonds allows the two parts of contact to transfer force and moment to each other. The relative motion that occurs after the creation of a parallel bond results in the creation of forces and moments within the bonded material. If either of these maximum forces or moments exceed the corresponding bond strength, the parallel bond will break. Numerous joints with different orientations and trace lengths form a discrete fracture network, which is then embedded in the particle model to form a synthetic rock mass, as shown in Figure 2. The linear parallel bond model is generally used between mineral

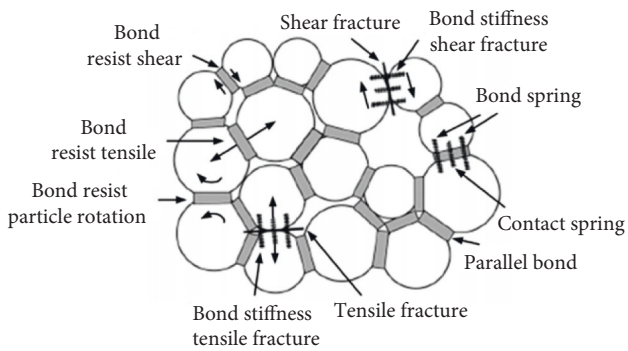

Figure 1: Linear parallel bonding model.

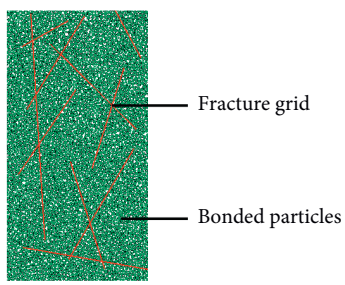

Figure 2: Synthetic rock mass map.

particles in rock, and the smooth joint model is used at the intersection of particles and fracture networks.

3. Particle Flow Model for Joint Rock Slope

A rock slope model with a width of 120 m and a height of 76 m was established and excavated in 8 stages, as shown in Figure 3. The minimum radius of particles in the model is selected as 0.15 m, and the ratio of the maximum and minimum particle sizes is equal to 2. The porosity is taken as 0.1.

According to the field investigation of Zhongkai Highway, the elastic modulus of moderately weathered granite is taken as 11 GPa, and the uniaxial compressive and tensile strengths are 28.3 MPa and 4.5 MPa, respectively. The trial-and-error method is used to calibrate the microscale parameters of moderately weathering granite used in DEM, and the main parameters of the particle model are shown in Table 1.

From the statistical results of structural surface (see Figures 4 and 5), the tendency of structural surface and slope surface is closely consistent, and there are two groups of the dominant structural surface with the dip angle of 72° and 8°, respectively.

According to the on-site investigation of the slope, the joints are mainly developed below stage 5. Hence, two groups of intermittent joints, named groups I and II, are inserted in the area below the slope of stage 5. The dip angles of the two groups of joints are 72° and 8°, respectively, and the lengths of both are 8 m, as shown in Figures 6 and 7. According to the condition of the on-site joints, the parameters of the joints can be obtained as shown in Table 2.

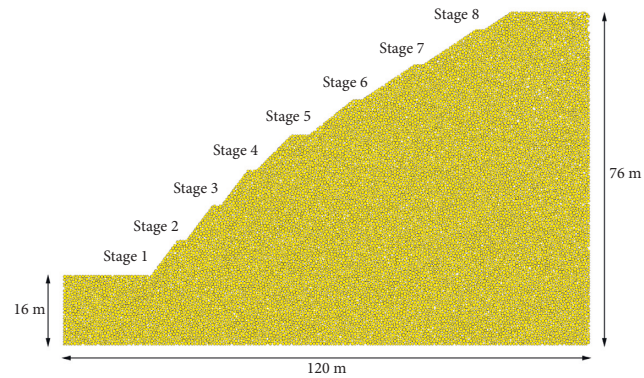

Figure 3: Particle flow model of the slope.

4. Micromechanical Analysis of the Instability of Slope

4.1. The Spatiotemporal Evolution of Microfracture in the Jointed Rock Slope. The failure mechanism of jointed rock slope in the process of instability is analyzed from the perspective of micromechanics in this section. Figure 8 shows the development of microfractures in the failure process of rock slopes controlled by two groups of bedding discontinuous joints. Microfracture was a contact fracture caused by the fact that interparticle stress exceeds its bonding strength. It can be divided into two categories according to the different fracture modes, that is, tensile fracture (denoted in red in Figure 8) and shear fracture (denoted in green in Figure 8).

It can be seen from Figure 8 that the contact fractures of the smooth joint model can be observed when the calculation reaches 1,000 time steps. Then microfractures that mainly result from tension failure are generated at the end of the joint at the state of 5,000 time steps of calculation and gradually expand to the end of the surrounding joint along the rock bridge. As shown in Figure 8, one can observe the breaking and penetration of rock bridges, such as rock bridges between the upper end of the first joint in the third layer of group I and the left end of the second joint in the second layer of group II, between the lower end of the second joint in the sixth layer of group I and the right end of the third joint in the second layer of group II, and between the upper end of the second joint in the fifth layer of group I and the right end of the second joint in the fourth layer of group II. Besides, the microfracture develops from the inside out according to the spatial position. At the state of 10,000 time steps, the crack occurs on the surface of the slope, and the internal crack continues to develop. The lower end of the second joint in the third layer of group I breaks and connects with two joints, which are the right end of the first joint in the fourth layer of group II and the left end of the first joint in the fifth layer, respectively, and rupture blocks formed on the slope surface. The rock bridge between the upper end of the three joints and the right end of the first joint in the sixth layer of group II is broken and connected, and the rock bridge between the right end of the third joint of the third layer of the group II and the left end of the third joint of the

Table 1: Model parameters of particle model.

Minimum particle radius (R_{min}/m)	Particle size ratio (R_{max}/R_{min})	Particle density, ρ (kg/m^3)	Interparticle friction coefficient, μ	Particle effective modulus, E_c (GPa)	Particle normal-to-shear stiffness ratio (kn/ks)
0.15	2	2,500	0.5	5.0	1.0
Radius multiplier, λ	Bond effective modulus, E (GPa)	Bond normal-to-shear stiffness ratio (kn/ks)	Tensile strength, pb_ten (MPa)	Cohesion, pb_coh (MPa)	Friction angle, pb_fa (°)
1	5.0	1.0	4.8	4.8	35

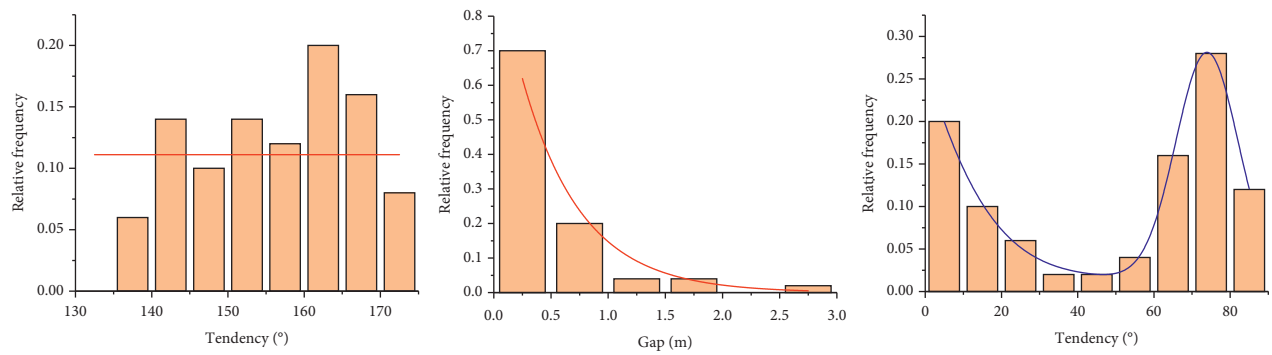

Figure 4: Histogram and probability density curve of joint tendency and dip angle.

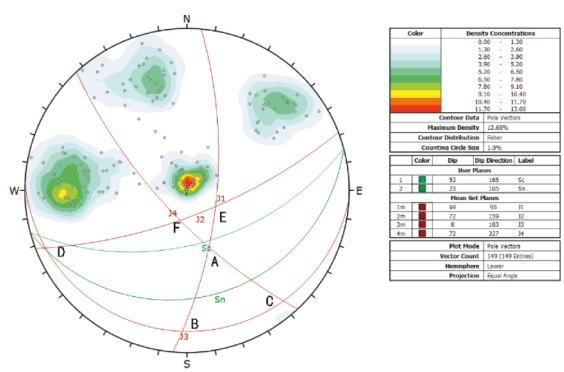

Figure 5: Isomorphic structure of joints and their poles.

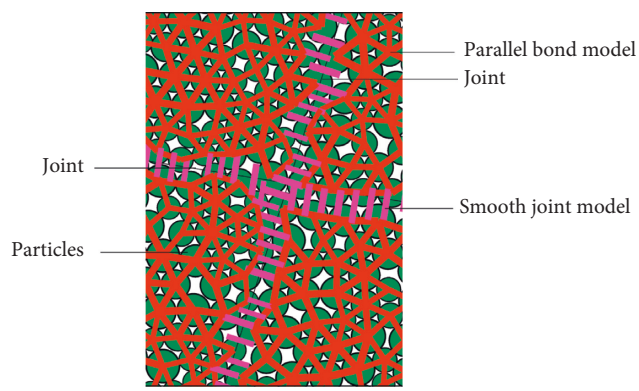

Figure 7: Discrete fracture network.

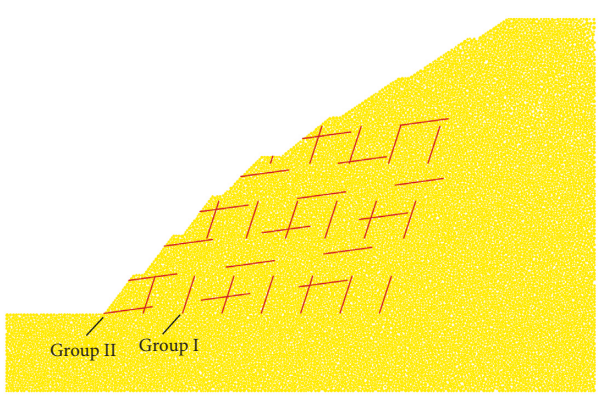

Figure 6: Discontinuous jointed rock slope model.

fourth layer of group II is broken and connected. At time step 15,000, the slope surface cracks further increase, and the right ends of the two joints in the sixth layer of group II both had ruptures with the slope surface; a macroscopic rupture zone appeared between the lower end of the third joint in the seventh layer of group I and the right end of the third joint in the fourth layer of group II. At time step 20,000, a large number of ruptures occur at the end of the first joint in the second layer of group I and the first joint in the fourth layer of group I and expand to the end of the surrounding joints; the rock bridge between the upper end of the first joint in the fifth layer of group I and the left end of the third joint in the second layer of group II broke through; and the upper end of the first joint in the sixth layer of group I develops and runs through the middle of the third joint in the second layer of group II. When the model calculates to 25,000 time steps, a large number of fissures developed in the joints at the bottom of the slope, especially at the upper end of the first joint in the second layer of group I and the left end of the third joint in the first layer of group II, and almost all of the joints have penetrating failures. Microfractures continued to occur in the fractured zones that had been penetrated in

Table 2: Main parameters of joint.

Normal stiffness (sj_kn/MPa)	Shear stiffness (si_ks/MPa)	Friction coefficient, sj_fric	Dilation angle, sj-da (°)
2×10^7	2×10^7	0.2	0
Cohesion (sj_coh/MPa)	Tensile strength (sj_ten/MPa)	Joint bond state, sj_state	Joint friction angle, sj_fa (°)
0	0	3	0

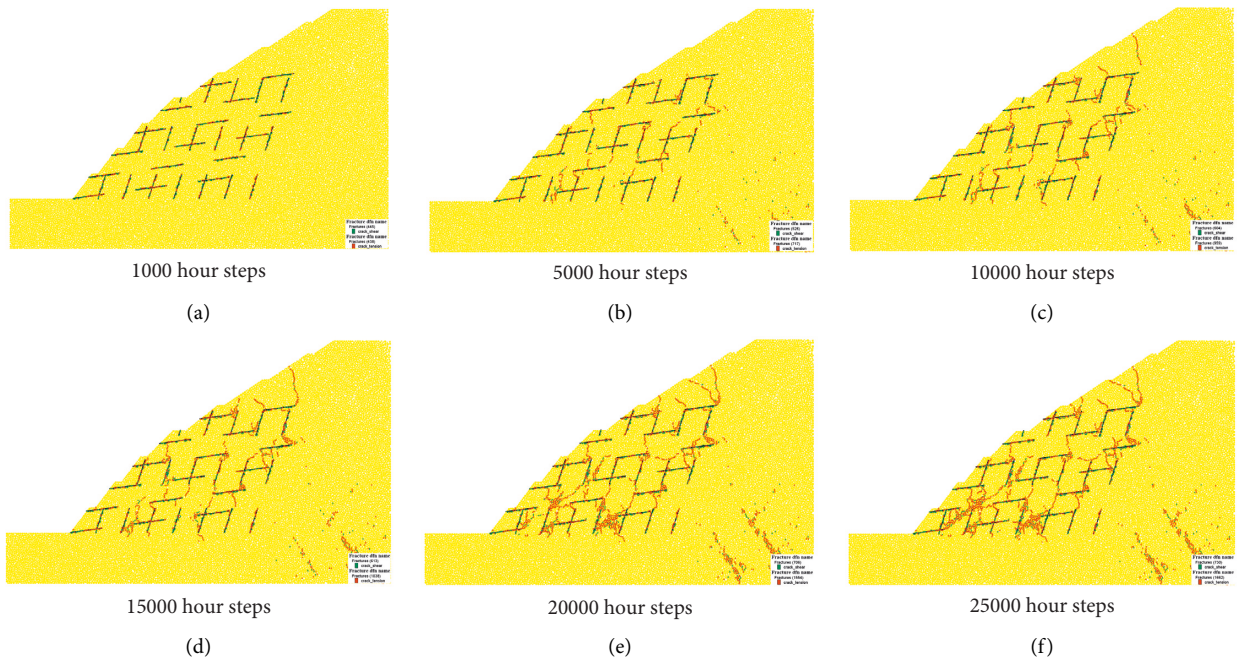

Figure 8: Mesoscale temporal and spatial development process of the rupture: (a) 1,000 hour steps, (b) 5,000 hour steps, (c) 10,000 hour steps, (d) 15,000 hour steps, (e) 20,000 hour steps, and (f) 25,000 hour steps.

many places, and the macrofracture zones were thickened and the fractures were more obvious.

As discussed above, it is found that there are two groups of layered intermittent joints (the slope angle is between the two groups of joint inclination angles) with the following failure laws: the landslide is mainly attributed to the fact that the cracks between the ends of the intermittent joints penetrate through and form a closed body separated from the parent body of the slope with the primary joints; under different time and space conditions, the microfractures are mostly tensile fractures with more vertical cracks and less transverse cracks; microcracks are preferentially generated at the joint ends of the bottom of the slope and gradually spread to the surface and upper part of the slope.

4.2. Spatiotemporal Development of Unstable and Ruptured Blocks of Jointed Rock Slopes. Figure 9 shows the time-space development process of fractured blocks, where different colors represent different fractured blocks, the fractured blocks are composed of granular bodies, and there are rock blocks separated from the rock mass due to the generation and penetration of mesofractures. The particles inside the broken block are still bound together and will continue to break into several small blocks under loading. When the model reaches 1,000 time steps, due to the rupture of smooth joints, ruptured blocks appear on the surface of the first-stage slope and the third-stage slope, in which the joints coincide with the edges of ruptured blocks, and their bottom and top are flat, and the trailing edge is steep. At the state of 5,000 time step, scattered small rupture blocks appear inside the slope, and small-area rupture blocks appear in the upper part of the first-level slope, the third-level slope, and the middle of the fifth-level slope. At 10,000 time steps, the number of scattered small fractured blocks inside continues to increase; the upper rupture block of the third-level slope continues to extend upward to the middle of the fourth-level slope; and its shape also has the characteristics of relatively gentle bottom and top and steep trailing edge. At 15,000 time steps, the scattered blocks inside the slope increase greatly, and an irregular wedge-shaped rupture block appeared from the middle of the fifth-grade slope to the middle of the seventh-grade slope on the surface; the trailing edge is steep and the bottom and left ends are flat, but the middle part is a quadrilateral embedded in the bottom. At 20,000 time steps, the internal fissures of the slope finally penetrate, and a large rupture block appears; the bottom of the large fractured block is irregular; and the trailing edge presents a steeply connected step shape. When calculation approaches 25,000 time steps, a large number of ruptured blocks appear inside,

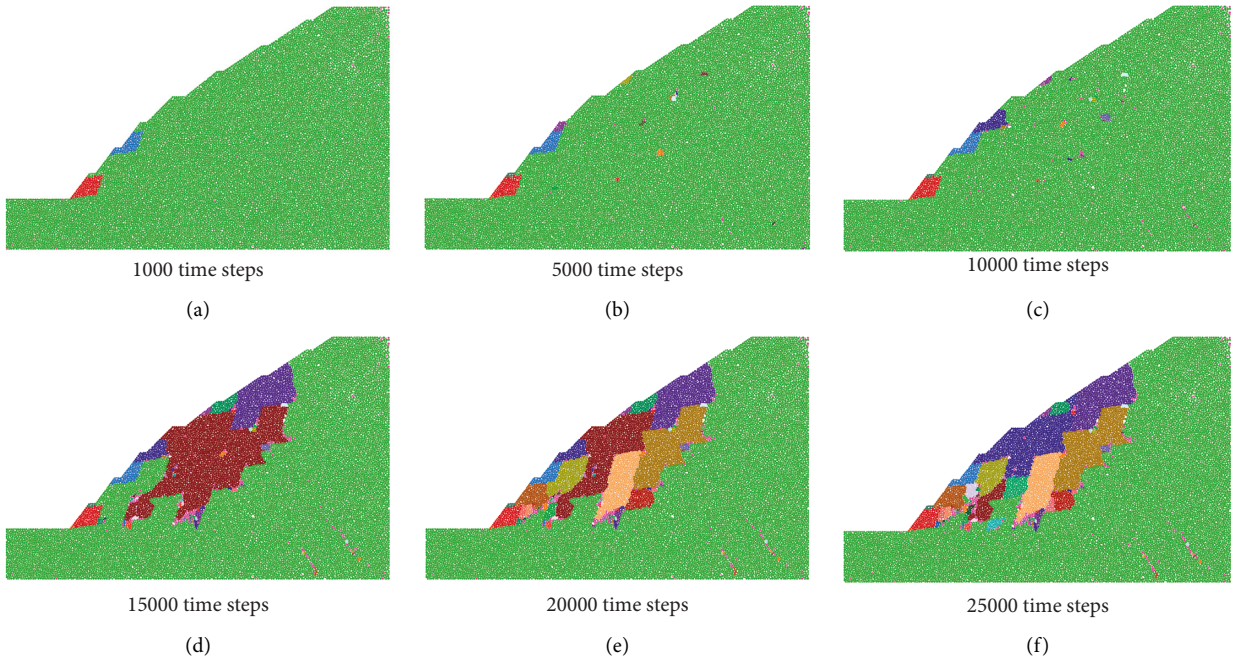

Figure 9: The spatiotemporal development process of the ruptured block: (a) 1,000 time steps, (b) 5,000 time steps, (c) 10,000 time steps, (d) 15,000 time steps, (e) 20,000 time steps, and (f) 25,000 time steps.

and on the surface of the slope, and the large inner ruptured blocks continue to rupture and divide into multiple blocks. There are ruptured blocks on the slope surface below the seventh-level slope, and most of them have the characteristics of gentle bottom and top and steep trailing edge.

Based on the analysis above, we can conclude that there are two groups of bedding discontinuous joints (the slope angle is between the two groups of joint dip angles) with the following rules when the rock slope fails: the fractured block first appeared in the lower part of the slope, then developed upward, and then occurred inside the slope; the ruptured blocks in the middle and lower parts are smaller, and the upper and inner rupture blocks are larger; most of the ruptured blocks are irregular in shape but generally show the characteristics of relatively gentle lower and upper edges and relatively steep trailing and leading edges.

4.3. Contact Force Chain and Displacement of Jointed Rock Slope. Figure 10 shows the comparison of the contact force chain before and after the instability of the jointed rock slope. As shown in Figure 10(a), the direction of the contact force on the slope surface is roughly the same as that of the slope surface. The contact force between particles inside the slope gradually recovered to the original state under the action of gravity, mainly distributing in the vertical direction and less in the horizontal direction. As shown in Figure 10(b), after the failure of the slope, the contact force between the particles at the end of the discontinuous joint is larger, which is consistent with the stress concentration phenomenon at the tip of the crack. This phenomenon is more obvious at the lower part of the slope, but near the upper and lower surfaces of the joint, the contact force is very small, and a stress arch is formed at the connection line of the rock bridge at the end of the joint, resulting in the microfracture of the slope along the end of joints.

Figure 11 shows the displacement field of particles at the end of the calculation. The displacement vector diagram of particles in Figure 11(a) directly reflects the moving direction of particles. The particles on the slope surface slide down along the slope direction, and the internal particles move downward approximately vertically. The displacement magnitude of particles is shown in Figure 11(b). The displacement of particles is larger on the slope surface and reaches a maximum of 0.4 m at the foot of the slope. However, it decreases with the location going deeper into the slope.

5. Slope Support Measures

In view that the displacement of the bottom of the slope is large and the microcracks in stages 1 to 3 of slopes are easy to be transfixed, a triple reinforcement program of anchor cable frame and grass planting is carried out. The prestressed anchor cable is combined with the reinforced concrete frame beam to form a prestressed anchor cable beam structure. In order to give full play to the antisliding ability of the landslide, the active antisliding method is adopted, and the traditional passive antisliding form is replaced by the prestressed anchor cable frame beam. The reinforcement mechanism is to transmit the anchoring force to the slope body through the interaction between the frame beam and the prestressed anchor cable, stabilize the slope surface and inside, and make the slope more stable.

According to the microscopic analysis results, the slope foot is poured with a concrete slope, and the third-level slope

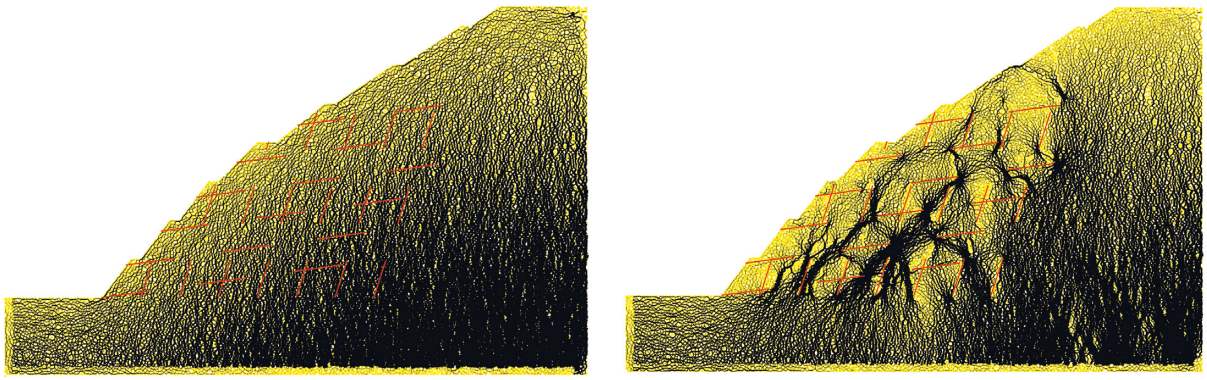

(a) (b)

Figure 10: Contact force chain diagram: (a) 0 time step and (b) 25,000 time steps.

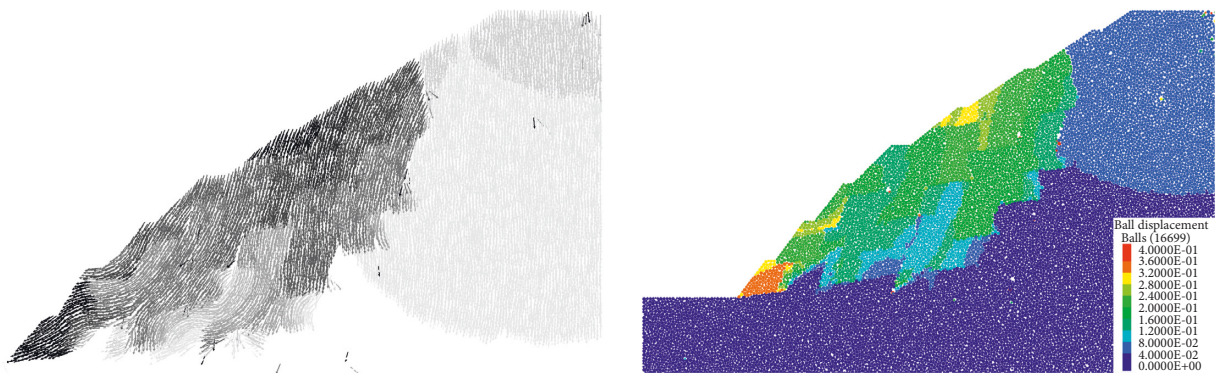

(a) (b)

Figure 11: Particle displacement diagram: (a) vector image and (b) cloud map.

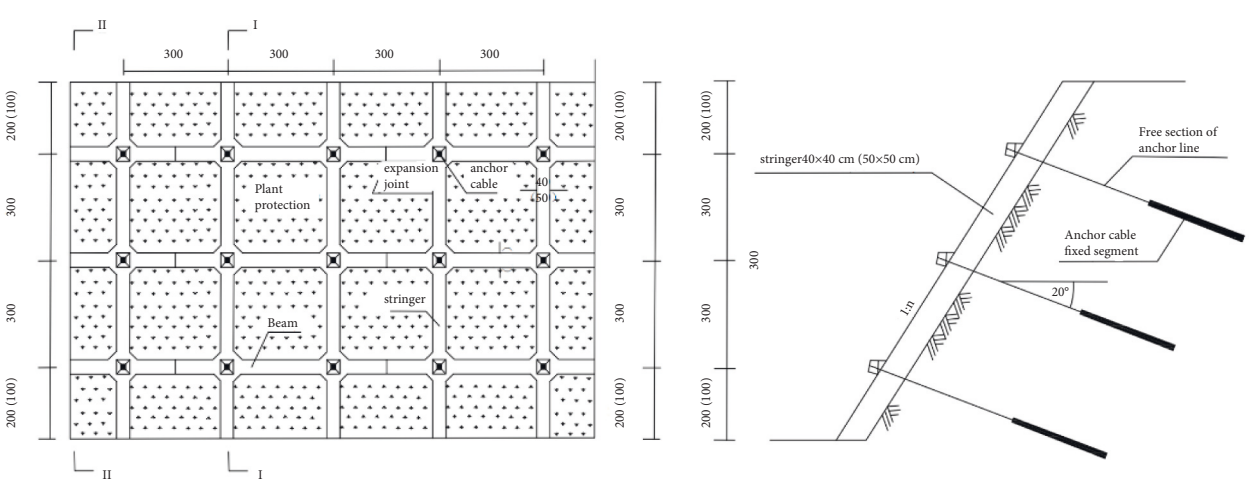

Figure 12: Construction of anchor cable frame.

uses anchor cable frame reinforcement measures. The steel strand anchors are installed by drilling holes in the slope, and the construction design of the anchor cable frame is shown in Figure 12. Three rows and six bundles of the anchor cable are adopted, of which the maximum length of the anchor cable is 20 m, the length of the anchor is 8 m with an angle of 20° with the horizontal plane, and the distance between anchor holes is 3 × 3 m. The type of six bundles of an anchor cable is OVM15-6 type, the tension strength of which is 600 kN. The reinforced concrete frame beam is set along

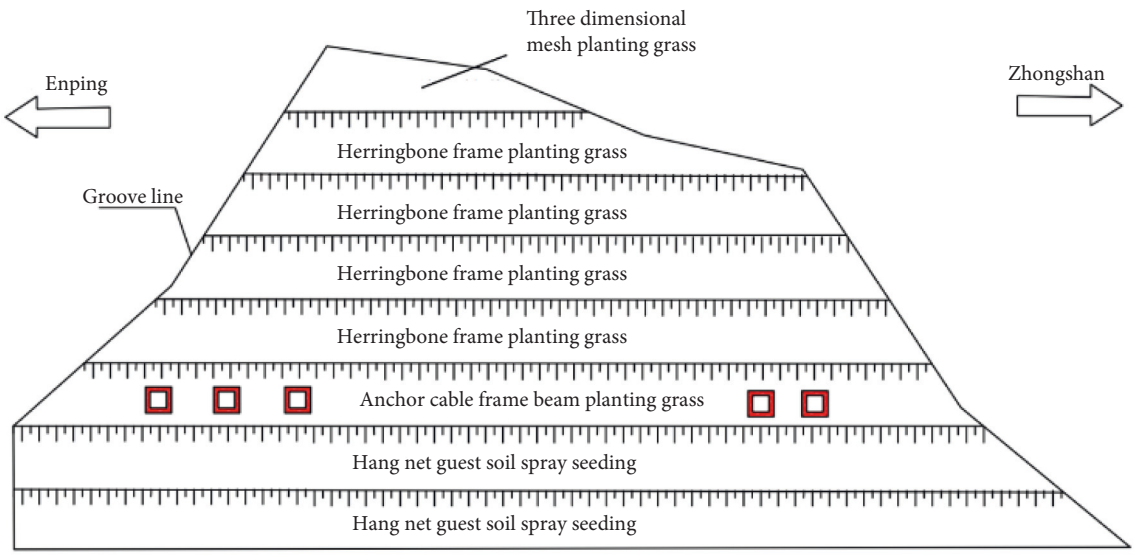

Figure 13: Schematic diagram of stress monitoring points.

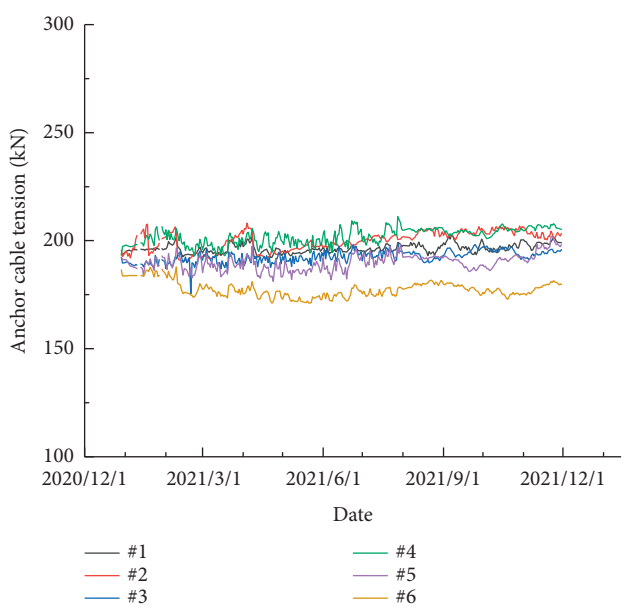

Figure 14: Stress monitoring results.

Figure 15: On-site completion situations.

the vertical and horizontal direction of the anchor hole with the rib width of 40 cm the length through the anchor hole. The frame beam is the main component of slope protection, and it is also the support point for anchor cable tensioning and anchoring. Therefore, the grass protection is made inside the frame beam, which finally constitutes the support system of the slope.

According to the anchor cable stress monitoring method, as shown in Figure 13, the anchor stress gauge is placed on the prestressed anchor cable to monitor the stress in the dangerous position shown in mesoscopic analysis (the slope of stage 3). The "real-time online display system for intelligent monitoring of high and steep road rift slopes" was developed independently to collect the monitoring data. According to the field investigations, six stress monitoring points were arranged on the slope of stage 3. The variations of stress before and after the anchor cable tensioning (see Figure 14) indicate that the reinforced slope using the above reinforcement measure is stabilized as shown in Figure 15.

6. Conclusions

In this paper a DEM model containing two groups of smooth interrupted joints of rock slopes (the slope angle is between the inclination of the two groups of joints) is constructed. The micromechanism of instability of rock slopes is analyzed from the points of microfracture, fracture block, contact force chain, and particle displacement. The detailed conclusions are as follows:

(1) The destabilization of the rocky slope is fundamentally caused by the rupture of rock intergranular adhesion, and the microfracture is mainly the result of tension failure. The microfractures firstly occur in

the internal and bottom joints of the slope and then gradually expand to the upper part of the slope with a large number of fractures in the vertical direction and fewer cracks in the horizontal direction.

(2) In the process of slope instability, the contact force at the end of the joints is large, while the contact force at the upper and lower surfaces of the joints is small, showing the phenomenon of stress arch of rock bridge.

(3) The broken particles slide down along the slope direction, and the damage is mainly located at the foot of the slope. Although a large number of cracks have occurred in the slope, there is no large-scale landslide, and the slope is generally stable. But the foot and the slope of stage 3 should be strengthened and protected.

Data Availability

The data used to support the findings of this study are available from the corresponding author upon request.

Conflicts of Interest

The authors declare that they have no conflicts of interest.

Authors' Contributions

Wei Zhu performed the data analyses and wrote the manuscript; Liang Gao established the numerical model and analyzed the results; Yingai Zhao contributed significantly to data analysis and manuscript preparation; Chao Yang and Wei Sun reviewed and edited the manuscript; Pengqiang Yu contributed to the conception and methodology of the study. All authors have read and agreed to the published version of the manuscript.

Acknowledgments

The authors gratefully acknowledge the financial support provided by PowerChina Roadbridge Group Co., Ltd. (no. LQKY2017-03).

References

[1] B. Bai, Q. Nie, Y. Zhang, X. Wang, and W. Hu, "Cotransport of heavy metals and SiO2 particles at different temperatures by seepage," *Journal of Hydrology*, vol. 597, Article ID 125771, 2021.

[2] B. Yuan, Z. Li, Z. Zhao, H. Ni, Z. Su, and Z. Li, "Experimental study of displacement field of layered soils surrounding laterally loaded pile based on transparent soil," *Journal of Soils and Sediments*, vol. 21, pp. 3072–3083, 2021.

[3] B. Bai, G. c. Yang, T. Li, and G. s. Yang, "A thermodynamic constitutive model with temperature effect based on particle rearrangement for geomaterials," *Mechanics of Materials*, vol. 139, Article ID 103180, 2019.

[4] Y. Liu and C. S. Chang, "Relationship between element-level and contact-level parameters of micromechanical and upscaled plasticity models for granular soils," *Acta Geotechnica*, vol. 15, no. 7, pp. 1779–1798, 2020.

[5] B. Bai, T. Xu, Q. Nie, and P. Li, "Temperature-driven migration of heavy metal Pb2+ along with moisture movement in unsaturated soils," *International Journal of Heat and Mass Transfer*, vol. 153, Article ID 119573, 2020.

[6] B. Yuan, Z. Li, Y. Chen et al., "Mechanical and microstructural properties of recycling granite residual soil reinforced with glass fiber and liquid-modified polyvinyl alcohol polymer," *Chemosphere*, vol. 286, Article ID 131652, 2022.

[7] Y. R. Zheng and S. Y. Zhao, "Application of strength reduction FEM in soil and rock slope," *Chinese Journal of Rock Mechanics and Engineering*, vol. 19, pp. 3381–3388, 2004.

[8] S. C. Wu, A. B. Jin, and Y. T. Gao, "Slope stability analysis by strength reduction method based on ubiquitous-joint model," *Rock and Soil Mechanics*, vol. 04, pp. 537–542, 2006.

[9] S. Zhong and Y. Miao, "Research on the influence of weak interlayer in open-pit slope on stability," *Advances in Civil Engineering*, vol. 2021, Article ID 4256740, 9 pages, 2021.

[10] Z. Ma, C. Zhu, X. Yao, and F. Dang, "Slope stability analysis under complex stress state with saturated and unsaturated seepage flow," *Geofluids*, vol. 2021, Article ID 6637098, 11 pages, 2021.

[11] Y. Hu, F. Ren, H. Ding, Y. Fu, and B. Tan, "Study on the process and mechanism of slope failure induced by mining under open pit slope: a case study from yanqianshan iron mine, China," *Advances in Civil Engineering*, Article ID 6862936, 26 pages, 2019.

[12] Z. Wang, Y. Tian, W. Zhou, Z. Liu, X. Lu, and R. Kong, "Steep end-slope mining and slope stability of extremely thick inclined coal seam open-pit mine," *Mathematical Problems in Engineering*, vol. 2022, Article ID 3807013, 9 pages, 2022.

[13] H. Wang, B. Zhang, G. Mei, and N. Xu, "A statistics-based discrete element modeling method coupled with the strength reduction method for the stability analysis of jointed rock slopes," *Engineering Geology*, vol. 264, Article ID 105247, 2020.

[14] Q. X. Meng, H. L. Wang, W. Y. Xu, M. Cai, J. Xu, and Q. Zhang, "Multiscale strength reduction method for heterogeneous slope using hierarchical FEM/DEM modeling," *Computers and Geotechnics*, vol. 115, Article ID 103164, 2019.

[15] Z. H. Zhou, Z. H. Chen, M. Bao, Q. G. Nian, and W. Zhang, "Stability of rock slope with bedding intermittent joints based on catastrophe theory," *Journal of China Coal Society*, vol. 45, pp. 161–172, 2020.

[16] M. J. Jiang, T. Jiang, G. B. Crosta, Z. M. Shi, H. Chen, and N. Zhang, "Modeling failure of jointed rock slope with two main joint sets using a novel DEM bond contact model," *Engineering Geology*, vol. 193, pp. 79–96, 2015.

[17] L. Scholtès and F. V. Donzé, "A DEM analysis of step-path failure in jointed rock slopes," *Comptes Rendus Mecanique*, vol. 343, no. 2, pp. 155–165, 2015.

[18] H. B. Wang, B. Zhang, G. Mei, and N. X. Xu, "A statistics-based discrete element modeling method coupled with the strength reduction method for the stability analysis of jointed rock slopes," *Engineering Geology*, vol. 264, Article ID 105247, 2019.

[19] K. Zhao, Y. W. Zeng, and C. Zeng, "Stability analysis of rock slope with weak structural surface based on particle flow method," *Science Technology and Engineering*, vol. 18, pp. 97–102, 2018.

[20] M. B. Victor and K. Tedius, "Wedge Failure Analyses of the Jointed Rock Slope Influenced by Foliations," *Geotechnical and Geological Engineering*, vol. 38, 2020.

[21] Z. Li, Z. Hu, W. L. Liu, G. J. Hu, S. G. Du, and Y. Zhou, "Plastic limit analysis of open-pit mine jointed rock slope considering

translation-rotation mechanisms," *Chinese Journal of Rock Mechanics and Engineering*, vol. 37, pp. 4056–4068, 2018.

[22] Y. C. Song and X. S. Sun, "Stability analysis of rock slope with connected joint," *Rock and Soil Mechanics*, vol. 35, pp. 365–372, 2014.

[23] Q. Shen, C. X. Chen, and R. Wang, "Study on stability of horizontal bedded rocky slopes in Three Gorges Reservoir area," *Rock and Soil Mechanics*, vol. 26, pp. 16–20, 2005.

[24] E. Z. Lajtai, "Brittle fracture in compression," *International Journal of Fracture*, vol. 10, no. 4, pp. 525–536, 1974.

[25] A. Bobet and H. H. Einstein, "Fracture coalescence in rock-type materials under uniaxial and biaxial compression," *International Journal of Rock Mechanics and Mining Sciences*, vol. 35, no. 7, pp. 863–888, 1998.

[26] B. Yuan, Z. Li, W. Chen et al., "Influence of groundwater depth on pile–soil mechanical properties and fractal characteristics under cyclic loading," *Fractal and Fractional*, vol. 6, no. 4, p. 198, 2022.

[27] M. Ma, M. Li, X. Qu, and H. Zhang, "Effect of passing metro trains on uncertainty of vibration source intensity: monitoring tests," *Measurement*, vol. 193, Article ID 110992, 2022.

[28] B. Bai and T. Li, "Irreversible consolidation problem of a saturated porothermoelastic spherical body with a spherical cavity," *Applied Mathematical Modelling*, vol. 37, no. 4, pp. 1973–1982, 2013.

[29] C. Zou, J. A. Moore, M. Sanayei, Z. Tao, and Y. Wang, "Impedance model of train-induced vibration transmission across a transfer structure into an over track building in a metro depot," *Journal of Structural Engineering*, vol. 172, 2022.

[30] Y. Liu, D. Zhang, S. Wu, and P. Yu, "DEM investigation on the evolution of fabric under true triaxial conditions in granular materials," *International Journal of Geomechanics*, vol. 20, no. 8, Article ID 04020110, 2020.

[31] X. S. Li and Y. F. Dafalias, "Anisotropic critical state theory: role of fabric," *Journal of Engineering Mechanics*, vol. 138, no. 3, pp. 263–275, 2012.

[32] B. Bai, Y. Wang, D. Rao, and F. Bai, "The effective thermal conductivity of unsaturated porous media deduced by pore-scale SPH simulation," *Frontiers of Earth Science*, vol. 10, 2022.

[33] C. S. Chang and P. Y. Hicher, "An elasto-plastic model for granular materials with microstructural consideration," *International Journal of Solids and Structures*, vol. 42, no. 14, pp. 4258–4277, 2005.

[34] X. Gu, X. Liang, Y. Shan, X. Huang, and A. Tessari, "Discrete element modeling of shear wave propagation using bender elements in confined granular materials of different grain sizes," *Computers and Geotechnics*, vol. 125, Article ID 103672, 2020.

[35] H. Jin, Q. Tian, and Z. Li, "Crack development of rebar rust in rubberized concrete using mesoscale model," *Construction and Building Materials*, vol. 321, Article ID 126409, 2022.

[36] B. Bai, R. Zhou, G. Cai, W. Hu, and G. Yang, "Coupled thermo-hydro-mechanical mechanism in view of the soil particle rearrangement of granular thermodynamics," *Computers and Geotechnics*, vol. 137, no. 8, Article ID 104272, 2021.

[37] H. Jin, J. Su, and C. Zhao, "Relationship between invert-filling disengaging and deformation of shield tunnel using staggered assembled segment," *KSCE Journal of Civil Engineering*, vol. 26, no. 4, pp. 1966–1977, 2022.

[38] D. O. Potyondy and P. A. Cundall, "A bonded-particle model for rock," *International Journal of Rock Mechanics and Mining Sciences*, vol. 41, no. 8, pp. 1329–1364, 2004.

[39] L. Xu and M. Ma, "Dynamic response of the multilayered half-space medium due to the spatially periodic harmonic moving load," *Soil Dynamics and Earthquake Engineering*, vol. 157, Article ID 107246, 2022.

[40] X. Wang, Y. Liu, and P. Yu, "Upscaling critical state considering the distribution of meso-structures in granular materials," *International Journal for Numerical and Analytical Methods in Geomechanics*, vol. 45, no. 11, pp. 1624–1646, 2021.

Hindawi
Advances in Civil Engineering
Volume 2022, Article ID 4031050, 10 pages
https://doi.org/10.1155/2022/4031050

Research Article

Prediction of Metro Train-Induced Tunnel Vibrations Using Machine Learning Method

Zhuosheng Xu,[1,2] Meng Ma,[1,2] Zikai Zhou,[2] Xintong Xie,[2] Haoxiang Xie,[2] Bolong Jiang,[3] and Zhongshuai Zhang[2]

[1]*Key Laboratory of Urban Underground Engineering of Ministry of Education, Beijing Jiaotong University, Beijing 100044, China*
[2]*School of Civil Engineering, Beijing Jiaotong University, Beijing 100044, China*
[3]*National Engineering Research Center of Rail Transit Digital Construction and Measurement Technology, China Railway Design Corporation, Tianjin 300142, China*

Correspondence should be addressed to Meng Ma; mameng@bjtu.edu.cn

Received 1 May 2022; Accepted 17 May 2022; Published 19 June 2022

Academic Editor: Quanmin Liu

The tunnel vibration level is usually employed as a vibration source intensity of the empirical prediction method. Currently, the analogy test and data base are two main means to determine the vibration source intensity. To improve the accuracy efficiency, the machine learning (ML) method was introduced to predict the tunnel vibration responses. To acquire model training samples, the measurements were performed in 80 different running tunnel sections of Beijing metro lines. Two types of method, back propagation neural network (BPNN) and generalised regression neural network (GRNN) were employed, which can make full use of characteristics of measured samples and reduce the data noise. The results indicate that the prediction efficiency is high and the mean square errors of the two ML methods are acceptable. Accordingly, both of the ML methods can be used as the reference of vibration source intensity in metro train-induced environmental impact evaluation. GRNN has relatively better predicting ability than BPNN.

1. Introduction

With the development of urban rail transit construction, the environmental vibration problem arising from metro operation is becoming more and more prominent [1–4]. A reasonable vibration mitigation design has put forward higher requirements to the environmental vibration prediction. Various types of prediction model can be employed in different construction stages of a metro project [5, 6]. In the feasibility study stage of developing a rail system, the scoping or preliminary prediction can be used to identify whether the environmental vibration is an issue for potential sensitive buildings along the rail transportation alignment. Empirical and semi-empirical models are widely used in this stage [7–9]. Recently, the machine learning (ML) method has been introduced in the scoping prediction, such as the researches by Paneiro et al. [10], Connolly et al. [11, 12], Chen et al. [13], Yao et al. [14], Paneiro et al. [15], Fang et al. [16] and Liang et al. [17]. In the scheme design stage, the determined prediction can be used, including various types of numerical [18–22], analytical/semi-analytical methods [23–26]. In the construction design stage, the detail prediction methods were developed, such as measurement-based transfer function method [27–29] and hybrid methods [30–34].

A chain-type formula based on the assumption of uncoupled sub-systems is a classical empirical prediction method. Its idea was originally proposed by Kurzweil [35] and Melke [36], and developed in different standards and guidelines [9, 37–39]. In Chinese code HJ 453-2018 [38], the predicted environmental vibration level VL_z can be calculated by the superposition of the vibration source level $VL_{Z,0}$ and a series of vibration level correction terms, details can be found in reference [40]. The value of $VL_{Z,0}$ is defined as the vertical weighted vibration acceleration level on the tunnel wall. Two main approaches can be used to determine $VL_{Z,0}$.

One is analogy test in a similar running tunnel section, which is regarded as the most accuracy method. Another is searching the database, in which the test has been performed in a similar tunnel section. However, there are disadvantages on both of the methods. The analogy test is time consuming, especially when the workload is heavy. Furthermore, the parameters of the test section should be consistent with the predicted section as far as possible. These parameters include train speed, route radius, tunnel shape and size, track type, soil parameters, etc. It is almost impossible to ensure that all parameters of the two sections are consistent, which introduces errors of the source intensity values. Owing to the large time and labor cost of the analogy test method, the database method is also recommended by standards. However, the database method has the same problem as the analogy test method, and the error is greater because the amount of data available for reference is not large enough.

To solve the problem and improve the prediction efficiency of $VL_{Z,0}$, ML method was introduced in the present study. The in-situ measurements were performed in 80 different tunnel sections of Beijing metro lines and the model training samples of $VL_{Z,0}$ were obtained. Finally, two types of ML method were analysed and the prediction results were validated.

2. Measurement in Metro Tunnel

2.1. Measurement Outline. To obtain the data of $VL_{Z,0}$ for training model, in-situ measurements were performed in 80 different running tunnel sections in Beijing metro. Various types of parameters were obtained and considered for each section, including track type, radius, tunnel shape, train speed and vehicle type, details as:

(i) Track type: regular slab track, steel spring floating slab track (FST), rubber isolator FST; ladder sleeper track, slab track with short sleeper, and slab track with elastic sleeper;

(ii) Radius: from 350 m to infinite (straight line);

(iii) Tunnel shape: horse-shoe tunnel and shield tunnel;

(iv) Train speed: between 15 and 92 km/h;

(v) Vehicle type: types A and B.

Figure 1 illustrates the measuring point location in a tunnel with FST. According to the specification HJ 453-2018 [38], the location of the vibration source intensity is defined at the tunnel wall, with 1.25 m height from the rail top. For the curved tunnel, the sensors were installed on the side of inner rails.

In these tests, the date acquisition equipment INV 3060S was employed with a maximum sampling frequency of 51.2 kHz. The accelerometer is Lance 0105T with a measurement range of 20 g and working frequency between 0.35 and 6000 Hz.

2.2. Measurement Result. The vibration source intensity $VL_{Z,0}$ is expressed as the maximum Z-vibration level, defined as:

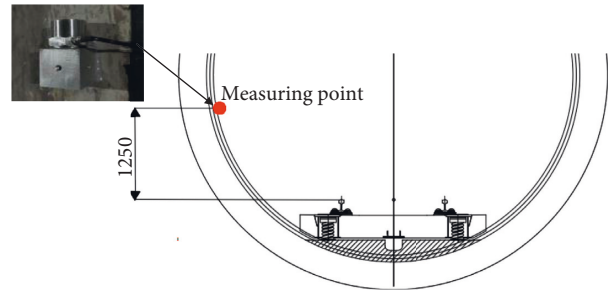

Figure 1: Measuring point location on the tunnel wall (unit: mm).

$$VL_{z,0} = \max_t \left[VL_Z(t)\right] = \max_t \left[20\lg \frac{a_{w,\tau}(t)}{a_0}\right],$$
$$a_{w,\tau}(t) = \sqrt{\frac{1}{\tau}\int_0^t a_w^2(\xi)\mathrm{d}\xi}, \quad (1)$$

where $VL_z(t)$ is the frequency-weighed vertical vibration acceleration level as a function of time t, $a_{w,\tau}(t)$ is the running root-mean-square weighted acceleration, $a_w(\xi)$ is the frequency-weighed instantaneous vibration acceleration at time ξ, τ is the integration time of the measurement, and t is the instantaneous time. The weighting factor suggested by ISO 2631/1 was employed in this study.

An illustration of the calculation method for maximum Z-vibration level was shown in Figure 2.

All the values of $VL_{Z,0}$ were averaged by five recording pass-by trains. Finally the averaged $VL_{Z,0}$ of the 80 test sections were listed in Table 1. Figure 3 illustrates the $VL_{Z,0}$ of different track type varies with train speeds. Generally, $VL_{Z,0}$ increases with train speed, especially below 40 km/h. Generally speaking, the vibration reduction effect of steel spring FST is better than that of rubber isolator FST. However, sections 10 and 12 were measured in a deep buried horse-shoe tunnel, where the surrounding rock condition and tunnel shape affect the test results of the tunnel responses.

3. Predicting $VL_{z,0}$ Using ML Method

To provide a fast and accuracy prediction of $VL_{z,0}$ based on the measured samples, two types of ML methods were used: back propagation neural network (BPNN) and generalised regression neural network (GRNN).

3.1. BPNN Based Prediction

3.1.1. Method Introduction. BPNN is a type of multilayer feedforward neural network which can acquire output vectors by processing input vectors through hidden layers (Figure 4). The output error can be evaluated by the error function. The error back propagation can be carried out by the gradient descent method based on the output error. Then, the connection weight w_i and threshold b_i between neurons can be modified. Finally, the error of the neural network can be decreased to the minimum. The weight

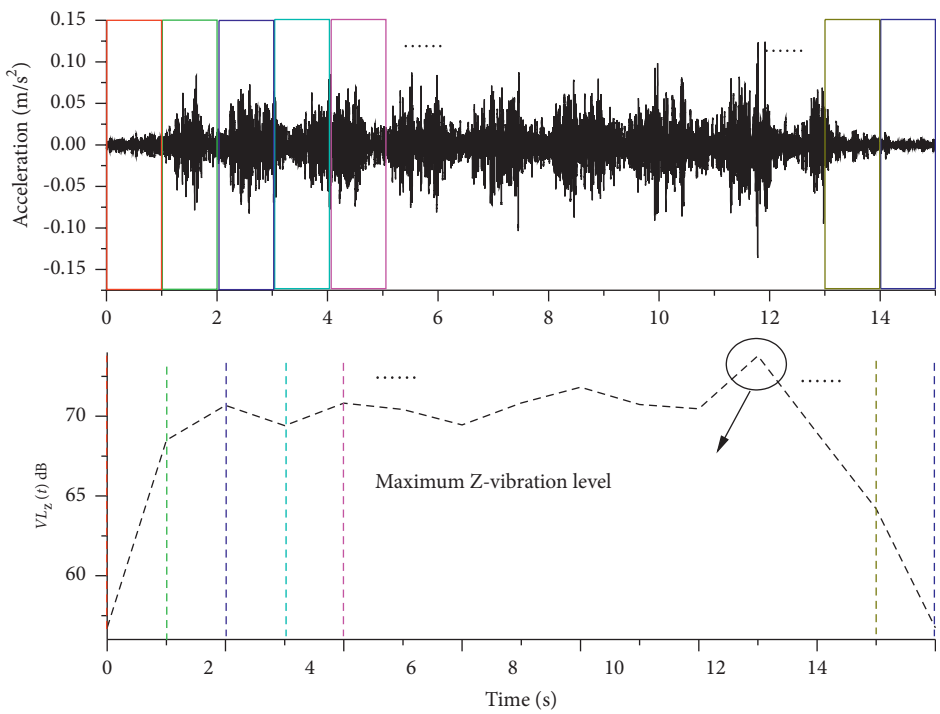

Figure 2: Illustration of calculation method for maximum Z-vibration level.

adjustment can be regarded as a prior probability distribution of the weight and threshold. Then, the posterior probability distribution of the weight and threshold are adjusted based on different input data. Finally, the network parameters can be modified and the generalisation ability of network is improved.

The BPNN can be optimised by introducing the Bayes' principle, by which a modification function for the performance function is introduced:

$$F(w) = \alpha E_w + E_d \beta, \tag{2}$$

where, α and β are hyper-parameters; E_w is the network coefficient related to the weight; E_d is the conventional error term. E_w and E_d can be expressed as:

$$\begin{aligned} E_w &= \frac{1}{m}\sum_{i=1}^{m} w_i^2, \\ E_D &= \frac{1}{N}\sum_{i=1}^{N} [y_i - t_i]^2, \end{aligned} \tag{3}$$

where m and N are the neurons number of output and hidden layers, w_i is the initial weight, and y_i is the output vector.

When predicting with BPNN, the initialised weight w_i and hyper-parameters α and β need to be randomised firstly. Subsequently, the training set **P** is input as training samples. After training, the weight w_{MP} is calculated at which the grad of equation (2) is the minimum. Finally, the hyper-parameters can be calculated:

$$\begin{aligned} a_{MP} &= \frac{\gamma}{2E_w(w_{MP})}, \\ \beta_{MP} &= \frac{(N-\gamma)}{2E_D(w_{MP})}, \end{aligned} \tag{4}$$

where, γ can be calculated based on w_{MP} and the renewed values of α and β can be re-determined. In equation (5), α_{MP} and β_{MP} are the α and β when w values w_{MP}. The steps above are repeated until the network converge [41].

According to the number of data eigenvalues, six nodes were set in the input layer, and the network layer number was set as 3 to lower the complexity of network and pretend over-fitting. One node was set in the output layer, and output value was the predicted vibration source intensity, e.g. maximum Z-vibration level.

The mean squared error (MSE) was used to analyse the prediction performance of the network. MSE is defined as:

$$\mathrm{MSE} = \frac{1}{n}\sum_{i=1}^{N} (\hat{y}_i - y_i)^2, \tag{5}$$

where y_i and $\hat{y}_i$ are the true and predicted values of the test set, respectively; N is the number of output layer.

In this study, the value of $VL_{Z,0}$ is expressed in dB, so MSE is measured in dB^2. Generally, the $VL_{Z,0}$ is between 60 and 80 dB. If the predicted average percentage error is 10%, the absolute error is approximately between 6 and 8 dB. That is, if MSE is below 36 dB^2, it can be regarded as an acceptable result.

Table 1: Average source intensity and parameter of 80 sections.

Test section nr.	Track type	Radius (m)	Tunnel type	Speed (km/h)	Vehicle type	Average $VL_{z,0}$ (dB)
1	Regular slab track	650	Shield tunnel	70	B	77.8
2	Steel spring FST	650	Shield tunnel	70	B	60.53
3	Steel spring FST	Straight line	Shield tunnel	70	B	59.5
4	Regular slab track	Straight line	Shield tunnel	70	B	80
5	Steel spring FST	Straight line	Shield tunnel	70	B	64.5
6	Steel spring FST	Straight line	Shield tunnel	70	B	66
7	Regular slab track	Straight line	Shield tunnel	75	B	64.7
8	Steel spring FST	450	Horse-shoe tunnel	59.8	B	45.1
9	Regular slab track	450	Horse-shoe tunnel	64.7	B	66.2
10	Rubber isolator FST	490	Horse-shoe tunnel	75.4	B	51.9
11	Regular slab track	505	Horse-shoe tunnel	66.2	B	64.9
12	Rubber isolator FST	505	Horse-shoe tunnel	77.5	B	52.4
13	Regular slab track	505	Horse-shoe tunnel	66.2	B	64.9
14	Ladder sleeper track	Straight line	Shield tunnel	57.8	B	68.9
15	Regular slab track	Straight line	Shield tunnel	60.4	B	82.5
16	Steel spring FST	650	Shield tunnel	88	B	73.63
17	Steel spring FST	650	Shield tunnel	92	B	73.56
18	Ladder sleeper track	650	Shield tunnel	90	B	88.75
19	Ladder sleeper track	Straight line	Shield tunnel	90	B	79.96
20	Ladder sleeper track	650	Shield tunnel	75	B	82.91
21	Ladder sleeper track	1156	Shield tunnel	87	B	75.93
22	Slab track with short sleeper	350	Shield tunnel	15	B	68
23	Slab track with short sleeper	Straight line	Shield tunnel	15	B	65.2
24	Slab track with short sleeper	Straight line	Shield tunnel	15	B	61.2
25	Steel spring FST	Straight line	Shield tunnel	15	B	47
26	Slab track with elastic long sleeper	350	Shield tunnel	15	B	63.2
27	Steel spring FST	Straight line	Shield tunnel	15	B	53.1
28	Slab track with short sleeper	350	Shield tunnel	25	B	74
29	Slab track with short sleeper	Straight line	Shield tunnel	25	B	67.2
30	Slab track with short sleeper	Straight line	Shield tunnel	25	B	59.2
31	Steel spring FST	Straight line	Shield tunnel	25	B	50.5
32	Slab track with elastic long sleeper	350	Shield tunnel	25	B	69.1
33	Slab track with elastic long sleeper	500	Shield tunnel	25	B	68.1
34	Slab track with elastic long sleeper	Straight line	Shield tunnel	25	B	60.9
35	Steel spring FST	Straight line	Shield tunnel	25	B	58.8
36	Slab track with short sleeper	350	Shield tunnel	35	B	76.3
37	Slab track with short sleeper	Straight line	Shield tunnel	35	B	77.6
38	Slab track with short sleeper	Straight line	Shield tunnel	35	B	69.5
39	Steel spring FST	Straight line	Shield tunnel	35	B	54.5
40	Slab track with elastic long sleeper	350	Shield tunnel	35	B	74.7
41	Slab track with elastic long sleeper	500	Shield tunnel	35	B	80.7
42	Slab track with elastic long sleeper	Straight line	Shield tunnel	35	B	70.5
43	Steel spring FST	Straight line	Shield tunnel	35	B	55.6
44	Slab track with short sleeper	350	Shield tunnel	45	B	78.7
45	Slab track with short sleeper	Straight line	Shield tunnel	45	B	81.7
46	Slab track with short sleeper	Straight line	Shield tunnel	45	B	71.8
47	Steel spring FST	Straight line	Shield tunnel	45	B	56.3
48	Slab track with elastic long sleeper	350	Shield tunnel	45	B	74.8
49	Slab track with elastic long sleeper	500	Shield tunnel	45	B	78.2
50	Slab track with elastic long sleeper	Straight line	Shield tunnel	45	B	72.8
51	Steel spring FST	Straight line	Shield tunnel	45	B	57.4
52	Slab track with short sleeper	350	Shield tunnel	57	B	81.4
53	Slab track with short sleeper	Straight line	Shield tunnel	57	B	82.4
54	Slab track with short sleeper	Straight line	Shield tunnel	57	B	72.6
55	Steel spring FST	Straight line	Shield tunnel	57	B	57.2
56	Slab track with elastic long sleeper	350	Shield tunnel	57	B	74.6
57	Slab track with elastic long sleeper	500	Shield tunnel	57	B	77.2
58	Slab track with elastic long sleeper	Straight line	Shield tunnel	57	B	71.3
59	Steel spring FST	Straight line	Shield tunnel	57	B	57.4
60	Ladder sleeper track	Straight line	Horse-shoe tunnel	64	B	68.795

Table 1: Continued.

Test section nr.	Track type	Radius (m)	Tunnel type	Speed (km/h)	Vehicle type	Average $VL_{z,0}$ (dB)
61	Ladder sleeper track	Straight line	Horse-shoe tunnel	64	B	68.63
62	Regular slab track	Straight line	Shield tunnel	67.7	B	83
63	Steel spring FST	350	Shield tunnel	45	B	61.5
64	Ladder sleeper track	Straight line	Shield tunnel	60.6	B	71.5
65	Steel spring FST	Straight line	Shield tunnel	75	B	64.5
66	Steel spring FST	Straight line	Horse-shoe tunnel	68.6	B	61.5
67	Steel spring FST	Straight line	Horse-shoe tunnel	67.6	B	68
68	Regular slab track	Straight line	Horse-shoe tunnel	68.3	B	78
69	Regular slab track	Straight line	Horse-shoe tunnel	69.3	B	68
70	Regular slab track	Straight line	Shield tunnel	69.4	B	78
71	Regular slab track	Straight line	Shield tunnel	36	B	81.2
72	Regular slab track	Straight line	Shield tunnel	40	B	84.9
73	Regular slab track	Straight line	Shield tunnel	69	B	85.9
74	Regular slab track	Straight line	Shield tunnel	76	B	82
75	Regular slab track	Straight line	Shield tunnel	78	B	81.6
76	Regular slab track	Straight line	Shield tunnel	69	B	85.8
77	Regular slab track	Straight line	Shield tunnel	69	B	78.8
78	Regular slab track	Straight line	Shield tunnel	72	B	79.7
79	Regular slab track	Straight line	Shield tunnel	68	A	84.5
80	Regular slab track	Straight line	Shield tunnel	68	A	87.5

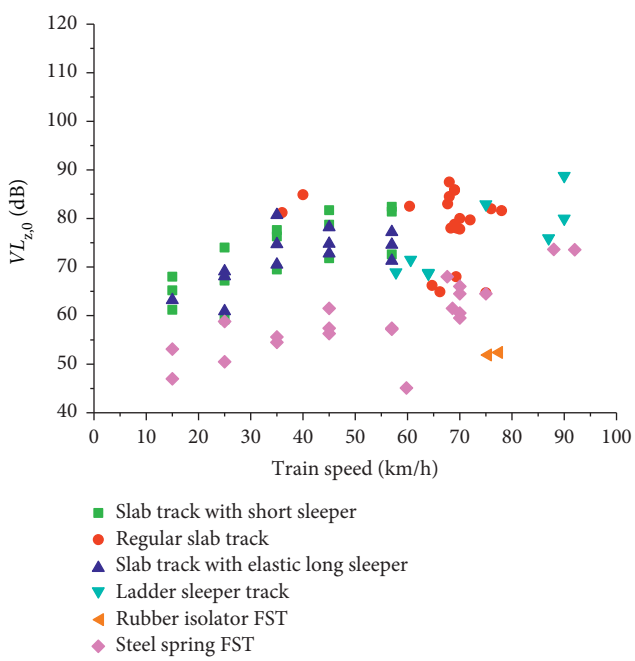

Figure 3: Tunnel vibration responses vary with train speed.

The relationship between node number of hidden layers, eigenvalue number and input/output node number can be expressed as [42].

$$s = \sqrt{m + n} + a, \tag{6}$$

where s and m are node numbers of the hidden layer and input layer.

3.1.2. Sample Training and Results. According to equation (6), the test begins with three nodes of the hidden layers. With the same training set and test set, the node number of the hidden layer can be increased gradually. The training is repeated three times for each hidden layer, and the averaged value can be obtained. The training results are illustrated in Figure 5 and the final optimised node number was six.

The model was building using the neural network toolbox in MATLAB. The activation function for the hidden layer was Sigmod function and for the output layer was purelin function. The maximum convergence times was set as 1000, and the maximum training accuracy was 0. The Bayesian regularisation method (trainbr) was selected as the training method. A total of eight groups of data were randomly selected for test and the rest 72 groups of data were used as the train set. After training the neural network with the train set, the test set was predicted.

When training, a weight matrix was randomly generated and then weight was modified with the transmission error.

Figure 6 illustrates the training results by comparing measured and predicted values. Based on equation (5), MSE of this test set can be calculated as 29.98, which proves the accuracy of training model is good enough to perform the prediction. According to detailed information in Figure 6, the absolute error of MSE is controlled within 10%, ranging from −7.57% to 9.86%, which demonstrates an acceptable prediction ability of this model.

3.1.3. Test and Verification. To ensure the generalisation ability of the network, a cross validation was performed. After arranging data randomly, the data were divided into ten subsets. Every subset was selected as a test set, and the remaining were training sets. The cross validation were repeated ten times following the above steps. Figure 7 demonstrates MSE of ten cross validation results and the averaged MSE is 32.28, which demonstrates a good generalisation ability of this method.

Furthermore, the method of leave-one-out-cross-validation (LOOCV) was used to calculate and analyse the errors between measured and predicted values. Figure 8

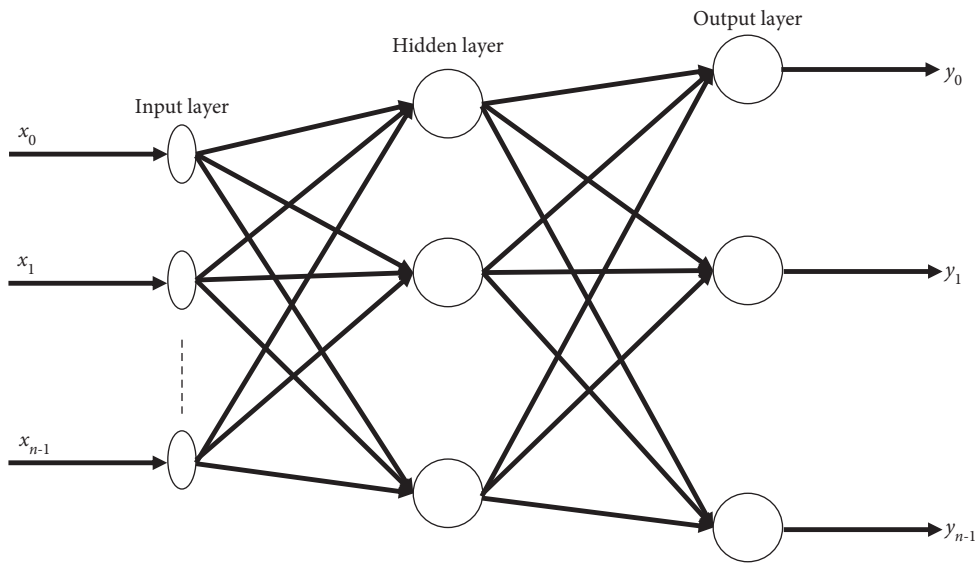

Figure 4: Topology of BPNN.

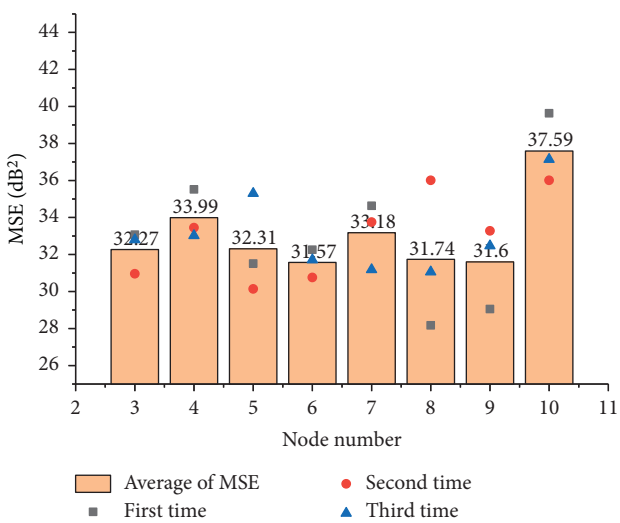

Figure 5: MSE of different node number of hidden layer.

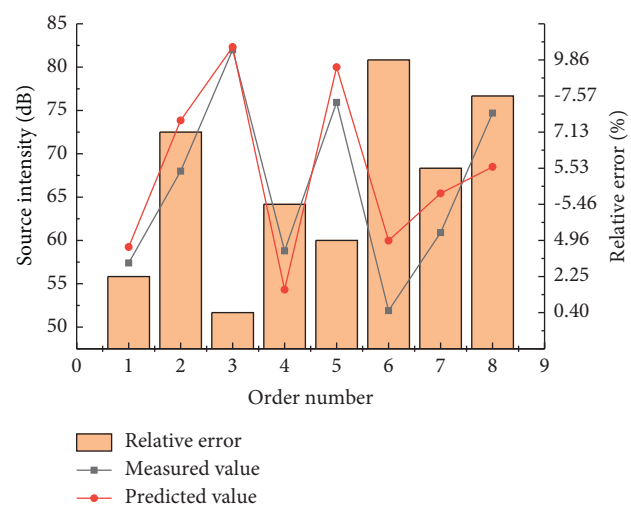

Figure 6: Predicted result of back propagation neural network.

illustrates the error normal distribution of BPNN using LOOCV.

Based on the verification of LOOCV and cross validation, the prediction error is generally below 10% and the average MSE is less than 35. Accordingly, BPNN can be used to undertake a preliminary prediction of the source intensity vibration of a running metro train.

Moreover, coefficient of determination R^2 can be used to evaluate linear correlation degree of network fitting result. The coefficient of determination is defined as

$$R^2 = \frac{\mathrm{SSR}}{\mathrm{SST}},$$
$$\mathrm{SSR} = \sum_i (\hat{y}_i - \overline{y}_i)^2, \tag{7}$$
$$\mathrm{SST} = \sum_i (y_i - \overline{y}_i)^2,$$

where, y_i is the true value, $\hat{y}_i$ is the predicted value, and $\overline{y}_i$ is the average of true value.

Coefficient of determination R^2 ranges from 0 to 1. The closer R^2 approaches to 1, the better the linear correlation degree of network fitting result is. After calculation, R^2 of BPNN is 0.9464, which reflects the BPNN model can also be used to predict the vibration source intensity.

3.2. GRNN Based Prediction

3.2.1. Method Introduction. GRNN is a type of radial basis function (RBF) neural network, which has strong non-linear mapping capability, fault tolerance and robustness. Besides, it has the advantage in the approaching ability and learning speed. The model of radial basis neural network includes two main independent variable and basis function. The

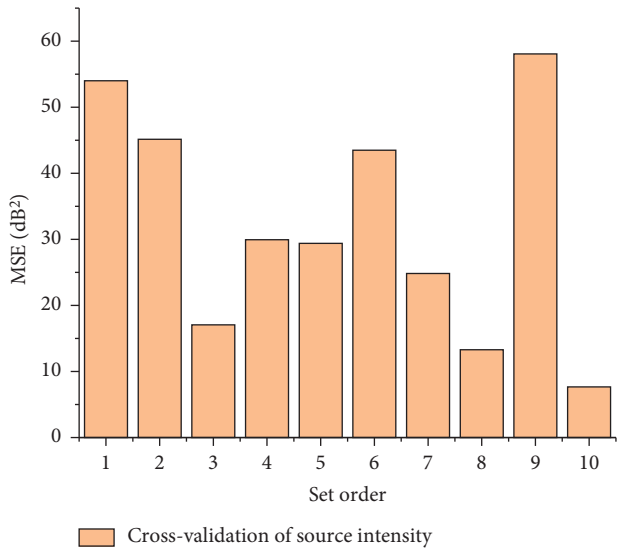

Figure 7: Cross validation of source intensity prediction.

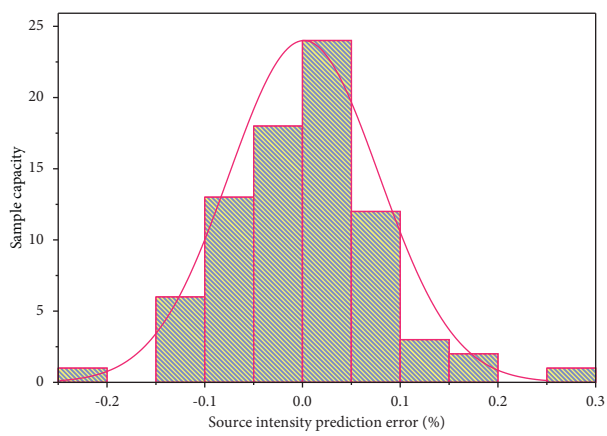

Figure 8: Error distribution of vibration source intensity predicted using BPNN.

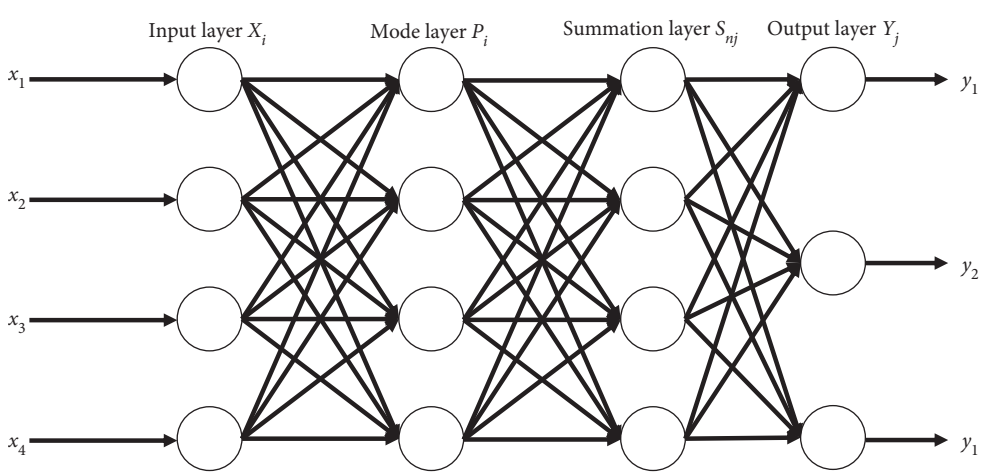

Figure 9: Topology of GRNN.

independent variable is the Euclidean distance between the points to be measured and sampling. The basis function is a radial function. GRNN can transform a multi-dimensional problem into a one-dimensional problem. After transformation, the independent variable of one-dimensional issue turns into the Euclidean distance mentioned above. Any function can be obtained by making weighted combination of basis functions. Figure 9 demonstrates the topology of GRNN.

In the calculation and analyse by GRNN, the training set **P** is firstly input as a learning sample, and then S_D and S_{Ni} are calculated and output to the summation layer. S_D and S_{Ni} are neurons in the hidden layer, calculated by two different methods. One is the summation of denominator neurons, i.e. straightly summing up all the neurons in hidden layers. The other is the summation of molecular neurons, i.e. making a weighted summation of neurons in mode layers. S_D and S_{Ni} can be calculated by

$$S_D = \sum_{i=1}^{n} P_i = \sum_{i=1}^{n} \exp\left[\frac{(x-x_i)^T(x-x_i)}{2\sigma_i^2}\right], i = 1, 2, 3 \ldots n,$$
$$S_{N_i} = \sum_{i=1}^{n} Y_i P_i = \sum_{i=1}^{n} y_{ij} \exp\left[\frac{(X-X_i)^T(X-X_i)}{2\sigma_i^2}\right], j = 1, 2, 3 \ldots n, \quad (8)$$

where σ_i is a network expansion constant, y_{ij} is the connecting weight of the i-th neuron in the summation layer and the j-th neuron in the mode layer. Finally, the output network predicted value can be obtained: $y_j = S_D/S_{Ni}$ [43].

According to the characteristic of RBF neural network, the data should be expressed in the form of scientific counting before normalisation. Then, the route radius was multiplied by 0.01 and the train speed was multiplied by 0.1. Based on the fast learning speed of GRNN, building a large network and performing mutual authentications are possible. Then, the network was built for all 80 groups of data one by one. The i-th group of data was selected as the test set and the remaining were the train sets. Thus, a total of 80 networks can be established and the data can be made full used.

3.2.2. Results, Test and Verification. After training, 80 groups of predicted results can be obtained using LOOCV. Figure 10 demonstrates the comparison between predicted and measured values.

Figure 11 demonstrates MSE values under different values of σ. According to Figure 11, the value of σ have little influence on the result of this experiment. When $\sigma = 1$ the MSE value is the minimum. Accordingly, this value was determined in this experiment.

Both of the MSE and coefficient of determination R^2 were used to evaluate linear correlation degree of network fitting result. After calculation, MSE is 17.9205, and R^2 is 0.8153. Figure 12 demonstrates the error distribution. For its normal fitting curve, average value is 0.004664 and standard deviation is 0.07571.

The above results and verification proves that GRNN can be used to predict the vibration source intensity with considering different parameters. Compared with BPNN,

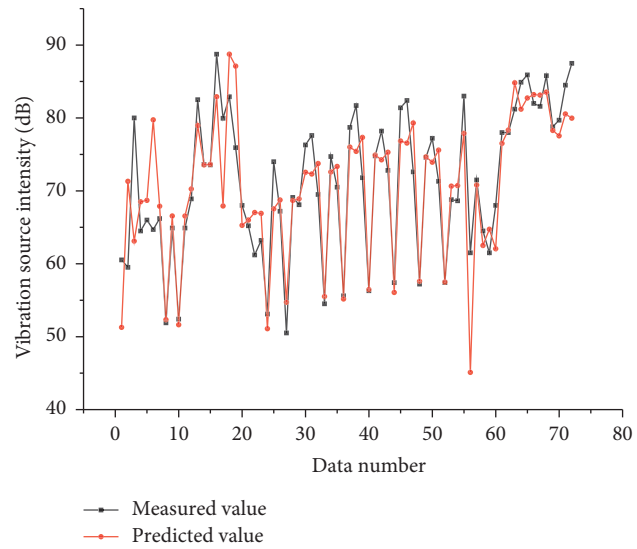

Figure 10: GRNN based predicted result.

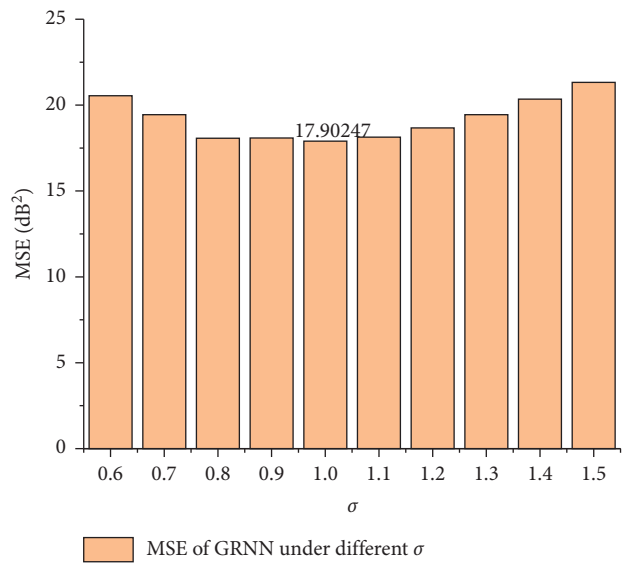

Figure 11: MSE of GRNN under different values of σ.

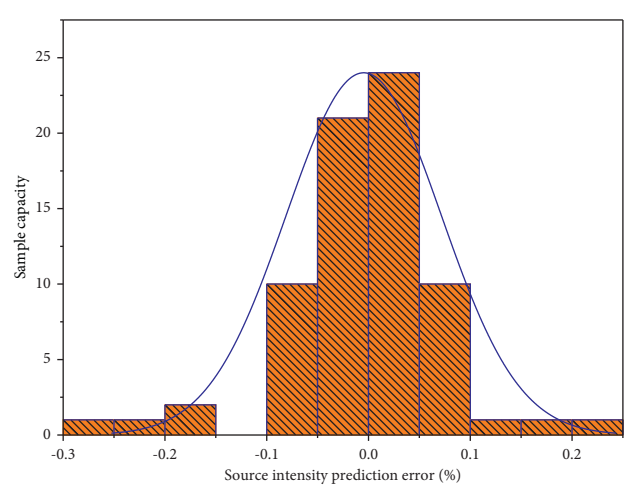

Figure 12: Source intensity prediction error distribution predicted by GRNN.

both of the calculation efficiency and the accuracy of GRNN are higher. Accordingly, GRNN is more recommended to predict the vibration source intensity.

4. Conclusion

To improve the prediction efficiency of $VL_{Z,0}$ in the empirical prediction formula, ML method was introduced in the present study. In-situ measurements were performed in 80 different running tunnel sections of Beijing metro and the model training samples of $VL_{Z,0}$ were obtained. Two types of ML method were employed and compared for the prediction results. The results indicate that:

(1) Both of BPNN and GRNN can be used to predict the tunnel vibration responses $VL_{Z,0}$. Proved by LOOCV, predicting by neural network has good extensionality. In the preliminary prediction phase, the neural network based prediction results can be used as reference values in the preliminary prediction.

(2) GRNN has relatively better predicting ability than BPNN.

This study only explores the application of ML for predicting $VL_{Z,0}$. As the number and quality of test samples used for training determine the accuracy of prediction results, more test work is suggested to be carried out in future to enrich training samples.

Data Availability

The data used to support the findings of this study are available from the corresponding author upon request.

Conflicts of Interest

The authors declare that they have no conflicts of interest.

Acknowledgments

The study was supported by National Engineering Laboratory for Digital Construction and Evaluation Technology of Urban Rail Transit with the open project fund (No. 2021JZ03) and the Scientific and Technology Research and Development Program of China State Railway Group Co., Ltd. (No. L2021G010).

References

[1] J. J. Yang, S. Y. Zhu, W. M. Zhai et al., "Prediction and mitigation of train-induced vibrations of large-scale building constructed on subway tunnel," *Science of the Total Environment*, vol. 668, pp. 485–499, 2019.

[2] T. Xin, S. Wang, L. Gao et al., "Field measurement of rail corrugation influence on environmental noise and vibration: a case study in China," *Measurement*, vol. 164, Article ID 108084, 2020.

[3] C. He, S. Zhou, and P. Guo, "An efficient three-dimensional method for the prediction of building vibrations from underground railway networks," *Soil Dynamics and Earthquake Engineering*, vol. 139, Article ID 106269, 2020.

[4] L. H. Xu, M. Ma, R. N. Cao, X. Y. Tan, and R. H. Liang, "Effect of longitudinally varying characteristics of soil on metro train-induced ground vibrations based on wave propagation analysis," *Soil Dynamics and Earthquake Engineering*, vol. 152, Article ID 107020, 2022.

[5] ISO Standard, "Mechanical vibration – ground-borne noise and vibration arising from rail system—part 1: general guidance," ISO Standard, Geneva, Switzerland, ISO 14837-1, 2005.

[6] M. Ma, W. N. Liu, and W. F. Liu, "Research progresses of prediction method and uncertainty of train-induced environmental vibration," *Journal of Traffic and Transportation Engineering*, vol. 20, pp. 1–17, 2020.

[7] C. With, M. Bahrekazemi, and A. Bodare, "Validation of an empirical model for prediction of train-induced ground vibrations," *Soil Dynamics and Earthquake Engineering*, vol. 26, no. 11, pp. 983–990, 2006.

[8] C. Madshus, B. Bessason, and L. Hårvik, "Prediction model for low frequency vibration from high speed railways on soft ground," *Journal of Sound and Vibration*, vol. 193, no. 1, pp. 195–203, 1996.

[9] M. Bahrekazemi, *Train-induced Ground Vibration and its Prediction*, Royal institute of technology, Stockholm, Sweden, 2004.

[10] G. Paneiro, F. O. Durão, M. Costa e Silva, P. Falcão Neves, and P. Neves, "Prediction of ground vibration amplitudes due to urban railway traffic using quantitative and qualitative field data," *Transportation Research Part D: Transport and Environment*, vol. 40, pp. 1–13, 2015.

[11] D. P. Connolly, G. Kouroussis, A. Giannopoulos, O. Verlinden, P. K. Woodward, and M. C. Forde, "Assessment of railway vibrations using an efficient scoping model," *Soil Dynamics and Earthquake Engineering*, vol. 58, pp. 37–47, 2014.

[12] D. P. Connolly, G. Kouroussis, O. Verlinden, A. Giannopoulos, P. K. Woodward, and M. C. Forde, "Scoping prediction of re-radiated ground-borne noise and vibration near high speed rail lines with variable soils," *Soil Dynamics and Earthquake Engineering*, vol. 66, pp. 78–88, 2014.

[13] Y. J. Chen, C. J. Chen, and Y. J. Shen, "Development of automatic prediction model for ground vibration using support vector machine," *Journal of Vibroengineering*, vol. 17, no. 5, pp. 2535–2546, 2015.

[14] J. B. Yao, H. Xia, N. Zhang, and B. Yu, "Prediction on building vibration induced by moving train based on support vector machine and wavelet analysis," *Journal of Mechanical Science and Technology*, vol. 28, no. 6, pp. 2065–2074, 2014.

[15] G. Paneiro, F. O. Durão, M. Costa e Silva, and P. Falcão Neves, "Artificial neural network model for ground vibration amplitudes prediction due to light railway traffic in urban areas," *Neural Computing & Applications*, vol. 29, no. 11, pp. 1045–1057, 2018.

[16] L. Fang, J. B. Yao, and H. Xia, "Prediction on soil-ground vibration induced by high-speed moving train based on artificial neural network model," *Advances in Mechanical Engineering*, vol. 11, no. 5, Article ID 168781401984729, 2019.

[17] R. H. Liang, W. F. Liu, M. Ma, and W. N. Liu, "An Efficient model for predicting the train-induced ground-borne vibration and uncertainty quantification based on Bayesian neural network," *Journal of Sound and Vibration*, vol. 495, Article ID 115908, 2021.

[18] P. Amado-Mendes, P. Alves Costa, L. M. C. Godinho, and P. Lopes, "2.5D MFS-FEM model for the prediction of vibrations due to underground railway traffic," *Engineering Structures*, vol. 104, no. 1, pp. 141–154, 2015.

[19] M. Ma, W. N. Liu, C. Y. Qian, G. H. Deng, and Y. Li, "Study of the train-induced vibration impact on a historic Bell Tower above two spatially overlapping metro lines," *Soil Dynamics and Earthquake Engineering*, vol. 81, pp. 58–74, 2016.

[20] Q. Jin, D. J. Thompson, D. E. Lurcock, M. G. R. Toward, and E. Ntotsios, "A 2.5D finite element and boundary element model for the ground vibration from trains in tunnels and validation using measurement data," *Journal of Sound and Vibration*, vol. 422, pp. 373–389, 2018.

[21] C. He, S. H. Zhou, P. J. Guo, H. G. Di, and X. H. Zhang, "Modelling of ground vibration from tunnels in a poroelastic half-space using a 2.5-D FE-BE formulation," *Tunnelling and Underground Space Technology*, vol. 82, pp. 211–221, 2018.

[22] M. Ma, L. H. Xu, L. L. Du, Z. Z. Wu, and X. Y. Tan, "Prediction of building vibration induced by metro trains running in a curved tunnel," *Journal of Vibration and Control*, vol. 27, no. 5-6, pp. 515–528, 2021.

[23] S. H. Zhou, X. H. Zhang, H. G. Di, and C. He, "Metro train-track-tunnel-soil vertical dynamic interactions - semi-analytical approach," *Vehicle System Dynamics*, vol. 56, no. 12, pp. 1945–1968, 2018.

[24] Z. Yuan, Z. Cao, A. Boström, and Y. Q. Cai, "The influence of pore-fluid in the soil on ground vibrations from a tunnel embedded in a layered half-space," *Journal of Sound and Vibration*, vol. 419, pp. 227–248, 2018.

[25] Z. Yuan, A. Boström, Y. Q. Cai, X. D. Pan, Z. G. Cao, and L. Shi, "The wave function method for calculation of vibrations from a twin tunnel in a multi-layered half-space," *Soil Dynamics and Earthquake Engineering*, vol. 125, Article ID 105716, 2019.

[26] L. H. Xu and M. Ma, "Dynamic response of the multilayered half-space medium due to the spatially periodic harmonic moving load," *Soil Dynamics and Earthquake Engineering*, vol. 157, Article ID 107246, 2022.

[27] N. Zhang, H. Xia, W. G. Yang, and S. Y. Zhao, "Prediction and control of building vibration under metro excitations," in *Proceedings of the 8th International Conference on Structural Dynamics*, pp. 705–711, Leuven, Belgium, July 2011.

[28] T. Jaquet and V. Salcedo, "Ensuring acceptable vibration levels in listed buildings by means of precise vibration measurements and highly-efficient floating slab track," in *Proceedings of the AREMA. 2012 Annual Conference and Exposition*, pp. 1–11, Atlanta, GA, USA, June 2012.

[29] W. F. Liu, Z. Z. Wu, C. Y. Li, and L. H. Xu, "Prediction of ground-borne vibration induced by a moving underground train based on excitation experiments," *Journal of Sound and Vibration*, vol. 523, Article ID 116728, 2022.

[30] H. Verbraken, G. Lombaert, and G. Degrande, "Verification of an empirical prediction method for railway induced vibrations by means of numerical simulations," *Journal of Sound and Vibration*, vol. 330, no. 8, pp. 1692–1703, 2011.

[31] H. Verbraken, *Prediction of Railway Induced Vibration by Means of Numerical, Empirical, and Hybrid Methods*, University of Southampton, Southampton, UK, 2013.

[32] K. A. Kuo, H. Verbraken, G. Degrande, and G. Lombaert, "Hybrid predictions of railway induced ground vibration using a combination of experimental measurements and numerical modelling," *Journal of Sound and Vibration*, vol. 373, pp. 263–284, 2016.

[33] K. A. Kuo, G. D. Lombaert, and G. Degrande, "Quantifying dynamic soil-structure interaction for railway induced vibrations," *Procedia Engineering*, vol. 199, pp. 2372–2377, 2017.

[34] G. Kouroussis, K. E. Vogiatzis, and D. P. Connolly, "Assessment of railway ground vibration in urban area using in-situ transfer mobilities and simulated vehicle-track interaction," *International Journal of Reality Therapy*, vol. 6, no. 2, pp. 113–130, 2018.

[35] L. G. Kurzweil, "Ground-borne noise and vibration from underground rail systems," *Journal of Sound and Vibration*, vol. 66, no. 3, pp. 363–370, 1979.

[36] J. Melke, "Noise and vibration from underground railway lines: proposals for a prediction procedure," *Journal of Sound and Vibration*, vol. 120, no. 2, pp. 391–406, 1988.

[37] A. Koopman, S. Lentzen, R. Steenbergen R, A. V. Metrikine, J. S. Hoving, and Srm-T, "The Dutch standardized prediction model for railway vibration and induced noise," in *Proceedings of the 4th International Symposium on Environmental Vibration (ISEV2009)*, vol. 86, Beijing, China, December 2009.

[38] Chinese code of Ecology & Environment, "Technical guidelines for environmental impact assessment – urban rail transit," Chinese code of Ecology & Environment, Beijing, China, Hj 453-2018(in Chinese), 2018.

[39] Chinese Industry Standard, "Code for application technique of metro noise and vibration control," Chinese Industry Standard, Beijing, China, DB11/T 838-2019(in Chinese), 2019.

[40] M. Ma, M. H. Li, X. Y. Qu, and H. G. Zhang, "Effect of passing metro trains on uncertainty of vibration source intensity: monitoring tests," *Measurement*, vol. 193, Article ID 110992, 2022.

[41] D. Wei, M. L. Zhang, Z. J. Jiang, and M. Sun, "Neural network non-linear modelling based on Bayesian methods," *Computer Engineering and Applications*, vol. 11, pp. 5–8, 2005.

[42] D. H. Qi and J. C. Kang, "Design of back propagation neural network," *Computer Engineering and Design*, vol. 2, pp. 47–49, 1998.

[43] J. Yang and Z. G. Yang, "Non-intrusive load monitoring method aircraft electrical equipment based on GRNN algorithm," *Acta Aeronautica et Astronautica Sinica*, vol. 42, no. 3, pp. 403–413, 2020.

Hindawi
Advances in Civil Engineering
Volume 2022, Article ID 3173567, 10 pages
https://doi.org/10.1155/2022/3173567

Research Article

A Case Study on Annoyance Noise Caused by Metro Railway at a TOD Developed Depot

Qiang Liu, Zhongxu Kang, Hougui Zhang, Ruixiang Song, and Ge Li

Institute of Urban Safety and Environment Science, Beijing Academy of Science and Technology, Beijing 100054, China

Correspondence should be addressed to Hougui Zhang; zhanghougui@bmilp.com

Received 14 February 2022; Accepted 16 March 2022; Published 25 April 2022

Academic Editor: Chao Zou

As an importance strategy to finance the transport infrastructure investment, transit-oriented development (TOD) for railway depot is rapidly growing in China. However, railway-induced noise emerged as the leading environmental nuisance triggering one of the most common public complaints. In order to discuss the influence of railway-induced noise on the neighbourhood residents in a TOD developed depot, a special case study is provided in this study. Measurement campaigns were conducted for responding to the complaints, and noise map was calculated for finding out a noise control solution. Based on the recommendation awakening threshold value of 42 dB (A) summarized from the Night Noise Guidelines for Europe (WHO, 2009), the measurement results confirmed that the neighbourhood residents were indeed suffering from the instantaneous railway noise, and the sleep disturbance correlated indicator L_{Amax} was more than 56 dB (A) at outside of buildings. Furthermore, calculation results indicated that the lower office buildings became mirrors which reflected the noise across over the cover structure to the higher stories of residents' buildings. At the ends, a kind of dissipative splitter muffler was proposed as a potential solution, and its performance was also simulated.

1. Introduction

A metro depot is a facility where trains are regularly parked for maintenance, testing, and storage. Traditional metro depots always require massive land; thus, they were commonly located far always from city center. But with the cities expanded rapidly in last decades in China, the areas of metro depots were developed as part of central urban [1–4]. The boundary of depot became barriers to isolate the land from not only the city but also the increasing value of housing. Transit-oriented development (TOD) is therefore recognized as a sustainable mode of development for depots which were located in highly dense megacities. Under the guiding principles of TOD, the basic ideas are to design an urban form in a relatively high density, compact, and mixed form and to provide high quality, efficient mass transportation services, together with a pedestrian friendly environment [5]. More important, the TOD mode improves the accessibility of housing to be developed and hence increases the land value, which helps finance the transport infrastructure investment [6–8].

However, the most serious impediment for TOD strategy conducted on metro depot is the environment issue. The main negative consequence of railway traffic is that the vibrations and noise induced by the train passage are easily transmitted to nearby buildings [9, 10], which results in disturbance of inhabitants, with consequences on living quality and health. Although such vibration usually do not imply damage on buildings, it manifests itself in two ways: low frequency vibration in the range 1–80 Hz is perceived by line side residents as whole-body feel able vibration, whereas higher frequency vibration in the range 16–250 Hz is radiated as sound inside buildings and is known as structure-borne noise [11–13]. Besides structure-borne noise, various sources contribute to the airborne noise, including rolling noise, engines and gear noise, and so on, which transmit directly through the air [14, 15]. In last decades, many solutions for railway noise have been suggested [16–19], partly based on common sense but sometimes also based on a deep

understanding of the physical phenomena involved. By common consents, the railway noise reduction should be best started at the source or isolated by barriers installed at the propagation path or even relocated the residents to a greater distance from the railway lines. Traditionally, according to the Chinese environment law, the residential district must be keep at least 30 m off the railway line. To solve the conflicts between the noise problem and the TOD strategy, it requires considering control measures during all the steps of TOD development, including prediction, design, construction, and routine maintenance.

In this study, a special case study was provided to discuss the influence of railway-induced noise on the neighbourhood building in a TOD metro depot section. The research was carried out for responding to complaints from neighbourhood residents about railway noise; even the depot section almost totally covered under a hanging garden structure, which was considered as the barriers to isolate the direct propagation of noise. Measurement was therefore conducted for obtaining noise data at the positions of source, out-room, and in-room during the rush hours. After that, the software CadnaA was adopted to simulate the influence area of railway noise. Finally, the potential solution for noise reductions was suggested.

2. Project Background

The presented residential building is located in a TOD metro depot and close to the entrance/exist area. In this area, the train speed was limited under 25 km/h. However, in practice, the speed would be a little higher than 25 km/h when trains go out of the depot, while the speed would be lower than 25 km/h when trains go back. As in this area, there were quite a lot turnouts and rail joints which would result in high level of impact force related to low frequency vibration, and under ballast mat was therefore used to reduce the railway-induced vibration.

Furthermore, in this area, trains are always in the condition of speeding up or breaking down, causing higher annoy roll noise and breaking noise. As the result, although the railways are all ground lines, they were covered by a hanging garden structure for connecting the north and south land of the depot in one hand and reducing the noise impact for the other hand. The north side of cover structure was closed for noise isolation, while the south side was open for fire safety consideration.

The minimum distance between the foundation of building and the nearest track center is 31 m, while the distance between the building and the outward side of the cover structure is more than 60 m. Besides that, there are two office buildings located at the south side of the cover structure. The detailed location and real photos are shown in Figures 1 and 2.

However, although the result of the investigation indicated that it had already adopted many types of measures to attempt controlling the railway-induced vibration and noise, it seems to be failed because complaints come from neighbourhood residents once when the depot is under operation. In order to provide the solution, research studies were carried out as the responding to the complaints.

3. Measurement

3.1. Measurement Setup. Measurement campaign was conducted in the apartment of a cooperative complainant, which located on 15th floor. One sound meter was installed at the open balcony out of the bedroom (marked as MR1), while another was installed inside of the bedroom with windows totally closed (marked as MR2), as shown in Figure 3.

More than that, sound meters were located at outside of the depot cover structure to record the noise sourced from railway, as shown in Figures 4 and 5. It should be figured out that because the trains were not passing through the same track, it was not easy to collect the noise data according to ISO3095 [20], in which the noise source measurement points need to be installed at 7.5 m from track center. Thus, the edge of the cover structure was redefined as the noise source in this project.

The sound level measurement device adopted in this project was sound level meter B&K2270 (Brüel and Kjær, Denmark). The B&K2270 sound level meter is a flexible hand-held analyser with large frequency range, spanning from 20 Hz to 20 kHz. It is capable of measuring both the railway-induced airborne noise and structure-borne noise.

3.2. Noise Indicator Choose. To choose a reasonable noise indicator, need to consider both the equivalent sound pressure level and the number of sound events. Traditionally, many previous research studies indicated that the railway-induced noise was obviously characterized by high levels per event and low numbers. They even raised a conclusion that railway traffic noise causes less annoying other than road and air traffic noises due to the lower numbers because the A-weighted long-term average sound level was quite lower during a continuous period of time. But for the presented case in this study, the TOD development made residents suffering much high-frequency events during the rush hours in middle night and early in the morning. From a practical point of view, the sound level for each pass-by event is better useful to explain the instantaneous effects such as sleep disturbance to public, so that they can understand intuitively other than the yearly average of noise level.

According to the recommendation of the Night Noise Guidelines for Europe published by the WHO in 2009 [21], sleep disturbance correlates best with short-term effects that are mainly related to maximum levels per event $L_{Amax,inside}$. Table 1 provides the summary of effects and threshold levels for effects where sufficient evidence was available for the $L_{Amax,inside}$.

Therefore, considering the reality purpose of the case presented in this study is to provide responses to complaint from residents for waking up in the night and/or too early in the morning; the indicator $L_{Amax,inside}$ was selected, and the value should be not limited at 42 dB (A). Moreover, considering the desire of a large part of the population to sleep with windows (slightly) open, in this study, the noise level

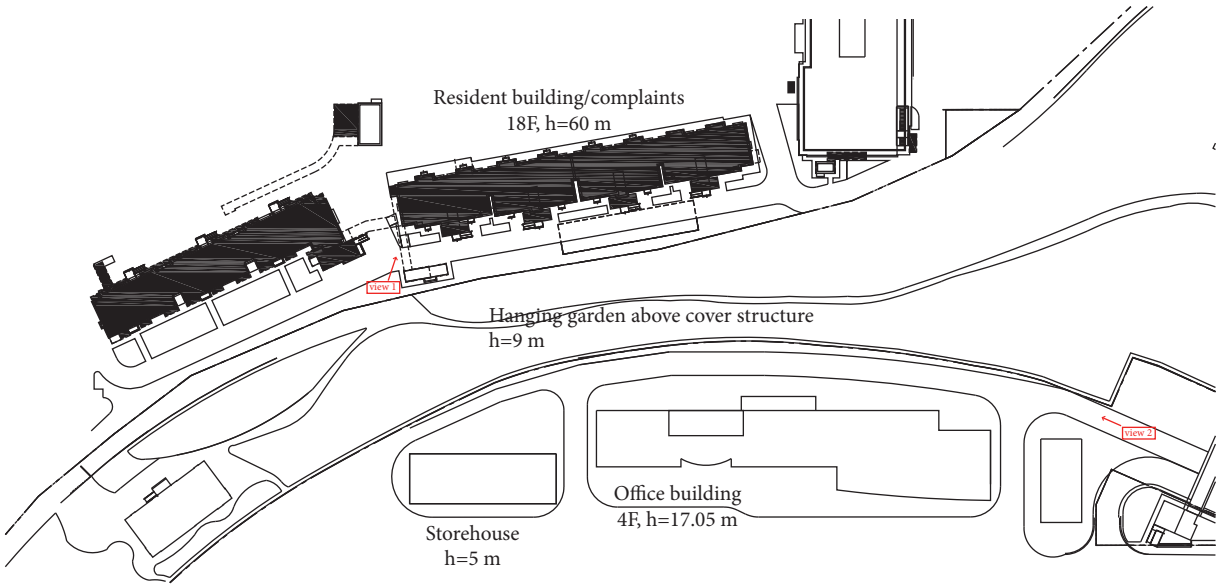

Figure 1: The plan view of presented TOD project.

(a) (b)

Figure 2: The real photos for (a) view 1: looking down angle at 15th floor and (b) view 2: looking up angle at east side.

outside $L_{\text{Amax,outside}}$ was adopted as the prediction indicator and the limited value should be less than 42 dB (A).

3.3. Measurement Results

3.3.1. Time History Record. Measurements were conducted during the rush hours. Especially, during 16 : 30 to 17 : 30, measurement was carried out for the noise that trains left out of the depot and passed though the measurement position in acceleration condition, while during 19 : 30 to 20 : 30, trains come back to the depot and passed through the measurement position in deceleration condition.

A-weighted sound pressure level (LA) during the measurement time history was recorded. An example of time history taken from the source measurement at position MS3 is shown in Figure 6. The reference time interval is 1 second.

3.3.2. Pass-By LA for Single Train. In order to identify the contribution of the train caused noise from other source, the detailed time history of pass-by LA for each single train was also selected, respectively. An example for trains left out of the depot is shown in Figure 7 and the condition when trains came back to depot is shown in Figure 8.

According to Table 2, the measurement data showed the excellent repeatability at all measurement positions for at least 16 pass-by trains selected simply according to the time order. It indicted that at bedroom when windows were fully closed, the short-term noise level per each pass-by event was less than 42 dB (A), but considering people have good reasons to sleep with their windows open, the outside noise level exceeded 12.6 dB (A) to 17.7 dB (A) than the sleep disturbance threshold value according to the recommendation of the Night Noise Guidelines for Europe published by the WHO in 2009.

3.3.3. 1/3 Octave Frequency Spectrum. In order to find out what was the typical spectrum than railway noise transit via such a long distance to the building, 1/3 octave frequency spectrum for all the measurement points was provided in this section and shown in Figures 9–13.

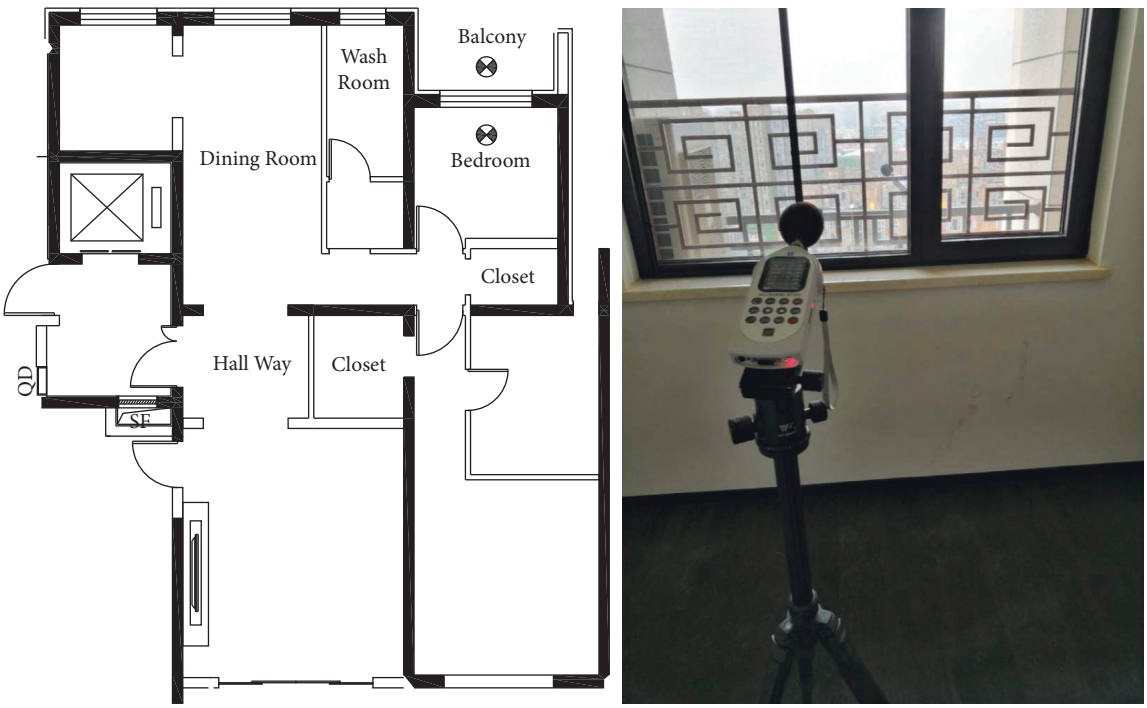

Figure 3: The location and view of measurement points for MR1 and MR2.

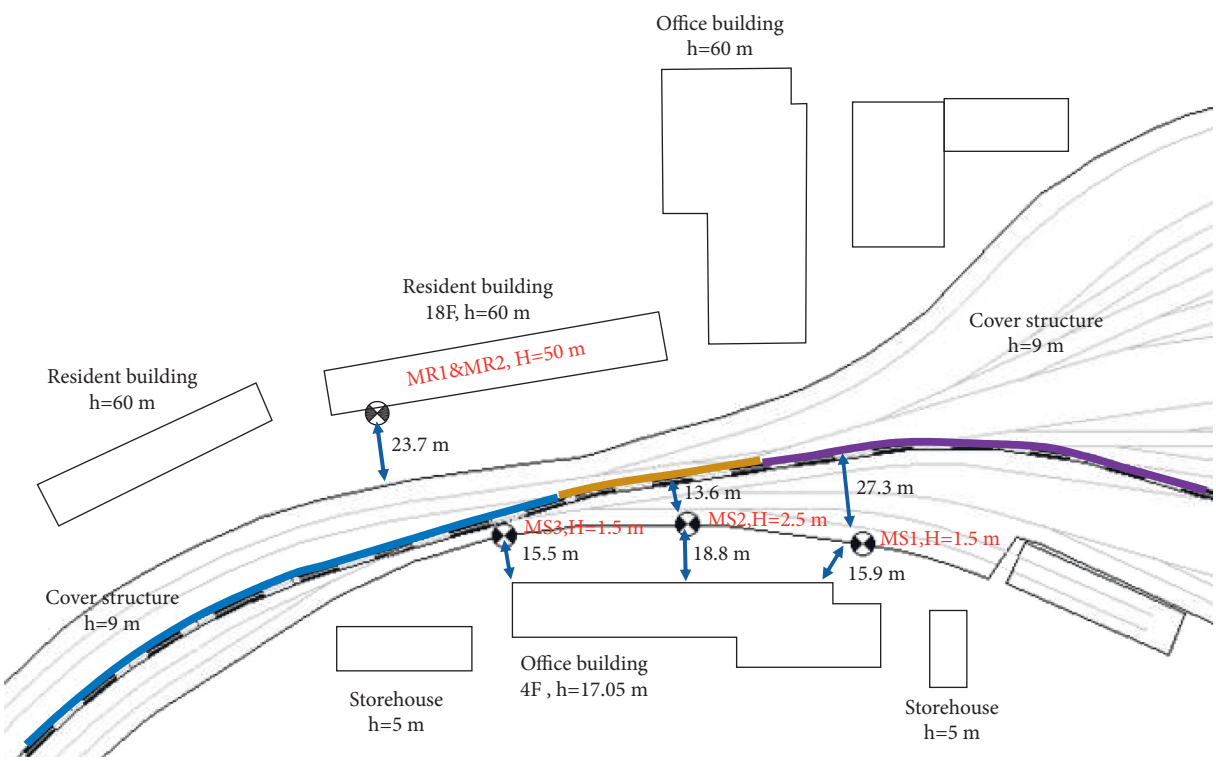

Figure 4: The detailed location of measurement points.

At the measurement point MS1, the sound meter was located at outside of the cover structure with the distance of 27.3 m from the track center of busy main line and 1.5 m in height. From Figure 9, it is clear that the sound pressure level remarkably raised from the background curve when metro trains passed by. Moreover, the typical frequency band occurred at the band of 40 Hz. It should notice that in this area, the trains were passing through turnout zone and the speed started increasing approximately from 5 km/h to 20 km/h when trains left out of depots.

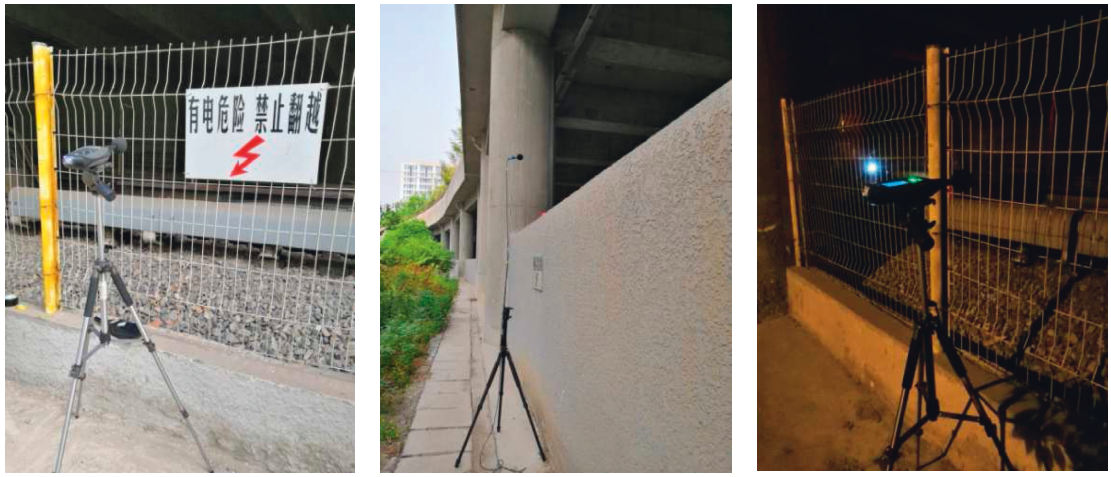

(a) (b) (c)

Figure 5: The real photo of sound meters installation at the source. (a) MS1. (b) MS2. (c) MS3.

Table 1: The summary of effects and threshold levels on healthy for $L_{Amax,inside}$.

Effect	Detailed effects	Threshold, dB (A)
Biological effects	EEG awakening	35
	Motility, onset of motility	32
	Changes in duration of various stages of sleep, in sleep structure and fragmentation of sleep	35
Sleep quality	Waking up in the night and/or too early in the morning	42

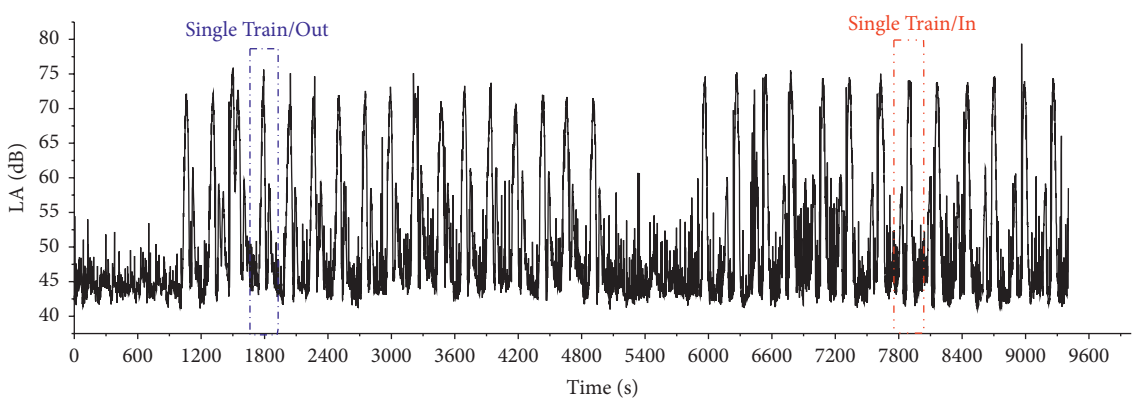

Figure 6: Example of time history for the whole measurement in rush hours (MS3).

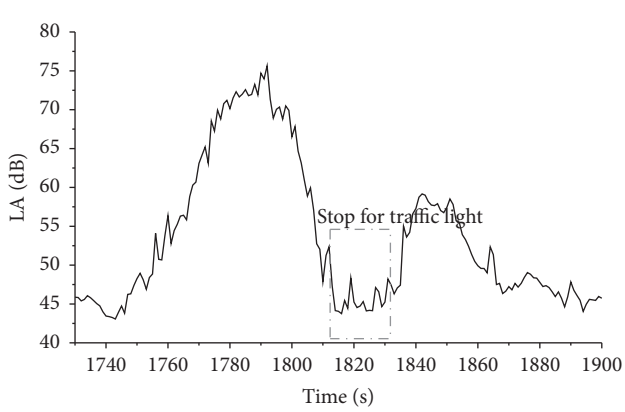

Figure 7: Example of selection of measuring time interval for a whole train passage (leaving out).

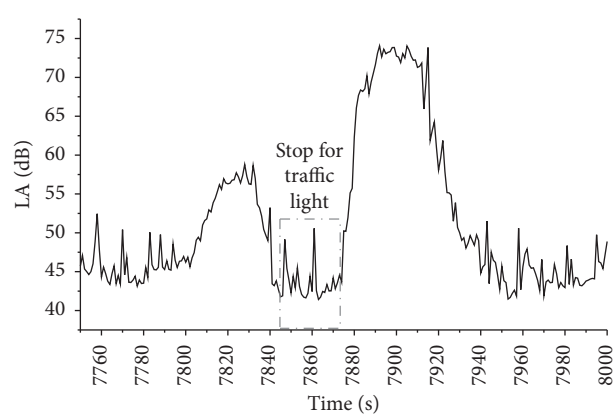

Figure 8: Example of selection of measuring time interval for a whole train passage (coming back).

Table 2: The maximum A-weighted sound pressure level per each pass-by.

No.	Time	Maximum A-weighted sound pressure level/dB (A)				
		MS1	MS2	MS3	MR1	MR2
1	Left out	72.7	81.2	74.5	56.6	33.1
2		71.5	84.5	73.3	58.3	32.7
3		77.0	84.1	74.6	59.7	33.9
4		71.6	78.9	76.8	56.1	32.4
5		71.8	77.5	73.7	57.3	32.1
6		76.0	80.4	74.0	57.3	33.1
7		77.9	85.0	73.5	56.9	33.2
8		77.5	85.2	73.7	56.7	32.7
1	Came back	75.2	86.9	76.5	57.4	34.2
2		77.1	87.1	76.1	57.1	33.8
3		68.2	80.8	78.7	55.9	32.9
4		76.5	78.5	75.7	56.1	33.1
5		69.0	79.8	76.1	58.8	32.6
6		74.7	80.8	77.5	55.6	32.4
7		66.4	78.9	76.0	56.0	33.1
8		67.6	79.6	76.7	56.1	33.2

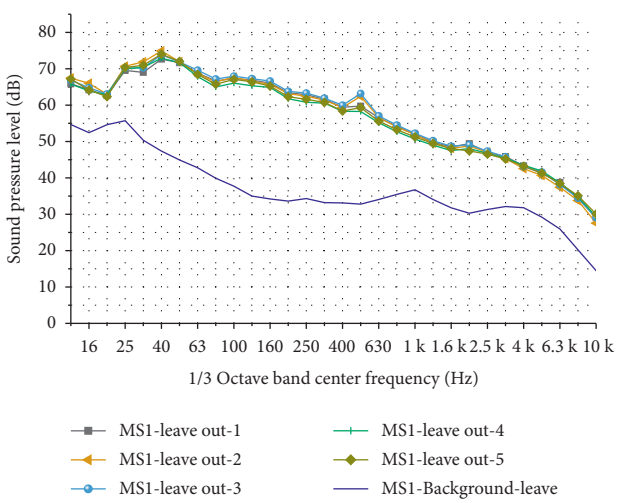

Figure 9: 1/3 octave frequency spectrum for measurement points MS1.

At the measurement point MS2, as the cover structure was half closed (Figure 5), the sound meter was located at outside of the cover structure with the distance of 13.6 m from the track center and 2.5 m in height. From Figure 10, it clear that the sound pressure level remarkably raised from the background curve when metro trains passed by. It may because that in this area, the trains were running at a higher speed than MS1 around 25 km/h, and the measurement position was in a shorter distance from the track center, the value of sound pressure level was larger than MS1, and the typical frequency band occurred at the band of 125 Hz.

At the measurement point MS3, the sound meter was located at outside of the cover structure and close to the track center of busy main line with 1.5 m in height. In this area, the trains decelerated from 25 km/h to 0 km/h for traffic light

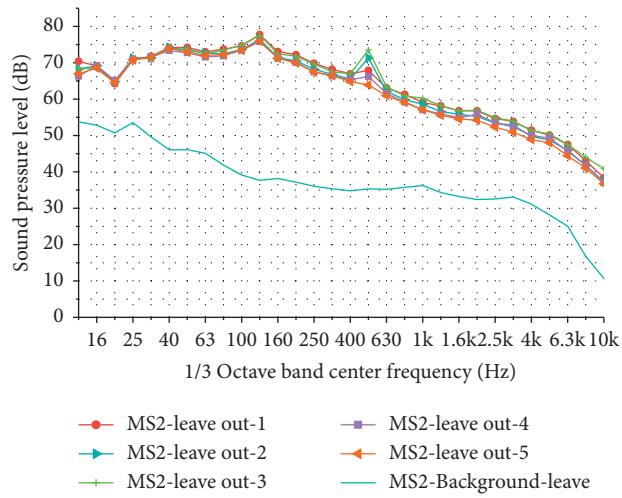

Figure 10: 1/3 octave frequency spectrum for measurement points MS2.

sign. From Figure 11, it clear that the sound pressure level remarkably raised when trains passed by. A remarkable peak appeared at 63 Hz, which was traditionally considered as one typical frequency of railway-induced rolling noise.

At the measurement point MR1, the sound meter was located at the outside balcony of 15th floor with about 50 m height from the ground. From Figure 12, it clear that the value slightly raised along all of the frequency bands, although the tendency of the pass-by curve remained almost the same with the background in the range of 20–100 Hz and 200–2000 Hz. It was able to identify the influence of railway at the bands of 40 Hz and 125 Hz, which, respectively, related to the typical frequency captured from MS1 and MS2.

Moreover, in the range of 2000 Hz–10 kHz, even though it not appeared as good reproducibility as in the range below 2000 Hz for all the pass-by train, the value dramatically increased against the background curve. It indicated that railway-induced noise provided significant contribution in the range of 2k–10 kHz at the position of MR1.

At the measurement position of MR2, the sound meter was installed in the bedroom with windows fully closed. From Figure 13, it clear that the pass-by sound pressure level curves tend to get close to the background curve. Especially, in the range of more than 800 Hz, there was no obvious difference between the background and pass-by curve. But in the range of 50–800 Hz, typical railway-related frequency bands were still able to be identified at 63 Hz and 125 Hz. Considering there were typical peaks on the background curve at 20 Hz, 31.5 Hz, 63 Hz, 125 Hz, and 200 Hz bands, which were normally related to the railway-induced vibration, it indicated a conclusion that the noise at 63 Hz and 125 Hz would be more likely as structure-borne noise other than airborne noise that came from outside via the direct path.

3.3.4. Findings. Based on the measurement results, it was clear that the neighbourhood residents were indeed suffering from the railway-induced noise. Considering people have

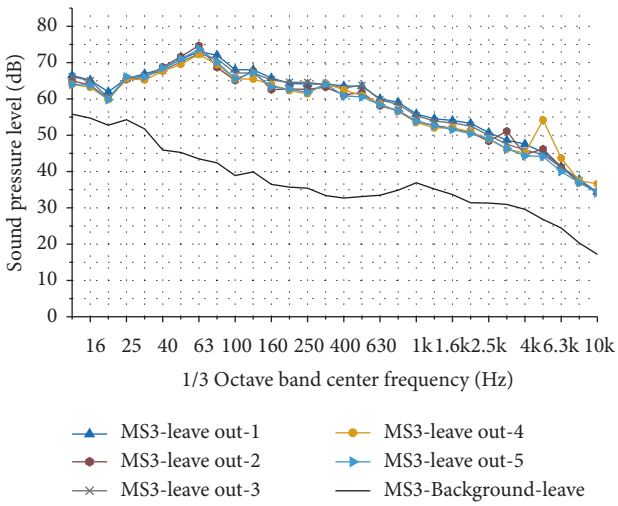

Figure 11: 1/3 octave frequency spectrum for measurement points MS3.

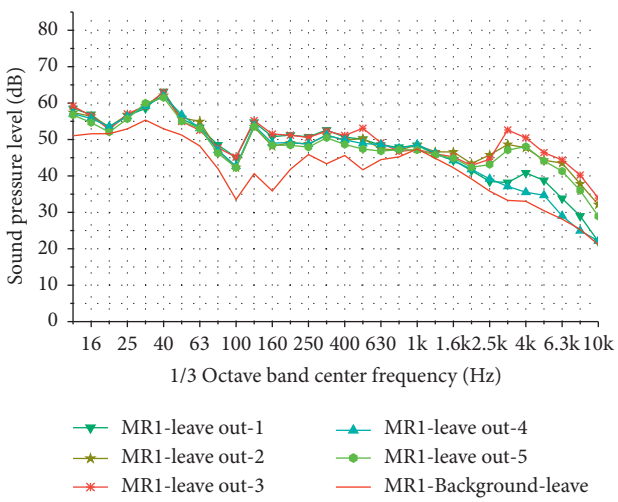

Figure 12: 1/3 octave frequency spectrum for measurement points MR1.

good reasons to sleep with their windows open, the outside noise level exceeded 12.6 dB (A) to 17.7 dB (A) than the sleep disturbance threshold value of 42 dB (A) according to the recommendation of the Night Noise Guidelines for Europe published by the WHO in 2009.

Although it was certain that the annoying noise was the consequence of railway system, the transit path for outside noise was still unclear. The noise in bedroom was more likely as structure-borne noise other than airborne noise that came from outside.

4. Noise Map Simulation

In order to find out the noise propagation path and make a noise control proposal, the noise map was simulated in this study. The software CadnaA was used to build the 3D model of the considered area with all structures and neighbourhood buildings in full scale, as shown in Figure 14. The default

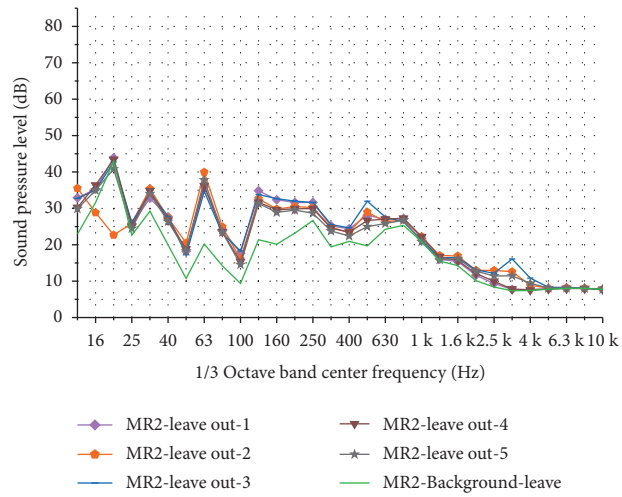

Figure 13: 1/3 octave frequency spectrum for measurement points MR2.

railroad module in software was used to simulate the noise generated by the metro trains.

In this simulation, the Schall03 (2014) prediction method was used, considering the order of reflection was 2 and the default ground absorption factor was 0.8.

Furthermore, selected one single train in random and reprocessed the source measurement data in the form of one octave frequency spectrum. The input data given in Table 3 were adapted as the railway noise emission for calculation.

The simulation model verification in the form of spectrum is shown in Figure 15. It is clearly indicated the simulation result agreed with the measurement data acquainted from the near field in MS1 ($L = 27.3$ m, $H = 1.5$ m). Even in the far field, the sound transits would be affected by some uncertain issues, such as temperature and winds speed. At the check point MR1 ($L > 50$ m, $H > 50$ m), the sound pressure spectrum remained in the highly accordant tendency.

Then, the simulation results were verified by the measurement data in the form of A-weighted sound pressure level, as given in Table 4. The maximal tolerances for calculation results were less than 0.5 dB (A), which indicated that the calculation was efficient for describing the noise influence scale. Therefore, the calculated noise map was provided as shown in Figure 15.

From Figure 16, the noise map indicated that the railway-induced noise resulted in obvious influence on the residents building at this TOD-developed depot. More than 90% area at the facade of neighbourhood residents' buildings that faced to the depot side were under the exposure of more than 45 dB (A) noise condition when metro trains passed by.

It was also clear that the partial closed side of cover structure became a new noise source. The shapes, locations, and adjacent relations of buildings played an important role on the acoustic field in this area. The comprehensive factors made the lower office buildings become mirrors which reflected the railway-induced noise across over the cover structure to the higher stories of residents building.

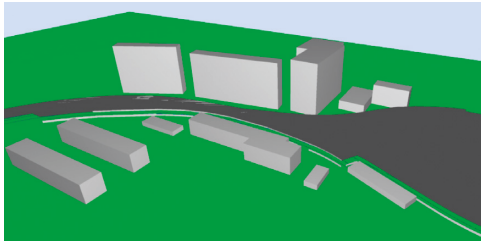

Figure 14: The 3D model of considered area established by CadnaA.

Table 3: The maximum A-weighted sound pressure level per each pass-by.

Frequency (Hz)	Value (dB)		
	MS1	MS2	MS3
63	93.7	94.9	87.6
125	91.1	94.6	80.1
250	87.0	88.4	79.3
500	83.8	88.9	76.2
1000	76.3	78.7	71.1
2000	72.5	75.4	67.3
4000	69.0	71.8	61.4
8000	64.4	66.8	55.0

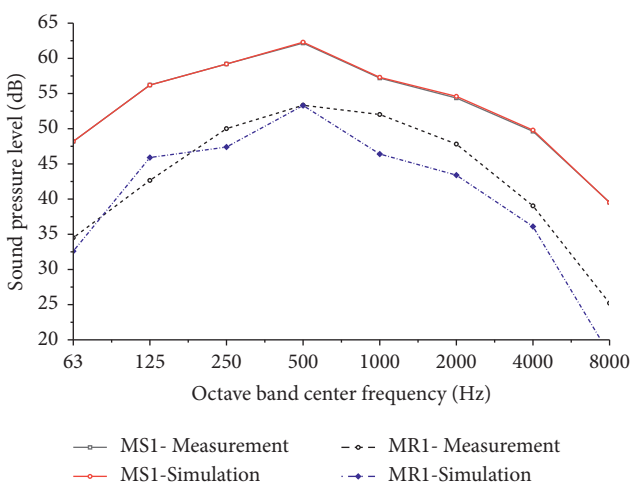

Figure 15: Simulation results verification.

Table 4: Simulation results verification.

	A-weighted sound pressure level/dB (A)			
	MS1	MS2	MS3	MR1
Measurement	72.7	81.2	74.5	56.6
Calculation	72.9	81.5	74.7	57.1
Tolerances	+0.2	+0.3	+0.2	+0.5

5. Proposal for Noise Control

For this existed project, it was too late to rearrange the locations of buildings or optimize the railway system; the noise control proposal would only be focused on setting

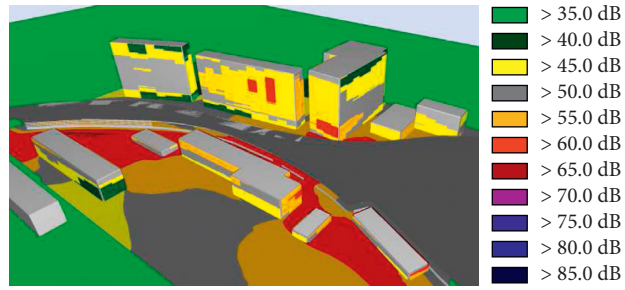

Figure 16: The map of calculated railway-induced noise.

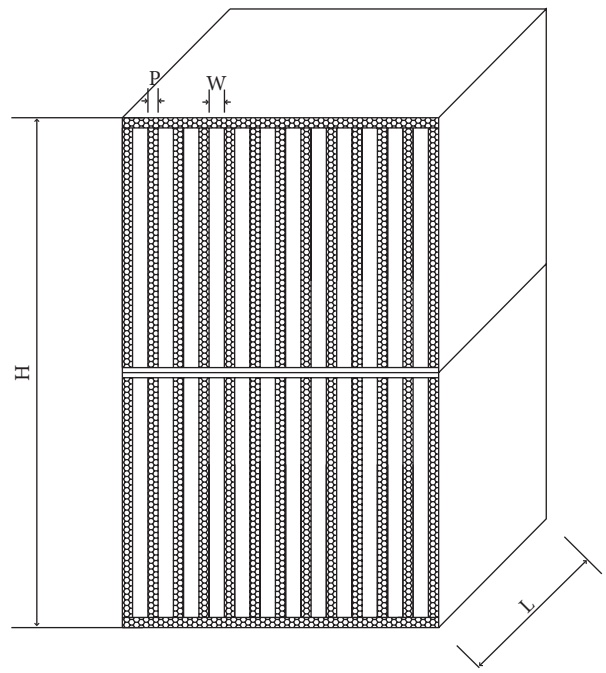

- *The height H=5 m*
- *The thickness of each muffler sheet P=0.1 m*
- *The depth of each muffler sheet L=1.5 m*
- *The interval between two muffler sheet W=0.15 m*
- *The ventilation Rate ref. without mufflers*: 60%
- *Filling material : Sound absorbing glass wool*

Figure 17: Detailed parameter for splitter mufflers.

Figure 18: Noise map calculated with mufflers.

noise isolation barriers at the transit path. Therefore, the dissipative splitter muffler was proposed as a potential solution in this project. The sound transit gaps under the cover structure were full filled by splitter muffler which was considering the effective working frequency range and remaining at least 60% ventilation for the fire safety. The detailed parameter for one cell of the splitter muffler is shown in Figure 17.

The performance of proposed mufflers was calculated using the same simulation model of CadnaA. The results showed the A-weighted sound pressure level was obviously reduced to the value under 42 dB (A) (Figure 18).

6. Conclusions

Based on the presented case study in this study, findings could be summarized as follows:

(1) Railway-induced noise emerged as the leading environmental nuisance triggering one of the most common public complaints in the TOD development

(2) The measurement results indicated that the inside short-term noise level per pass-by event was less than 35 dB (A) when windows were fully closed, while the indicator L_{Amax} was more than 56 dB (A) at outside of buildings. Considering people have good reasons to sleep with their windows open, the outside the noise level exceeded 12.6 dB (A) to 17.7 dB (A) than the sleep disturbance threshold value according to the recommendation of the Night Noise Guidelines for Europe published by the WHO in 2009.

(3) The calculation results indicated that even though the direct transit path was cut down, the reflection and diffraction would play a nonnegligible role on the noise influence. Therefore, the noise map evaluation should be necessary taken into consideration in new construct project.

(4) The way to install mufflers would be effective for noise reduction for this project

Data Availability

The data used to support the findings of this study are available from the corresponding author upon request.

Disclosure

The funders had no role in the design of the study, in the collection, analyses, or interpretation of data, in the writing of the manuscript, or in the decision to publish the results.

Conflicts of Interest

The authors declare that they have no conflicts of interest.

Authors' Contributions

H. G. Zhang and Q. Liu conceptualized the study. Z. X. Kang developed methodology, collected resources, and investigated and supervised the study. G. Li. developed software. Q. Liu, Z. X. Kang, and G. Li. validated the study. Q. Liu performed formal analysis and visualized the study. H. G. Zhang wrote, reviewed, and edited the article and acquired fund. R. X. Song administered project.

Acknowledgments

This research was funded by the Beijing Natural Science Foundation (8202040) and Beijing Academy of Science and Technology Funds (BJAST-RD-BMILP202102).

References

[1] C. Zou, Y. Wang, X. Zhang, and Z. Tao, "Vibration isolation of over-track buildings in a metro depot by using trackside wave barriers," *Journal of Building Engineering*, vol. 30, Article ID 101270, 2020.

[2] Z. Tao, Y. Wang, M. Sanayei, J. A. Moore, and C. Zou, "Experimental study of train-induced vibration in over-track buildings in a metro depot," *Engineering Structures*, vol. 198, Article ID 109473, 2019.

[3] C. Zou, Y. Wang, P. Wang, and J. Guo, "Measurement of ground and nearby building vibration and noise induced by trains in a metro depot," *The Science of the Total Environment*, vol. 536, pp. 761–773, 2015.

[4] Z. Cao, T. Guo, Z. Zhang, and A. Li, "Measurement and analysis of vibrations in a residential building constructed on an elevated metro depot," *Measurement*, vol. 125, pp. 394–405, 2018.

[5] B. P. Y. Loo, C. Chen, and E. T. H. Chan, "Rail-based transit-oriented development: lessons from New York city and Hong Kong," *Landscape and Urban Planning*, vol. 97, no. 3, pp. 202–212, 2010.

[6] X. Ma and H. K. Lo, "On joint railway and housing development strategy," *Procedia-Social and Behavioral Sciences*, vol. 80, pp. 7–24, 2013.

[7] S. Shi, "Study on land development strategy for inter-city railway transport hub A case study of h station of the intercity railway from wuhan to x," *Procedia-Social and Behavioral Sciences*, vol. 216, pp. 172–180, 2016.

[8] D. Olaru, B. Smith, J. H. E. Taplin, and E. Taplin, "Residential location and transit-oriented development in a new rail corridor," *Transportation Research Part A: Policy and Practice*, vol. 45, no. 3, pp. 219–237, 2011.

[9] M. Ma, W. Liu, C. Qian, G. Deng, and Y. Li, "Study of the train-induced vibration impact on a historic Bell Tower above two spatially overlapping metro lines," *Soil Dynamics and Earthquake Engineering*, vol. 81, pp. 58–74, 2016.

[10] M. Ma, V. Markine, W.-n. Liu, Y. Yuan, and F. Zhang, "Metro train-induced vibrations on historic buildings in Chengdu, China," *Journal of Zhejiang University-Science*, vol. 12, no. 10, pp. 782–793, 2011.

[11] D. J. Thompson, *Railway Noise and Vibration: Mechanisms, Modeling and Means of Control*, Elsevier, Oxford, UK, 2008.

[12] G. Lombaert, G. Degrande, S. François, and D. J. Thompson, "Ground-borne vibration due to railway traffic: a review of excitation mechanisms, prediction methods and mitigation measures," in *Proceedings of the 11th International Workshop on Railway Noise*, pp. 9–13, Uddevalla, Sweden, September 2013.

[13] H. Zhang, Z. Ren, H. Zhang, and Q. Liu, "Simulation on metro railway induced vibration. Part I: effect of out-of-round wheels," *Vibroengineering Procedia*, vol. 29, pp. 130–135, 2019.

[14] C. Stüber, "Air- and structure-borne noise of railways," *Journal of Sound and Vibration*, vol. 43, no. 2, pp. 281–289, 1975.

[15] P. J. Remington, "Wheel/rail rolling noise: what do we know? What don't we know? Where do we go from here?" *Journal of Sound and Vibration*, vol. 120, no. 2, pp. 203–226, 1988.

[16] X. Zhang, R. Liu, Z. Cao, X. Wang, and X. Li, "Acoustic performance of a semi-closed noise barrier installed on a high-speed railway bridge," *Measurement and Analysis Considering Actual Service Conditions. Measurement*, vol. 138, pp. 386–399, 2019.

[17] L. Xu, M. Ma, R. Cao, X. Tan, and R. Liang, "Effect of longitudinally varying characteristics of soil on metro train-induced ground vibrations based on wave propagation analysis," *Soil Dynamics and Earthquake Engineering*, vol. 152, Article ID 107020, 2022.

[18] P. H. De Vos, "Railway noise: the physics of airborne sound generation and propagation," *Journal of Sound and Vibration*, vol. 193, no. 1, pp. 77–82, 1996.

[19] C. Talotte, P.-E. Gautier, D. J. Thompson, and C. Hanson, "Identification, modelling and reduction potential of railway noise sources: a critical survey," *Journal of Sound and Vibration*, vol. 267, no. 3, pp. 447–468, 2003.

[20] B. S. Institution, *ISO3095: 2005 Railway Applications—Acoustics—Measurement of Noise Emitted by Rail-bound Vehicles*, British Standards Institution, London, UK, 2005.

[21] C. Hurtley, *Night Noise Guidelines for Europe*, World Health Organization, Geneva, Switzerland, 2009, https://www.euro.who.int/__data/assets/pdf_file/0017/43316/E92845.pdf.

Hindawi
Advances in Civil Engineering
Volume 2022, Article ID 7864160, 9 pages
https://doi.org/10.1155/2022/7864160

Research Article

Clock Synchronization Algorithm for Structural Modal Measurement

Junliang Hu,[1,2] **Kai Li**,[3,4] **Chaoxian Yan**,[5] **Huawei Guo**,[5] **Nannan Cui**,[6] **Shiping Huang**,[3,4] **and Xiaoyan Ding**[7]

[1]*State Key Laboratory for Health and Safety of Bridge Structures, Wuhan 430034, China*
[2]*China Railway Bridge Science Research Institute, Ltd., Wuhan 430034, China*
[3]*School of Civil Engineering and Transportation, South China University of Technology, Guangzhou 510640, China*
[4]*China-Singapore International Joint Research Institute, Guangzhou, 510700, China*
[5]*Guangzhou Highway Engineering Group Co., Ltd, Guangzhou 510000, China*
[6]*School of Transportation Engineering, Shandong Jianzhu University, Jinan 250101, China*
[7]*Shandong Hi-Speed Group Co., Ltd., Jinan 250098, China*

Correspondence should be addressed to Nannan Cui; cuinannan18@sdjzu.edu.cn

Received 17 March 2022; Accepted 8 April 2022; Published 22 April 2022

Academic Editor: Wei He

The modal of a structure is the natural vibration characteristic of the structure, which is very important for damage identification of the system. To accurately measure the structural modal, it is necessary to perform clock synchronization operations on the vibration sensors at each measuring point of the structure. This paper uses an improved TSPN algorithm for clock synchronization. It is assumed that the delay of the data in the transmission process obeys normal distribution. The fitting degree of a normal distribution is tested by fitting the delay distribution curve. Then, an interval estimation method is used to estimate the delay. The synchronization of multiple sensors and onsite structural modal testing verifies the correctness of the process after synchronization. The method in this paper is suitable for MCU-based vibration sensors to perform clock synchronization for structural modal measurements.

1. Introduction

A modal corresponds to the natural frequency of a structure [1], and the system will show different vibration characteristics under the excitation of an external force at different frequencies. Clock synchronization is a critical issue [2]. Structural modals are usually obtained through conventional experimental modal analysis and testing methods. Vibration measurement points are arranged at different structure positions to obtain vibration information [3]. To ensure that each measuring point collects data simultaneously, it is necessary to synchronize the clock of each measuring point sensor device [4]. If the clocks are not synchronized, the vibration data collected by the terminal will have clock errors. For structural modal measurements, millisecond-level clock errors will cause deviations in structure modal acquisition [5].

To date, satellite navigation timing technology is the primary time synchronization scheme used in the new generation of wireless node instrument systems [6]. Due to the influence of machine error and too few tracking satellites [7], it is challenging to guarantee short-term accuracy and stability. In 2002, J. Elson and K. Romer [8] first proposed the concept of time synchronization in wireless sensor networks. Then, Elson designed a reference broadcast synchronization (RBS) algorithm. It is a receiver-receiver time synchronization algorithm for exchanging local time information for synchronizing a group of wireless sensors within the transmission range of a reference sensor node. MengYuan Chen et al. [9] proposed an improved RBS

algorithm. Based on the RBS algorithm, the algorithm adopts broadcast grouping and the least-squares linear regression method to realize the time synchronization of the whole network. Yong-Heng et al. [10] proposed an energy-efficient wireless sensor network reference broadcast time synchronization algorithm. Noh et al. [11] offered a receiver-only synchronization (ROS) algorithm, which presupposes a Gaussian distribution of random network delays to estimate clock skew. Gang Xiong et al. [12] studied the asymptotic expectation and mean square synchronization error of the SO-DCTS algorithm when a Gaussian delay occurs between network nodes. Panigrahi N et al. [13] improved network lifetime and reduced network latency by applying various techniques, especially node-balanced sets. Ganeriwal et al. [14] proposed a pairwise timing-sync protocol for sensor networks (TPSN). It is a simple method based on traditional send-receive time synchronization that synchronizes the entire network by exchanging timing messages along each branch (edge) of the hierarchical tree. Shi-Kyu Bae et al. [15] proposed a polling-based TPSN scheme that not only shortens the synchronization time of the whole network of TPSN but also reduces the conflicting traffic that leads to unnecessary power consumption. But it considers that the transmission delay is constant. Maroti et al. [16] proposed the flooding time synchronization protocol (FTSP), a sender-receiver time synchronization algorithm that cleverly eliminates network delays. Liang Qingjian et al. [17] proposed an improved FTSP time synchronization to eliminate the interference algorithm of outliers. Hai-ping Huang et al. [18] calculated the relative time drift and phase offset of nodes using a linear programming method based on the collection and selection principle of multitime data point tuples and finally achieved time synchronization in the process of building a data aggregation tree. Yun Peng Zhang et al. [19] improved the routing integrated time synchronization (RITS) protocol by averaging multiple sets of data received by the target node and constructing a best-fit straight line with numerous receiving pairs. Feng Mei Liang et al. [20] proposed an improved time synchronization algorithm for wireless sensor networks based on cross-layer optimization. The stability of crystal oscillation and the linearity of crystal deviation at the physical layer are considered. Maes et al. [21] quantified the error between the modal mode shape identified after the acquisition error and the actual situation by systematically collecting the MP value between the structural displacement (out of synchronization) and the structural strain modal shape. Du Yong-wen et al. [22] combined the one-way broadcast and two-way pairing mechanisms and proposed a hierarchical wireless sensor network time synchronization algorithm. Dragos et al. [23] achieved acquisition data synchronization by imposing an expected relationship between the phase angles of the Fourier spectra of the acceleration response dataset at peaks corresponding to vibration modes.

Based on the research above, this paper proposes an improved clock synchronization algorithm based on a TSPN, which is suitable for measuring the actual engineering structural modal using a sensor based on the MCU (microcontroller unit). This method assumes the random delay as Gaussian normal distribution. The fitting degree of the normal distribution of the delay is checked by combining the delay distribution curve, and then the local clock deviation between each sensor device and the terminal is estimated to perform time synchronization on the sensor devices at each measuring point. Finally, the method proposed in this paper is verified by onsite structural modal tests.

2. Wireless Sensor Clock Synchronization Algorithm

2.1. Wireless Sensor Time Synchronization Principle. In a structural modal measurement system, the terminal and vibration sensor devices are nodes, and each node is in the same network. Due to the different clock sources that each node obtains time information from, the starting timing point between nodes is different, and there is a time offset between the time the vibration sensor data of each node is sent and the time the terminal receives the data. This time offset consists of each node's local clock skew (S_t) and the nonfixed transmission delay (Δt).

The local clock skew (S_t) is the deviation of the starting point of the travel time caused by the different starting timing of each node. S_t is an essential parameter of clock synchronization. Without considering the influence of the vibration error of the internal quartz crystal of the clock, each node has its own time after adding S_t to the local time. Therefore, each node will be at the same starting time point, which can achieve the purpose of primary clock synchronization.

The nonfixed transmission delay (Δt) is the information transmission delay. When each node synchronizes the clock, it needs to obtain the timestamp information of other nodes. There will be a delay in the transmission of the timestamp between nodes. This delay is Δt.

A wireless sensor network time synchronization scheme aims to provide a standard timestamp for the local clocks of the nodes in the network.

2.2. TSPN Clock Synchronization Algorithm. A sensor time synchronization protocol TPSN is a two-way time synchronization algorithm based on a sender and receiver, providing time synchronization between nodes in the whole network. A TSPN assumes that each sensor node in the network has a unique ID. The wireless communication link between nodes is bidirectional, which can realize the time synchronization of nodes via a bidirectional message exchange.

The algorithm has two stages: grading and synchronization. The root node is set in the grading stage, the corresponding level of the root node is level 0, and the corresponding level is set for each node by using the root node. In the synchronization phase, the i-level node is synchronized with the $(i-1)$-level node, the $(i-1)$-level node with the $(i-2)$-level node, and the $(i-2)$-level node with the $(i-3)$-level node. Nodes are synchronized from bottom to top, and finally, all nodes are synchronized with the root

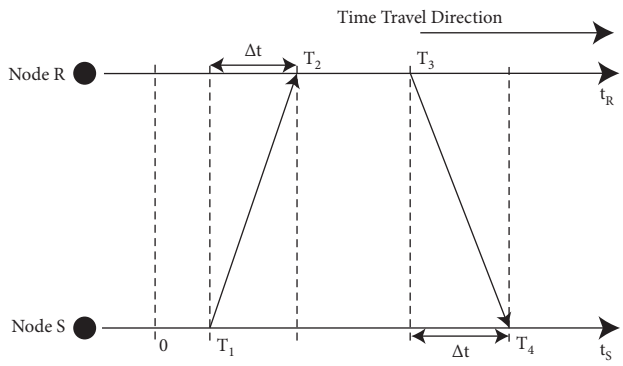

Figure 1: Time synchronization of adjacent level nodes.

node to achieve the time synchronization of the entire network.

Figure 1 shows the time synchronization process between adjacent level nodes exchanging two messages. Assume that, within a short period for single message exchange, there is no deviation in the internal quartz crystal vibration of the two node clocks and the transmission delay Δt is also constant in both directions. Node S belongs to the i-level node, and node R belongs to the $(i-1)$-level node. Node S sends a synchronization request to node R at time T_1. The synchronization request includes the level of node S and timestamp T_1. Node R receives the synchronization request at time T_2 and then sends a response at time T_3 to node S. The reply signal includes T_2 and T_3 time information. Node S receives the reply at time T_4. Times T_1 and T_4 are recorded by node S with timestamps, and T_2 and T_3 are recorded by node R with timestamps.

S_t is the local clock skew of the two nodes; then,

$$\begin{cases} T_2 = T_1 + S_t + \Delta t, \\ T_4 = T_3 - S_t + \Delta t. \end{cases} \tag{1}$$

You can obtain

$$\begin{aligned} S_t &= \frac{(T_2 - T_1) - (T_4 - T_3)}{2}, \\ \Delta t &= \frac{(T_2 - T_1) + (T_4 - T_3)}{2}. \end{aligned} \tag{2}$$

After node S calculates the time local clock skew S_t, it can synchronize it to node R.

In the delay component of network information transmission, access time is often the most uncertain factor in the delay of wireless transmission of messages. To improve the event synchronization accuracy between two nodes, the TPSN protocol adds a label to the synchronization message when the MAC layer message starts to be sent to the wireless channel, which eliminates the time synchronization error caused by the access time.

2.3. Improved TSPN Clock Synchronization Algorithm. The improved TSPN algorithm is based on the TSPN synchronization phase synchronization method. It considers the transmission delay in the two directions of the TSPN algorithm to be variable and considers that the transmission delay obeys a Gaussian normal distribution. The method is suitable for MCU-based vibration MEMS (micro-electro-mechanical system) sensors for clock synchronization of structural modal measurements [24].

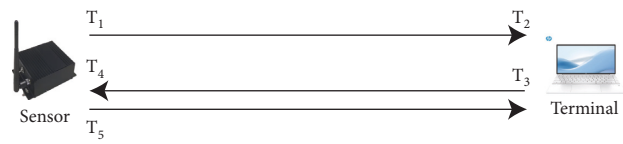

Figure 2: A timestamp exchange between a sensor and the terminal.

Figure 2 shows the timestamp information exchange between the vibration sensor and the terminal global clock device. The vibration sensor sends the value of timestamp T_1 to the terminal. The terminal receives the data at time T_2. At the same time, it obtains the data, sends an instruction to the vibration sensor at time T_3, and records timestamp T_3. Finally, the vibration sensor receives the instruction at time T_4. It records the value of timestamp T_4 (to record the value of timestamp T_4, timestamp T_4 needs to be sent to the terminal, as shown in Figure 2, and the vibration sensor sends timestamp T4 to the terminal at time T5 after receiving the terminal information). Such a model of exchanging timestamp information in one round is completed. At this time, four timestamps are recorded in one synchronization process between the vibration sensor and the terminal.

Assuming that the transmission delay from the sensor to the terminal is Δt_1 and the transmission delay from the terminal to the sensor is Δt_2, then

$$\begin{cases} T_2 = T_1 + S_t + \Delta t_1, \\ T_4 = T_3 - S_t + \Delta t_2. \end{cases} \tag{3}$$

$(\Delta t_1 + \Delta t_2)$ for a round trip can be obtained as

$$\Delta t_1 + \Delta t_2 = (T_2 - T_1) + (T_4 - T_3). \tag{4}$$

Delays Δt_1 and Δt_2 obey a Gaussian normal distribution because the primary source of random noise in the hardware circuit is thermal noise, which has Gaussian distribution characteristics, and the random jitter of crystal vibration is independent of each other at each time point, and according to the central limit law, many independent and uncorrelated noise sources are superimposed and approach a Gaussian distribution [25].

According to Gaussian normal distribution and statistical principles [26], when Δt_1 and Δt_2 obey a Gaussian normal distribution, $(\Delta t_1 + \Delta t_2)$ and $(\Delta t_1 + \Delta t_2)/2$ both obey a normal distribution. If $\Delta t_1 \sim N(\mu_1, \sigma_1^2)$ and $\Delta t_2 \sim N(\mu_1, \sigma_2^2)$, then $(\Delta t_1 + \Delta t_2) \sim N(\mu_1 + \mu_2, \sigma_1^2 + \sigma_2^2)$ and $(\Delta t_1 + \Delta t_2)/2 \sim N(\mu_1 + \mu_2/2, \sigma_1^2 + \sigma_2^2/4) \sim N(\mu_1 + \mu_2/2, \sigma_1^2 + \sigma_2^2/4)$.

On the premise of taking a sufficiently large sample of the transmission delay, after n rounds of timestamp information exchange, the transmission delay Δt between a vibration sensor and the terminal can be estimated by the sample mean $\overline{\Delta t_{12}} = \overline{\Delta t_1 + \Delta t_2}/2$:

$$\overline{\Delta t_{12}} = \frac{1}{2n}\sum_{i=1}^{n}\left[\Delta t_1(i) + \Delta t_2(i)\right]. \quad (5)$$

The transmission delay $\overline{\Delta t_{12}}$ sample variance S^2 is

$$S^2 = \frac{\sum_{i=1}^{n}\left[\left(\Delta t_1(i) + \Delta t_2(i)/2 - \Delta t\right)\right]^2}{n-1}. \quad (6)$$

Δt_1 and Δt_2 are independent of each other, and another calculation method for the obtained sample variance $S^2(\overline{\Delta t_{12}})$ is

$$\begin{aligned} S^2 &= \frac{S^2(\Delta t_1) + S^2(\Delta t_2)}{4}, \\ &= \frac{\sum_{i=1}^{n}\left(\Delta t_1(i) - \overline{\Delta t_1}\right)^2 + \sum_{i=1}^{n}\left(\Delta t_2(i) - \overline{\Delta t_2}\right)^2}{4(n-1)}. \end{aligned} \quad (7)$$

Δt is estimated, and the clock deviation S_t of the sensor and the device is further obtained by

$$S_t = T_i - T_{i-1} - \Delta t \quad i = 1, 2, \ldots, n. \quad (8)$$

In engineering structural modal measurement, when the acquisition frequency is 250 Hz and the real-time clock deviation of a vibration sensor does not exceed ± 2 ms, the data collected by the vibration sensor can be guaranteed at one point in time. When the vibration sensor and terminal exchange timestamp information, the terminal reads its own time and bounces an instruction to the vibration sensor while receiving the timestamp information of the vibration sensor. The time when the terminal readout corresponds to T_2 in Figure 2 and when a command is bounced to the vibration sensor corresponds to T_3 in Figure 2. It can be seen that the time difference between T_3 and T_2 is only the time required for terminal time operation. If the central frequency of a terminal CPU is 2.0 GHz, the oscillation period is 0.5 ns. It takes 12 oscillation periods to read an instruction in the memory, so the terminal reading time only takes tens of nanoseconds, which is the nanosecond level. Therefore, T_3 can be equivalent to T_2. Similarly, corresponding to the vibration sensor, the time difference between T_5 and T_4 is the time taken by the vibration sensor to read its clock. If the vibration frequency of the vibration sensor's CPU crystal oscillator is 32 MHz, the time required to read its clock is only a few microseconds, so T_5 can be equated to T_4.

After ignoring the time when the terminal and the vibration sensor execute their reading time, the n round-trip timestamp information interaction between the vibration sensor and the terminal is shown in Figure 3.

From Figure 3, the transmission time of one round trip can be obtained by only using the two adjacent time differences of the vibration sensor or the terminal. The transmission delay $(\Delta t_1 + \Delta t_2)$ is

$$\left(\Delta t_1(i) + \Delta t_2(i)\right) = T_{2i} - T_{2i-2} \quad i = 1, 2, \ldots, n. \quad (9)$$

In (9), $\Delta t_1(i)$ and $\Delta t_2(i)$ represent the delay of the i-th timestamp interaction.

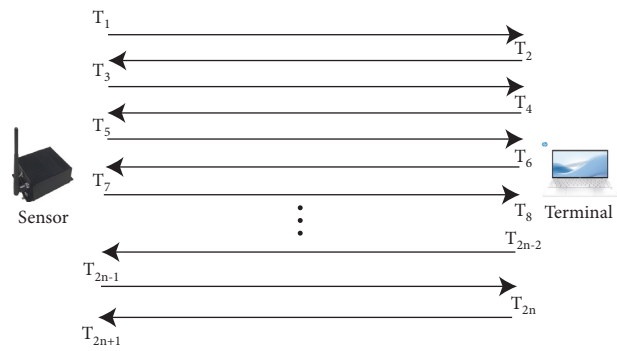

Figure 3: Actual sensor and terminal timestamp exchange.

3. Clock Synchronization Experiment

3.1. Random Delay Distribution Fitting Verification. The author's self-developed vibration sensor is used in the clock synchronization experiment. The sensor MCU integrates a real-time clock, and its central clock vibration frequency is 32 MHz. The terminal is an HP EliteDesk 880 G5 TWR, and the internal PC processor is an Intel(R) Core(TM) i7-9700 CPU @ 3.00 GHz.

This experiment collects four sets of data, approximately 10,000 data transmissions for the first and second times and approximately 20,000 data transmissions for the third and fourth times to verify that the round-trip transmission delay $(\Delta t_1 + \Delta t_2)$ distribution obeys a normal distribution and fits a normal distribution curve using MATLAB to fit the normal distribution curve. The results of the four sets of randomly selected data are shown in Figure 4 and 5.

Figures 4 and 5 show that the round-trip transmission delay $(\Delta t_1 + \Delta t_2)$ distributions of the four sets of data are fitted by MATLAB and fit normal distribution very well.

Through formulas (5) and (6), the sample mean $(\overline{\Delta t_{12}})$ and sample standard deviation (S) of the transmission delay of the four sets of data are further obtained, as shown in Figures 6 and 7, respectively.

As seen from the above figures, the sample mean $(\overline{\Delta t_{12}})$ and standard deviation (S) are very stable, and the random delay data are highly stable and obey the same normal distribution.

The sample mean $(\overline{\Delta t_{12}})$ and standard deviation (S) of the delay distribution in the above four sets of experiments are shown in Table 1.

3.2. Random Delay Credibility Validation. It can be seen from the above normal fitting that the transmission delay Δt conforms to a normal distribution, and when a sample is used to replace the population, that is, $\Delta t \sim N(\overline{\Delta t_{12}}, S^2)$, the probability that the transmission delay is in a specific interval range can be calculated from four sets of experimental data as shown in Table 2.

When the above four sets of samples are used to replace the population, when $4.2 < \Delta t < 6.2$, that is, the interval probability that the mean distance $\overline{\Delta t_{12}}$ is ±1 ms

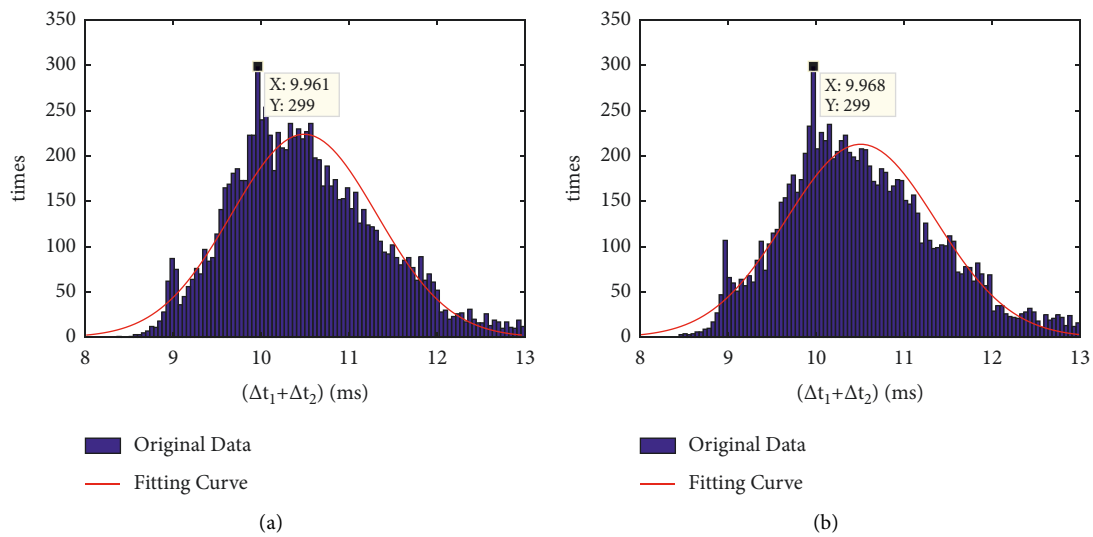

Figure 4: Distribution of 10,000 random data delays. (a) The first set. (b) The second set.

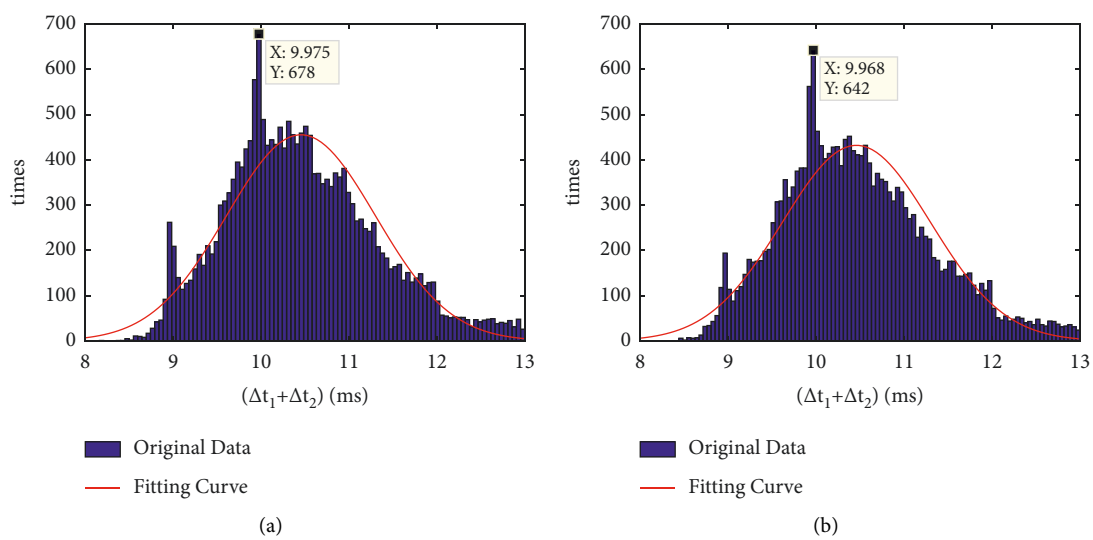

Figure 5: Distribution of 20,000 random data delays. (a) The third set. (b) The fourth set.

which is approximately 0.98, the requirements of the actual engineering structural modal measurement of 500 Hz are met.

3.3. Random Delay Value. Section 3.2 verified that the random delay sample has a high degree of convergence near the sample mean, which meets the requirements of the clock synchronization error for modal measurement of an actual engineering structure.

According to the principle of a normal distribution, when the random variables are in $X \sim N(\mu, \sigma^2)$, $X_1, X_2 \ldots, X_n$ are the samples of population X and $\overline{X}$ and S^2 are the sample mean and sample variance, respectively; then,

$$T = \frac{\overline{X} - u}{S/\sqrt{n}} \sim t(n-1). \tag{10}$$

In formula (10), $t(n-1)$ is the t distribution with $n-1$ degrees of freedom, and $t(n-1)$ is a standard normal distribution $N(0,1)$ when $(n \longrightarrow \infty)$.

In the above transmission delay experiment, the sample value is large enough, and if μ_z is the population mean, the random delay value is

$$\frac{\Delta t - \mu_z}{S/\sqrt{n}} \sim N(0,1)\mathbb{Z}. \tag{11}$$

Furthermore, the confidence interval of the population mean μ is obtained using an interval estimation method. Interval estimation is a strict interval estimation theory

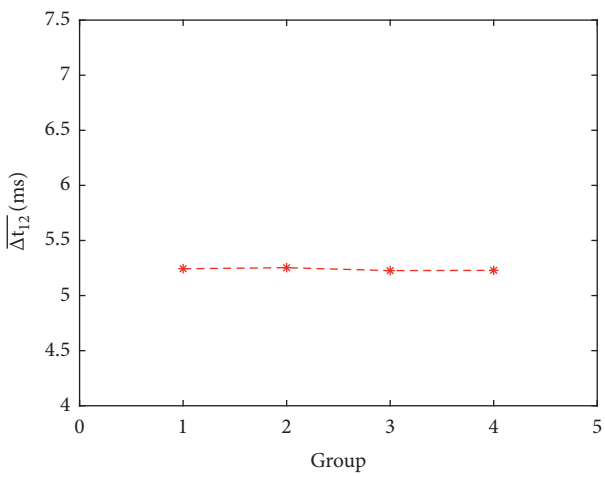

Figure 6: Distribution of the random delay sample mean ($\overline{\Delta t_{12}}$).

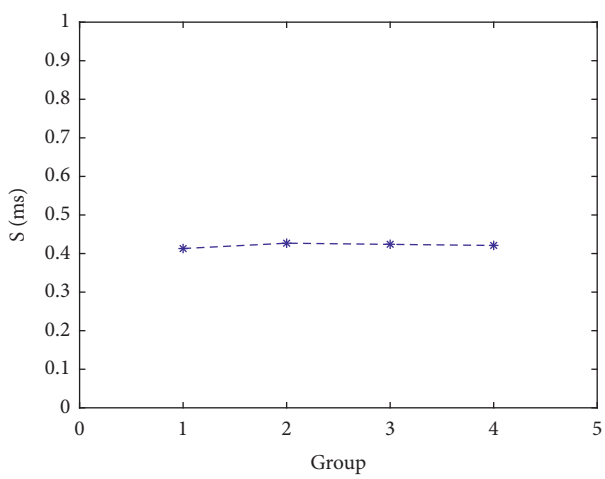

Figure 7: Distribution of the random delay sample standard deviation (S).

Table 1: Random transmission delay sample mean ($\overline{\Delta t_{12}}$) and sample standard deviation (S).

Transmission delay set	$\overline{\Delta t_{12}}$ (ms)	S (ms)
Set 1	5.2436	0.4130
Set 2	5.2530	0.4268
Set 3	5.2265	0.4241
Set 4	5.2290	0.4211

created by statistician Neiman in 1934. According to the samples drawn and the requirements of certain correctness and precision, an appropriate interval is constructed as an estimate of the range of the actual value of the unknown parameter of a population distribution or a function of the parameter. For example, it is often said that a particular value is guaranteed to be within a specific range by a certain percentage, which is the most straightforward application of interval estimation.

Let $F(x, \theta)$ be the distribution function of population X, θ is the unknown parameter to be determined, and $X_1, X_2, \ldots, X_n$ are the samples of the population X. For a given parameter $(1-\alpha)\cdot(0<\alpha<1)$, if there is a statistic, $\theta_2 = \theta_2(X_1, X_2, \ldots, X_n)$,

$$\begin{aligned} P\{\theta < \theta_1\} &= P\{\theta > \theta_2\}, \\ &= \frac{\alpha}{2}. \end{aligned} \tag{12}$$

Therefore, $P\{\theta_1 < \theta < \theta_2\} = 1-\alpha$, (θ_1, θ_2) is called the two-sided confidence interval of $(1-\alpha)$ of θ, $(1-\alpha)$ is called the confidence degree, and θ_1 and θ_2 are the lower line and upper limit of the two-sided confidence interval of θ, respectively.

The confidence interval of each confidence level for the population mean μ_z of the four sets of data is as follows.

Table 3 shows that when the confidence levels of μ_z are guaranteed to be 0.95, 0.98, and 0.99 for each set of data, the value range of μ_z is within the scope of a gap of 0.6 ms, and the total capacity is 5.21~5.27 ms.

μ_z is obtained when the highest confidence of 0.99 is used. The overlapping part of each sample (excluding the second set) ranges from 5.2330 ms to 5.2342 ms, and the mean value of 5.2336 ms is taken as the overall mean μ_z, that is, the delay Δt between the vibration sensor and the terminal is measured at this time.

4. Clock Synchronization Experimental Verification

4.1. Clock Synchronization Verification. Δt between the vibration sensor and the terminal is obtained using Gaussian normal distribution statistical theory to obtain S_t from formula (8), and this S_t is added to the local sensor clock to synchronize with the terminal global time.

To further verify the correctness of the method, the clock of another vibration sensor is synchronized with the terminal according to the above process, and its timestamp is sent to the terminal device every 10 ms after synchronization is completed to verify whether the real-time clocks of the two sensors are consistent.

Table 4 shows the real-time clock times of the two sensors after clock synchronization.

From Table 4, the transmission delay is approximately 5 ms. After the clock is synchronized, the real-time clocks of the two sensors are consistent, and clock synchronization has been completed accurately.

4.2. Onsite Modal Measurement Experiment. The onsite modal measurement structure is a 60 m aerial corridor in the Guangzhou Financial City. The corridor structure is a simply supported truss beam structure. The modal measurement points are arranged as shown in Figures 8 and 9.

Vibration sensors are arranged at each measuring point after clock synchronization is completed. Using the resonance method [27], the corridor is continuously excited using a fundamental frequency load, and the data of

Table 2: Distribution probability of random delay (Δt).

Set	Distribution probability of Δt (ms)				
	$3.2 < \Delta t < 7.2$	$4.2 < \Delta t < 6.2$	$4.7 < \Delta t < 5.7$	$\overline{\Delta t_{12}} - S < \Delta t < \overline{\Delta t_{12}} + S$	$\overline{\Delta t_{12}} - 2S < \Delta t < \overline{\Delta t_{12}} + 2S$
Set 1	0.9999	0.9834	0.7713	0.6826	0.9544
Set 2	0.9999	0.9801	0.7554	0.6826	0.9544
Set 3	0.9999	0.9812	0.7606	0.6826	0.9544
Set 4	0.9999	0.9822	0.7636	0.6826	0.9544

Table 3: The population mean μ_z takes the two-sided confidence interval of each confidence level.

Interval confidence set	0.95	0.98	0.99
Set 1	(5.2355, 5.2517)	(5.2339, 5.2532)	(5.2330, 5.2542)
Set 2	(5.2446, 5.2613)	(5.2431, 5.2629)	(5.2420, 5.2639)
Set 3	(5.2206, 5.2324)	(5.2195, 5.2335)	(5.2187, 5.2342)
Set 4	(5.2232, 5.2348)	(5.2221, 5.2359)	(5.2213, 5.2367)

Table 4: Sensor real-time clock times.

Sensor 1	Sensor 2	Terminal reception time
17 : 24 : 01.872	17 : 24 : 01.872	17 : 24 : 01.878
17 : 24 : 01.882	17 : 24 : 01.882	17 : 24 : 01.887
17 : 24 : 01.892	17 : 24 : 01.892	17 : 24 : 01.897
17 : 24 : 01.902	17 : 24 : 01.902	17 : 24 : 01.907
17 : 24 : 01.912	17 : 24 : 01.912	17 : 24 : 01.917
17 : 24 : 01.922	17 : 24 : 01.922	17 : 24 : 01.927
17 : 24 : 01.932	17 : 24 : 01.932	17 : 24 : 01.937

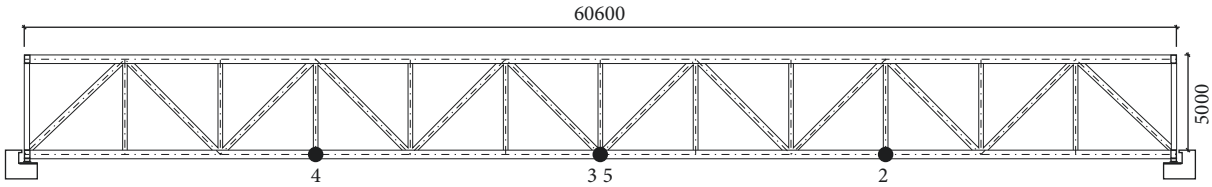

Figure 8: 60 m aerial corridor structure vibration test point layout (front view).

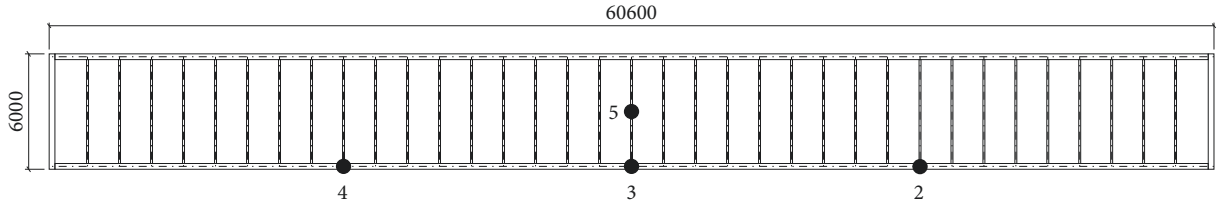

Figure 9: 60 m aerial corridor structure vibration test point layout (top view).

Table 5: Displacement of measuring points at each time.

Time (ms)	Displacement of each position (mm)		
	1/4 span (left)	Midspan	1/4 span (right)
40	−0.4189	−0.6184	−0.4012
80	−0.6322	−0.9742	−0.6787
120	−0.0316	−0.0511	−0.0297
160	0.3919	0.5639	0.3816
200	0.6634	0.9281	0.6711
240	0.4812	0.6734	0.4796

measurement point 2 (the right 1/4 span of the corridor), measurement point 3 (the middle side of the span), and measurement point 4 (the left 1/4 span of the corridor) are obtained. The displacements of the right 1/4 span at 50 ms, 100 ms, 150 ms, 200 ms, 250 ms, and 300 ms are as follows (Table 5).

The fitting diagram of the displacement of the measuring points at each time is shown in Figure 10).

In Figure 10, It can be seen from the displacement data of each measuring point that, in the case of fundamental

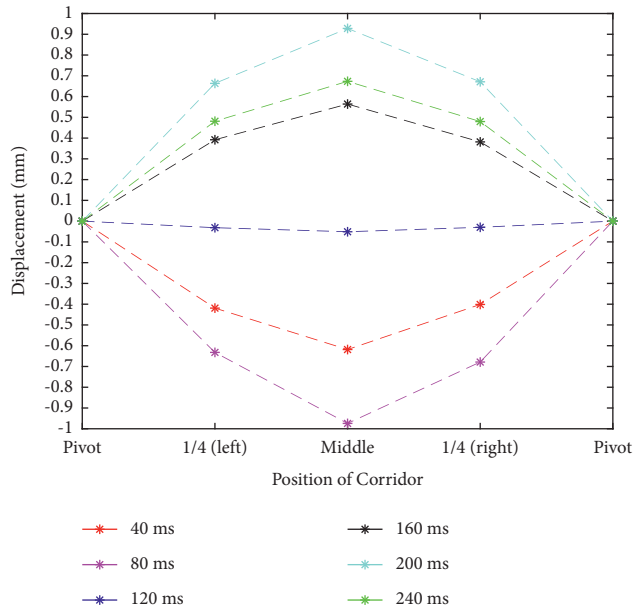

Figure 10: Real-time displacement curve of the corridor.

frequency excitation, the first-order modal of the corridor structure conforms to a sine function, and no time synchronization occurs, indicating that the clock synchronization is successful.

5. Conclusions

The clock synchronization algorithm for structural modal measurement proposed in this paper improves the TSPN algorithm. It is assumed that the random delay of the data in the transmission process obeys Gaussian normal distribution, and the correctness of the random delay following a Gaussian normal distribution is verified experimentally.

(1) Various hierarchical classifications of delay in the transmission process are simplified. The entire transmission delay Δt is considered as a whole, and it is statistically verified that Δt obeys normal distribution.

(2) Based on the structural modal measurement, data receiving time T_2 and data sending time T_3 in the TSPN transmission process are reduced to one time, simplifying the delay calculation method.

(3) When considering the error range of random delay Δt, this method can be combined with statistical knowledge to probabilistically verify the degree of convergence of the random uncertainty to its mean.

(4) When selecting the value of the random delay Δt, the interval estimation of the random delay Δt can be carried out according to the method in this paper to meet the confidence level of the modal measurement requirements. The most accurate statistical value of Δt can be obtained.

(5) In the modal measurement of an actual engineering structure, the method of this paper is combined with a vibration sensor based on MCU, the programming is simple and convenient, and it is suitable for user development.

(6) To verify the correctness of the clock synchronization algorithm, the feasibility of modal measurement using the clock synchronization algorithm for an actual engineering structure is demonstrated through an example analysis.

Data Availability

The data used to support the findings of this study are included within the article.

Disclosure

Junliang Hu and Kai Li are co-first authors.

Conflicts of Interest

The authors declare that they have no conflicts of interest.

Authors' Contributions

Junliang Hu conceptualized the study; Junliang Hu and Nannan Cui took part in methodology; Kai and Shiping Huang provided software; Xiaoyan Ding and Nannan Cui validated the study; Chaoxian Yan and Huawei Guo contributed to data curation; Kai Li wrote the original draft; Shiping Huang and Junliang Hu reviewed and edited the manuscript; Nannan Cui supervised the study. Junliang Hu and Kai Li contributed equally to this work.

Acknowledgments

This paper was supported by the Natural Science Foundation of China (NSFC) (Grant nos. 11672108 and 11202080) and

Science and Technology Project of Shandong Transportation Department (2020B69). This work was also supported by "the Fundamental Research Funds for the Central Universities."

References

[1] S. Huang, H. Zhang, P. Chen, Y. Zhu, and E. Zuazua, "An energy-based vibration model for beam bridges with multiple constraints," *Structural Engineering & Mechanics*, vol. 82, no. 1, pp. 41–53, 2022.

[2] B. Sundararaman, U. Buy, and A. D. Kshemkalyani, "Clock synchronization for wireless sensor networks: a survey," *Ad Hoc Networks*, vol. 3, no. 3, pp. 281–323, 2005.

[3] C. M. Ferregut, R. A. Osegueda, and J. Ortiz, "Artificial neural networks for structural damage detection and classification," in *Smart Structures and Materials 1995: Smart Systems for Bridges, Structures, and Highways: International Society for Optics and Photonics*, San Diego, CA, USA, pp. 68–80, 1995.

[4] J. Elson, L. Girod, and D. Estrin, "{Fine-Grained} network time synchronization using reference broadcasts," in *Proceedings of the 5th Symposium on Operating Systems Design and Implementation (OSDI 02)*, vol. 36, no. SI, Boston, MA, USA, December 2002.

[5] V. Krishnamurthy, K. Fowler, and E. Sazonov, "The effect of time synchronization of wireless sensors on the modal analysis of structures," *Smart Materials and Structures*, vol. 17, no. 5, Article ID 055018, 2008.

[6] S. Zhou, X. Hu, L. Liu, F. He, C. Tang, and J. Pang, "Status of satellite orbit determination and time synchronization technology for global navigation satellites system," *Acta Astronomica Sinica*, vol. 60, no. 4, p. 32, 2019.

[7] J. A. R. Rose, J. R. Tong, D. J. Allain, and C. N. Mitchell, "The use of ionospheric tomography and elevation masks to reduce the overall error in single-frequency GPS timing applications," *Advances in Space Research*, vol. 47, no. 2, pp. 276–288, 2011.

[8] J. Elson and K. Römer, "Wireless sensor networks," *ACM SIGCOMM - Computer Communication Review*, vol. 33, no. 1, pp. 149–154, 2003.

[9] M. Chen and C. Zhu, "Research on time synchronization algorithm of high precision and low power consumption based on IRBRS WSNs," *Wireless Personal Communications*, vol. 95, no. 3, pp. 2255–2270, 2017.

[10] Z. Yong-Heng and Z. Feng, "A new time synchronization algorithm for wireless sensor networks based on internet of things," *Sensors & Transducers*, vol. 151, no. 4, p. 95, 2013.

[11] K.-L. Noh and E. Serpedin, "Pairwise broadcast clock synchronization for wireless sensor networks," in *Proceedings of the 2007 IEEE International Symposium on a World of Wireless, Mobile and Multimedia Networks*, pp. 1–6, IEEE, Espoo, Finland, June 2007.

[12] G. Xiong and S. Kishore, "Discrete-time second-order distributed consensus time synchronization algorithm for wireless sensor networks," *EURASIP Journal on Wireless Communications and Networking*, vol. 2009, Article ID 623537, 12 pages, 2008.

[13] N. Panigrahi and P. M. Khilar, "Multi-hop consensus time synchronization algorithm for sparse wireless sensor network: a distributed constraint-based dynamic programming approach," *Ad Hoc Networks*, vol. 61, pp. 124–138, 2017.

[14] S. Ganeriwal, R. Kumar, and M. B. Srivastava, "Timing-sync protocol for sensor networks," in *Proceedings of the 1st international conference on Embedded networked sensor systems*, Virtual Event, Japan, pp. 138–149, November 2003.

[15] S.-K. Bae, "A revised timing-sync protocol for sensor networks by a polling method," *Journal of the Korea Society of Computer and Information*, vol. 20, no. 8, pp. 23–28, 2015.

[16] M. Maróti, B. Kusy, G. Simon, and A. Lédeczi, "The flooding time synchronization protocol," in *Proceedings of the 2nd international conference on Embedded networked sensor systems*, Baltimore, MD, USA, pp. 39–49, November 2004.

[17] Q. Liang, S. Ji, P. Guo, X. Xu, and J. Wang, "Study on time synchronization algorithm for structural health monitoring based on wireless sensor networks," in *Intelligent Systems and Applications*IOS Press, Amsterdam, Netherlands, 2015.

[18] H.-p. Huang, R.-c. Wang, L. Liu, L.-j. Sun, and W.-f. Li, "Time synchronization algorithm of wireless sensor networks based on data aggregation tree," *The Journal of China Universities of Posts and Telecommunications*, vol. 17, pp. 24–29, 2010.

[19] Y. P. Zhang, Z. Zheng, S. X. Zheng, Y. T. Huang, and Y. H. Karanfil, "The research of RITS time synchronization algorithms in WSN," in *Applied Mechanics and Materials*, Trans Tech Publ, Zurich, Switzerland, 2013.

[20] F. M. Liang and B. Liu, "Self-correcting time synchronization based on cross layer for wireless sensor network," in *Applied Mechanics and Materials*Trans Tech Publ, Zurich, Switzerland, 2012.

[21] K. Maes, E. Reynders, A. Rezayat, G. D. Roeck, and G. Lombaert, "Offline synchronization of data acquisition systems using system identification," *Journal of Sound and Vibration*, vol. 381, pp. 264–272, 2016.

[22] D. Yong-wen, X. Ning, L. Hui-ling, L. Wei, and F. Ke, "A hierarchical time synchronization algorithm for WSN," *Procedia Computer Science*, vol. 131, pp. 1064–1073, 2018.

[23] K. Dragos, M. Theiler, F. Magalhães, C. Moutinho, and K. Smarsly, "On-board data synchronization in wireless structural health monitoring systems based on phase locking," *Structural Control and Health Monitoring*, vol. 25, no. 11, Article ID e2248, 2018.

[24] J. Zhu, W. Wang, S. Huang, and W. Ding, "An improved calibration technique for mems accelerometer-based inclinometers," *Sensors*, vol. 20, no. 2, p. 452, 2020.

[25] J. Michalowicz, J. Nichols, and F. Bucholtz, "Calculation of differential entropy for a mixed Gaussian distribution," *Entropy*, vol. 10, no. 3, pp. 200–206, 2008.

[26] G. Casella and R. L. Berger, *Statistical Inference*, Cengage Learning, Boston, MA, USA, 2021.

[27] C. R. Farrar and James III, "System identification from ambient vibration measurements on a bridge," *Journal of Sound and Vibration*, vol. 205, no. 1, pp. 1–18, 1997.